STRUCTURAL FAILURE AND FRACTURE OF IMMATURE BONE

Vee San Cheong

Department of Bioengineering

Imperial College London

A thesis submitted for the degree of Doctor of Philosophy of Imperial College London and the Diploma of Imperial College

October 2014

DECLARATION

This dissertation is the result of my own work and all work that is not my own, including any assistance received, have been acknowledged. It has not been previously submitted, in part or whole, to any university of institution for any degree, diploma, or other qualification.

Every child deserves a chance

at a life filled with love,

laughter, friends and family.

-Marlo Thomas

Oh God, I am thinking Thy thoughts after Thee

- Johannes Kepler

ABSTRACT

Radiological features alone do not allow the discrimination between accidental paediatric long bone fractures or those caused by child abuse. Therefore, for those cases where the child is unable to communicate coherently, there is a clinical need to elucidate the mechanisms behind each fracture to provide a forensic biomechanical tool for clinical implementation. 5 months old ovine femurs and tibiae were used as surrogates for paediatric specimens and were subjected to μCT scans to obtain their geometrical and material properties. A novel methodology to align long bones so that they would be loaded in a state of pure bending and torsion was developed and compared against the use of a standard anatomical coordinate system. The second moment of area and its coefficient of variation (COV) for each alignment method were calculated to ascertain the reference axes that minimised the effect of eccentric loading. Wilcoxon-signed rank test showed a significant reduction in COV of the second moment of area using this new method, indicating that the bone has a more regular cross-section when this methodology is implemented. The algorithm generated the locations of subject-specific landmarks that can be used as a reference to align the bones in experimental testing. A low-cost platform that synchronized the data acquisition from the tensile testing machine and the strain gauges was built and used with a high speed camera to capture the fracture pattern in four-point bending at three strain rates and in torsion at two different strain rates, following commonly reported case histories. Finite element (FE) models of ovine tibiae in their optimised alignment were generated to replicate the fracture patterns that were obtained. Fracture initiation and propagation was simulated through the use of element deletion with a maximum principal strain criterion. The experiments produced transverse, oblique, and spiral fractures consistently, which were correlated with the finite element analysis, demonstrating the ability of this pipeline to now be adapted for use in forensic analysis.

ACKNOWLEDGEMENTS

I am immensely thankful to my supervisor Professor Anthony Bull for all his help and guidance over the past few years. His passion and enthusiasm for research has inspired and influenced me greatly while his critical analysis and innovativeness have honed my thinking skills and analytical capabilities. Dr Pocha Meher has shown me clinical insights that I never imagined I would have the opportunity to be a part of, and has inspired me through her constant belief that the quality of life can always be improved.

I would like to extend my deepest thanks to Professor Andrew Amis and Camilla Halewood for their kindness and support given in the experimental work. They have provided valuable resources and advice that made all the testing work possible.

I am especially grateful for the friendship of Dr Kaiyu Zhang, who provided valuable counsel, thought-provoking discussions, and encouragement throughout the course of my PhD.

A thesis of this nature would not have been made possible without the pastoral support of various people. I owe my since thanks to Rikke Juul, Leila Steeds, Sarah-Jo McClellan and Mary Bowe who walked with me at different stages of my PhD journey. I am also immensely thankful to Marsh Moyle and Merram Paul for showing me how to order chaotic thoughts and made the production of this thesis a reality. The drawing of a sheep in this dissertation is especially dedicated to Marsh.

Special thanks also to John Barrs who helped to proofread the initial drafts of this thesis and gave valuable suggestions on developing my writing style. I am also thankful to my family for the feedback provided on the diagrams and pictures in this thesis.

I am extremely grateful for the financial support from the Department of Bioengineering and the Singapore Institute of Management, without which this research would have never happened.

Finally, I like to thank the creator of wonders, without whose help none of these would have happened.

CONTENTS

LIST OF TABLES

LIST OF FIGURES

1 INTRODUCTION

Bone plays an important role in the healthy functioning of the human body by supporting its weight, protecting vital organs, interfacing with muscles to enable locomotion and providing a reservoir of minerals for homeostasis. Bone fracture, the final catastrophic failure of bone, is thus always tragic as it brings about severe disruption to life with further impact on the social economy. Improvements in the assessment, detection, and prevention of injuries may be achieved through developing an understanding of the biomechanics of the injury and failure mechanism, but existing work on the structural behaviour of mature bone is not applicable for immature bones. The growing child has a different bone structure from an adult, and thus the fracture pattern that a child sustains is different from an adult given the same injury mechanism (Ogden, 2000). Moreover, with the formative years of the child remaining, the bone will continue to remodel and grow but the injury must be treated aptly to prevent further damage on the bone. This involves the proper diagnosis of the injury at the first instance, including the identification of occult causes of injuries, which may then require the child to be removed from the care-givers for their protection.

The field of child abuse is believed to be under-diagnosed clinically, despite the 2004 estimate of 860,000 child abuse victims in the United States, and the incidence rate of 1/1000 children in the United Kingdom, in 2007 (Gaudiosi et al., 2006; Singleton, 2010). There are numerous challenges surrounding the detection of child abuse, but the primarily cause is the propensity of the guilty care-giver to attribute the cause of the injury to an accident. Moreover, very little is

known about how immature bone breaks at the structural level, making it difficult to distinguish between accidental injuries, and those caused maliciously. The characterization of the structural behaviour of immature bone is an essential part of understanding its response to loads at different strain rates. This, combined with a database of experimentally validated fractures that are correlated with common case histories, could help to develop an objective platform that forensically identifies the cause of the injury.

1.1 Aims

The long-term aim of this research is to develop an objective tool that may be used in forensic analysis to give an assessment of the confidence that the verbal case history of an injury as given by the care-giver is an accurate reflection of the injury mechanism. To allow non-accidental injuries to be identified, work needs to be done to ascertain the force required to cause a fracture and also to generate patient-specific models that are consistently able to predict the fracture patterns observed in radiological images. Since access to paediatric specimens is very limited for the identification of the required load to failure to be carried out, the immediate aims are to understand the mechanisms behind some common fracture patterns through the generation of consistent fracture patterns in experimental testing at different strain rates and replicating these in computer simulations. By ensuring that the underlying physics is correct, the qualitative evidence that is required to ascertain the consistency of the provided narrative is thus produced. This was to be achieved via a series of intermediate aims:

i. selection of an appropriate surrogate model for human paediatric bone,

ii. development of an alignment method so that bone may be subjected to a state of pure bending and pure torsion,

iii. designing and building a platform that synchronizes the acquisition of results, and minimizes the effect of eccentric loading in experimental testing,

iv. successful generation of consistent fracture patterns at different strain rate in bending and torsion, and

v. development of finite element models that replicate the fracture patterns that were generated in experimental testing.

1.2 Thesis Organisation

This thesis is divided into 7 chapters including the introduction.

Chapter 2 describes the clinical factors motivating this research. The types of bones to study and the fracture morphologies to focus on are discussed in this chapter.

Chapter 3 reviews the available literature on the material and mechanical properties of immature bones, and surveys the characteristics of various animal models before deciding on the appropriate surrogate model for human paediatric bone.

Chapter 4 details the development of the methodology that aligns bone to its principal direction so that it may be subjected to a state of pure bending or torsion when an appropriate load is applied. The results are compared against the use of an anatomical coordinate system.

Chapter 5 discusses the development of the experimental setup that minimises the effect of eccentric loading. The results of testing ovine tibiae in four-point bending and torsion at two different strain rates in-vitro are documented here.

Chapter 6 describes the modelling approach that was used to replicate the fracture patterns generated in experimental testing, at the two strain rates. It also presents the results of the fracture propagation process and its comparison with experimental results

Chapter 7 is a summary of the work in this thesis with recommendations for future work

2 Clinical Drivers for Immature Bone Fracture Research

2.1 Introduction

The presence of multiple injuries on a child often suggests to clinicians that he or she may be suffering from non-accidental injuries (NAI). In situations where NAI is missed, the child may suffer from further physical and emotional abuse, thereby stunting his/her eventual growth, intellectual and emotional development, or even death (Jayakumar et al., 2010; Stotts, 2007). Yet, despite advances made in the identification of clinical features of NAI, it still makes up 49% of all trauma admission of children below 1 years old and it remains the main cause of homicide in children below the age of 5, suggesting that recognizing NAI remains challenging for some injuries (Leventhal, 1999). Conversely, a wrongful accusation of innocent families may lead to the unwarranted separation of the child from his/her family (Kowal-Vern et al., 1992; Pierce & Bertocci, 2008).

The difficulty in recognizing an abused child is exacerbated when a child presents with a single injury that is commonly seen in clinical practice, but not specific for abuse, and with a seemingly plausible case history that explains the cause of fracture (Leventhal, 1999; Pierce et al., 2004).

Common fractures that have a low specificity include mid-clavicular fractures, simple linear skull fractures and single long-bone fractures. However, fractures of the extremities stand out as the most common orthopaedic occurrence in infants and young children, and they account for 31-76% of all fractures in NAI cases (Caffey, 1946; King et al., 1988; Loder et al., 2006; Worlock et al., 1986).

The figures for NAI cases are obtained from retrospective studies of NAI where the cases have been confirmed either through an admission of abuse by the caregiver; or the cases were later treated as NAI, through the presentation of multiple fractures for example; or further investigation by a social care team lead to the conclusion that it was a NAI (Strait et al., 1995; Tenenbein et al., 1990). The range of values reported above reflects differences in the population of patients, sample size, and the composition of the types of fracture, which may affect the incidence rate that was reported Therefore, the purpose of this chapter is first to review the fracture incidence of various long bone fractures, followed by fracture morphology. Thirdly, the current methods for detecting NAI are discussed and finally, how the development of a tool that allows for the simulation of paediatric injuries could potentially shed light on the direction, magnitude, and route of forces that cause one injury or another, and improve injury assessment.

2.2 Incidence rate and epidemiology of long bone fractures

The incidence of NAI peaks between 0-3 years of age and the probability that a fracture was inflicted intentionally is inversely proportional to age (Hoskote et al., 2003; Loder et al., 2006; Skellern et al., 2000). NAI makes up 49% of all trauma admission of children below 1 year old (Loder & Bookout, 1991), but may be as high as 80% (Worlock et al., 1986). For children younger than three years old, Kowal-Vern et al. (1992) found the figure to be 23%. In these 3 studies, all cases of trauma were included in their studies, which may have affected the results, depending on the number of automobile-related cases.

Among battered children, Loder and Bookout (1991) found that 40% of the victims were 6 months of age or less, 67% were less than 1 year of age and 80% were less than 2 years of age. An earlier study of 189 paediatric victims by King et al. (1988) found that 130 (69%) children

were below 1 year old, 26 (14%) were above 2 years old and 23 (12%) were between 1 to 2 years old. Similarly, Akbarnia and colleagues (1974) and Loder et al. (2006) found that infants below the age of 1 composed the bulk of the children studied at about 48%. These results have convinced many authors that young and immobile children are most vulnerable to child abuse (Jayakumar et al., 2010; Kraft, 2011; Schwend et al., 2000).

2.2.1 Fracture location

Mid-shaft or diaphyseal injures have been found to occur four times more frequently than metaphyseal injuries, with the most common of them involving the humerus, tibia or femur (King et al., 1988). Unlike the Classic Metaphyseal Lesion (CML), which is caused by shearing forces in bone not commonly caused in accidents, a single diaphyseal long bone fracture can be caused in both accidental and non-accidental cases (Caffey, 1946). Indeed, single long bone fractures that made up 28-53% of NAI cases in children under the age of one was the result of NAI (Carty, 1993; Kowal-Vern et al., 1992; Loder & Bookout, 1991). The clinical challenge in diagnosing NAI from long bone fracture can be seen in the huge variation in the prevalence of NAI reported in epidemiology studies. Moreover, it must be noted that many studies focussed on the sum total of fractures, which does not paint an accurate picture due to a large range of multiple fractures that were considered. The emphasis on the total number of fractures instead of the number of children does not truly reflect the fact that clinicians deal with children one at a time.

2.2.2 Femoral shaft fracture

Femoral shaft fractures may only make up 28-45% of all isolated long bone fracture (Carty, 1993; King et al., 1988; Loder & Bookout, 1991), but the risk that a femoral fracture is the result of abuse may be as high as 92% (Rex & Kay, 2000). However, the detection of NAI in femoral shaft fracture is compounded by the fact that similar injuries could be sustained in children who fall while learning to walk (Thomas et al., 1991). A conflicting view has also been presented, as a rather controversial paper by Schwend and workers in 2000 stated that femoral fractures are hardly caused by child abuse, which is contrary to the mainstream belief that femoral fractures are highly suggestive of abuse (Carty, 1993; Thomas et al., 1991). In their

studies, 139 children under the age of 4 with an isolated femoral shaft fracture were studied, and it was concluded that 91% of the children were likely to have suffered the fracture as a result of an accident. This figure is much higher than that reported by other teams previously. Their method of classification was based on the 7-point scale developed by Thomas et al. (1991), which has been widely adapted for use by many teams. Nevertheless, the inclusion of motor vehicle accidents and only femoral shaft fractures in their studies would bias the result towards fractures that are accidental in nature. The lack of follow up on the final outcome of the injury means that the true situation is not reflected and the child continues to be exposed to further risk of being harmed by an abusive caregiver

2.2.3 Humeral shaft fracture

Among the three most common types of fractures in the long bones, humeral fracture carries the highest risk of having been the result of abuse at 48% (Kemp et al., 2008). However, variations in population and differences in criteria used in conducting the studies, has resulted in a range of probability of abuse reported by different authors. Strait et al. (1995) reported that they found humeral fractures that were caused by abuse to be less common than expected, which is a product of the use of a stricter criteria in their studies. All other available studies believe that fractures of the humerus point strongly to abuse, at a prevalence of 46-78% (Merten et al., 1983; Thomas et al., 1991; Worlock et al., 1986). However, the lack of comparison among various case histories and their biomechanics means that no definite conclusion can be drawn.

2.2.4 Tibial and fibular fractures

Tibial fractures are the third most common long bone fractures after humeral and femoral fractures, but the incidence rate has also been found to vary widely. In a retrospective study involving 95 isolated tibial fractures in patients between 3 months to 17 years old, Yang and Letts (1997) reported only 3 cases of NAI. The youngest subject was a victim of NAI and it is unfortunate that the authors did not provide any more details about the age of the other victims. In another study involving patients below the age of three, one out of eight tibial fracture was reported to be caused by abuse (Kowal-Vern et al., 1992). However, the statistics continue to

go on an increasing trend as the age range is decreased to less than 18 months old; in a study of this age group 23 out of 24 tibial fractures were the product of NAI (Coffey et al., 2005).

In children, complete fracture of the tibial complex has been found to occur in only 30% of all tibial fractures. Such fractures often have an accompanying history of the patient being involved in a high-energy traumatic event (Shannak, 1988; Yang & Letts, 1997). Nevertheless, isolated oblique or spiral fractures of the tibia caused by low-energy impact are often subtle and difficult to identify in radiological images (Mashru et al., 2005). Moreover, in a retrospective study involving tibial midshaft and distal fractures, four out of thirty-seven tibial fractures occurred in the midshaft and were the result of maltreatment. It is disconcerting to note that half of them were originally treated as accidental injuries and NAI was only picked up when the further injuries were presented. There were also two fractures that occurred in the distal tibial where abuse was suspected on the basis of the trivial case history provided. However, the two cases were subsequently determined to be caused unintentionally (Tenenbein et al., 1990). Although it has been suggested that abuse-related fractures are found more frequently in the femur than the tibia or fibula (Kemp et al., 2008; Kowal-Vern et al., 1992), there is no discriminating clinical feature to back up such a claim. Historically, femoral fracture has attracted the attention of more researchers, as 15 studies involving the femur, 4 involving the humerus and only 2 involving the tibia were found and included in a large scale system review of NAI (Kemp et al., 2008), indicating a clear clinical need to understand tibial fractures better.

2.3 Failure Analysis

A fracture is a manifestation of the final catastrophic failure of a material, and the fracture pattern that results is a product of the microscopic and macroscopic properties of the object. More details on the structure of bone will be covered in Chapter 3, and although the geometry of bone prevents it from being treated as an Euler-Bernoulli or even Timoshenko beam, it is nevertheless useful to consider the behaviour of such a structure, as it represents the simplest case possible. From a structural perspective, materials can either be classified as ductile or brittle. The fracture patterns that result are thus different as ductile materials fail in shear whereas brittle materials fail in normal stress (or normal strain). Therefore, the orientation where normal or shear stress (or strain) is a maximum is where an object is most likely to fail. Moreover, when

an object is in this alignment, maximum principal stress or maximum shear stress (or the strain counterparts) can be used as failure criteria to model the propagation of crack (see Chapter 6). The following section is interpreted and explained primarily using Hibbeler and Fan (2004) as a source, but similar information can also be found in any good solid mechanics textbook.

Stress (or strain) transformation is the name given to the engineering practice that calculates the stress and strain components associated with each orientation. For the ease of discussion, only stresses will be referred to thereafter. The principal stresses then refer to the orientations where the stress is at a maximum and a minimum and their corresponding axes are known as the principal axes. Any object that is loaded will experience 6 independent normal and shear stress but for simplicity, the two-dimensional case of plane stress will be discussed below to illustrate how the principal directions may be found.

Figure 2.1A shows the general case of plane stress when an object in loaded. No shear stress is present in the state of principal stresses, as seen in Figure 2.1B, and the magnitudes may be found using the equation below:

$$\sigma_{I,II} = \frac{1}{2}(\sigma_x + \sigma_y) \pm \sqrt{\left[\frac{\sigma_x - \sigma_y}{2}\right]^2 + {\tau_{xy}}^2}$$

where σ refers to the normal stress components, τ to the shear stress, and the subscripts I and II refer to the maximum and minimum principal stress respectively.

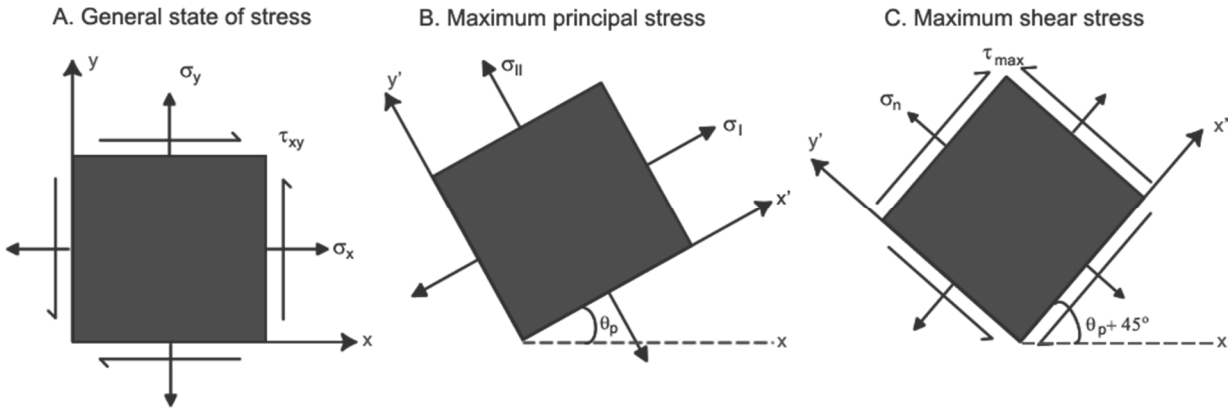

Figure 2.1: For any object that is loaded, its general state of stress at a point (A) can be used to find the orientations (θ_p) where maximum principal stress, σ_I , and minimum principal stress, σ_{II}, are experienced (B). No shear stress is experienced in this state. The object experiences maximum shear stress at 45° to the principal axis, and normal stress σ_n is also present (C). These are directions where an object is most likely to fail.

The maximum shear stress always occurs at 45° to the direction of the principal stress (Figure 2.1C) and its magnitude is:

$$\tau_{max} = \sqrt{\left[\frac{\sigma_x - \sigma_y}{2}\right]^2 + {\tau_{xy}}^2}$$

However, unlike the case in principal stresses where no shear stress exists, there are normal stresses acting on the planes of maximum in-plane shear stress:

$$\sigma_n = \frac{\sigma_x + \sigma_y}{2}$$

The two simplest cases of loading that an object can experience are pure torsion and axial loading. In pure torsion, only a shear component is applied and the maximum shear stress is experienced in the same direction as the applied stresses (Figure 2.2).

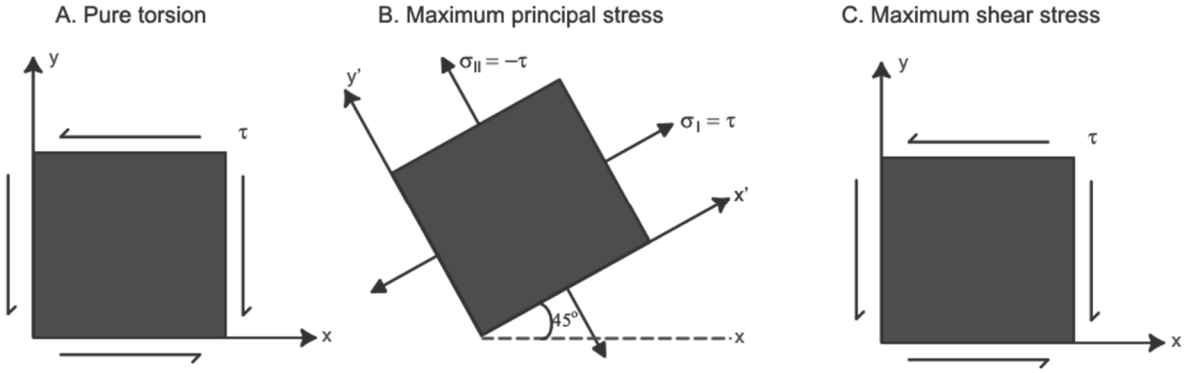

Figure 2.2: When an object is subjected to pure torsion, it experiences only shear stress, and the direction where maximum shear stress is experienced (C) is the same as its general state of stress (A). A ductile material fails in shear and a transverse (orthogonal) fracture will result whereas a brittle material at 45° due to normal stress (maximum principal stress) (B).

In contrast, when an axial load is applied, the orientations of the maximum principal stress and the maximum shear stress are opposite to the case of pure torsion (Figure 2.3).

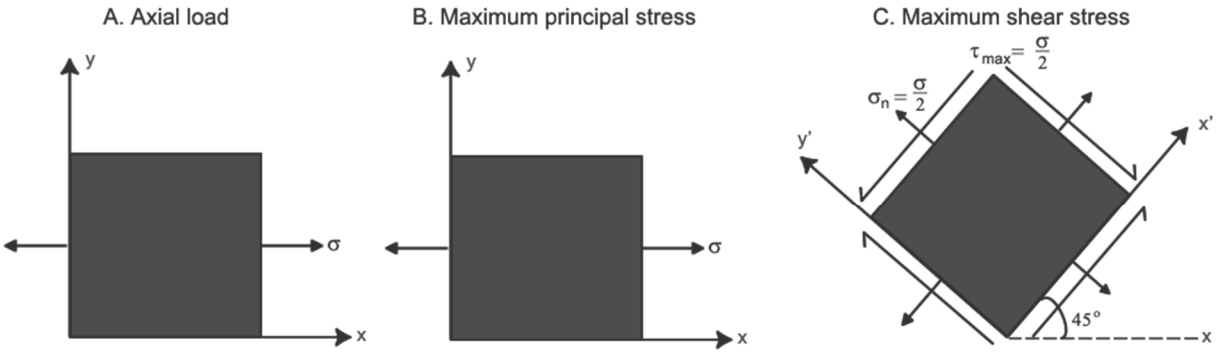

Figure 2.3: The general state of stress at a point (A) is the same as its state of maximum principal stress (B) when an axial load is applied. The state of maximum shear stress occurs 45° to the principal direction with normal stresses present. Brittle materials exhibit a transverse fracture pattern when subjected to axial loading whereas ductile materials fail at 45° due to shear stress.

Building up from the two examples given above, in all other conditions of combined loading, the principal directions are thus located between 0 and 90° and that depends on the magnitude of the normal and shear components. The directions of the principal stress, θ_p, and maximum shear stress, θ_s, are thus:

$$\tan 2\theta_p = \frac{2\tau_{xy}}{\sigma_x - \sigma_y}$$

$$\tan 2\theta_s = \frac{-\frac{1}{2}(\sigma_x - \sigma_y)}{\tau_{xy}}$$

The three-dimensional case falls under the theory of 3D elasticity, and may be extended from the Euler-Bernoulli beam theory discussed thus far, although it must be noted that beams are a special case of the former. In the 3D case, there are three planes that exhibit zero shear stress. The normal stresses on these planes are also at a maximum or a minimum, resulting in three principal stresses with maximum, intermediate, or minimum intensity.

2.4 Fracture Morphology

Spiral fractures have traditionally received much attention, even though oblique and transverse fractures have also been observed to occur widely (King et al., 1988; Loder et al., 2006; Stotts,

2007; Worlock et al., 1986). All common fracture patterns will be discussed here as no fracture is pathognomonic of abuse (Leventhal, 1999) (Figure 2.4).

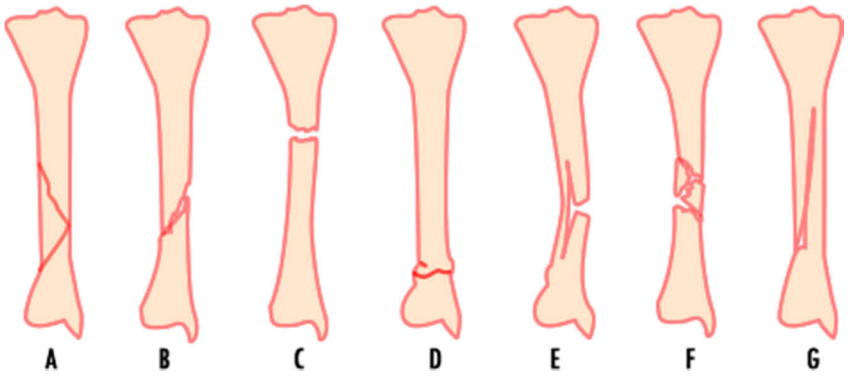

Figure 2.4: Some possible fracture patterns in the tibia of a child: (A) spiral; (B) oblique; (C) transverse; (D) buckle; (E) greenstick, (F) comminuted and (G) longitudinal [adapted from Ogden (2000)]

2.4.1 Spiral fracture

Femoral spiral fracture is one of the most common fracture patterns in children less than 15 months old (King et al., 1988; Rex & Kay, 2000), and may be caused by accidents such as tripping while running (Thomas et al., 1991). Spiral fracture is viewed clinically as the result of a torsional force applied along the longitudinal axis of the bone (Figure 2.5A), where the torque causes one part of the bone to be subjected to compression while the other side undergoes tension at an angle from the longitudinal axis (Pierce & Bertocci, 2008; Turner & Burr, 1993). Since bone fails in tension, the result is a fracture plane that encircles a portion of the shaft (Figure 2.4A) (Pierce et al., 2004). From a straightforward mechanical understanding this is incorrect as torsion produces pure shear and no axial stress (see Section 2.3). In a study conducted by Kress and colleagues in 1995, it was found that spiral fractures in mature bones were caused only by torsional loading. However, in-vitro torsional loading conducted on femurs of the piglet failed to generate spiral fractures consistently (Pierce et al., 2000), causing doubts on the proposed etiology for immature bones.

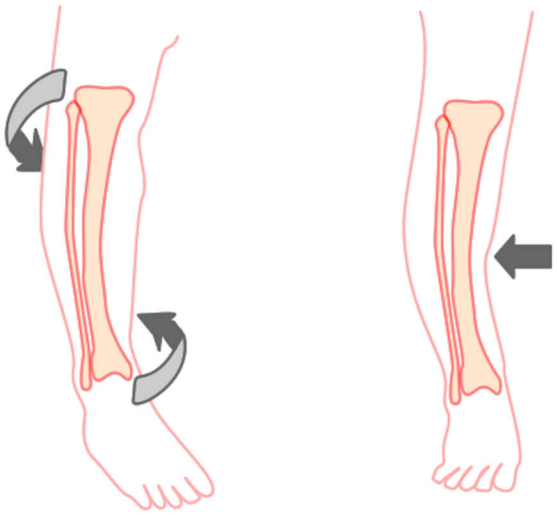

Figure 2.5: Clinically accepted mechanisms of injury that will produce (A) a spiral fracture and (B) a transverse fracture [adapted from Cramer and Green (2009)].

2.4.2 Oblique fracture

Oblique fractures often look similar to spiral fractures on X-ray, yet unlike spiral fracture which is thought to be caused by pure torsion, oblique fracture is believed to be caused by a combination of loading (Pierce et al., 2004). Oblique fractures are currently classified into 2 forms: long oblique fractures angled at 30-45° that results from torsional loading that dominates compressive forces (Figure 2.4B), and short oblique fractures that occur due to the increased effect of transverse loading caused by compressive or bending forces over torsional loads (Levine, 2002). However, the authors have not considered the possibility of tensile forces, which would affect the final fracture pattern. Moreover, as seen in Section 2.3, the current classification of oblique fractures is highly simplistic as the types of fracture patterns that may result is dependent on the magnitude and directions of the compressive, tensile and shear stresses present.

A combination of compressive load and bending moment applied together can result in an oblique fracture if the bone exhibits higher elasticity, or comminuted fractures if it has a lower elasticity (Kress et al., 1995; Pierce et al., 2004). Nevertheless, the former group noted that oblique fracture with multiple fragments may also be caused by transverse loading of the long bone.

2.4.3 Transverse fracture

Transverse fractures are characterized by fracture lines normal to the longitudinal axis of the bone (Figure 2.4C), and can be caused by tensile loads or bending moments in three-point bending (Jones, 2009, p. 12; Ogden, 2000, p. 51). In the case of bending, the force applied causes bone to be subjected to compression at one region but under tension in another region. The transverse fracture that results will reflect both types of loading (Levine, 2002; Turner & Burr, 1993).

Transverse fractures may be caused directly, such as when an object is used to impact the bone, or indirectly, such as when the child falls and hits an object or surface (Figure 2.5B). The fracture tends to be comminuted and displaced when a direct trauma, especially one of high linear momentum, is applied to the bone (Figure 2.4F) (Pierce & Bertocci, 2008). However, greenstick (or incomplete) fractures could be caused when a blow is dealt to a bone as well (Figure 2.4E) (Jones, 2009, p. 11).

2.4.4 Buckle fracture

Buckle (or torus) fracture commonly occurs at the metaphyseal region, and at the proximal and distal third end of the bone Figure 2.4D). It results from axial loading that causes compressive forces to be transmitted to the bone, such as when a child falls from a significant height and lands on his knee (Pierce et al., 2004). A widely accepted view amongst doctors is that this fracture pattern occurs due to differences in the strength of the diaphyseal and metaphyseal bones (Jones, 2009, p. 11). The fracture pattern results when failure in compression causes the stronger diaphyseal bone to crush into the weaker metaphyseal bone.

A general consensus amongst clinicians is that that buckle fractures may result when toddlers and older children stretch out their arms to break a fall, but being less stiff means that it was not possible for them to withstand the impact (Pierce et al., 2004). However, this viewpoint is faulty as stiffness is not a measure of strength, even though there is often a relationship between stiffness and strength (Zioupos & Currey, 1998). In cases of abuse, it has been found that the bone was intentionally hyperflexed in order to inflict pain on the child (Pierce et al., 2004).

2.4.5 Greenstick fracture

Greenstick fracture occurs only in children and only when a bone is loaded under bending. The tension side breaks but the cortex and the periosteum remain relatively intact on the compressive side (Figure 2.4E). The compressive bone is plastically deformed and cannot return to its original state. In adult bones, the fracture will propagate through the compressive side resulting in a transverse fracture. However, in children, greenstick fractures are incomplete and stable fractures because part of the bone remains intact and unbroken (Jones, 2009, p. 12; Ogden, 2000, p. 53).

2.4.6 Comminuted fracture

Comminuted fracture (Figure 2.4F) shows the presence of several fracture planes, which indicates that the load applied is large. However, this fracture pattern is not prevalent in young children (Ogden, 2000, p. 51).

2.4.7 Longitudinal fracture

An incomplete fracture with little sign of plastic deformation of the bone, longitudinal fracture is characterised by a fracture plane that is parallel to the long axis of the bone shaft (Figure 2.4G). It can occur in combination with other fracture patterns, but is seen more commonly with spiral fractures (Ogden, 2000, p. 51).

2.5 Detection of child abuse

A multidisciplinary approach is required for the detection of child abuse, but often the first suspicion of NAI begins as the examining physician evaluates the injuries of the young patient (Carty & Pierce, 2002; Radesky & Sugar, 2009). Care is taken to record a detailed history and evaluate its compatibility with the observed injury, taking into account the developmental status and medical conditions of the patient. There are two parts in this process, and the first is to check if the fracture morphology on the radiographs is possibly caused by the explanations given. The fracture patterns that are highly suggestive of child abuse, such as the metaphyseal corner, are also marked. Secondly, the radiologist needs to date all pathological features on the X-rays, especially for signs of previous fractures that are healing.

A full skeletal survey is then conducted on all patients with suspected NAI below the age of two, with the aim to detect bone malformations and the presence of other occult fractures and their age. Details on the requirements of the skeletal survey may be found in the standards set out by the Royal College of Radiology (RCR) and Royal College of Paediatrics and Child Health (RCPCH) in the UK or the American College of Radiology in the United States, which are identical apart from the requirements of oblique radiographs of the ribs (Offiah et al., 2009).

Thereafter, any radiological finding of metaphyseal fractures, rib fractures, multiple fractures, fractures at different stages of healing, complex skull fractures, occult fractures, and long bone fractures in a pre-ambulatory child warrants further assessment and the paediatric team or child protection team would be called in. Further images may be taken 11-14 days after the initial skeletal survey. As signs of healing have a better contrast on radiographs, this procedure is carried out as a check against the original X-rays taken. Furthermore, sometimes hairline fractures may not show up on day one and a later X-Ray would reveal the original injury because of the signs of healing.

At this stage, histological analysis may also be conducted to detect for signs of inflammation of other injuries. It has the added aim of confirming or ruling out any existing nutritional deficiency or metabolic conditions, such as osteogenesis imperfecta or rickets which may elevate the propensity of sustaining a fracture even with negligible injury or force, such as during normal day to day activities.

In the UK all cases of suspected NAI are referred to Children's Social Care who will arrange a multi-agency Child Protection Case Conference to determine the best way to take forward the investigation and management of the child and family. Some of the cases are referred either to a Family Court for a Care Order or to a Criminal Court for prosecution of the suspected perpetrator. For the former the level of evidence is on the "balance of probability" and for the latter "beyond reasonable doubt" that NAI has occurred.

The child will then come under the care of social services if the accused were found to be guilty. However, at any one point during the investigation, authorized agencies may apply for a court order to safeguard the wellbeing of the child, such as for authorization to remove the child to a safe place.

2.6 Proposed framework

The child protection framework set out in the UK is robust, but it is not without its shortcomings. As seen in this chapter thus far, the detection of child abuse falls under the category of evidence-based medicine. The onus of picking out potential cases of NAI falls primarily on the clinician examining the child together with the radiologist. However, limited formal education on child abuse and the low incidence rate of NAI pose a great challenge for doctors to become proficient at diagnosing NAI (Leventhal, 1999). Moreover, although clinicians are taught the various mechanisms of injuries, little research has been done to confirm these fracture patterns and with their mechanisms, hence the mechanisms are likely to be incorrectly described as discussed above, and there is no objective tool that exists to check the fracture threshold of each child's bone. Therefore, clinical judgement is still required in estimating the force required to cause the injuries, and in deciding if the case history provided is probable or not (Leventhal, 1999; Worlock et al., 1986).

The cost to society is high as money is wasted on litigation, loss of jobs, loss of man-hours, and taxpayers' money wasted on investigations and incarceration (Pierce & Bertocci, 2008). In 2003, at the conclusion of the inquiry into the death of Victoria Climbié, a victim of child abuse, Lord Laming recommended that cases of non-accidental injuries should be treated with the same rigour as any life-threatening condition. Moreover, he stated that there is a need to develop models to equip clinicians in the diagnosis of deliberate harm (Laming, 2003, p. 300). Therefore, a system to test objectively the possibility that an injury is caused non-accidentally to augment the current system is proposed. The case history provided by the caregiver is put through a transfer (a quantitative interpretation) to convert the words of the case history into an envelope of specific possible force(s) and moment(s) that were applied to the child. Information on the geometry and material properties would also be obtained through the use of a suitable imaging technology, such as computed tomography, to build up a model of the child's bone. These two pieces of information would be put through finite element analysis to obtain the plausible fracture patterns. This would then be compared with the fracture pattern in the radiological images to give a confidence indicator on the extent to which the case history is supported by the radiological features seen (Figure 2.6).

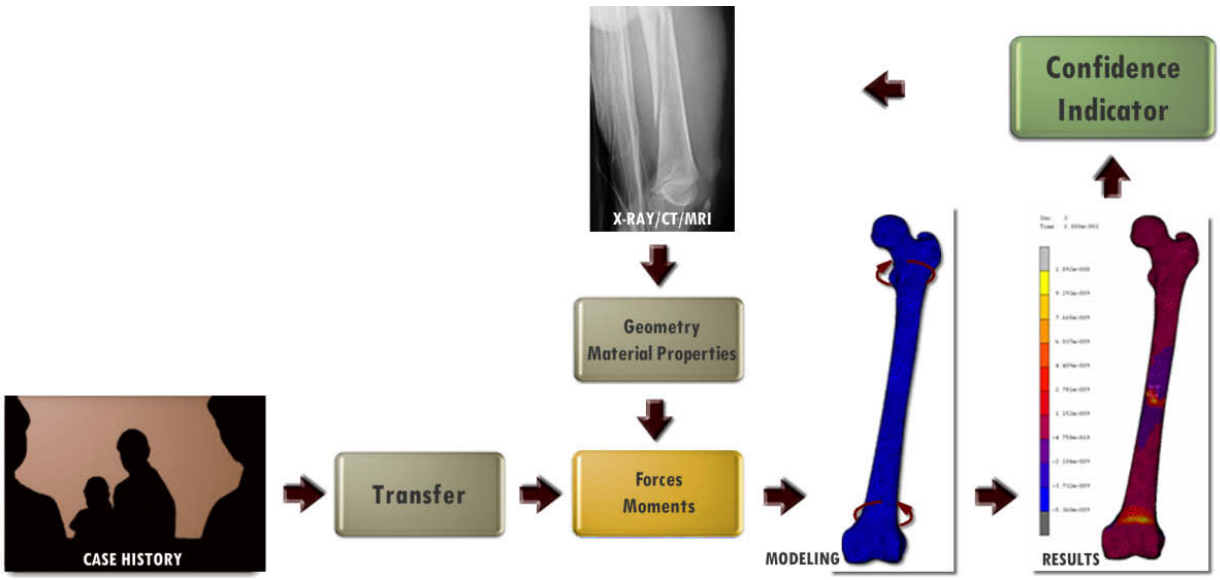

Figure 2.6: Proposed framework to augment the current method of detecting non-accidental injuries (NAI) by adding an objective method to validating the case history provided by the caregiver against images of the fractured bones taken.

Therefore, by focussing on the mechanism of injury and producing fractures in the state of pure bending and torsion, the work of this thesis falls within the second part of the proposed framework – to build up a fidelic subject-specific model of the long bone and check the simulation results with the fracture morphology on the radiological images. Another part of the system that needs developing is a methodology that is able to translate the case history given by the caregivers into a set of loads, with appropriate magnitudes and directions, to be input into the computer model. This requires extensive work through the use of anthropomorphic models to build up a database of resultant forces that are mapped to common case histories. Further work on statistical shape modelling would also need to be undertaken to make the system workable for any child bone morphology at any age and weight. Being limited by the unavailability of a detailed case history and taped recording to estimate the amplitude and direction of loads, this thesis will focus on replicating common fracture patterns of spiral, transverse and oblique types by testing bones in a state of pure bending and torsion. The results will then serve as a validation method for the finite element model. Thus this thesis represents the first attempt at understanding the mechanism of injury under the conditions of pure bending and torsion.

2.7 Summary

Inaccurate assessment of paediatric fractures that lead to incorrect diagnosis of NAI is highly undesired. An abused child that slips through the current system of detecting NAI is exposed to higher risk of further harm and damage. Conversely, a wrongful accusation of an innocent caregiver is equally damaging to the family, with an added cost to society on the money spent on unnecessary investigations.

The greatest challenge in identifying NAI occurs when clinicians are faced with a single, diaphyseal fracture. No one single pattern of fracture points definitively to child abuse and doctors are often required to call upon their clinical experience. In addition, epidemiology studies conducted through the years on the probability of the types and locations of fractures caused by NAI has added little value to the detection of NAI. This is unfortunate as they have no common standards or criteria and each study has its own inherent biases. Moreover, the prevalent beliefs on the causes of fractures that make one suspicious of abuse have not been backed up by rigorous research, and thus there is little education available for clinicians to become skilled at detecting NAI. All these problems and challenges point to a need for a better approach to understand bone fractures.

The development of a model that allows for the simulation of case histories and that could differentiate abusive from accidental injuries would have an impact on the detection of NAI. However, the complex biological nature and geometry of bone require the model to be validated against experimental results before it could be useful in injury prediction. As available paediatric specimens are very scare, a suitable surrogate animal model needs to be carefully selected to develop this framework further. Therefore, the topic of the next chapter will be on the literature review of animal models for bone fracture research.

3 Animal Models for Bone Fracture Research in Children: A Review

3.1 Introduction

There are many comparative studies on the selection of animal models for orthopaedics or biomaterial research, but they pertain mainly to the adult population, with scarce comparative discussion on the features and qualities of the immature bone. As mentioned in Chapter 2, a comparative approach is appropriate for the analysis of immature bone due to the lack of availability of paediatric data. As such, this chapter presents a review of the pertinent features of paediatric bones first, then the factors of consideration in selecting an animal model, before considering the similarities and difference between the model and humans.

3.2 Features of the immature paediatric bones

3.2.1 Strength

One of the earliest insight into children's bone was on how their ultimate tensile stress increased with age, but the average tensile strain showed no significant difference with age thus suggesting stiffening of the bone with increasing age. This information was gleaned from the work of

Hirsch and Evans (1965) who obtained bone material from femurs of infants and a 14 year old boy at autopsies. Having made them into dumbbell shape in the longitudinal direction, with a minimum of dimension of 25 mm long, 1mm thick and 3-4mm wide, fillets were then made to reduce the width of the middle section to 1.3mm, leaving the length 5mm long. A strain gauge was fixed to the middle of the specimen before tensile testing was conducted at a constant speed of 0.1cm/min.

Although the authors grouped the results into two groups – newborn to 6 months old and the 14 years old boy, it would have been more appropriate to further classify the infant group into two groups – newborn to 2 months old infant, and 6 month old infant, as some babies begin sitting up at 6 months. The changes in bone architecture that allows a child to begin to sit up would definitely show up as changes in material properties. In this new classification, the ultimate tensile stress increased from 9.55 (±2.34) kg/m^2 to 11.34 (±0.31) kg/m^2 to 17.63 (±2.10) kg/m^2 (Hirsch & Evans, 1965).

However, Vinz (1970), who later expanded Hirsch and Evans (1965)' studies by studying the material properties of cortical bones from new-borns to the eighty-five years old in tension, showed conclusively that there were was an increase in ultimate tensile stress and elastic modulus throughout the process of skeletal maturity until the age of about forty, matched by an increase in mineralization. The positive correlation between age and ash density, resulting in greater strength and elastic modulus was confirmed in bending by Currey and Butler (1975), who conducted three-point bending of 20mm long beams at a rate of 5mm/min. They found that bending strength of children's cortical bones under the age of five was lower at 150 to 180 MN/m^2 but adult bones have a higher value of 180 to 210 MN/m^2. Although the above-mentioned studies were conducted at a static rate, the same relationship between strength and mineral content was later found to hold for cortical bone tested at a dynamic impact rate of 0.1 s^{-1} in compression (Öhman et al., 2011). Öhman and co-workers (2011) also found that the adult bones have higher values in elastic modulus and compressive yield stress. The idea that mineral content of bone increases with age and can act as a predictor for bone strength has also been found to be true for trabecular bone (Mueller et al., 1966).

3.2.2 Strain and plastic deformation

In Hirsch and Evans (1965)' study, the ultimate tensile strain difference was found to change from 1.67(±0.79)% to 2.33(±0.47)% to 1.92(±0.47)% for the aforementioned age groupings, which was not found to be statistically different. Although this seems to suggest that significant structural changes took place in the bone as a child become ambulatory, this was only confirmed in the more comprehensive study conducted by Vinz (1970), who found that ultimate tensile strain decreased with age generally. Similar finding was found to hold in bending and compression (Currey & Butler, 1975; Öhman et al., 2011).

However, the observation that children's bone undergoes greater plastic than elastic deformation, leading to a higher energy to failure, is a lot more significant in Currey and Butler (1975)'s work than Öhman et al. (2011)'s study. Furthermore, the former reported that a small drop in load is often seen before failure in children bone, but this was not observed in the study conducted by the latter. The greater disparity in plastic deformation could be the result of loading the bone statically, which causes the bone to behave as a ductile material and fail in strain. This would augment the view of Nalla et al. (2003), who conducted fracture mechanics of adult cortical bone samples at a very low strain rate and found fracture in bone to be strain-controlled.

It is interesting to note in the graphs from Currey and Butler (1975) that inter-specimen variation is much larger in the load-deformation curves of the 2 years old than the 46 years old. The authors did not explain this difference but the authors stated that they had limited their samples to the mid-shaft of the femur. This may suggest that the mineral content and extent of bone remodelling is not the same in the anterior, posterior, medial and lateral aspects of the immature bone (Figure 3.1).

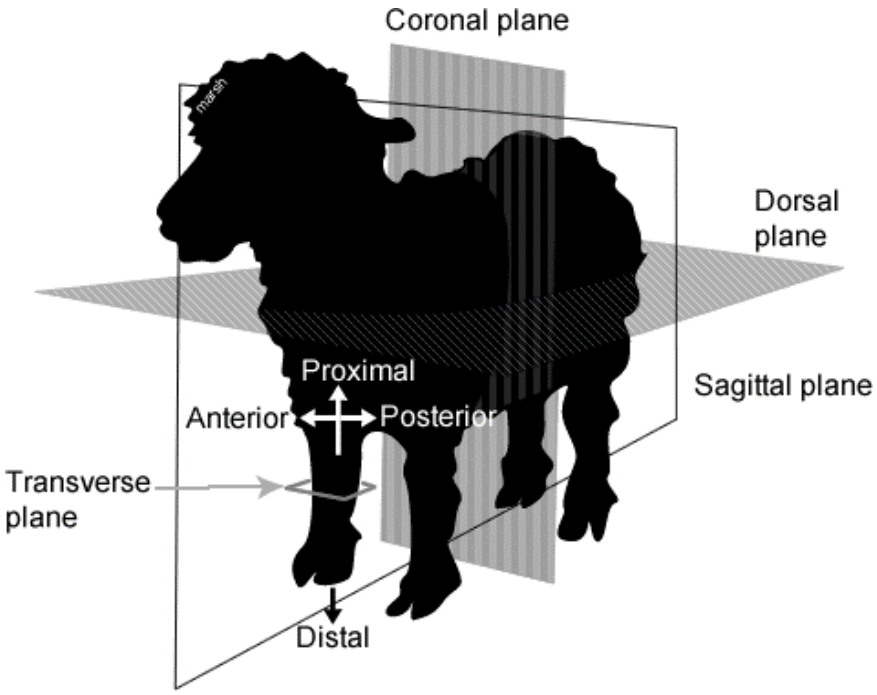

Figure 3.1: The anatomical terms that describes directions and plane

To obtain yield strain for children's bone, Öhman et al. (2011) made 18mm high and 3mm wide (or 14mm high and 2mm wide) cylindrical sample from cortical bone and loaded them compressively at a strain rate of 0.1 s^{-1} until the specimen free height reduced by 5%. In this large-scale study, it was found that compressive yield strain is an invariant for children and adult cortical bones, at about 1.1%.

3.2.3 Fracture pattern

When tested in compression, only one type of fracture pattern – a fracture pattern greater than 45° to the horizontal - was reported for adult specimens in the work of Öhman et al. (2011). In contrast, immature bones failed in buckling, with internal longitudinal cracks or with the same oblique fracture pattern described above (Öhman et al., 2011).

Greenstick fractures (see Chapter 2) have been reported to result when a test was halted prior to the observation of fracture (Currey & Butler, 1975). The authors further observed that fracture initiation took place quickly during testing before slowing down to match the speed of the crosshead of the machine. Furthermore, a fast travelling crack resulted in a smoother surface than the slowly propagating crack. In general, the fracture surface of the immature specimens appeared very rough even under high magnification. These observations seem to agree with the

earlier point that ductile and brittle fractures are the results of slow and fast travelling cracks, respectively. Moreover, the authors hypothesized that the small amount of strain energy remaining for fracture after plastic deformation and the preference for shear crack propagation contributed to the occurrence of greenstick fractures in children.

3.3 Factors of consideration in selecting an animal model

The plethora of animal models used in different research is evidence that there are many layers of decisions behind the choice of a model, and that no animal is able to model the human perfectly (Pearce et al., 2007). Underpinning all factors of consideration is the fact that the exact choice of species is dependent on the research question being addressed, which in turn influences the animal selection factors that need to be considered (Pearce et al., 2007). Nevertheless, there is considerable agreement over the important characteristics to consider in selecting an appropriate model for a wide range of applications from orthopaedics to biomaterials research, which first includes bone physiology in terms of its architecture and material characteristics (Liebschner, 2004; Martini et al., 2001; Pearce et al., 2007; Reichert et al., 2009).

3.3.1 Bone architecture and material properties

3.3.1.1 Dog

Being a companion animal, the dog has been most studied extensively in veterinary fields compared to all other large mammals (Martini et al., 2001). It primary advantage is its similarity in bone composition (bone mineral content, hydroxyproline, extractable proteins and IGF-1 content) to humans. Some differences in bone microstructure have been described, as remodelling of the canine bone takes place primarily in the middle, along the length of the diaphysis, with the peripheral of the bone containing lamellar bone (Pearce et al., 2007). This is in contrast to humans with extensive Haversian remodelling throughout the cortical bone in adults. In addition, dogs experience a higher rate of bone remodelling than humans (Reichert et al., 2009).

Nevertheless, canine bones are closely representative of human bones as they have a large proportion of their bone remodelled to secondary bone by skeletal maturity, while rats, rabbit

and sheep have a primary plexiform bone structure predominately, which is an interwoven combination of collagen fibres with osteocytes distributed randomly that results in a brick-like appearance. This is an important consideration in fatigue testing, due to a difference in mechanical strength (Liebschner, 2004; Martini et al., 2001). This makes dogs the most preferred animal of choice among the different large animals (Liebschner, 2004; Martini et al., 2001; Pearce et al., 2007; Reichert et al., 2009).

3.3.1.2 Pig

As an animal farmed for food, pig poses less ethical problems in research than dogs, which are sometimes seen as members of the household when they are kept as pets. The pig is physiologically similar to human as it has growing and adult skeletal phases, with similar rates of mineralization, remodelling and healing closer to humans than dogs (Martini et al., 2001; Pearce et al., 2007). Their femoral cross-sectional geometry is also a good representative of adult bones (Pearce et al., 2007), but it must be noted that pig bones are also much shorter in length than other large mammals (Reichert et al., 2009). However, the main limitation of using pigs as an animal model is its rapid growth rate and excessive weight (Martini et al., 2001; Pearce et al., 2007). Therefore, porcine bones are ideal in experiments involving implants and bone healing, but are unsuitable in other areas of orthopaedic research (Pearce et al., 2007). Smaller breeds such as miniature breeds may overcome this problem, but they are cost prohibitive, difficult to source (Martini et al., 2001; Pearce et al., 2007), and have a non-representative length to cross section ratio.

3.3.1.3 Sheep/Goat

The sheep exhibits far less Haversian remodelling than dogs, but instead has a widespread plexiform structure typical of large, fast-growing animals, compared to an extensive secondary structure seen in humans (Martini et al., 2001; Reichert et al., 2009). In addition, secondary osteons only start to appear a few years after sexual maturity (Kilborn et al., 2002; Reichert et al., 2009), and they tend to be found mainly in the anterior, lateral and medial part of the bone depending on the anatomical site, with lamellar bone making up the remaining posterior side (Pearce et al., 2007). This is in contrast to the homogenous distribution of osteons found in skeletally mature humans. In addition, Nafei et al. (2000) have found ovine bone to have a

denser trabecular structure than human bone, contributing to its increased strength (apparent density 0.61 vs 0.43g/cm^3; apparent ash density 0.41 vs 0.26g/cm^3, although care must be taken as the data obtained from Liebschner (2004) did not have any accompanying information on the age of humans used).

Despite all these disadvantages, sheep remains a valuable animal model in orthopaedic studies for several reasons. Firstly, ovine bones have been found to be similar to human bones in bone mineral composition, bone remodelling and metabolic rate (Reichert et al., 2009). Moreover, the greatest advantage of sheep or goat is its similar bodyweight to humans (Martini et al., 2001) (A 5-months old lamb weighs approximately 20kg at the time of slaughter, but this is dependent on the breed). Moreover, the mechanical loading and gait of sheep have been studied extensively (Bertollo et al., 2011; W. R. Taylor et al., 2006) and it has been determined that the sheep experiences about half the loading in its hind limbs because of its quadruped (W. R. Taylor et al., 2006). Finlay et al. (1995) and Osterhoff et al. (2011) have also ascertained that ovine tibia has a similar aspect ratio to human tibia and the former can be considered similar to the latter but scaled down by a third. It is for the reasons that mature sheep and goats possess a bodyweight and bone aspect ratio similar to adult humans, show no major differences in bone mineral composition with similar metabolic and bone remodelling rates in adults, that they are considered a valuable model for fracture research (Martini et al., 2001).

3.3.2 Comparative osteology

As discussed in Chapter 2, the focus of this thesis is on the reproduction of fractures in whole bones. Therefore, it is insufficient to consider only the composition and microstructure of the bone when the entire shape of the bone needs to be taken into account. In particular, the weight and length of the bone have been reported to play a role in experiments involving the whole bone, such as in gait and implant fixation studies (Goel et al., 1982; W. R. Taylor et al., 2006). Moreover, since the geometrical properties of the cortical shell has been reported to be a good predictor for failure strength (Augat et al., 1996), a suitable surrogate model should have similar osseous features as human bones.

A large scale osteology study has been conducted by Adams and Crabtree (2011), whose results are adapted and presented in Figure 3.2 and Figure 3.3. The bones have been arranged

according to their length, and it can be noted that some animal bones are not as straight as human bones. It can be seen that the adult porcine femur is a bit longer than ovine femurs, but much thicker. This would suggest a greater disproportion in width and length for the pig than the sheep when compared to human. However, no nonhuman quadruped seems to have a shaft that is as slender as human femur when scaled to size, except for dog.

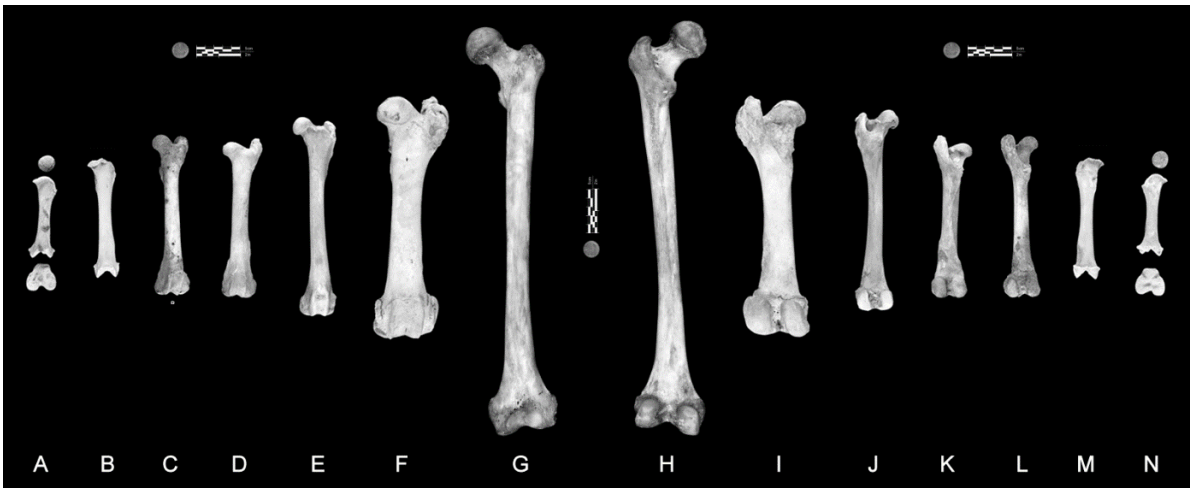

Figure 3.2: A visual comparison of the left femurs of (A) immature pig, (B) immature goat, (C) goat, (D) sheep, (E) dog, (F) pig and (G) human in the anterior view. (H) to (N) show the posterior view of the bones in reverse order [adapted from http://booksite.elsevier.com/9780123884374/zoomify.php]

This situation is repeated in the case of tibia (Figure 3.3), where the width of the pig tibia is much thicker, caused possibly by the need to support its heavier weight (Martini et al., 2001; Pierce et al., 2000). As such, the porcine tibia is definitely not suitable as an animal model for human tibia from the osteology point of view, despite great similarities in bone architecture to human bone as seen in Section 3.3. On the other hand, the ovine stifle can be approximated as a third of the size of a human knee (Osterhoff et al., 2011) and it is widely used in surgical training (Allen et al., 1998; Martini et al., 2001). Since the resemblance of the microstructure of ovine cortical bone to human bone is only slightly inferior to that of porcine and human bone, ovine long bone is a more appropriate model in studying bone fractures at the structural level.

Figure 3.3: A visual comparison of the left tibiae of (A) immature pig, (B) immature goat, (C) pig, (D) goat, (E) sheep, (F) dog and (G) human in the anterior view. (H) to (N) show the posterior view of the bones in reverse order [adapted from http://booksite.elsevier.com/9780123884374/zoomify.php]

3.3.3 Age selection of animal model

While extensive literature exists for adult bones, few have undertaken the task to compare immature bone across species. Indeed, this is potentially complicated, as animals do not necessarily show synchrony between age at sexual maturity and skeletal maturity. In the case of the cat, dog, rabbit and horse, their physis closes at about the same time when they become sexually mature. In the second category, humans, cow and sheep have growth plate closure after sexual maturity has taken place, sometimes into adulthood. The third scenario is seen in rats, whose bone formation continues even after sexual maturity, as evidenced by the presence of an opened physis for as long as 29 months, well into adulthood (Kilborn et al., 2002).

Kilborn and team (2002) suggested that by calculating the ratio between physis closure and lifespan, an estimate of the age when the animal stops growing may be calculated. This information is useful for coming up with an approximate age correlation with humans for animals in the same category as humans. However, they did not go as far as to calculate the age correlation for different animals. Nevertheless, it has been stated elsewhere that weeks of life in pigs and months of life in sheep are comparable to months and years in humans respectively (Baumer et al., 2009; Nafei et al., 2000). Epiphyseal closure for the ovine femur and tibia occur between 18-26 months, while skeletal maturation stops between the age of 18 and 25 for humans (Martini et al., 2001).

3.3.4 Summary of literature review

A summary of the factors of consideration in selecting an animal model is presented in Table 3.1. The sheep and the goat are grouped together as they are considered to be very similar (Pearce et al., 2007). It can be seen that dog bone has the closest microstructure to human bones, followed by the pig and the sheep. However, emotional attachment to animals kept as pets makes it difficult to use dog bones for any experimental work, thus ruling the use of this animal out. The osteology of pig bones is also very different from human bones, which arises out of the animal's need to support its weight. It would therefore not be a good approximation of the geometry of human bones and the fracture pattern generated might be very different. Therefore, sheep bones are selected to be surrogates to study bone fracture in this thesis.

A further advantage of sheep bones is that their age-related changes for trabecular bone is well documented (Nafei et al., 2000). The elastic modulus, ultimate stress, energy absorption to failure, and elastic energy absorption were found to be positively correlated with age. However, an inverse relationship between the absorption of viscoelastic energy and ultimate strain with age that parallels the decrease in deformation at failure with age was observed. Indeed ovine bone experiences a big drop in its ability to absorb viscoelastic energy in the first few months of life before it stabilizes. This property expands the explanation that greater deformation is observed in immature bone prior to a fracture. This same relationship was first established by Currey and Butler (1975) who studied the mechanical and material properties of cortical bone in children.

For elastic energy absorption and elastic modulus, their results were only significantly different in the sagittal and longitudinal directions, with the values in the coronal direction being very close to that in the sagittal direction. The same trend was also observed when compared between the pooled immature and mature specimens. Therefore, it would be sufficient to model immature lamb bone with inversely isotropic material properties.

Finally, the sex of the immature animal was found not to have a significant influence on the variables measured, and therefore, the results from both male and females lambs may be pooled together.

Table 3.1: Some features of dog, sheep/goat, pig and human bones that are used in deciding an appropriate animal model are compared [adapted from Reichert et al. (2009)]

	Micro-structure	Macro-structure	Disadvantages	Advantages	Bone Composition	Mechanical & Mass Properties
Dog	o Plexiform bone found near the periosteum and endosteum o Secondary osteons in the middle of the cortical bone (and increases in number with age).	Femur: o Pronounced curvature at distal third of shaft; narrow in the middle Tibia: o Length Similar to sheep; proximally convex medially, distally convex laterally; proximal ⅓ prismatic, remainder cylindrical	o Full weight bearing on joints due to its quadrupedal gait o Ethical issues involving the use of domestic animals o Large interspecies variation depending on the breed	o Similar bone mineral density to humans o Large presence of secondary osteons like in humans o Similar shape as human femur	o Canine bone composition (organic, inorganic, water and ash fraction) is the closest to humans o Similar organic composition to human o Significantly higher mineral density than human bone.	o Trabecular bone: Similar to human bones in mechanical and mass properties. o Higher ultimate compressive strain than humans Humerus (bending) E: 2.66 GPa Ultimate Stress: 193.23 MPa
Sheep/ Goat	o Plexiform bone structure in sheep up to 3-4 years of age. o Haversian modelling begins at 7-9 years of age and increases each year o Haversian system found in the anterior, lateral and medial side of the tibial diaphysis o Lamellar bone found on the posterior side.	Femur: o Rounded (cylindrical) shaft; convex dorsally; curved in distal ⅔; regular in diameter Tibia: o Major weight-bearing bone of crus; long and slender; shaft curved medially and caudally at centre; round in middle, triangular proximally, flattened craniocaudally in distal third; medial surface is subcutaneous	o Different bone histology to humans o Large interspecies variation depending on the breed o Mature bone has fewer Haversian canals than humans, and are of irregular shape and size	o Similar body weight to humans o Aspect ratio of long bones are similar to human's o Mechanical loading in sheep joints is known	o Similar mineral composition, bone remodelling and metabolic rate to humans.	o Higher trabecular bone density than humans ($0.61 g/cm^3$ vs $0.43 g/cm^3$) *Femur* (Compression) E: 19.3 GPa Ultimate Strain: 0.019 *Tibia* (Bending) E: 278.08 MPa Bending Strength: 46.24 MPa
Pig	o Large network of secondary osteons of medium-sized canals that increases with age o Plexiform bone present	Femur: o Relatively wide & massive diaphysis with 4 surfaces Tibia: o Slightly curved diaphysis, convex medially	o High growth rates and excessive body weight o Short length of femur and tibia	o Similar femoral cross-sectional area and width o Lamellar bone structure similar to humans	o Similar bone mineral density and concentration to humans	o Denser trabecular network Femur E: 14.6 GPa (plexiform) 8.3 GPa (Haversian)
Human	o Plexiform bone found in young children or in adults, only in rapid bone repair and remodelling or bone pathology o Healthy adult bone consists of circumferential lamellar bone o Humans have more secondary osteons than quadrupeds (12.87 vs. 5.5a)	o Epiphysis- proximal and distal-spongy bone o Metaphysis- transition zonespongy bone distal to epiphyseal line o Diaphysis - shaft of the bone – compact bone			Trabecular bone density: 0.43 g/cm	*Femur* (Compression) E:14.7-19.7 GPa Ultimate Stress: 167-215 MPa *Tibia* (Compression) E: 24.5-34.3 GPa Ultimate Stress: 183-213 MPa

3.4 Comparative anatomical features of ovine and human femur and tibia

Despite the suitability of ovine bone as an appropriate surrogate model, most veterinary textbooks' treatment of ovine anatomy has been perfunctory, with the use of bovine anatomy to describe all ruminants (Allen et al., 1998; Osterhoff et al., 2011). Furthermore, many differences exist between humans and sheep due to differences in the way they walk. Humans walk on two legs and thus are termed Plantigrade bipeds, whereas sheep are Unguligrade quadrupeds, animals that walk on their hoof and have their knees always in flexion. Thus, changes in experimental set-up and computer simulation work may need to be made in consideration of the differences between anatomical features of the two species of bones, which are summarised from the two sources stated above (Allen et al., 1998; Osterhoff et al., 2011).

3.4.1 Ovine femur

With reference to Table 3.2, the ovine femur exhibits a greater curvature than human femur and it is convex in the midshaft, but it maintains a valgus of 5-10° like in humans. Similarly, a sheep's medial femoral condyle is the smaller of the two condyles in both the anterior-posterior and medial-lateral directions. The medial ridge of the trochlea is also more prominent as it extends further anteriorly and proximally than the later ridge.

Table 3.2: The prominent similarities and differences of the human and ovine femur

Features	Human Femur	Ovine Femur
Condyles and trochlea	The condyles and the trochlea forms a smooth articular surface	Its articular surface is interrupted by a very distinctive trochlea
Trochlear width	Broader trochlear width/ shallow groove	Narrower trochlear width/ deep groove
Trochlear groove	Trochlear groove runs approximately to the sagittal plane	Trochlear groove runs medially from proximal to distal
Articular plane	Articular plane slants towards the medial	Articular plane slants towards the lateral
Intercondylar fossa	Broader intercondylar fossa	Narrower intercondylar fossa
Supercondylar fossa	Not present	Supercondylar fossa present on the posterior-lateral side of the distal diaphysis
Line aspera	This midline is prominent on the posterior part of the femur	Line aspera that bisects the femur longitudinally is not distinct in sheep
Most proximal landmark	Most proximal point is the femoral head	Most proximal point is the greater trochanter
Valgus	5-10°	
Size of condyles	Medial femoral condyle is smaller than the lateral femoral condyle	
Ridge of the trochlea	Medial ridge is more prominent and it extends further anteriorly and proximally than the lateral ridge	

The most proximal point of the ovine femur is the greater trochanter, but it is the femoral head in humans (Figure 3.4b). Along the diaphysis, sheep do not have a distinct linea aspera that bisects the bone in the longitudinal direction. Distally at the condyles (Figure 3.4c), a very prominent trochlea with a deep groove disrupts the continuous articular surface of the condyles in sheep; in humans, the articular surface extends over the condyles and the trochlea. Furthermore, although the trochlear groove runs medially from proximal to distal in sheep at an angle of 20 ± 5 degrees from the longitudinal axis of the femur, it runs parallel to the femoral shaft in humans. The direction of the articular plane is also different, as it slants towards the lateral in sheep but in the opposite direction in humans. Finally, ovine femur is also marked by

the following landmarks, not seen in humans: a deep and narrow intercondylar fossa, and a supracondylar fossa that is present on the posterior-lateral side of the distal diaphysis.

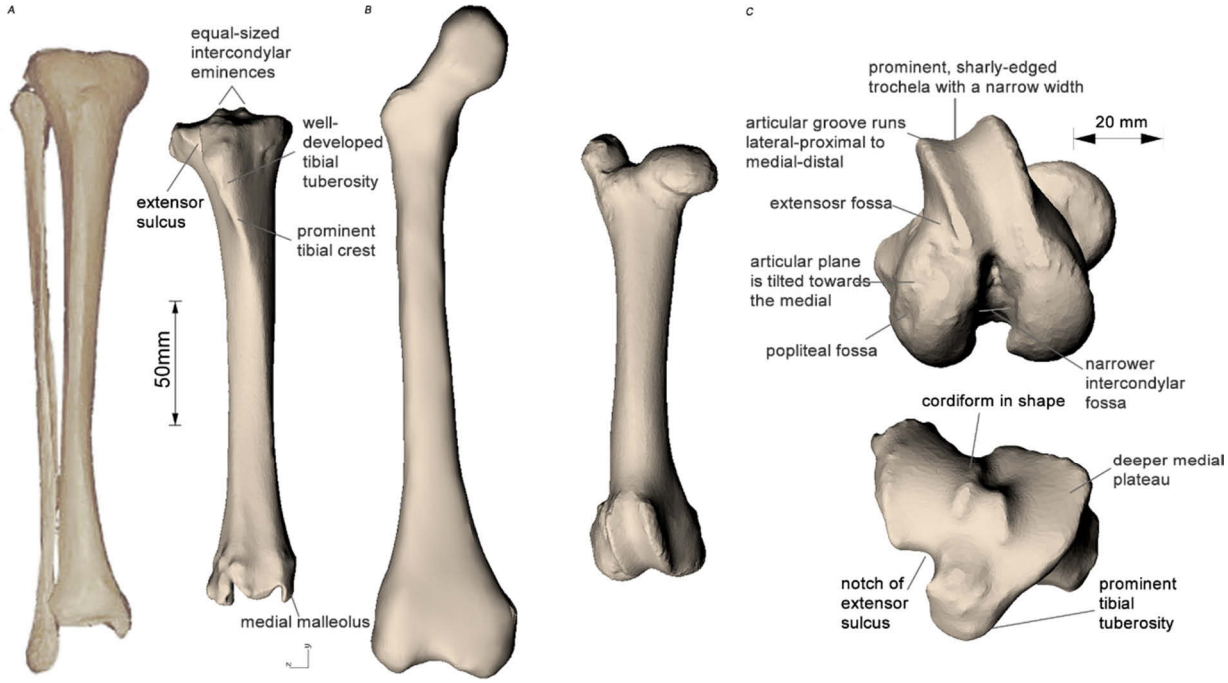

Figure 3.4(A & B): A 5-year old human right tibia and femur is compared with a 5-months old lamb right tibia and femur (anterior view). The most proximal point of the sheep is the greater trochanter, but it is the femoral head in humans. (C): Some unique features of the ovine stifle joint are summarized here. The human bone images were obtained from a MRI scan of a 5-year old child.

3.4.2 Ovine tibia

The cross-section of the human tibia approximates a circle in the mid-diaphysis but it becomes more oblong towards the ends (Osterhoff et al., 2011). In sheep, the tibia is triangular in the proximal section before varying slowly to an oval in the middle then finally to approximately a circle distally. This difference in cross-section results from a pronounced tibial tuberosity and greater tibial slope in sheep than humans. In contrast, the human tibial plateau joins quickly into the shaft without a big transition in shape. Unlike in humans, where the insertion of the patellar tendon is easily identifiable, it is difficult to differentiate between the insertion sites of different tendons in sheep due to the lack of any distinguishing feature on the tibial crest. Another characteristic feature of the ovine tibial plateau is the presence of a notch on its anterior-lateral side called the extensor sulcus. This is the consequence of a more distal insertion

of the tendon of the M. extensor digitorum longus (EDL), which also results in a larger lever arm in sheep.

Despite these differences, some similarities also exist on the tibial plateau (Table 3.3). The medial tibial plateau is the larger of the two condyles, while the medial and lateral intercondylar eminences are of similar sizes. A posterior tilt of the tibial component exists in both species, even though the angle is higher at 20˚ for sheep than 10˚ for humans. The steeper tibial slope limits the range of motion in sheep to about 72-145˚, so the ovine stifle (knee)is always in flexion, and contact between the tibial plateau and the femoral condyles takes place only on the posterior part.

Table 3.3: The prominent similarities and differences of the human and ovine tibia

Features	Human Tibia	Ovine Tibia
Cross-sectional shape of tibial plateau	Oval	Triangle
Morphology of tibial plateau	The tibial plateau tapers quickly into the shaft	Pronounced tibial tuberosity and greater tibial slope
Extensor sulcus	Not present in humans	Notch (extensor sulcus) present on the proximal-lateral edge of the tibial plateau, caused by a more distal insertion of the tendon of the M. extensor digitorum longus (EDL)
Insertion of patellar tendon	Easily identifiable on the tibial tuberosity	No characteristic feature on the tibial crest that differentiates the insertion of the patellar tendon from other tendons
Distal surface of tibia	Shallow articular surface	Two distinct articular surfaces with deep curvature
Size of tibial plateu	The medial plateau is bigger than the lateral plateau	
Intercondylar eminences	Similar in size	
Most distal landmark	Medial malleolous	
Slope of the tibial plateu	A posterior tilt exists in the tibia component of the two species	

As no other animal that we can reasonably experiment with is a bipedal like humans, many differences exist on the distal end of the tibia. Most notably, sheep have two distinct and deep grooves for articulation, whereas humans have a shallow articulation surface. Remnants of the distal fibula can also be seen on the lateral side of the distal tibia, as the fibula is rudimentary in most sheep these days. Nevertheless, both species share the common feature of having the medial malleolous as the most distal landmark.

3.5 Summary

In this chapter, a review of the material properties has been presented to inform the choice of a suitable animal surrogate model for this thesis. It has been shown that skeletally immature trabecular and cortical bones of both lambs and children are weaker, have a lower elastic modulus, have greater ability to absorb energy and thus undergo greater plasticity before failure. However, both immature and mature sheep bone were found to have inversely isotropic material properties. The relationships between the above-mentioned mechanical properties with age, including ultimate strain, have been mapped out, but yield strain has been found to be strain-invariant. This suggests that failure of immature bone might be more strain controlled than stress controlled, which suggests the use of a strain-based failure criteria to model bone fracture. This is discussed in more detail in Chapter 6.

Although the architecture of the bone is one of the most important factors to consider in the selection of an appropriate model, the macroscopic structure or osteology of the bone also needs to be factored in when the structural response of the bone is required instead of its material behaviour. The features of pig, dog and sheep/goat cortical bone were presented in this chapter and while the canine bone has the most similar anatomy and microstructure to human bones, increasing concern for the use of domestic animals for research restricts the use of this animal for research. Porcine bone ranks next in terms of microstructure, but its excessive weight and massive diameter of the bone shaft compared to humans disqualifies its use in a study where the fracture of the whole bone needs to be studied. This leaves the immature sheep, which ranks third in terms of its bone microstructure, but with a more similar osteology to human femur and tibia as the choice of animal model for bone fracture research in children. Furthermore, even though ovine bone predominately has a plexiform structure, the work done by Nafei et al.

(2000) shows that ovine immature bone has a strong correlation between mineral density and mechanical properties, which is similar to human bones.

Finally, attention was turned to the anatomical features of ovine and human femurs and tibias as provisions in later experimental and modelling work may need to be made in view of their differences. The most notable differences of the ovine femur include a greater curvature of the midshaft, and the greater trochanter lies at the most proximal point of the femur rather than the head. For the tibia, in sheep it has the shape of an inverted pyramid at the tibial plateau that morphs into a cylinder approximately in the diaphysis. However in humans, the cross-section remains oblong, even though it tends towards a more circular shape in the midshaft. Since differences exist in the osteology of human and sheep bones, a suitable alignment system needs to be chosen so that the results obtained from the animal model may be applicable to humans as well. Therefore, the topic of next chapter is on the development of a novel methodology to optimise the alignment of long bones in pure bending and torsion.

4 A Novel Methodology to Optimise the Alignment of Long Bones

4.1 Introduction

The fracture of bone at the tissue level has been the focus of much research in recent years (Ebacher et al., 2007; Nalla et al., 2003). However, a direct correlation between the behaviour of bone at the tissue level and at the structural level has not been found (Juszczyk et al., 2011). As seen in Chapter 2, studying the mechanical behaviour of failure in whole bone in a state of pure bending and torsion is essential in understanding how bone breaks at the structural level. Yet, unlike the characterization of bones at the tissue level where bone samples are machined into regular specimens, the complex geometry of bone needs to be taken into consideration at the structural level. Therefore, an alignment method that allows for bones to be as close possible to a state of pure bending and torsion needs to be utilized in biomechanical testing.

Currently, an anatomical reference frame is always specified to set the bone up for experimental testing (Cristofolini, 1997). A reference coordinate system defines the movement of joints in the body and it withstands the complex loading that locomotion brings, including bending and torsion. Although a thorough review has been previously carried out on the repeatability of a

few standard coordinate systems in humans (Conti et al., 2008), the performance of each system's ability to optimally resist bending and torsion has never been compared. Moreover, as noted in Chapter 3, humans are Plantigrade bipeds, whereas sheep are Unguligrade quadrupeds, therefore differences in osteology exists and the reference frames used for humans may not be directly applicable for sheep. Therefore, a review of all available anatomical coordinate system for the ovine femur and tibia is necessary.

4.1.1 Definitions of anatomical reference frames

Three anatomical reference frames for sheep were found in the literature, and whilst they were used in very different contexts, they show a range of methods and landmarks that can be used. Additionally, the Ruff and Hayes (1983) method for human bones will also be discussed as this was adapted for ovine studies by Finlay and co-workers (1995). Moreover, an understanding of the coordinate system used in humans has an additional aim of locating the appropriate landmarks in sheep to define the reference frames.

4.1.1.1 Tibia

Ruff and Hayes (1983)

The Ruff and Hayes (1983) method was developed to be used in-vitro, and thus relies on the identification of prominent features on the bone surface (Figure 4.1). The first required landmarks on the tibial plateau are the centres of the lateral tibial condyle (LTC) and medial tibial condyle (MTC). With these points located, the midpoint between the two condyles (MP) is then calculated. On the distal ends, the centrepoint of the surface that articulates with the talar (TAS) is identified with the aid of callipers. The biggest drawback in this methodology is that in the identification of all but one (MP) of the above-mentioned landmarks, measurements need to be repeated until equi-distance is obtained in the medio-lateral and anterior-posterior directions.

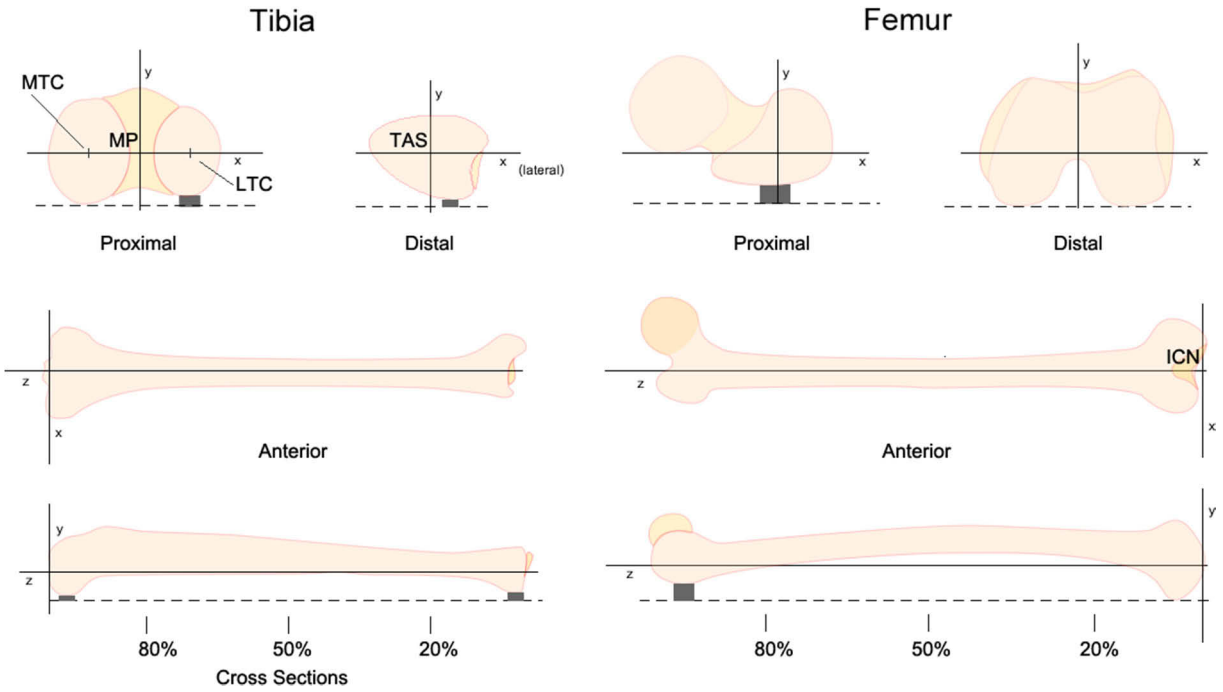

Figure 4.1: The anatomical landmarks used to define the reference frames (MP: midpoint between the lateral and medial tibal condyles; TAS: midpoint of talar; ICN: deepest point of iniercondylar notch). [Adapted from Ruff and Hayes (1983)].

The frontal plane is defined as the plane that contains the LTC, MTC and the TAS. The sagittal plane lies perpendicular to the frontal plane and passes through the MP and the TAS. Finally, the longitudinal axis is defined as the line connecting the MP and the TAS, and is obtained from the intersection of the frontal and sagittal plane.

Finlay et al. (1995)

Starting with a similar objective to study the cross-sectional geometry of tibias, Finlay and co-workers (1995) adapted the Ruff and Hayes (1983) method for use in mature Arcott sheep. The longitudinal direction is defined in a similar manner to the Ruff and Hayes' method by first locating the middle of the intercondylar eminences on the proximal tibia and the centre of the articulating surface on the distal tibia. Instead of finding the frontal and sagittal planes, the authors defined the AP position in a two-step procedure. Firstly, the posterior part of both the proximal condyles is laid against a flat horizontal surface, with the condyle on the distal tibia making one point of contact. Holding the bone in place, a hole is drilled in the crest of the tibial tubercle and a wooden skewer is inserted into it to mark the AP direction.

In using the tibial tuberosity, the authors took advantage of a prominent landmark that is found in sheep. However, as noted in Chapter 3, the human tibia has less pronounced features compared to ovine tibiae and thus their alignment system is not easily reproducible in other animal models or even humans. Unlike other coordinate system for the tibia-fibula complex, Ruff and Hayes' method utilizes only landmarks on the tibia. While this makes it easily adaptable to sheep as the fibula is rudimentary in most animals, the functional anatomy of the ovine tibia is rather different from that of human tibiae as the ovine knee is always in flexion, as noted in Chapter 3.

Tapper et al. (2004)

As the purpose of their study was to measure three-dimensional (3D) joint kinematics of the ovine stifle joint, Tapper and co-workers defined an anatomical coordinate system based on very different landmarks in-vitro, after the sheep has been sacrificed. Instead of using bony prominences, the authors chose the insertion site of various ligaments as landmarks. However, as noted in Chapter 3, there is a lack of a distinguishing feature on the tibia crest, which makes the consistent identification of landmarks in sheep very challenging when surface models are used for geometrical analysis.

The centroid of the femoral attachment site of the anterior cruciate ligament is first located and the origin of the coordinate system is defined to be coincident at this point. The longitudinal axis is defined by fitting a cylinder to the diaphysis. Thereafter, by locating the centroids of the attachment of the medial and lateral collateral ligaments, the frontal plane can be defined using these points and the longitudinal axis. Like other standard right-handed coordinate systems, the axes are positive in the lateral and anterior directions.

Bertollo et al. (2011)

An alternative coordinate system for motion analysis in sheep was utilized by Bertollo and co-workers in 2011. Unlike the technique used by Tapper et al. (2004), their reference frame was determined from geometrical models created from 3D computed tomography scans of the lower back limb.

The centre of the intercondylar eminences is first located to define the origin. The transverse plane or anterior axis is defined perpendicular to the longitudinal axis and passes through the tibial tuberosity. However, as a third landmark was not mentioned, it is not clear how the longitudinal axis was created.

4.1.1.2 Femur

Ruff and Hayes (1983)

The first two required points in the Ruff and Hayes (1983) method are the midpoints of the proximal and distal ends of the femoral diaphysis from the lateral view. These are located at the junction to the lesser trochanter and the femoral condyles, respectively. The femur that is laid flat on a surface is then raised until the marked points are level with each other. The frontal plane is then defined to be parallel to the supporting surface and passes through the centre of the articulating centre of the femoral condyles.

To form the sagittal plane, the deepest point of the inter-condylar notch (ICN) is required on top of the medial-lateral midpoint at the proximal diaphysis as defined above. A plane that is orthogonal to the frontal plane and passes through the above-mentioned points is then created. Finally, like in the case of the tibia, the longitudinal axis lies perpendicular to the sagittal and frontal plane.

In a review conducted by Conti et al. (2008), the use of the Ruff and Hayes method was found to give the best repeatability in in-vitro measurements among other anatomical reference frames. Yet unlike the case for the tibia, the Ruff and Hayes method has not been applied to ovine femur. However, as noted in Chapter 3, the narrow and sharply-edged trochlea keeps the ovine stifle joint always in flexion and thus the functions of the ICN in human and sheep may not be the same.

Tapper et al. (2004)

In a similar manner to the definition of the coordinate system for the tibia by the same authors (Tapper et al., 2004), the centroid of the insertion site of the anterior cruciate ligament, and the attachment sites of the medial and lateral collateral ligaments are used as landmarks in defining

the origin and frontal plane respectively. The longitudinal axis is defined by approximating the diaphysis as a cylinder.

The use of cylindrical approximations of the shaft is one of the approaches used to define the longitudinal axes of the tibia in humans. In the case of the ovine tibia, this approach may be reasonable, as the tibia is relatively straight. However, as seen in Figure 3.4 in Chapter 3, the ovine femoral diaphysis displays a curvature and thus makes this approach questionable. Furthermore, the curvature of the diaphysis is likely to vary across the population and the difference in size of the fitted cylinder may possibly cause huge standard deviations in the results obtained, since bone curvature will result in significant eccentric loading during bending and axial loading in-vivo (Ruff & Hayes, 1983).

Bertollo et al. (2011)

The coordinate system origin on the femur is defined from the intersection of three surfaces. The first surface is obtained by best fitting a cylinder to the posterior femoral condyles. The second surface is a plane that bisects a line that joins the most posterior points of the femoral condyles. The final surface is the distal cortical surface of the trochlear groove.

Next, the volumetric centroid of the femoral head is located. Connecting this point and the origin forms the longitudinal axis. The frontal plane is defined to be parallel to the cylinder and contains the longitudinal axis. Finally, the anterior-posterior (AP) axis is obtained from creating a line that is perpendicular to the frontal plane.

By using the centroid of the femoral head as one of the points in defining the longitudinal axis of the femur, the joint-kinematics of the ovine stifle can be captured more accurately than Tapper's method. Nevertheless, this methodology does not account for the huge curvature present in the ovine femur, and as such, the bone would not be close to a state of pure bending or torsion, which is required for bone fractures of the same kind to be reproduced consistently. Therefore, a method to optimise the alignment of long bones in bending and/or torsion is required.

4.1.2 Aims and objectives

The survey conducted on the anatomical reference frames in the previous section shows that they have been defined based on the movement of joints in-vivo. These systems have been used in in-vitro experiments that attempt to model physiological conditions or forces, and also in experiments in four-point bending and torsion to characterise the mechanical properties of bones (Cristofolini & Viceconti, 2000; Cristofolini et al., 1996). However, the use of this approach has resulted in large standard deviation in the results of bending and torsional loading tests in human bones.

Although alternative alignment methods for sheep are available, the Ruff and Hayes (1983) method has shown to be most thorough in its definition and suitable for use in this chapter as the anatomical reference frame. However, as seen in Chapter 3, there exists a set of principal axes where maximum and minimum principal stresses could be experienced. At this orientation, no shear stress is present and the failure mechanism as a result of normal stress can be elucidated. Similarly, the axes where maximum shear stress exists can also be found. Yet no work has been done to generate an alignment system where the bone will be subjected to a state of pure bending or torsion. Furthermore, the extent to which the use of the anatomical reference frame allows bone to be subjected to pure bending and torsion is also not known. Therefore the aims and objectives of this chapter may be summarised as follows:

i. to develop a methodology that calculates the principal directions of bone from surface models,

ii. to compare the second moment of area and its coefficient of variation across the cross-section using the anatomical reference frame and the proposed methodology in the principal directions and anatomical directions, and

iii. to obtain suitable landmarks in lamb bones to be used to define the alignment system for in-vitro testing in four-point bending and torsion.

4.2 Materials and Methods

11 ovine tibia and 9 ovine femurs from 5 months old British Texel lambs were harvested after slaughter from a local butcher. As discussed in Chapter 3, ovine bones have been found to be suitable surrogates for paediatric human bones. The lambs weighed approximately 20kg at the time of death. The bones were cleaned of all soft tissues, leaving the periosteum intact as far as possible (Figure 4.2). Thereafter, they were wrapped in cloth soaked in 1% Phosphate Buffer solution (PBS). The bones were then double bagged and frozen at -20°C for storage. The strength of bone has not been found to be reduced by the process of freezing (Moreno & Forriol, 2002).

Figure 4.2: These ovine tibiae have been clean off all soft tissues, and are laid on cloth that has been soaked in 1% PBS.

4.2.1 Image acquisition details

To calculate the principal directions where bone may be subjected to a state of pure bending and torsion, and to compare this alignment system against the gold standard of using anatomical reference frames, an imaging-based method needs to be used.

The frozen bones were thawed at room temperature in a cool box for at least 3 hours prior to undergoing micro-CT scan. The bones were scanned with the tissue paper intact in a Metris X-Tek HMX ST 225 CT System (Nikon Metrology, Tring, UK), using reflection target and a focal spot size of 5μm. Copper filter of 1mm was used as the reflection target, and the X-rays were set at 200kV and 200uA. An aluminium phantom was included in the scan to calibrate the density of the bone. A resolution of 97 micron was achieved for the ovine femurs but a higher resolution of 115μm was used for ovine tibia due to its longer length.

4.2.2 Image segmentation

The acquired volumes were constructed using CT PRO (Metris X-Tek, Tring, UK) and converted to DICOM format, which were then loaded into Mimics x64 15.0 (Materialse NV, Leuven, Belgium). Each bone was manually segmented, by applying a threshold value to highlight the pixels of the bone to create a mask. The mask was cleaned up by using the eraser tool to enhance the contrast between the bone and the cloth, especially at regions near the aluminium phantom. As the trabeculi are not required, the Magic Lasso tool was used to outline the boundary between the trabecular and cortical bone to create a second mask. The eraser tool was also utilized to clean up any noisy area, yielding a result similar to that in Figure 4.3. The two masks were then exported separately to Geomagic Studio 12.0 (3D Systems, North Carolina, USA), where the meshes were repaired and smoothed. The two final files were exported as surface meshes in STL format, ready for the principal axes of the bone to be determined.

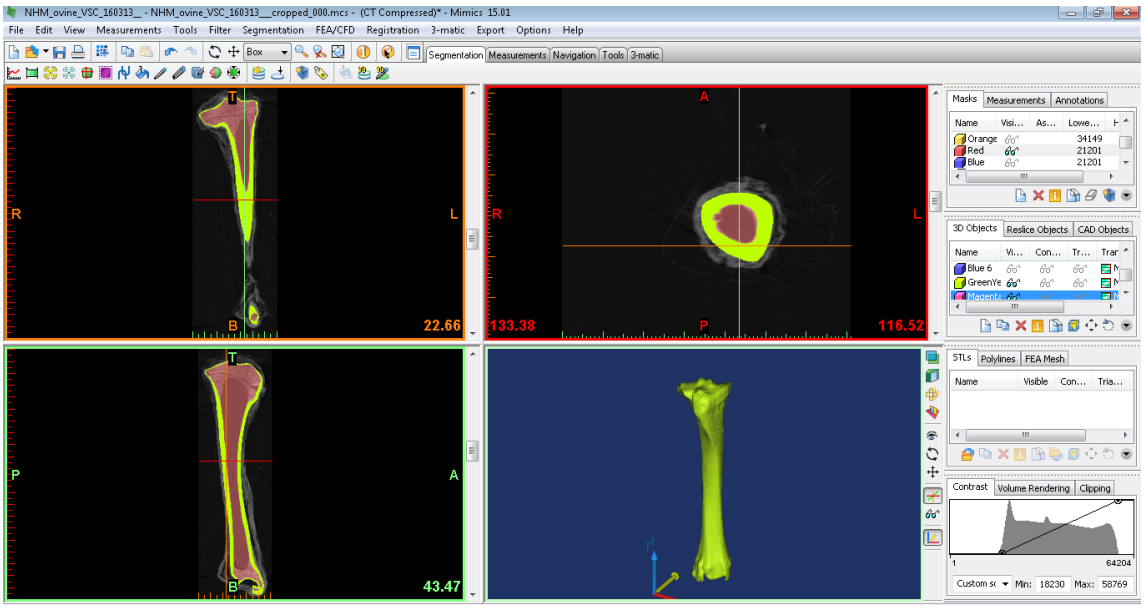

Figure 4.3: The reconstruction of 3D surface model of the cortical bone in Mimics 15.0 (in yellow).

4.2.3 Determination of geometrical properties

The geometrical properties of an object arise from its shape and various calculations of geometrical parameters can shed light on the object's mechanical properties. For example, the cross sectional area affects the compressive/ tensile stress experienced by the bone in axial loading, whereas the second moment of area determines an object's resistance to bending and torsion. Therefore, this section looks at some key geometrical parameters related to bending and torsion, which are summarised from Hibbeler and Fan (2004).

4.2.3.1 Second moment of area

The area second moments or I have units of length^4 and measure the distribution of material of points with respect to an arbitrary axis. The second moment of area is defined about a specific axis and thus may be defined about the world coordinate axis or centroid coordinate axis. In both cases, the symbols I_{xx}, I_{yy}, and I_{zz} are used to denote the area moments of inertia about the x-axis, y-axis, and z-axis, respectively:

$$I_{xx} = \int_A y^2 + z^2 dA$$

$$I_{yy} = \int_A x^2 + z^2 dA$$

$$I_{zz} = \int_A x^2 + z^2 dA$$

The polar second moment of area ***J*** is a special term for the area moments of inertia about the longitudinal axis. It is a measure of an object's ability to resist torsion, and is a summation of the values of the two second moments of area in its orthogonal directions. As the International Society of Biomechanics' recommendation for axes convention was adopted, the y direction is defined to be the proximal-distal directions, therefore, $I_{yy} = I_{xx} + I_{zz}$

4.2.3.2 Second moment of volume

Volume moments of inertia are defined in a similar manner, such that:

$$I_{xx}(vol) = \int_V y^2 + z^2 dV$$

and similarly for the other directions.

4.2.3.3 Product Moments

Due to the possibility that an applied load's line of action may fall outside the bone, it is useful to compute the products of inertia about axes that are not parallel to the coordinate axis:

$$I_{xy} = \int_A xy\, dA$$

$$I_{yz} = \int_A yz\, dA$$

$$I_{zx} = \int_A zx\, dA$$

Although the second moments and moments of inertia are always positive in their values, product moment of inertia may be positive or negative depending on the axis chosen and the shape of the object. The product moment may even be zero when the area or volume in consideration has an axis of symmetry.

4.2.3.4 Principal Axes

As explained earlier, the second moments of area may be calculated about any defined axes. However, there exists a set of axes where the second moments of area, and therefore bending strength, would be at a maximum and a minimum. Physically, a structure that is aligned along its principal axes would experience maximum and minimum stress at these orientations

respectively. These are called the principal stresses and their directions are termed the principal directions. The principal directions are orthogonal to one another and the principal moments are traditionally designated as I_1, I_2 and I_3, in descending order of its second moment of area.

The product and area moments can be assembled to form the following characteristic equation to solve for the principal moments I:

$$\begin{vmatrix} I_x - I & -I_{xy} & -I_{xz} \\ -I_{yx} & I_y - I & -I_{yz} \\ -I_{zx} & -I_{zy} & I_z - I \end{vmatrix} = 0$$

From the equation, a given second moment is at a maximum when its product moment is zero. It is always possible to solve for a specific coordinate system when all the product moments are zero simultaneously, so that the object is in an orientation where it can best resists torsion and bending. Mathematically, as the product moments reduce to zero, the matrix becomes a diagonal, and therefore the principal axes are orthogonal to one another. The $\boldsymbol{I}$ matrix may thus be expressed as:

$$I = \begin{bmatrix} I_1 & 0 & 0 \\ 0 & I_2 & 0 \\ 0 & 0 & I_3 \end{bmatrix}$$

Therefore, by solving for the principal directions of a bone about its volumetric centroid, the second moments of area would be maximized. A bone that is aligned along its principal directions would have the highest bending rigidity and best be able to resist bending and torsion. In such an orientation, the bone would approximate the state of pure bending and torsion respectively.

4.2.4 Algorithm

The following algorithm was developed in RhinoScript to align long bone along its principal directions to minimize the presence of shear stress in bending. This is a scripting tool based on Microsoft's Visual Basic Language that interfaces and extends the functionality of Rhinoceros 5.0 SR5 (Robert McNeel & Associates, Seattle, USA). The entire analysis was carried out in this CAD package to enable easy visualization and exportation of the results afterwards. The algorithm can be split into three sections (Figure 4.4) and are discussed as follows.

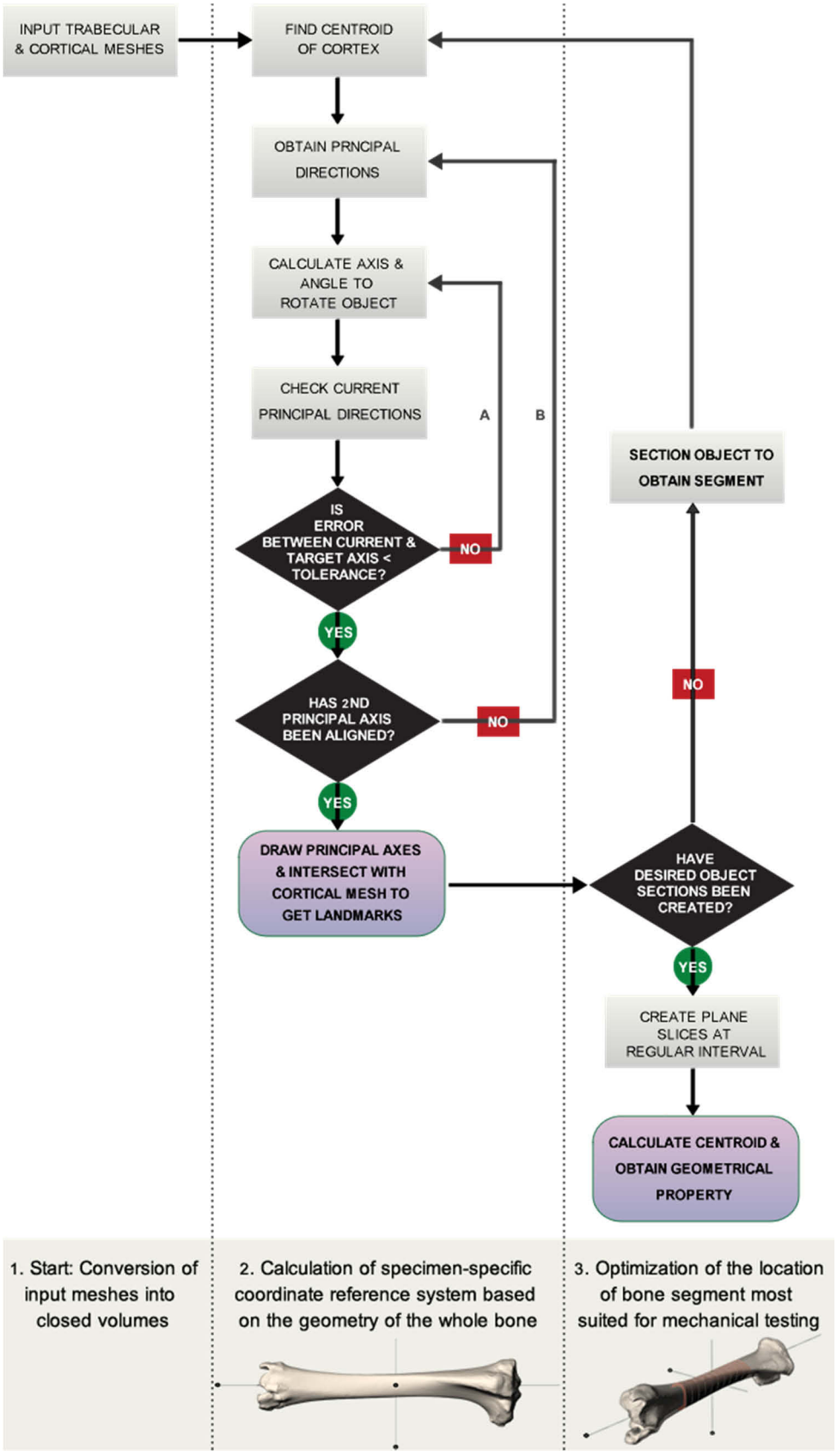

Figure 4.4: Optimization of bone segment best suited for bending and torsional tests can be obtained by running this algorithm. The code first processes input STL meshes so that they are suitable for later calculations, before optimizing the alignment based on the whole bone and bone segment.

4.2.4.1 Conversion of input meshes into closed volumes

The inner and outer surface meshes of the bone were imported in this pre-processing step to ensure that proper calculations take place in later steps. As the cortex is the region of interest, the meshes needed to be joined together in a manner that the CAD package can detect the volume of the cortex instead of the combined volumes of the inner and outer meshes. To achieve this, the meshes are joined before a cut is made transversely. The two sections were then rejoined to form the one mesh and checked if it forms a closed volume. When the check fails, the mesh is repaired by filling any existing holes, checking that the mesh edges match and all surface normals point outwards (Figure 4.5).

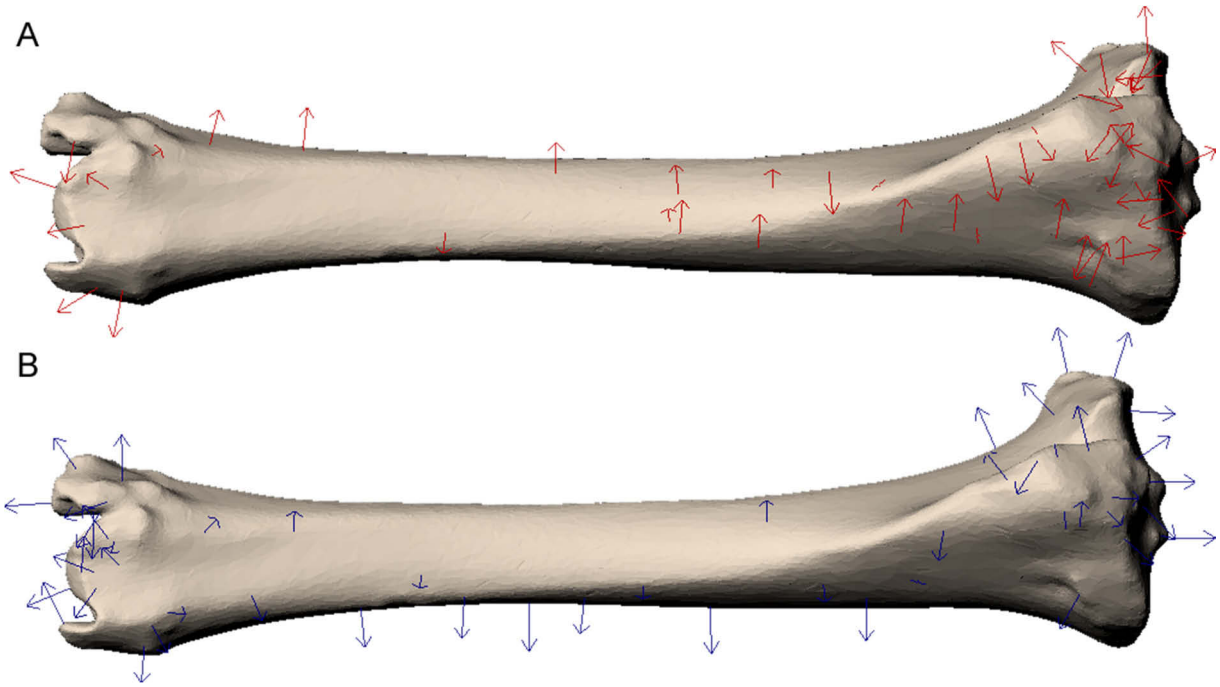

Figure 4.5: A mesh that has undergone pre-processing will have its surface normal pointing in all directions (red arrows) (A). The surface normal will point outwards (blue arrows) after the mesh normals have been rebuilt. The mesh will now form a closed volume and the calculations can proceed.

4.2.4.2 Calculation of specimen-specific coordinate reference system

The key feature of this algorithm is the alignment of the bone to its principal directions and finding the appropriate landmarks, which are achieved in this part of the algorithm. To obtain these outputs, the volume centroid of the cortex mesh was first calculated, to act as the origin for the principal axes. To account for differences in the initial orientation of the original meshes,

the values of the three orthogonal directions were calculated and sorted so that the values of I_1, I_2, I_3 are in descending order.

The next series of steps rotates the bone so that the principal directions coincide with the global axes. Dot product and cross product of the first principal axis and the global y-axis were used to obtain the angle between the two axes and the axis of rotation respectively. However, due to the discretized nature of computational calculations, these steps had to be repeated until the error between the current and target axis, which is the value of the dot product, equals to zero (loop A of Figure 4.4). Thereafter, these series of steps were reiterated for the second principal axis I_2, as seen in loop B of the diagram. When both axes have been aligned to the global axes, the algorithm proceeded to provide visual feedback to the user by drawing the principal axes and creating the landmarks from the intersection of the lines and the cortical mesh, as seen in Figure 4.6:

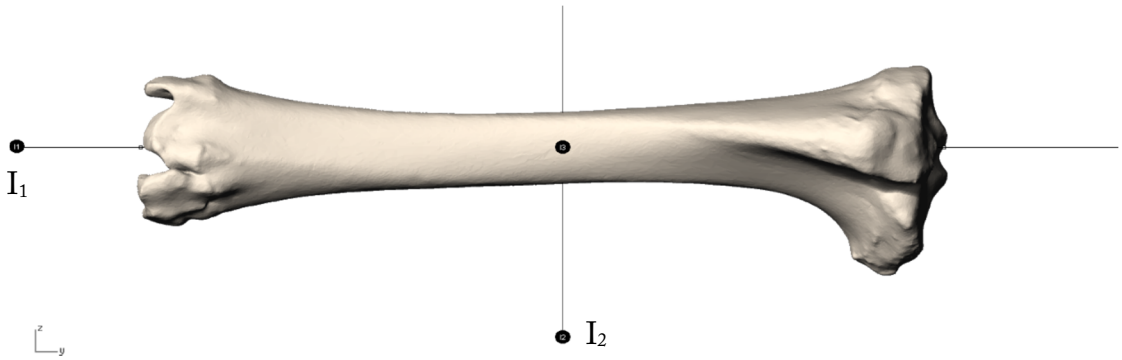

Figure 4.6: To align the bone, the algorithm first calculates direction of the principal axes. Since the first principal axis I_1 has the largest value, it is thus used first to orientate the bone to the global y axis. Thereafter, the second principal axis I_2 is used to rotate the bone to the global z-axis.

4.2.4.3 Optimization of the location of bone segment

In bending tests, only the span of the bone (which is between the external two rollers) is relevant in the analysis, likewise in torsional loading, which is the free region that is not embedded. Therefore, by focussing on the section of the bone that will be directly used in experiments and simulations, an improvement in alignment could be obtained, leading to a decrease in the variation of the second moment of area across the bone section.

Firstly, a cutting plane perpendicular to the long axis is used to obtain the cross section of the distal diaphysis. Using this information, the minimum length of the bone that is required for simple bending theory to be valid was then calculated. The result of this calculation gives the position of the second cutting plane. However, as the variation in geometry across the diaphysis affects the maximum width of the bone, the locations of the first and second cut were allowed to translate by a small range to ensure that the cut section would fulfil the minimum criteria after it is aligned to its principal axes later. Thereafter, by translating the two cutting planes across the diaphysis, bone sections that fulfilled the minimum span-to-width ratio of 4:1 were created (Hardy & Pipelzadeh, 1991) (Figure 4.7). Each created bone section was passed through the second part of the algorithm to align it. The span-to-width ratio of the aligned section was then recalculated to ensure that it still fulfils the minimum criteria after alignment.

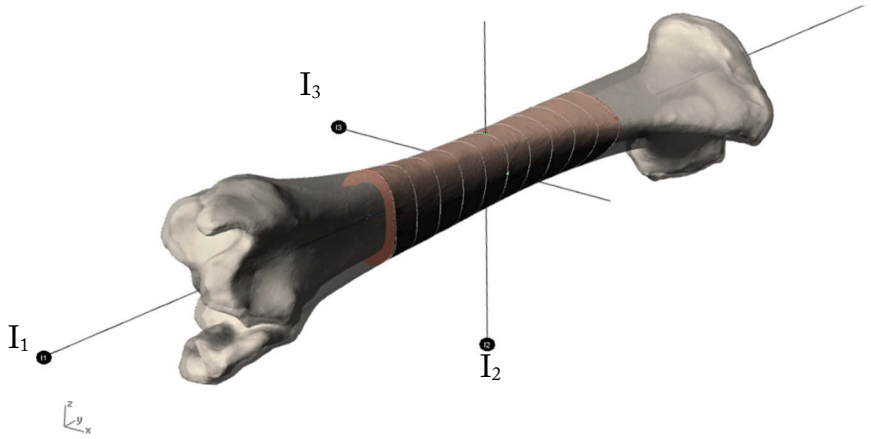

Figure 4.7: A segment of a bone calculated based on the minimum length-to-width ratio and aligned to its principal axes, as shown in pink.

4.2.4.4 Results Output

In both the second and third sections of the algorithm, cutting planes were used to section the bone or bone segment at 5% interval along the long axis, as seen in Figure 4.8. The point where the neutral axis passes through was calculated for each slice (back dots). These were used as the reference points for the calculation of the second moment of area. The results were then exported automatically to Microsoft Excel.

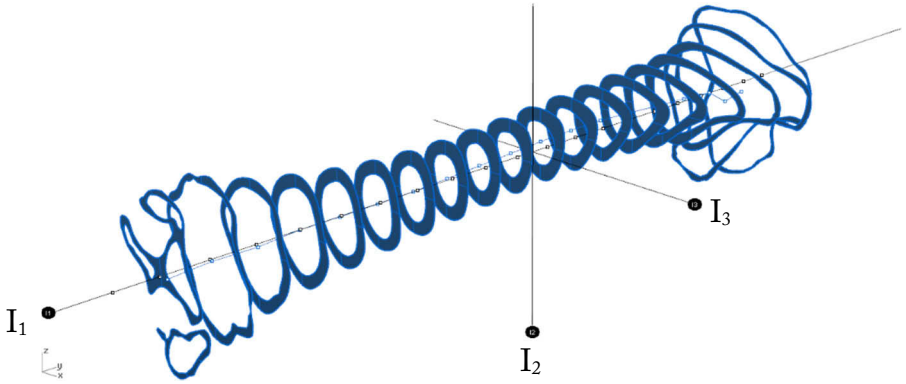

Figure 4.8: Slices of bone sectioned at 5% interval along the long axis, after the bone (or bone segment) has been aligned to its principal directions. The blue dots show the position of the centroid of each slice while the black dots show the intersection between the first principal axis and each slice (termed neutral axis point).

Finally, and not shown in the flowchart, the bone segment with the lowest coefficient of variation of the second moment of inertia in the first and second principal directions was selected (see Section 4.2.5). The locations of the cutting planes used were retrieved and the second part of the algorithm was run once through to align the bone segment. The cutting planes were also used to create 4 points that marked the position of the rollers. Another cutting plane was used to intersect with the bone segment at the centroid to create 2 points that marked the two positions where the bone would experience the greatest tension and compression. These points, together with the aligned cortex mesh, were exported to be used in finite element analysis, which is discussed in Chapter 6 of this thesis.

Codes were also written to obtain the location of 6 prominent features at the ends of the bones to be used as reference in aligning the bone, with 3 on each end of the bone. A plane at a small offset from the desired end was created to be used as a cutting surface to split the mesh to obtain a smaller section to speed up computational time. The mesh vertices that were furthest away from the cutting plane were obtained through an iterative process and marked as seen in Figure 4.9 for ovine tibia below, which are used as features in aligning the bone for experimental testing, as discussed in Chapter 5. The codes that calculates the principal directions and aligns the bone to its principal axes may be found in the Appendix.

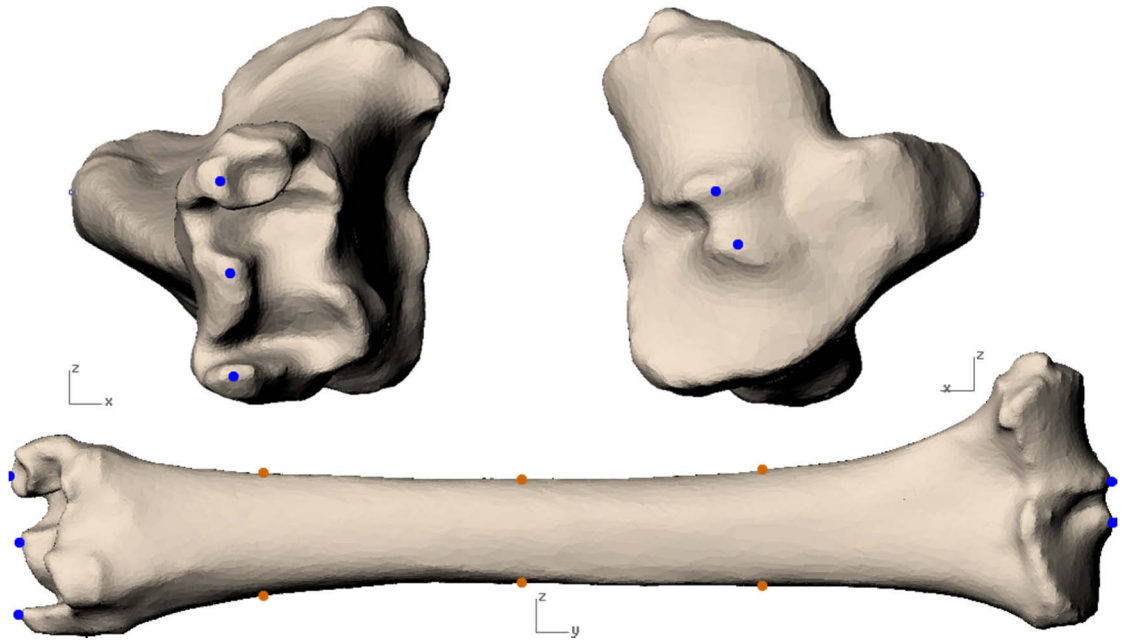

Figure 4.9: The algorithm calculates and plots the location of six prominent features (in blue) to be used in aligning the bone during experiments. The position on the bone where the roller should contact is marked in orange.

4.2.5 Statistical analysis

A regularly-shaped object that experiences pure bending or torsion would have a constant second moment of area along its long axis. In bone, the cross-section varies across the biomechanical length, so the goal would be to minimize the variation in the second moment of area. Therefore, the second moment of area about the neutral axis was measured at 5% intervals along the length of the bone and/or segment in each alignment method. The coefficient of variation (COV) of the second moment of area for each alignment method for each bone was determined by calculating the ratio between the standard deviation and the mean value of the second moment of inertia. The Shapiro-Wilks test was used to determine if the second moment of area followed a normal distribution as the maximum sample size is only 11. This was followed by Levene's and Brown-Forsythe tests to test the homogeneity of variance.

The second moment of area across the cross-section did not follow a normal distribution (Shapiro-Wilks test; $p < 0.05$, which signifies that there is a 95% probability that the data was not sampled from a normally distributed population) in all cases. Therefore, Friedman one-way analyses of variance were used to test the hypothesis that there is no difference in the COV of the second moment of area of the bone among the three alignment methods. When the null

hypothesis was rejected, then the one-tailed paired sample Wilcoxon signed rank test was used to test the hypothesis that the use of the proposed alignment method decreased the median COV.

4.3 Results

4.3.1 Tibia

4.3.1.1 Second moment of area

The second moments of area for whole ovine tibiae in the principal directions are represented in Figure 4.10. In all the figures, the data is represented from the distal to the proximal end. It can be seen that the methodology optimises the alignment of long bones by ensuring that $I_1 > I_2 > I_3$ in the midshaft. By focussing on the diaphyseal section and optimizing the bone segment to be used in analysis, the spread of values decreased as seen in the bottom of Figure 4.10.

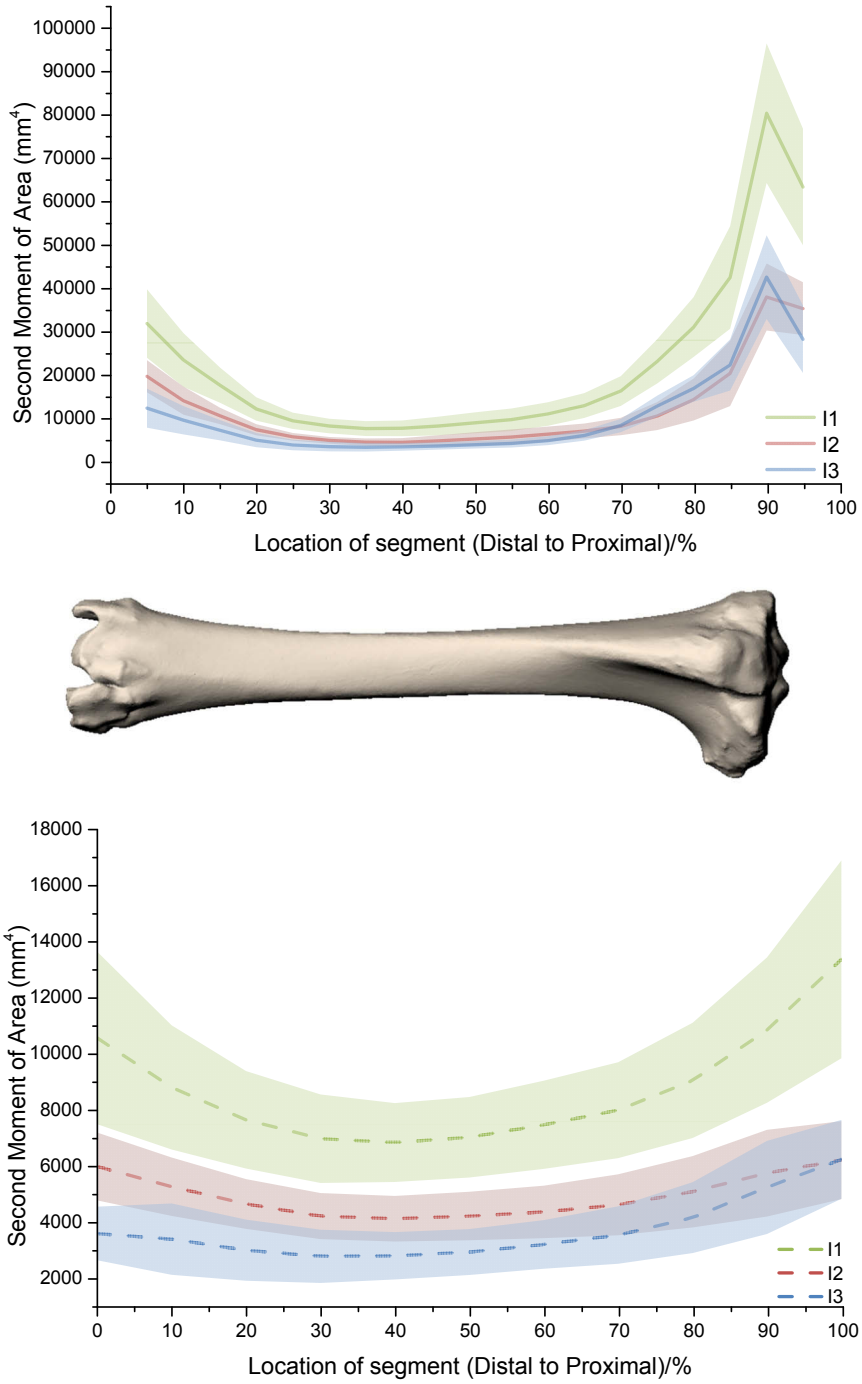

Figure 4.10: The second moment of area in its principal directions (N=11), for optimised whole ovine tibiae (top) and optimised tibia diaphyses (bottom), plotted against the distance along the tibia from distal to proximal. All lines are means ± standard deviation.

The location of the optimised segment was applied to other alignment methods to obtain the second moment of area across the same region (Table 4.1). The use of the three different alignment method resulted in a statistically significant difference in the second moment of area recorded in the I_1 direction (Friedman ANOVA, $\chi^2(2) = 20.182$, $p = 0.00004$). The effect of

applying the novel methodology is a reduction in the mean second moment of area across the segment. The results were similarly significantly different in the I_2 and I_3 directions ($\chi^2(2) = 9.455$, $p = 0.009$ and $\chi^2(2) = 16.545$, $p = 0.0003$ respectively).

Table 4.1: Range and median (N=11) of the second moment of area in the I_1, I_2 and I_3 directions for three different alignment methods for the ovine tibiae

Alignment Method		**I_1**	**I_2**	**I_3**
Anatomical	Range	7865.69639 - 14388.13134	3902.0605 - 7384.58957	2885.47939 - 7466.56977
	Median	9462.243	5355.27377	4286.38592
Optimised whole	Range	6915.61084 - 14654.00931	3971.45489 - 8170.88295	2944.15594 - 6483.12636
	Median	8940.44628	5151.59363	3788.85265
Optimised segment	Range	6235.93039 - 13246.32979	3476.5132 - 6902.21574	2759.41719 - 6344.11404
	Median	8520.22015	4941.99029	3510.15808

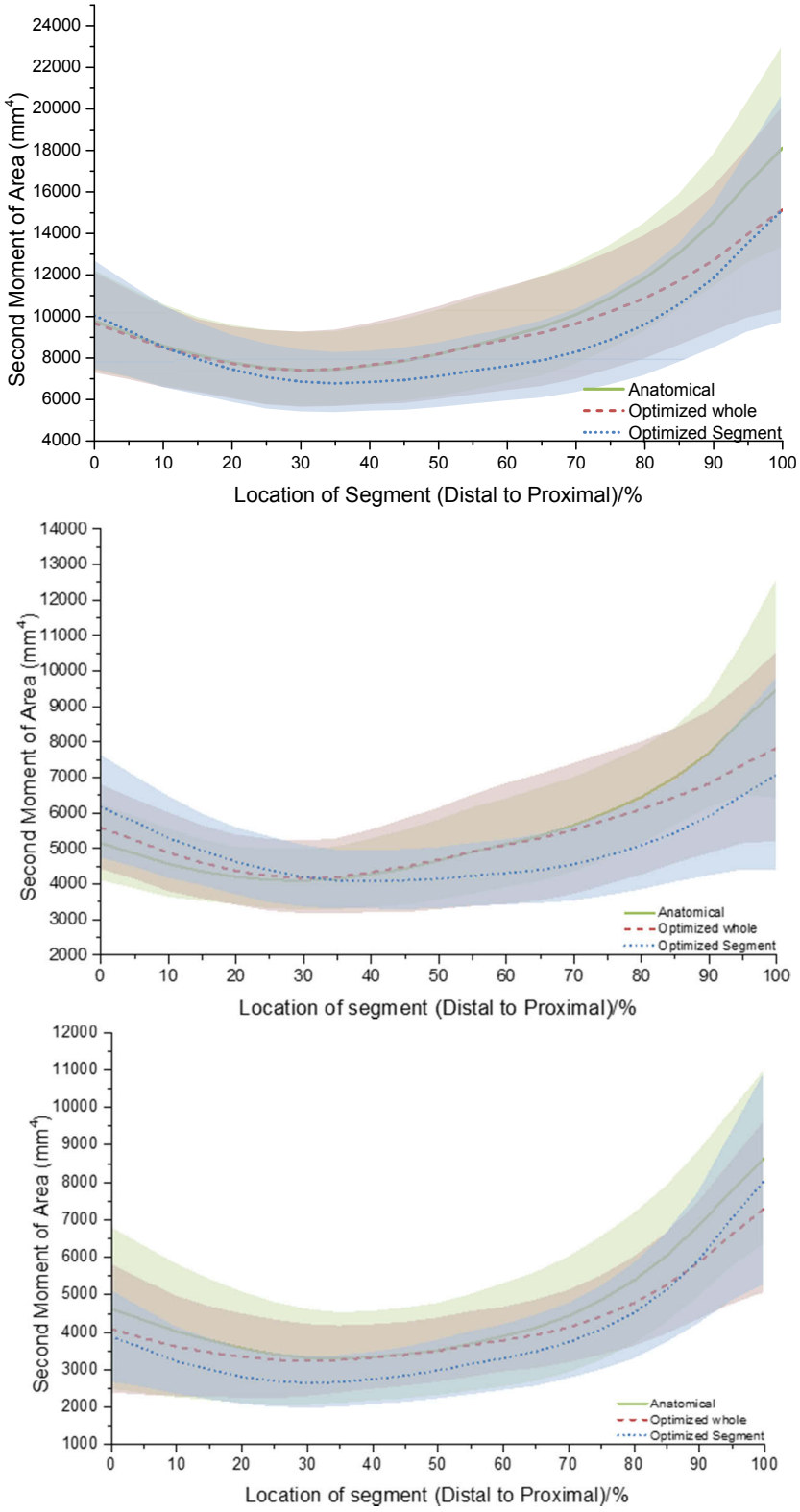

Figure 4.11: The second moment of area in its principal directions (N=11), for optimised tibia segment in the diaphyses, plotted against the distance along the tibia from distal to proximal, and compared against different alignment methods. Solid line: anatomical landmarks. Dash line: optimised whole bone. Dotted line: optimised bone segment. All lines are means ± standard deviation.

4.3.1.2 Coefficient of variation

The coefficient of variation (COV) found using the anatomical method corresponded well with the data reported by Finlay et al. (1995) (Table 4.2). The implementation of the new methodology resulted in a decrease in COV. There is a significant decrease in the COV in the anatomical vs. optimised whole group only in the I_1 and I_2 directions (Table 4.3) (Wilcoxon signed-rank with Bonferroni correction; p = 0.00255 and p = 0.006 respectively). The decrease was also significant in the anatomical vs. optimised segment group (p= 0.012 and p = 0.002), but the application of the optimised segment section of the methodology did not bring about any significant improvement to the results. With reference to Figure 4.11, the 'optimised segment' part of the methodology resulted in a more even curve that is flatter. The redistribution of the second moment of area resulted in a higher value to be recorded at the ends as compared to the results obtained using the 'optimised whole' algorithm. Therefore, the COV did not decrease significantly as expected.

Table 4.2: Range and median (N=11) of the coefficient of variation of I_1, I_2 and I_3 for three different alignment methods for the ovine tibiae

Alignment Method		I_1	I_2	I_3
Anatomical	Range	0.208-0.430	0.194-0.476	0.198- 0.620
	Median	0.301	0.285	0.351
Optimised whole	Range	0.143-0.313	0.117- 0.346	0.172- 0.477
	Median	0.222	0.193	0.288
Optimised segment	Range	0.157-0.401	0.103-0.355	0.267- 0.510
	Median	0.236	0.164	0.371

Table 4.3: A summary of the p-values of Friedman's analysis of variance on the second moment of area and its coefficient of variation, including further analyses carried out with the Wilcoxon signed rank test. Significant p values are in bold.

	I			COV		
Direction	1	2	3	1	2	3
Friedman ANOVA	**0.00004**	**0.009**	**0.0003**	**0.0008**	**0.006**	**0.004**
Wilcoxon signed rank						
Anatomical v optimised whole	**0.003**	0.252	0.084	**0.00255**	**0.006**	0.028
Anatomical v optimised segment	**0.002**	0.023	**0.002**	**0.012**	**0.002**	0.718
Optimised whole v optimised segment	**0.002**	**0.009**	**0.002**	0.998	**0.015**	0.998

4.3.1.3 Anatomical directions

As I_2 and I_3 directions are not easy to distinguish in a clinical setting, the data was checked manually and regrouped so that they reflected anterior-posterior (AP) and medial-lateral (ML) directions (Figure 4.12). It can be seen that the AP direction has a higher second moment of area than the ML direction.

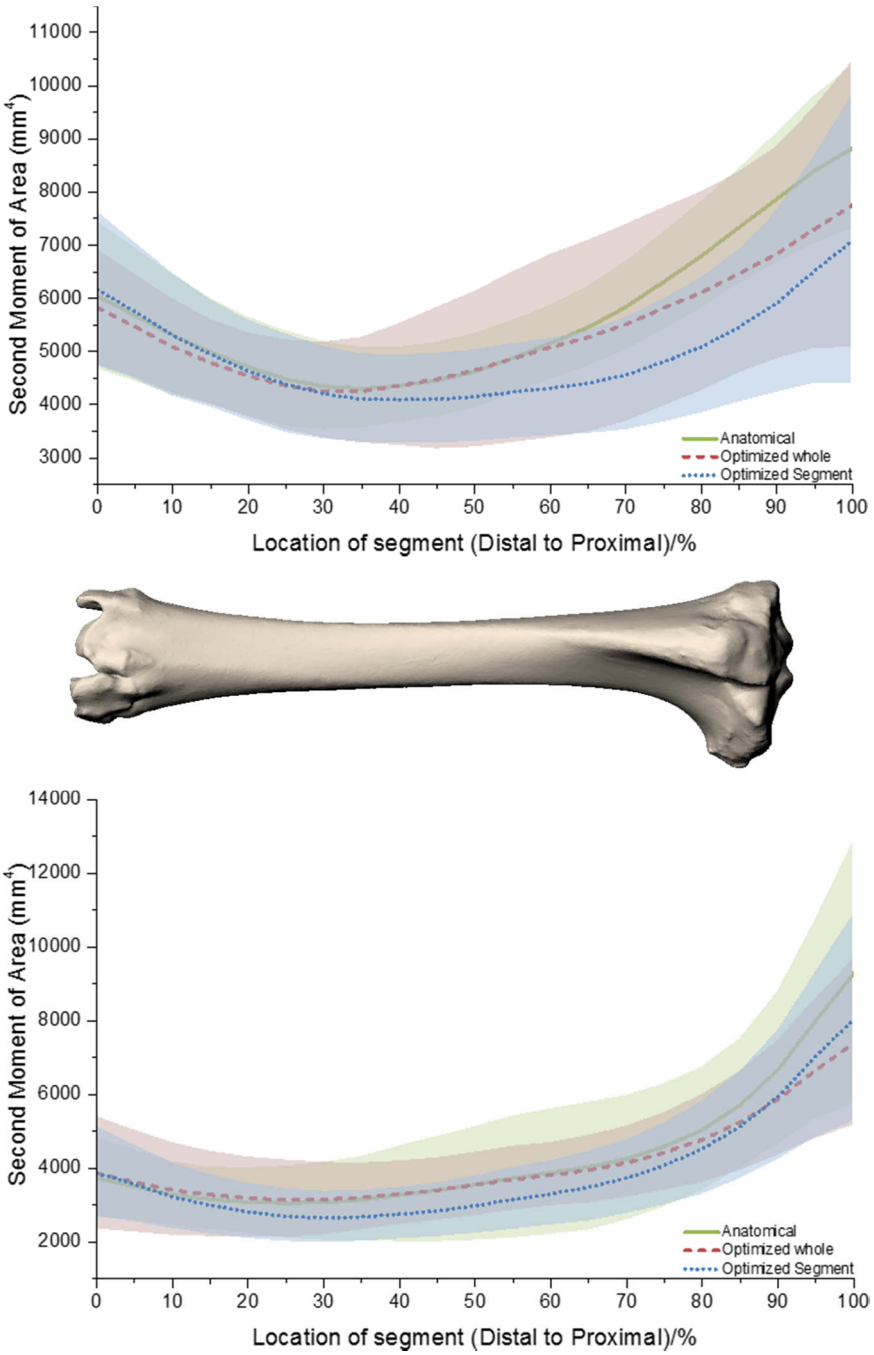

Figure 4.12: The second moment of area (N=11), for optimised tibia segment, grouped about its AP (top) and ML directions (bottom). The values are similar to results obtained in the I2 and I3 directions, but exhibit higher standard deviation in the middle of the segment for results obtained from the optimised whole algorithm. All lines are means ± standard deviation

4.3.1.4 Location of landmarks

The intersection between the principal axis and the cortical bone in each alignment method was marked and plotted in Figure 4.13. On the tibial plateau, red dots show the anatomical landmarks that were used, as described in Finlay et al. (1995) The blue squares show that the

reference landmarks are located more anteriorly on the proximal end when the whole bone is aligned based on its geometrical properties. The black crosses show that the landmark is shifted medially to the intercondylar eminence when the bone is aligned based on its optimised segment. On the distal end of the tibia, the landmarks shift posteriorly slightly with each alignment method.

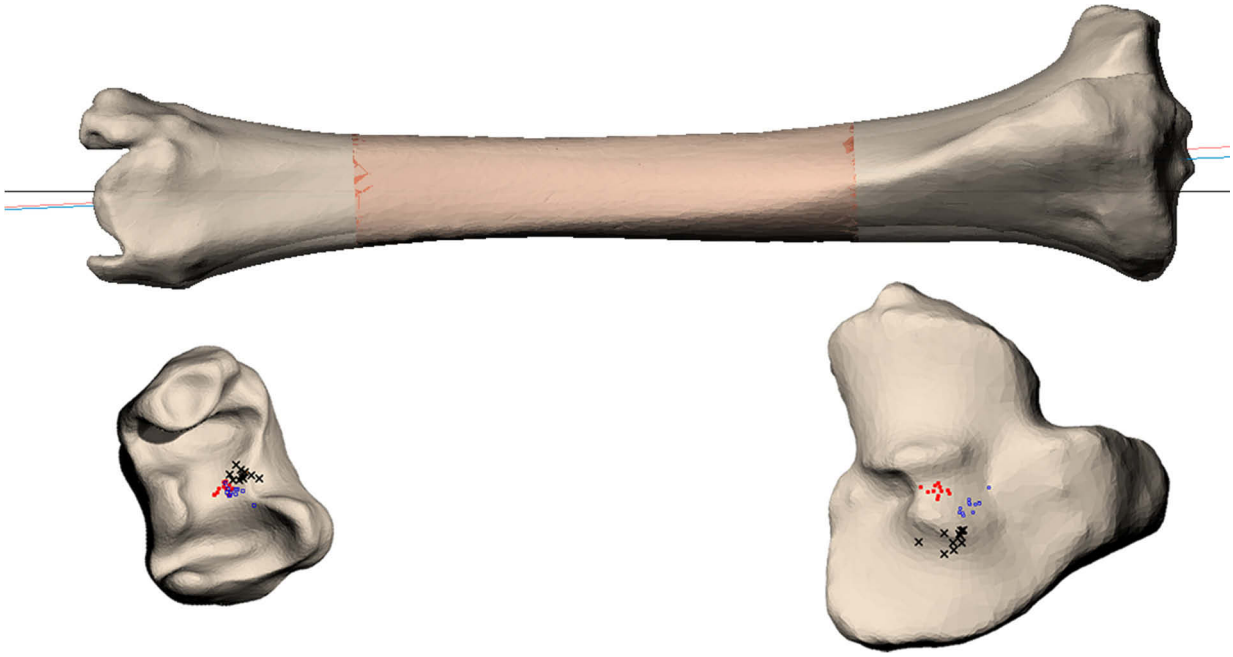

Figure 4.13: The landmarks that can be used to obtain the desired alignment are shown (bottom) for an optimised segment (top). Blue dots: anatomical. Red dots: optimised whole. Black crosses: optimised segment.

4.3.2 Femur

The second moment of area for ovine femur in its principal directions can be seen in Figure 4.14. Unlike the case for the ovine tibia, the coefficient of variation of the second moment of area was much higher in ovine femur. Furthermore, the I for the ovine femur was about 50% larger than that found for the tibia. On running the optimised segment algorithm, a flat middle region was also obtained. However, the gradients of the curves in Figure 4.14 rise sharply towards the end for the I_1 and I_2 directions before dropping quickly. This is caused by changes in the shape of the femur at the condyles and the femoral head. The curvature and bigger diameter of the femur diaphysis compared to the tibia requires a longer length of the bone to be used in mechanical testing in order to fulfil the minimum length to width ratio. The result of this is the inclusion of the epiphysis in the optimised segment. However, on checking the minimum span ratio a second time after the segment has been generated, half the femurs failed

this test. Using segments that ranked lower in the initial calculations did not yield any change in the result. Therefore, immature ovine femur is unsuitable to be used in mechanical testing because the minimum span-width ratio of 4:1 could not be fulfilled with its short length and a decision was made to terminate any further analysis on it.

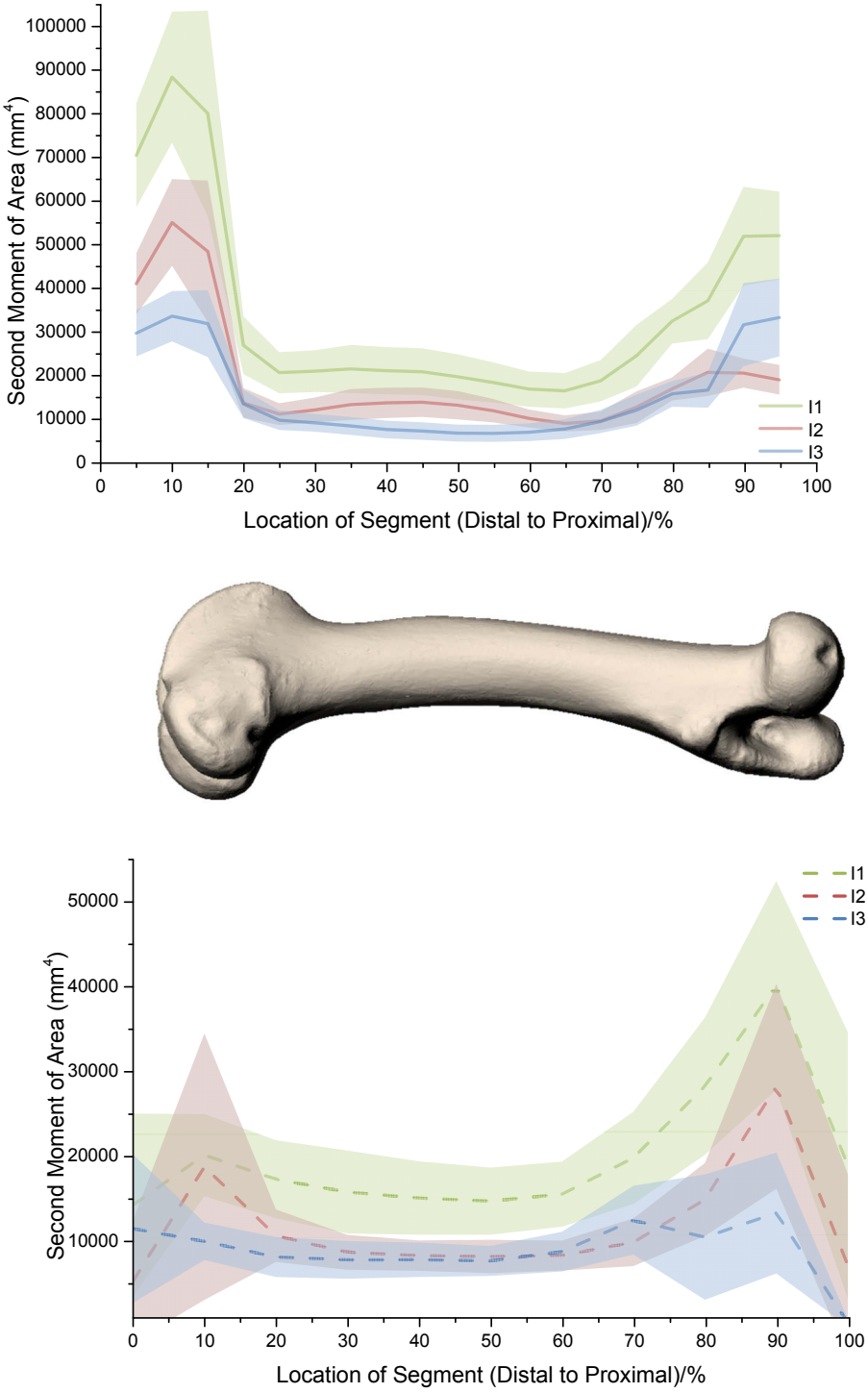

Figure 4.14: The second moment of area in its principal directions (N=9), for optimised whole ovine femurs (top) and optimised femur diaphyses (bottom), plotted against the distance along the tibia from distal to proximal. All lines are means ± standard deviation.

4.4 Discussion

A novel methodology that calculates the principal directions of bone, and aligns the bone to these principal axes so that it may be subjected to a state of pure bending and torsion has been developed. The ability of the anatomical reference frame to resist pure bending and torsion was also assessed by comparing the second moment of area and its variation across the cross-section with the proposed methodology. The Ruff and Hayes (1983)/Finlay et al. (1995) method was selected to be used as the anatomical reference frame as it was found to be the most complete. The results showed that the use of the 'optimised segment' part of the proposed methodology resulted in a more even distribution of the second moment of area that is accompanied by a lowering of its the coefficient of variation in the I_1 and I_2 directions. It was also found that a lower COV was experienced in the AP direction of the ovine tibia than in the ML directions. Since the cross section in the AP direction is more regular when the bones are aligned using this methodology, experimental testing to fracture should be conducted in the AP direction rather than the ML direction in order to minimise the eccentric loading on the bone due to the bending forces.

An added part of the methodology checks that the minimum length-to-width ratio has been fulfilled. While this condition was always fulfilled for ovine tibiae, it failed for more than half of the femurs that were tested. Therefore, ovine femurs are not suitable for four-point bending and torsional loading tests as their geometry prevents a pure state of loading from being achieved.

The third aim of this study was to generate landmarks that may be used as reference points for the alignment of bones during experimental testing. As seen in Figure 4.13, the landmarks that were generated using the novel methodology are located more medially on the tibial plateau than the midpoint between the two tibial condyles that the anatomical reference frame requires. However, the locations of reference points on the distal tibia are fairly similar regardless of the alignment method used (Figure 4.9).Figure 4.9

4.4.1 Comparison of geometrical properties against literature

It is difficult to compare the results obtained in this study with data available in the literature due to differences in the breed of sheep used and the definition used to define the principal axes. Nevertheless, the alignment of the whole bone using geometrical properties corresponded well with the results obtained by aligning the bone using an anatomical-by-eye reference system in the middle section (Finlay et al., 1995). The location of the lowest second moment of area was the same in both studies for each graph in Figure 4.15, in the diaphysis of the bone.

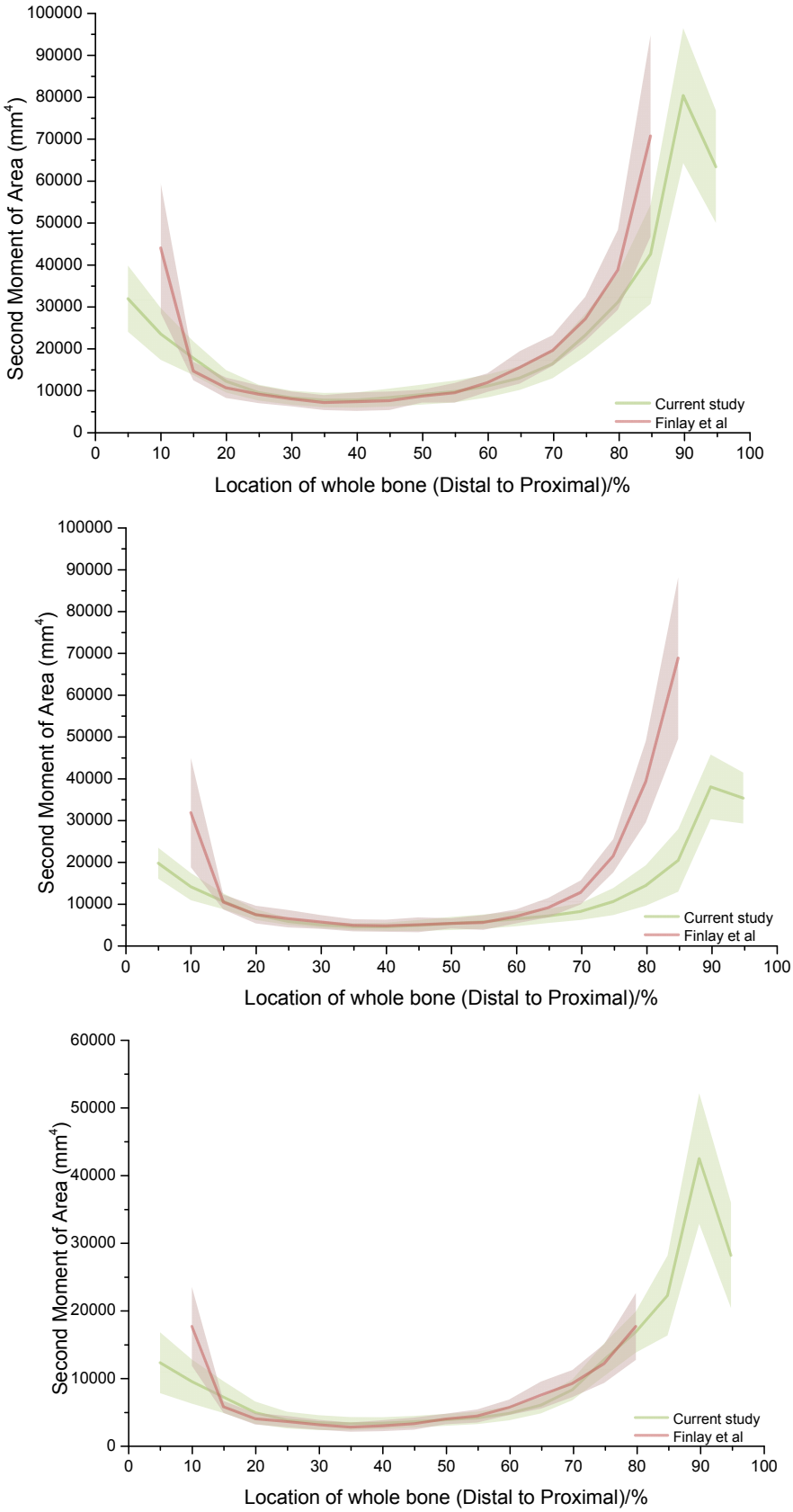

Figure 4.15: The second moment of area of whole ovine in its three principal directions, I_1 (top), I_2 (middle) and I_3 (bottom)(N=11), plotted against the distance along the tibia from distal to proximal, and compared with similar data replotted from Finlay et al (N=6). All lines are means ± standard deviation.

In all three directions, the second moment of area rises more gradually at the epiphyseal regions in the study here. Indeed, the second moment of area for immature Texel breed tibiae ranged from (7473 to 80335 mm^4) in the I_1 direction, (4293 mm^4 to 37874 mm^4) in the I_2 direction and (3153 to 42461 mm^4) in the I_3 direction for whole ovine tibiae, which is slightly different from the results obtained by Finlay et al. (1995), who carried out their studies using Arcott sheep.

One of the primary differences with this work compared to the work by Finlay et al. (1995); Perz et al. (2014); Ruff and Hayes (1983) is that the principal directions were determined from volume second moment of the cortex, which is based on its morphology in three-dimensions. In all their work, the geometrical properties were evaluated on a slice-by-slice basis, which is essentially a two-dimensional property. Therefore, existing techniques for studying the geometrical properties of bones is more an analysis of how the I_{max} or I_{min} axis vary across the cross-section of the bone, which does not yield further information on how the bone behaves as a structural entity. Indeed Finlay et al. (1995) reported a range of 1.76 to 86.1° of the angle between I_{max} and the anterior-posterior axis, with the smallest angle at the midshaft and the largest angle at the proximal and distal ends. Therefore, the second moment of area and standard deviations measured in the midshaft are similar, whereas the recorded values are dissimilar at the ends of the bone as the angle between the reference axes used is greater.

A further difference in the determination of the principal directions is the use of the centroid as the origin for other workers (Finlay et al., 1995; Forman et al., 2012; Perz et al., 2014) whereas the neutral axis point was used in this study. The neutral axis refers to the line about which an object experiences no compressive or tensile stress when it is subjected to pure bending, and the neutral axis can be assumed to coincide with the first principal axis. The neutral axis point is thus obtained by intersecting I_1 with each slice. As seen in Figure 4.8, these two points do not always coincide, and thus I_{max} that is calculated based solely on the slice would deviate from the I_2 that is calculated based on the cortex of the bone.

Previous studies have shown that I_{max} or I_2 acts about an axis in the AP direction (Finlay et al., 1995; Ruff & Hayes, 1983), thereby prompting the need to investigate if the reclassification of results obtained in the principal directions would make a difference to the results. As seen in

the result section, the second moment of area is more evenly distributed about the AP direction, and has higher mean value. However, there is a redistribution of the standard deviation, causing the COV to increase about the AP direction compared to the I_2 direction, and the COV to decrease about the ML direction compared to the I_3 direction. Further work with a larger population would thus be required to investigate the direction of the bone that resists bending better.

4.4.2 Alignment system in experimental testing

The reproducibility of any alignment method is a key question in light of large inter-specimen variability (Cristofolini, 1997). Since the identification of landmarks as seen in Figure 4.13 is not easy, the location of prominent features on the bone was generated instead (Figure 4.9). In the case of the ovine tibia, the two intercondylar eminences are the most proximal landmarks and are thus used as the first two landmarks. The next landmark is found in the most posterior feature on the tibial plateau. A minimum of six points were desired, to enable this methodology to be combined with a digitizing approach (Chapter 5), hence the remaining three points were obtained from the malleolus of the bone.

Currently in bending and torsional tests, bones are aligned using their maximum span (Varghese et al., 2011) or on a pre-defined fixed span marked out (Cristofolini & Viceconti, 2000). It is not clear if these methods fulfil the assumptions required in simple bending and torsion, as no attempt was made to quantify the width-to-span ratio in each bone. This study uses a span-to-width ratio of 4:1 as it has been shown that this is the minimum criteria for primary bending stresses to be dominant in bending test and for classical theory to be applicable (Hardy & Pipelzadeh, 1991). The use of a longer length-to-depth ratio of 8:1 up to 20:1 have been used in material characterization (Currey & Butler, 1975; Lanyon et al., 1979), where pieces of bone were machined to regular shapes. However, such ratios are not feasible when both the geometry and short length of ovine long bones need to be taken into account. As such, the use of the 4:1 slenderness ratio was chosen to satisfy the assumptions for classical theory of solid mechanics to be valid, and to minimize the COV across the bone segment.

The extended part of this methodology brought about an improvement in the analytical solution by isolating the mid-shaft of each bone that is relevant for experimental testing. This is the

effect of not factoring in the geometry of the tibia and femur at the meta- and epi-physes, where huge variation in shape exists, as the part of the bone that is outside the external span of the bone do not contribute significantly to the strength of the bone in testing (Ebacher et al., 2007). The graph of second moment of area of the cross section was symmetrical when the extended part of the algorithm was used, and there was a significant decrease in the COV when compared with the results from the anatomical reference frame. Therefore, the use of this alignment method reduces the presence of eccentric loading by calculating the principal axes where the cross-section across the bone is most regular. Previous work by Augat et al. (1996) has shown that the geometrical properties of the cortical shell can be used as a strong predictor for failure strength. Since failure of a structure tends to occur at the region of the thinnest cross section, using the extended part of the algorithm has the effect of focussing the failure to take place in the middle of the segment, which is in line with the aim of this thesis to model fractures consistently.

4.4.3 Limitations

One current limitation is that the surface meshes need to be pre-processed before the principal moments can be calculated. In this study, an approach to join, cut, and rejoin the objects was used, as it mimics how bone with a hollow core may be produced using rapid prototyping. The mesh is also ensured to be fully closed or watertight, otherwise the calculations would be wrong. However, the mesh sometimes does not rejoin successfully after a cut has been made. Therefore, the whole process had to be calculated with a cut made at a different position. An alternative method would be to create a pin hole through half the combined mesh to join the two surfaces together, but it is unclear the extent to which the presence of the hole would affect later calculations.

The cross sections, from which the second moment of area was calculated, were calculated at 5% intervals along the total length of the bone. The decrease of the slice spacing to 1% would increase the resolutions of the results but this would increase the memory was required to compute the location of the optimised segment. The use of a more powerful computer, or an optimisation of the codes could possibly overcome this issue.

4.5 Summary

A new methodology that calculates the alignment of bone based on its principal axes, so that a state of pure bending and torsion may be achieved in experimental testing, has been developed. This methodology differs from existing work in the literature as it accounts for the three-dimensional geometry of the bone and isolates the segment of the bone that is most optimised for experimental testing. The software written further ensures that the minimum assumption of length in bending tests has been satisfied, based on the 4:1 ratio as found by Hardy and Pipelzadeh (1991).

The results obtained from this work showed a significant reduction in COV of second moment of area across the bone in the first two principal directions (or along longitudinal axis and about the AP direction) ($p < 0.01$) when the principal axes are calculated based on the geometry of the whole bone. A further effect is the flattening of the curve of the second moment of area across the length of the bone segment. This focuses the middle of the bone segment to have the lowest second moment of area, which from an analytical point of view, would be the weakest region and thus most likely to break when loaded.

The extended part of the algorithm that generates the segment that is most optimised for experimental testing generally performed better than using the code that simply calculates the alignment based on the whole bone. However, even if long bone is aligned based on the geometrical properties of the whole bone and not only a bone segment, significant improvements in the results of the second moment of area and its COV was shown when compared to anatomical methods.

The generation of a reference coordinate system to achieve a state of pure bending and torsion is essential for the elucidation of failure mechanism of whole bones at the structural level. The successful validation of this novel methodology to optimise the alignment of long bones is thus dependent on the successful generation of consistent fracture patterns at various strain rates. Therefore the focus of next chapter is on the in-vitro testing of ovine tibiae in four-point bending and torsion.

5 THE STRUCTURAL FAILURE OF IMMATURE OVINE TIBIAE IN FOUR-POINT BENDING AND TORSION

5.1 Introduction

The benefits of understanding the failure mechanisms of whole bone fractures include the prevention of bone fractures through better design of equipment, improvement in treatment process and forensic characterization of the causes of injuries (Ebacher et al., 2007; Kress et al., 1995; Ouyang et al., 2003). Most existing work on bone fractures have focussed on the geriatric population (Forman et al., 2012), mainly in stance-phase loading to simulate fractures of the proximal femur (Cristofolini et al., 2007; Keyak et al., 2001), or to replicate fall conditions (Bessho et al., 2009), or dynamically in three-point loading in automotive injury prevention (Kress et al., 1995; Ouyang et al., 2003). Only three studies have investigated the fracture tolerance of the immature population, namely that by Forman and co-workers (2012) and Ouyang et al. (2003) for humans and Pierce and colleagues for pigs (2000). However, as noted in Chapter 2, spiral, oblique and transverse long bone fractures are the most common orthopaedic occurrence in NAI, therefore an understanding of long bone failure mechanisms

in immature bones in bending and torsion is especially required to add an objective tool to the detection of NAI.

5.1.1 Whole bone fracture in the immature population

Various injury etiology mechanisms have been proposed (Haney et al., 2009; Pierce et al., 2004), but only one work exists in the literature that had the intended aim of reproducing fractures seen in child abuse (Pierce et al., 2000). Although porcine femora were used in their study, where one week old in pigs is approximately equivalent to a year in humans (Baumer et al., 2009), all their experiments were conducted at quasi-static rates of 1mm/s for three-point bending and 1°/s for torsional loading. Therefore, their choice of loading rate falls under quasi-static strain rate (Cristofolini et al., 2010), which is too low to reproduce injuries caused during child abuse, as they happen at higher loading rates.

The two works involving whole bones of the paediatric population were carried out in three-point bending (Forman et al., 2012; Ouyang et al., 2003). The failure response of bones impacted at 0.083mm/s, 8.3mm/s (Ouyang et al., 2003) and 1.5m/s (Forman et al., 2012) showed that the yield strength, maximum deflection and bending moment at fracture increased with increasing strain rate. In terms of experimental methods, these studies ensured that the bones were appropriately simply supported (Hibbeler & Fan, 2004) so that they allowed for horizontal translation at the supports. They also allowed one degree of rotational freedom during testing so that the bones are self-aligned during the bending. In order to achieve this, the proximal and distal ends of their specimens were embedded in Poly(methyl methacrylate) (PMMA) to enable attachments to custom-made fixtures that act as rollers on a flat surface. Three-axis load cells placed below the rollers record the force response of the bone during testing.

5.1.2 Alignment method

The importance of the use of an anatomical reference frame has been covered in Chapter 3. However, there is no mention of a reference coordinate system in the study by Pierce and colleagues (2000), making it difficult to reproduce their work. The alignment of femurs used in Forman and co-workers' (2012) study involved potting their specimens such that the centre of

the femoral head was level horizontally with the centre of the distal femoral notch, in a method similar to that described in Ouyang et al. (2003). Although this method of bone alignment is straightforward and is claimed to be highly repeatable, it can cause the medial and lateral aspects of the bone to be at an angle from the horizontal, depending on the curvature of the bone. This creates a varying amount of shear stress to be present in three-point bending. Simplified beam analyses assume that shear stress is negligible, but their bone alignment technique introduces shear stress during loading which might affect their results if simple beam bending analysis is used.

5.1.3 Fracture morphology in three-point bending test

Among the many fracture patterns seen clinically, only transverse, oblique and spiral patterns have been replicated in-vitro in immature bones. Unlike the consistent transverse fractures reported by Pierce et al. (2000) in all 12 immature porcine femora at low strain rate, Forman et al. (2012) reported that fractures in the immature population were rarely initiated at the mid-diaphysis at high strain rate. Instead, oblique or comminuted fractures ensued from cracks that were initiated off-centre. The presence of multiple types of fracture patterns is consistent with the study conducted by Kress et al. (1995), who impacted 253 tibiae and 136 femurs from the geriatric population at a high velocity of 1.2-7.5m/s and found tension wedge (a type of comminuted butterfly fracture) and oblique fractures to be the most common. Unfortunately, no fracture patterns were available from the study by Ouyang and colleagues (2003) at both low and high strain rates as the tests were terminated when the slope of the force-time curve dropped to zero. Therefore, the generation of a consistent fracture pattern at low strain rate has not been confirmed.

5.1.4 Four-point bending test

In terms of modelling descriptions provided in case histories, the three-point bending test theoretically fares better than four-point bending as it is able to simulate the event when a bone is impacted by a single object (Pierce et al., 2000). However, loading an object in three-point bending will cause significant shear stress to be experienced near the middle of the specimen, which is exacerbated when the specimen is irregular in shape. This accentuates the possibility

of the object failing in shear, rather than in tension, making the analysis of the primary cause of failure difficult. In contrast, constant bending moment is experienced in the middle of the specimen in four-point bending, casting the region of high shear stress to be outside the external supports. A four point bending test is thus better able to study the case of pure bending better than the three-point bending tests. Moreover, it has been recommended that the specimens used in three-point bending tests should be straight and have a uniform cross-section (Athanasiou et al., 2000). Therefore, four-point bending tests are more appropriate for bones than three-point bending tests, due to the curvature and variation in cross-section across the length of the bones, as seen in Chapter 3 and 4.

5.1.4.1 Experimental setup

Four-point bending experiments have been used widely in the characterization of the structural properties of bones, most notably by the team from Bologna. One of their earliest designs features the use of internal supports that are adjustable in height to allow for equal load distribution between the rollers (Cristofolini et al., 1996). Later designs subsequently saw the shift of adjustable rollers to the external supports, with the internal supports being fixed in height (Cristofolini et al., 2010; Cristofolini & Viceconti, 2000; Gray et al., 2008). Their design setup was also adapted by Heiner (2008) who added a rocker mechanism that ensures that the inner supports maintain contact with the specimen and provide even loads even when the bone is aligned at an angle. No mention was made of the alignment method that was used to ensure the repeatable placement of specimens. Furthermore, they reported that the use of a clamp to tighten the specimens caused it to slip instead. Photographs of their setup showed that the internal rollers were not parallel to the ground surface, unlike the case in the work done by the team from Bologna. Even though the authors stated that their experimental design was based on the work from Bologna, it is probable that that they had not used the Ruff and Hayes (1983) coordinate system that the team from Bologna had adopted.

There is only one recorded work of four-point testing of whole tibiae tested to failure in the literature (Ebacher et al., 2007). No details on the four-point bending rig or alignment method used was provided in their paper. In contrast to the use of clamps to prevent the rotation of the bones during testing, as carried out by the team from Bologna (Cristofolini & Viceconti, 2000;

Cristofolini et al., 1996), the proximal and distal ends of the tibia were mounted in PMMA to maintain stability. Such a methodology may have resulted from the removal of the distal part of the tibia for a separate experiment.

In contrast to a pre-defined inner fixed span of 62mm as used by Heiner and Brown (2001) and the team from Bologna, Ebacher and co-workers (2007) used a subject-specific span that varied according to the length of the specimen. The inner supports were thus located at a distance of 50 to 66% from the distal end. The distance of the outer supports was set at three times the length of the inner support, consistent with the method used in other work.

With the exception of the work conducted by Heiner and colleagues (2001), all the four-point bending setups used fixtures to secure the bone during testing. The team from Bologna used clamps to stabilize the bone whereas Ebacher et al. (2007) fixed the ends of the bones in PMMA to ensure that the bone does not rotate during the experiment. Augmented with the use of a rocker, it implies that the setup used by Heiner and Brown (2001) is less constrained than other setups due to presence of an extra degree of freedom.

5.1.4.2 Testing rate

In contrast to the use of varying strain rate in three-point bending tests, four-point bending tests of whole bones to failure has only been conducted at quasi-static strain thus far. Ebacher et al. (2007), who studied the strain distribution and cracking behaviour of human bone during bending, tested their bone at a speed of 0.1mm/s. This is slower than the cross-head speed of 0.25mm/s and 0.5mm/s used by Heiner and Brown (2001) and Cristofolini and colleagues (2000; 1996). The use of physiological strain rates $0.05s^{-1}$ for the characterization of structural behaviour has also been reported (Cristofolini et al., 2010). However, it is difficult to compare with their previous tests as no cross-head speed was given, and it is difficult to calculate the strain rate in the previous experiment due to inter-specimen differences in cross-sectional area. Therefore, the choice of low testing speed is certainly influenced by the main purpose of conducting mechanical tests for mechanical characterization of the specimens. Furthermore, the testing loads were small with only a maximum force of 500N or displacement of 0.5mm allowed (Cristofolini & Viceconti, 2000; Cristofolini et al., 1996). In contrast to the plethora

of fracture patterns that have been obtained for three-point bending at different rates (Kress et al., 1995), such information is not available for four-point bending tests.

5.1.5 Torsional testing

The osteonal structure of bone at the microscopic level makes the bone vulnerable to failure in shear at the cement lines as discussed in Chapter 3. A torsional test is one method of measuring the properties of a specimen in shear and it essentially involves twisting the specimen to measure its torsional stiffness and/or strength. Testing to failure has been conducted on whole human (Varghese et al., 2011), chicken (D. Taylor et al., 2003) piglet (Pierce et al., 2000) and sheep bones (Wullschleger, 2010).

5.1.5.1 Experimental setup and testing rate

The greatest challenge in conducting torsional tests on bones is the difficulty of excluding other eccentric loading, due to the lack of a plane of symmetry in bone. To overcome this issue, the team from Bologna designed a system of hinges and cross-rails to eliminate undesired loads that might be transferred to the bone during the test (Cristofolini & Viceconti, 2000; Gray et al., 2008). Human femurs and tibiae were loaded at quasi-static or physiological strain rates, using a rate of 0.2°/s or 1Nm/s. The load or displacement ramp was generally applied for 20-25s, implying that the bone experiences only about 5° of rotation or 20Nm before the test was terminated.

Results reported by various authors suggest that the use of a system of cross-rail and hinges is necessary to ensure repeatability. Vaghese and co-workers (2011) who conducted torsional testing on their bones, but had a higher degree of constraints in their setup from the lack of a cross-rail system, showed a much larger standard deviation of values even within one specimen. In contrast, the highest coefficient of variation in Gray and co-worker's test (2008) was 1.7%, despite testing at similar strain rate. Therefore, all the bones that were tested to failure might not even be close to a state of pure torsion considering how the ends of the bones were rigidly affixed to the testing apparatus. Finally, more complex loading might arise during loading at high strain. The use of a mechanism to prevent the transfer of axial load is thus essential to study fracture mechanisms under pure torsion.

5.1.5.2 Fracture pattern

Spiral fractures have been consistently produced in all the works involving intact whole bones. Torsional loading of sheep femora produced spiral fractures in the mid-diaphysis consistently in the work of Wullschleger (2010). A combination of longitudinal and spiral fractures has been reported by D. Taylor et al. (2003), who tested mature chicken metatarsals to failure using torsional cyclic testing at 3Hz. It is therefore interesting to note that testing of immature porcine femur at a rate of 1°/s failed to generate a spiral fracture consistently (Pierce et al., 2000). Despite attempts made to reduce the working length of the specimens, growth plate separation continued to be the dominant failure mode. Spiral fractures have also been produced in the three-point bending work of Kress and co-workers (1995), who noted the correlation with the presence of a torsional load. With the exception of the setup used by the team from Bologna, all torsional testing of bone to failure were conducted with the bones experiencing only one degree of freedom, signifying that unintended axial loads may have played a part in the generation of spiral fracture. However, the failure to generate consistent spiral fractures in immature bone further compounds the problem by questioning when spiral fractures, which are seen so commonly among children (see Chapter 2), are produced.

5.1.6 Aims & objectives

The aims and objectives of this Chapter are thus summarized as follows:

i. to design an experimental setup that enables testing to be conducted in a state of pure torsion and bending;

ii. to determine the structural behaviour of immature bone to failure in four-point bending and torsion;

iii. to achieve a reproducible and natural fracture pattern;

iv. to investigate if spiral fractures are produced in pure torsion for immature bones;

v. to extend existing fracture work on four point bending to immature bones; and

vi. to conduct tests at different speed and strain rate, approximating the load commonly stated in case histories, to determine if there are differences in fracture patterns for immature bones in both bending and torsion.

5.2 Design of experimental setup

5.2.1 Hardware programming with LabVIEW

The Instron 8874 (Instron – Division of ITW Limited, High Wycombe, UK) is a dual-axis universal testing machine and it is the only available apparatus for conducting both bending and torsion tests. To characterise the structural behaviour of the lamb bones, strain measurements also need to be recorded. The following section describes the design and setup of the instrumentation system that was used to run the tests.

5.2.1.1 System requirement

The Instron 8800 controller that drives the Instron 8874 frame has one Integrated Axis Controller (IAC) Card that may act as the main data acquisition (DAQ) system for up to 2 strain transducers. This requires the principal directions of plain strain to be known in the specimen, which can only be achieved through the use of regularly-shaped samples. Since the principal directions are unknown, a minimum of one three-gauge rosette is required and thus a separate DAQ setup needs to be used.

The FE-MM8, a low-cost, 8-channel analogue amplification system (Fylde Electronic Laboratories Ltd, Preston, UK), was selected to acquire the data from strain gauges. The FE-MM8 is capable of recording data at up to 50kS/s per channel and has an analogue-to-digital resolution of 16 bits. As complete failure in bone has been reported to take place in 0.1-0.25ms (Juszczyk et al., 2011), Nyquist theorem stipulates a corresponding minimum sampling frequency of 2kHz to be used in the acquisition of data. The Instron controller is capable of logging a maximum of 32 bit data at 5kHz per IAC. Since each IAC has two outputs of force/torque and displacement/angle, there is a maximum resolution of 16 bits per channel and thus the two setups meet the minimum requirement and are suitably matched for the experiments conducted.

The use of two DAQ systems raises the need to synchronize measurement data from the Instron controller and the Fylde amplifier to ensure that they are in-time and in-step. The latter problem can be solved easily by ensuring that the sampling frequency of one setup is a multiple of the other. However, the problem of drift is inevitable in any independently-run setup without synchronization; starting the two systems concurrently and matching the data later would not work as each system has its own internal clock and thus the obtained samples will be out of phase. Moreover, previous experience with the Instron reveals a built-in time delay that is variable each time. As bone fracture is expected to take place in less than 1s, a solution to correlate the data in-time is required to prevent inaccuracies of later analysis.

5.2.1.2 Method of synchronization

All methods of synchronization involve the use of a common time base and a trigger between multiple devices. This may be achieved via the use of a hardware-based external timing source, or a software-based internal clock. However, the FE-MM8 was designed to be software controlled and thus it has no auxiliary input that can be used for the triggering of data acquisition. Therefore, synchronization can only be achieved by the use of software and LabVIEW (National Instruments, Austin, USA) was chosen for the system design.

The primary advantage of using LabVIEW is that its programs function as virtual instruments (VIs), allowing users to interact with the computer as if it were a custom-made electronic instrument. Furthermore, a special feature of LabVIEW is its nano-second engine, which is a time keeping mechanism that works by interfacing with the computer's system clock. The following section covers details in the specifics of the instrumentation design, which are referenced from Johnson and Jennings (2006) and Travis and Kring (2007), which also contains other general information about LabVIEW and graphical programming.

5.2.1.3 System behaviour

The data flow between the LabVIEW, the Instron controller and the Fylde amplifier can be seen in Figure 5.1 below. The main program acts as a virtual instrument that interfaces and synchronizes the running of the respective drivers. In turn, commands and responses are sent through dynamic-linked libraries (.dll) files, which directly control the devices. The Instron controller conforms to the HS488 IEEE standard and thus all communication takes place over

GPIB (General Purpose Interface Bus) (Instron and IST, Series 5800/8800 Test Control Systems Reference Manual - Programming). On the other hand, the Fylde amplifier is controlled using RAW USB commands. As LabVIEW drivers for the Instron controller were not available, Instron driver subVI had to be developed using GPIB commands, as highlighted by the boxes in the diagram. The main application VI also had to be developed to drive the entire setup.

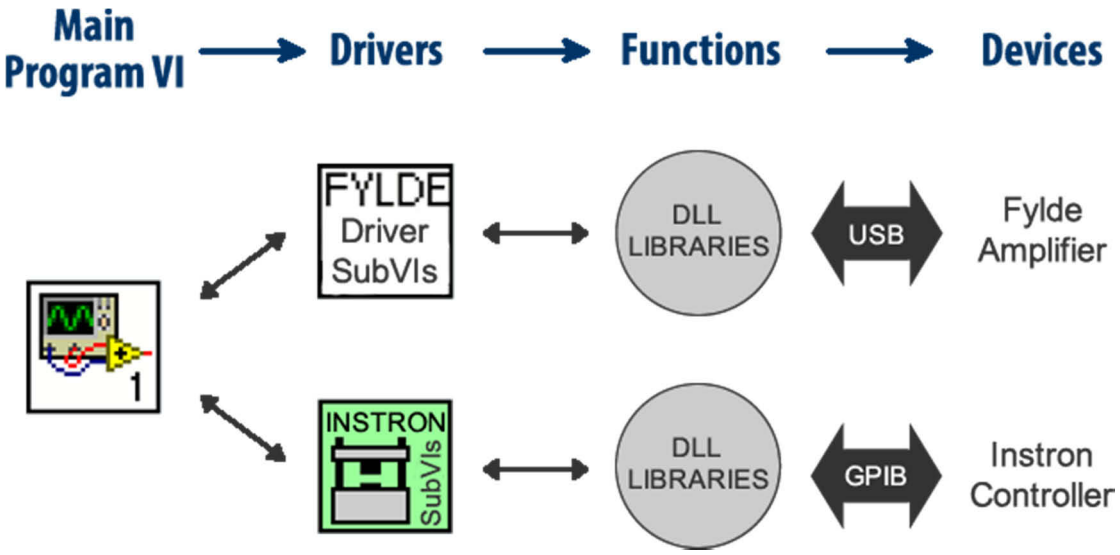

Figure 5.1: Data communication between LabVIEW drivers (shown in the boxes) and the devices

5.2.1.4 Timing source

As mentioned previously, the Instron controller has a variable time delay between the pressing of the 'start' button and the actual movement of the crosshead and data acquisition, making the manual synchronization of data with external devices very difficult. This is the drawback of the GPIB communication used and the fact that the controller needs time to process all the commands sent and set the Instron testing frame up. HS488 allows a maximum transfer speed of 8MB/s, compared to 12MB/s for the USB 1.1 interface used in the Fylde amplifier. However, GPIB wires are sensitive to noise which would affect the length of the delay. Furthermore, in GPIB communication, devices cannot talk and listen at the same time. Talking to a device when it is addressed to listen will cause errors to be produced. These characteristics of GPIB communication had to be factored in the designing of the synchronization mechanism.

The use of a serial poll can overcome the problem of delay and achieve synchronization. Serial poll is a function of GPIB and it is a hardware line exertion that does not involve the traditional

listener and talker functions but alerts the computer that it has something to say. A status byte message that is sent in binary format provides information of the devices that have requested for service. This result is dependent on the event bits that are programmed to be tied to the serial poll. Therefore, tying the bit function that the controller is not busy processing data to the serial poll enables the computer to check if the controller has finished processing all the commands to set the test up. This acts as a software-triggered timing source to set off data collection to the buffers in both the Instron and Fylde devices.

The algorithm in Figure 5.2 explains the main behaviour of the software and how synchronization was achieved. The common clock is provided internally by the computer that is supplied with the Instron controller, whereas the trigger for the start of data acquisition in both devices is provided by the status register of the Instron controller after conducting the serial poll. Upon receiving a signal that the data is ready for readout, through the use of another serial poll, as explained in the next section, LabVIEW retrieves the data and processes them before writing them to an output file. This method is advantageous over the traditional readout of the buffer after a fixed time period as it prioritizes the running of the test and data collection and reads out the data from a buffer only when the controller is ready.

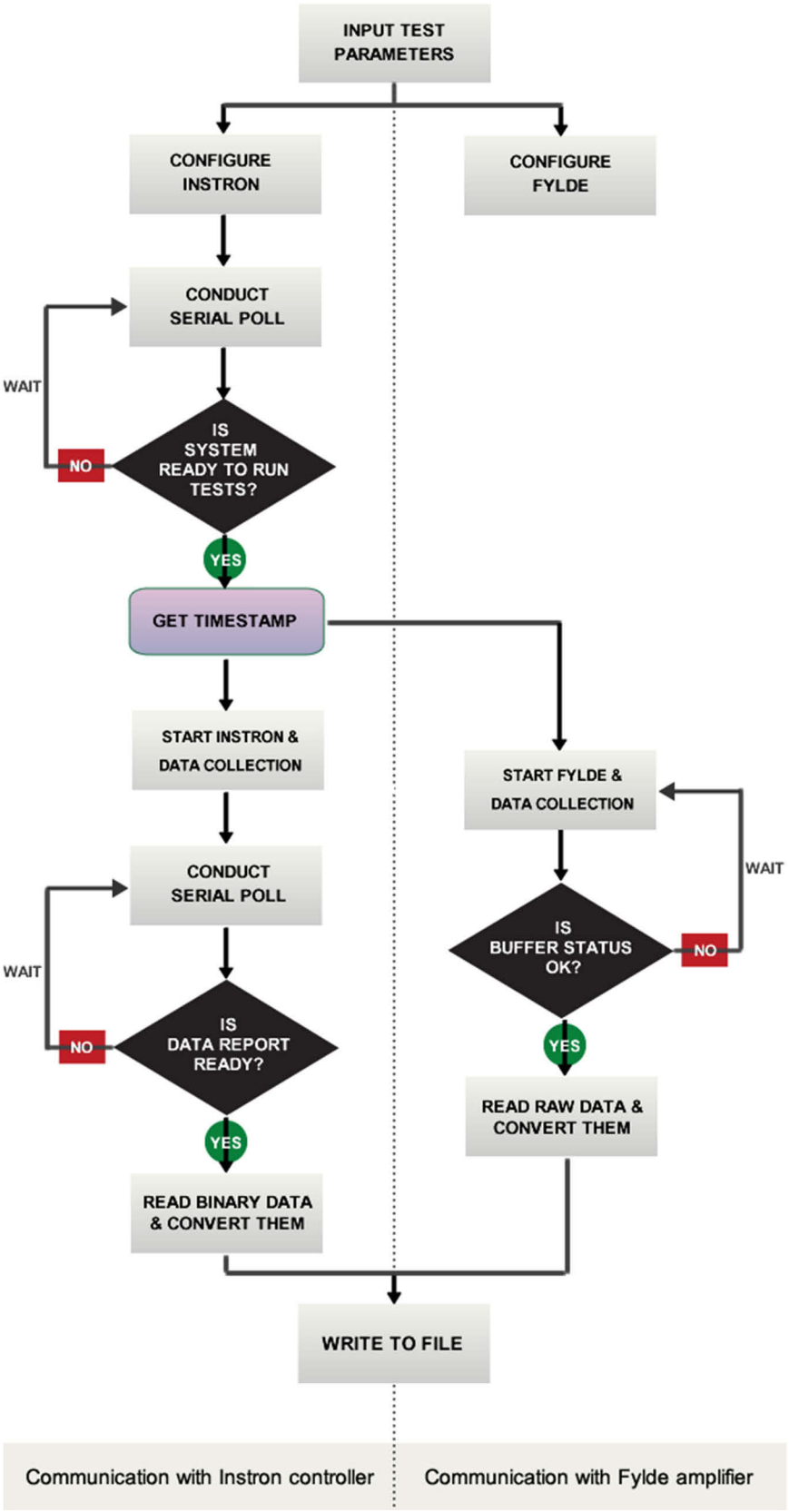

Figure 5.2: This algorithm shows the steps that were involved during the actual running of the tests. The actual testing only starts after the Instron has finished processing all the input parameters and sends a signal to start the Instron and the Fylde systems. Data readout occurs only when there is information in the buffer.

5.2.1.5 Data logging and readout

The Instron controller offers two different data logging modes depending on the sampling frequency selected. The normal rate ring buffer mode allows simultaneous collection and readout of the data but is limited to a maximum of 1ms between data points. The single burst rate buffer mode allows the time period of data acquisition to be as fast as 0.2ms. However, data can only be read out after the data logging has been stopped. This limits the duration of information that can be captured to a maximum of 4.096s. Therefore, all tests that are expected to take place over 2s are logged using the normal rate ring buffer and data is read out whenever the serial poll alerts the computer that information stored in the buffer is ready for transmission (Figure 5.2). The block diagram that explains how serial polling and buffer readout are achieved in LabVIEW for the Instron 8800 controller is shown in Figure 5.3.

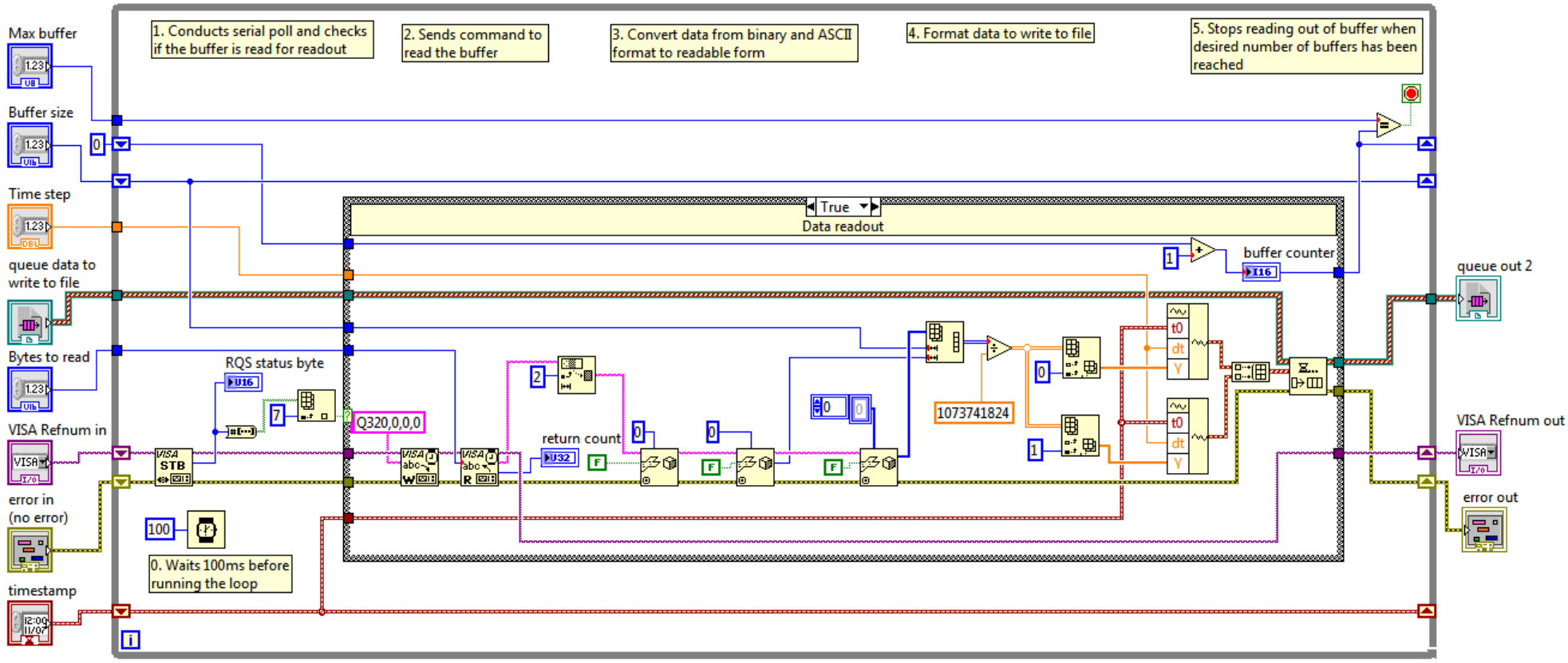

Figure 5.3: LabVIEW block diagram that shows how the buffer is read out from the Instron buffer during testing

5.2.2 Components and Fixtures

5.2.2.1 Junction box

A junction box was designed and built to allow quick and reliable attachment of strain gauges to the Fylde amplifier. Commercially available amplifiers usually use a screw terminal connector block, such as in National Instruments' NI 9225. Such a system might result in poor signal transmission were the wires from the strain gauges not placed properly in the socket or if the screws were not be tightened sufficiently. The custom-made junction box features a push terminal that uses a spring mechanism that ensures proper contact and eliminates the need of screwing and unscrewing each time to install and remove the wires. The setup saves time and minimizes the delay to the actual running of the test.

6-core shielded cables were used to minimize the effect of noise, as voltage signals from the strain gauges are relatively low.

5.2.2.2 4-point bending rig[1]

The 4-point bending rig has two features - a rocker mechanism for the internal rollers that are attached to the actuator, and external rollers that are adjustable in height (Figure 5.4). The results of the calculation from Chapter 4 showed that when bones are in their optimized alignment, their contact points are not level (see Figure 4.9). The inclusion of a hinge joint between the actuator and the rollers provides a rotational degree of freedom that ensures that the rollers maintain contact with the bone throughout the experiment. This prevents a break in the transmission of force from happening which was observed when a set of rigid internal rollers were used in earlier trial runs.

[1] The four-point bending rig was designed in collaboration with Angelo Karunaratne and built with the assistance of Satpal S Sangha and Paolo Lo Giudice

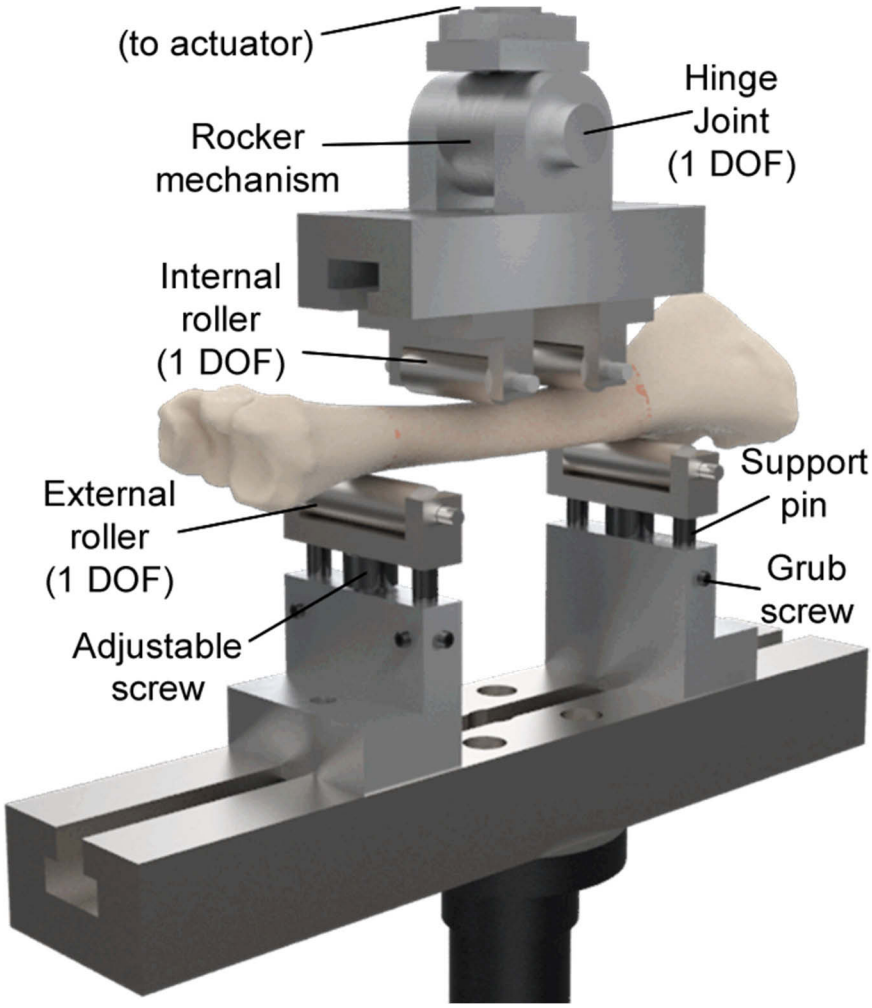

Figure 5.4: Experimental setup for four-point bending. A rocker mechanism that is attached to the actuator (not shown) ensures contact is always maintained with the bone. The external rollers are adjustable in height to allow alignment of the bones along its principal direction. DOF stands for degree of freedom.

The use of rollers that are adjustable in height has been presented before (Cristofolini & Viceconti, 2000). In their setups, grub screws were used to hold the rollers to the base. However, such a design does not allow for easy fine-tuning of the roller's height. To overcome this drawback, a new design was drawn up which features the use of a screw with a pitch of 0.5mm to allow easy adjustment of height. Since the bone will be tested to failure, large forces will be transmitted through the roller supports. Therefore, a further advantage of this design is that the screw provides a stable support that takes most of the load during testing, lowering the shear force that is transmitted to the grub screws and also prevents the bending of the adjustable support pins.

5.2.2.3 Torsional rig

The distal pot was attached to a rocker base, which has ball bearings attached to it to allow it to slide on an XY table (Figure 5.5). A pair of counterweights ensures the smooth vertical sliding of the distal pot. This setup prevents the specimen from being over-constrained during testing and eliminates unintended forces from transmitting to the bone, thereby allowing the bone to be in a state of pure torsion.

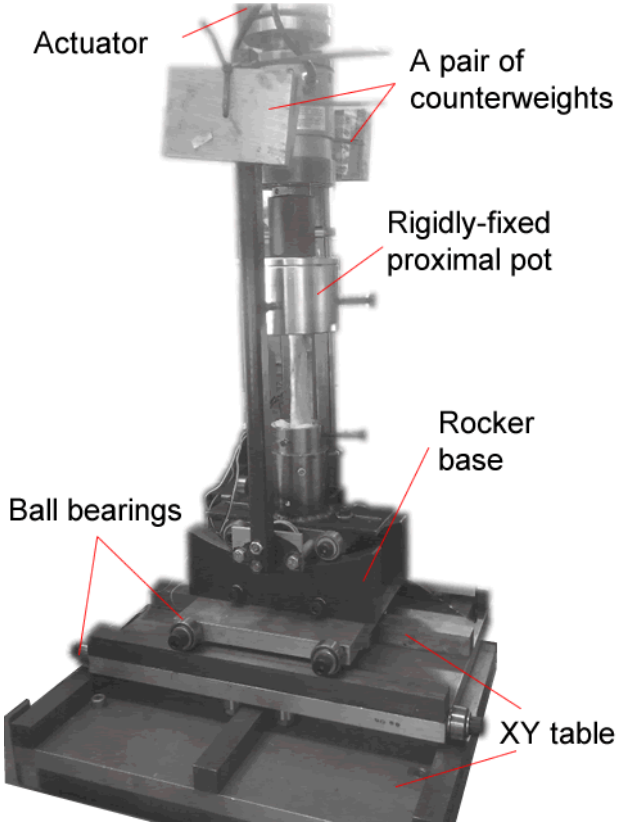

Figure 5.5: Overview of testing setup in torsional loading where the green light source to enable better capturing of the high-speed video has been switched on. The proximal pot is rigidly affixed to the actuator, while the distal pot is connected to a rocker, which can slide on the XY table. Mirrors were used to capture the full view around the bone.

5.2.3 Subject-specific alignment system

As seen in Chapter 4, the segment of bone that is most optimized for bending can be calculated from the 3D models of the bones. To find the point correspondences of the locations of the rollers, a least square fitting of two 3D points sets was carried out using the algorithm developed by Arun et al. (1987). Briefly, a covariance matrix assembled based on the centroid of the points

of the model and on the specimen can be decomposed using single value decomposition to find the rotation and translation matrices. The script was developed in Python and executed in the Rhinoceros 5.0 SR5 (Robert McNeel & Associates, Seattle, USA). Registration of the landmarks to the model was carried using a Polaris Optical Tracking System (Northern Digital Inc., Ontari, Canada). Three trials of preliminary testing using a 3D-protyped model revealed an at-worst resolution of 2.5mm. The steps that were taken to locate the point correspondence of the rollers are summarized below:

1. marking out of landmarks on bones based on the visual outputs in Rhino (Figure 5.6),
2. digitization of the landmarks,
3. running of script to check the accuracy of digitization,
4. running reverse script to locate the positions of the bones where the rollers should make contact, and
5. marking out the locations of rollers using a digitizer.

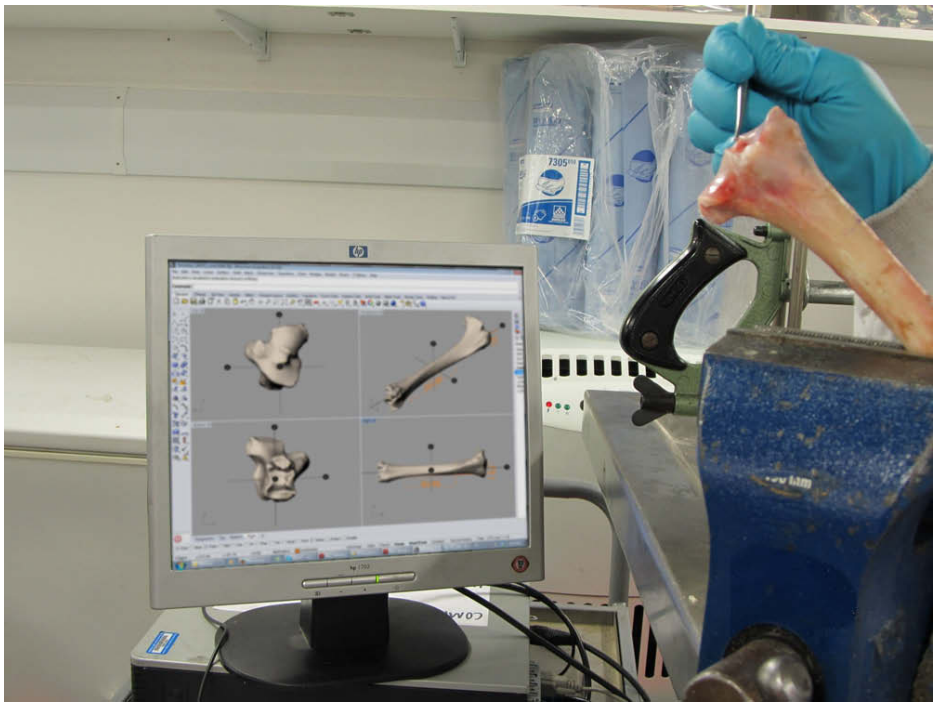

Figure 5.6: Digitization of landmarks conducted based on the results from Chapter 4.

5.3 Experimental procedures

Forty ovine tibiae from 5 months old British Texel lambs were used in this study. Four bone were used for each set of experiment, yielding a total of 16 bones that were used for torsional loading and 24 bones that were used for four-point bending tests. Torsional loading was done using only the right tibiae, so that extra-rotation was achieved in testing. Six of the tibiae (three each) were been previously scanned, and details on the image acquisition can be found in Chapter 4.

5.3.1 Torsional loading

For torsional loading, the bones were potted in stainless steel pots using Simplex Polymethyl Methacrylate (PMMA) bone cement (Simplex Rapid, Austenal Dental Products Ltd, UK). The bones were potted to a height as determined by the results obtained in Chapter 4. Approximately 60mm and 25mm of the proximal and distal tibia were embedded respectively. Three screws around the circumference of the pot ensured that the bone is centred along its first principal axis through the middle of the pot, as seen in Figure 5.7.

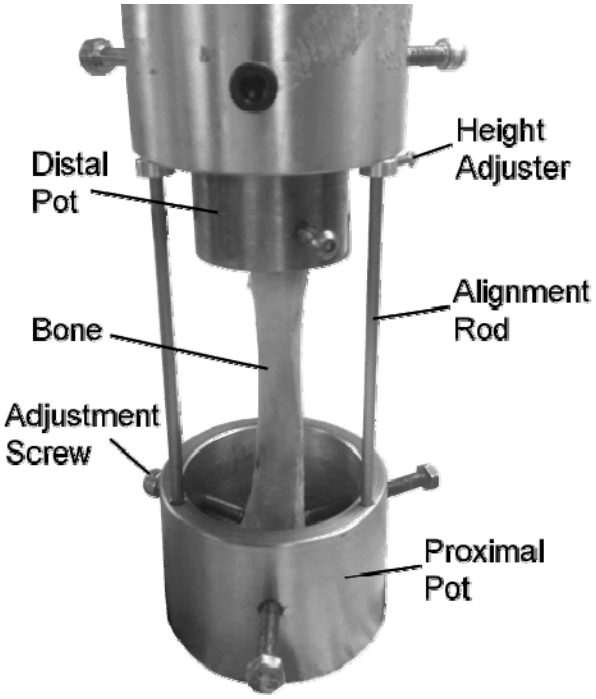

Figure 5.7: The device that was used to align the bone prior to fixing them in bone cement. The position of the bone is adjusted until the location where the principal axis intersects appears below the hole at the bottom of the pot.

Two rounds of preconditioning were carried out before the bone was tested to failure. An actuator speed of 5.6°/s was applied until a rotation of 5° was reached. Lowering the speed further gives a 'system is not in a static state error.' The bone was then unloaded at a rate of 0.05°/s. To relieve any residual stress, the distal pot was disconnected from the XY-table for a minimum of 5 minutes (Gray et al., 2008).

The tests were grouped into 2 different speeds. Testing at 'fast' speed was conducted by applying an angular control at a constant velocity of 196°/s until an angle of 39.2° was reached. The resulting failure took place in less than 0.2s. At 'slow' speed, the bone was loaded at a speed 10 times slower, resulting in a failure time of slightly less than 2s.

5.3.2 Four-point bending test

Four-point bending tests were conducted, as illustrated in Figure 5.8. A subject-specific span between the rollers was used, as per the results calculated using the methods calculated in Section 5.2.3. A distance of approximately 100mm separated the external rollers. The heights of the external rollers were adjusted using a 300mm double column digital height gauge (RS Components, Northants, UK). The bone was tested in the medial-lateral plane with the anterior side making contact with the internal rollers as the bone was found to rotate in the anterior-posterior plane. This models a scenario when a frontal force impacts the tibia. The effective functioning of a strain gauge requires a plane surface for it to be attached to, and thus filing is often conducted for this requirement to be met. Thus posterior aspect of the bone was suitable for the attachment of strain gauges as it is flatter, enabling less filing away of the bone to create a plane surface for the attachment of strain gauges.

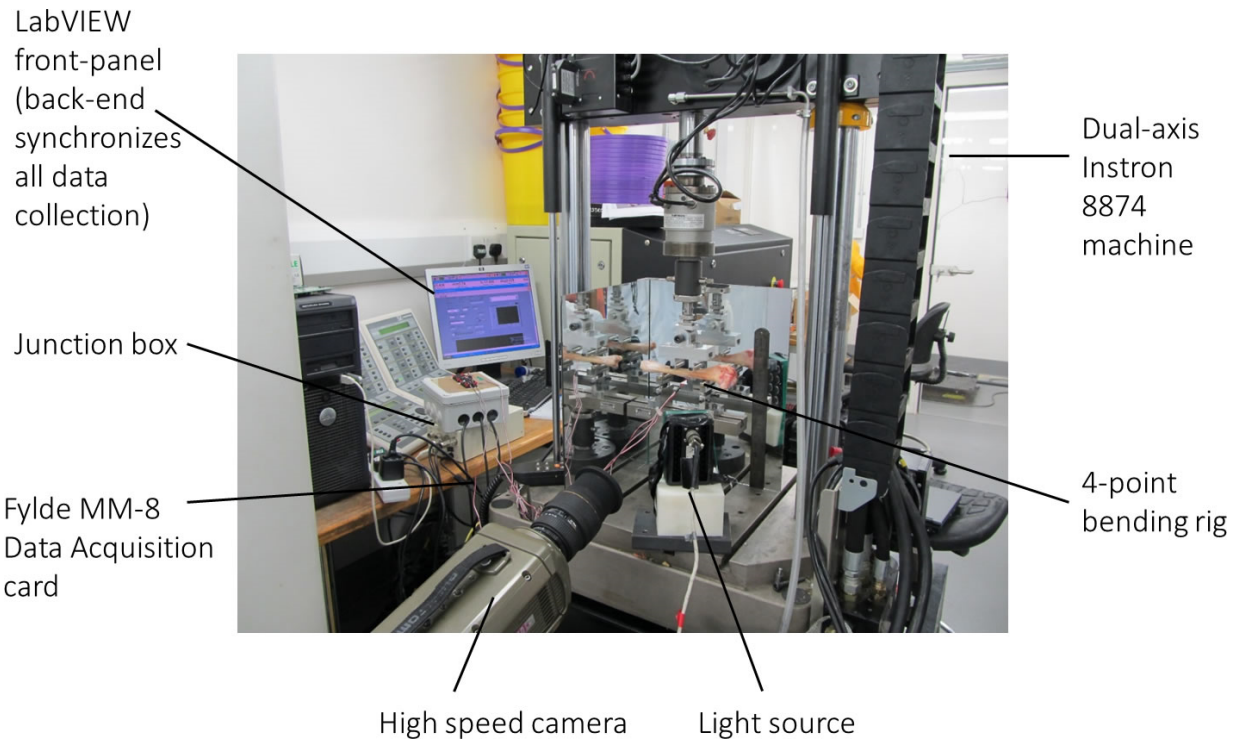

Figure 5.8: Experimental setup that was used to fracture the bone in four-point bending. The LabVIEW program, junction box and the bending rig were designed and created for this test.

Three different speeds were used in 4-point testing: fast, medium and slow at 50mm/s, 25mm/s and 1mm/s, which corresponded to strain rates of 0.1-0.4s^{-1}, 0.08-0.01s^{-1} and 0.003-0.004s^{-1}, respectively. For tests that were conducted at fast and medium speed, the loading was halted when a displacement of 4mm was reached whereas the amplitude was set to 5mm in the slowest tests. Therefore, the duration of the four-point bending test was 0.08s, 0.14s and 5s, respectively.

Similar to the procedures used in the torsion test, two rounds of preconditioning were carried out prior to testing it to failure. Each specimen was loaded at a constant velocity of 0.5mm/s using displacement control until the crosshead moved a distance of 1.5mm. The bone was unloaded at a speed of 0.01mm/s. Each run took place between intervals of 5 minutes.

5.3.3 Strain measurements

Each of the 3 strain gauges was connected through the junction box described in Section 5.2.2.1 to a quarter Wheatstone bridge circuit in the Fylde FE-MM8 8-channel amplifier. The gauges were connected with 3 wires to minimize the effect of wire resistance and thermal effects on

the voltage readings. A 5Vcurrent was applied across the bridge for sufficient resolution (-10 to 10V).

The method used for the attachment of strain gauges followed recommended procedures (Cordey & Gautier, 1999). The location of the intended position of the strain gauges was sanded down to remove the periosteum and to obtain a flat and smooth surface using two grades of sandpaper. Degreasing of the surface was done with isopropyl alcohol. The rosettes were then aligned and held with sellotape while M-Bond 200 was applied to the underside of the strain gauges. They were immediately bonded to the surface that has been coated with a thin layer of M-Bond 200 Catalyst. Supplementary coating was not used as the strain rosettes used were waterproofed in a layer of polyimide film. Instead, nail polish was used to coat the solder tabs that were not covered by the film to prevent short-circuiting of the strain gauges.

In consideration of the fact that bone offers poor thermal conductivity and has to undergo huge deformation in this experiment, 350Ω planar rectangular strain gauges of type C2A-06-125LR were chosen over stacked rosettes out of concern that heat generated in the strain gauges over a short loading period may interfere with other gauges' result were they to be stacked together. Furthermore, as stacked rosettes are stiffer, they are more likely to become detached in torsional testing. The drawback of using planar rosettes is that measured values do not approximate to strain measurements at a single point as well as stacked rosettes due to the large area of coverage. Nevertheless, this is a necessary trade-off for increased sensitivity of the rosettes to changes in strain. Smaller rosettes were initially used in some trial runs but they displayed a high degree of non-linearity.

The recorded voltages were processed using VBscript to obtain the corresponding strain measurements. All readings were first corrected for possible errors in transverse sensitivity (Vishay Measurements Group, Tech Note TN-509). Even though the Wheatstone bridge was balanced manually at the start of each run, they were not perfectly zero. Therefore, to correct for possible errors due to unbalanced bridge voltage and also for the effects of lead wire resistance (R_l), the following equation was used (Agilent Technologies, Application Note 290-1):

$$\varepsilon = \frac{4V_r}{GF(1+2V_r)} \cdot \left(1 + \frac{R_l}{R_g}\right)$$

where GF = gauge factor, $V_r = [(V_{out}/V_{in})_{strained} - [(V_{our}/V_{in})_{unstrained}]$, V_{in} = 5V and V_{out} = output readings after correcting for the amplification factor used.

Maximum principal strain, minimum principal strain and maximum shear strain were calculated using the following equations:

$$\varepsilon_{min,max} = \frac{1}{2}\left(\varepsilon_1 + \varepsilon_3 \pm \sqrt{(\varepsilon_1 - \varepsilon_3)^2 + 2(2\varepsilon_2 - \varepsilon_1 - \varepsilon_3)^2}\right)$$

$$\tau_{max} = \frac{\sqrt{2}}{2}\sqrt{(\varepsilon_1 - \varepsilon_2)^2 + (\varepsilon_2 - \varepsilon_3)^2}$$

5.3.4 High-speed videos

A high-speed camera (Phantom v126, Vision Research, Wayne, NJ, US) was used to capture the entire process of fracture propagation. A frame rate of 7000-10000 fps was used depending on the actual frame of view and lighting conditions. The synchronous acquisition of video frames was controlled by the Instron controller and the first appearance of crack initiation took place in less than 0.1ms.

5.3.5 Statistical analysis

To check for any issue of compliance of the four-point bending and torsion fixtures used, linear regression was calculated for the strain-force and strain-torque curves of each bone. The strain-force, force-displacement, strain-torque and torque-angle graphs obtained showed a high degree of linearity. Therefore, to detect the onset of plastic deformation, linear regression and the associated coefficient of determination (R^2) was also computed for 0-80%, 0-90%, 0-99% and 0-100% of each of the curves, using a method first detailed in Juszczyk et al. (2011).

The bending stiffness was subsequently calculated from the force-displacement curve for up to 90% of the fracture load as the R^2 showed a high linearity of 0.99 for each case with the exception of one (0.98). Data below 0.5kN were not used in the calculation as all the curves exhibited a toe-region at the initial region due to the internal rollers coming into full contact

with the bone. The energy to failure was calculated by integrating the area under the force-displacement curve for each bone, using the trapezoidal rule function in the statistical software. One-way analysis of variance across the three strain rates was conducted using the non-parametric Kruskal-Wallis test, due to the small number of specimens used for each test, followed by Mann-Whitney U test to elicit regions of significant difference. The bending stiffness was subsequently re-grouped according to the fracture patterns obtained to check for differences using the Mann-Whitney U test. The same procedure of analysis was also applied to the results of the torsional tests. All statistical analyses were conducted using OriginPro 9.0 (OriginLab Corp., Northampton, MA).

5.4 Results

5.4.1 Four-point bending test

Bone fracture took place in approximately 60ms, 100ms and 1200ms at fast, medium and slow four-point bending tests, corresponding to strain rates of 0.1-0.4s^{-1} and 0.08-0.1s^{-1} and 0.003-0.004s^{-1}, respectively. As seen in Figure 5.9 below, there are cases when the bone breaks suddenly without exhibiting much plastic deformation at all three strain rates. The figure also shows that bone fracture is characterised by an abrupt change in magnitude for both the strain and force readings in less than 0.2ms.

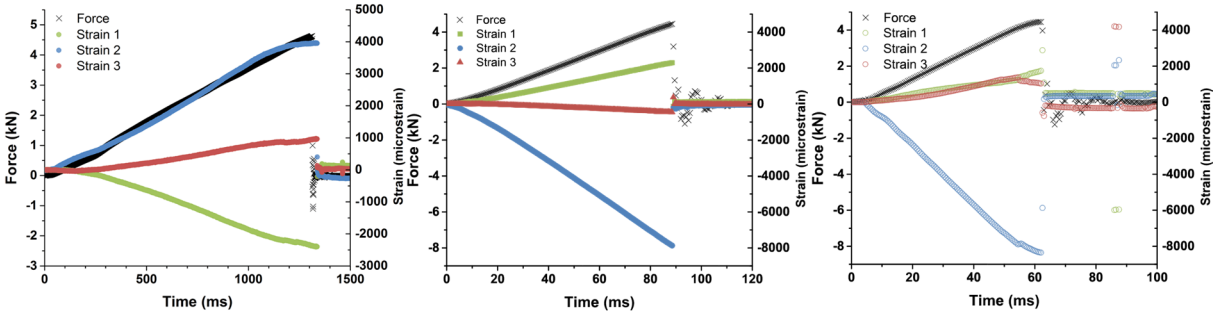

Figure 5.9: Example force-time curves for bone specimens from the slow, medium and fast groups respectively. The time difference between each data point is 0.2 ms, indicating that all fractures were characterised by a sudden drop in force.

Every measured force-displacement curve has almost the same curvilinear pattern, with a toe-region where the internal rollers of the four-point bending fixture comes into full contact with

the bone, followed by a highly linear region. The curves display varying amount of plastic deformation prior to failure (Figure 5.10) at each strain rate. To check for compliance issues that may have contributed to the initial toe-region, and also to check for the reliability of the strain gauges, strain-force curves were plotted for each specimen. The high linearity of the graphs in Figure 5.10 shows that the strain gauges were working well, and explains that the initial toe region is not caused by the viscoelastic response of bone. The non-linearity of some force-strain curves at higher force is caused by the strain gauges becoming detached from the bone during bone fracture, as revealed by the images from high-speed videos.

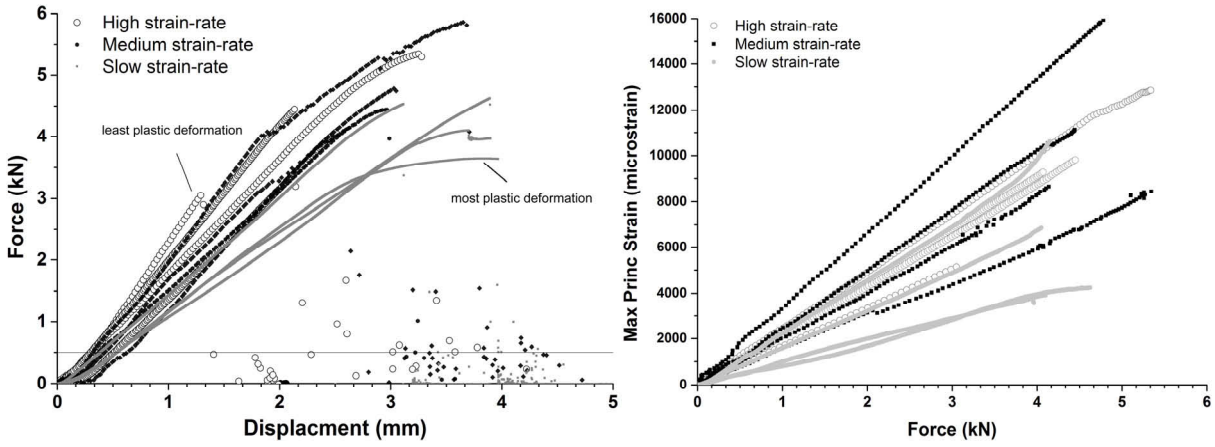

Figure 5.10: (Left) Force-displacement for all the tibiae. The part of the curve below the horizontal line was not included in the linear regression analysis. The two labelled curves showed the specimens that experienced the least and the greatest plastic deformation prior to failure. (Right) Force-strain curves for all the specimens. The curves showed good linearity at all strain rates.

The bending stiffness of all the bones is reported in Figure 5.11. On average, the tibiae experienced a bending stiffness of 1.94 ± 0.29, 2.12 ± 0.39 and 1.36 ± 0.15 kN/mm from the fast, medium and slow groups respectively. No significant difference can be found between the bending stiffness of bones from the fast and medium group, due possibly to the similarities in strain rate. However, bending stiffness of the tibiae in the fast group and medium group are both significantly greater than that from the slow group (Mann-Whitney U test, p = 0.014 for both).

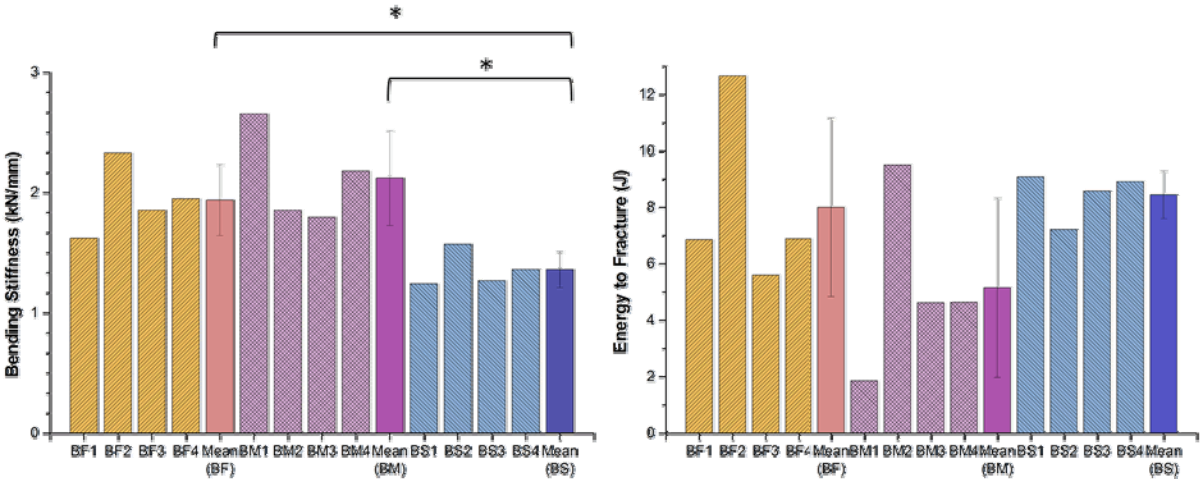

Figure 5.11: (Left) Bending stiffness for all the ovine tibiae. There was a significant difference between the bending stiffness of the bones tested at low strain rate and the ones from a higher strain rate. (Right) A huge variation in the energy absorbed to fracture can be seen at all the stain rates tested. BF, BM and BS stand for bones from the fast, medium and slow groups respectively.

The energy absorbed to failure shows a much larger range in the fast and medium group at 5.60-12.66J and 1.86-9.50J, respectively, compared to that from the slow group at 7.22-9.08J (Figure 5.11). Kruskal-Wallis ANOVA test conducted shows that this difference in energy absorbed is not significant.

The peak force for all the tests ranged from 3.05 to 5.86kN. Six out of the eighteen specimens tested experienced a slight drop in force at fracture point. The coefficients of determination calculated for increasing portions of the force-displacement curves shows that the curves are highly linear up to 99% of the fracture force, with a minimum R^2 value of 0.98 for all three groups (Figure 5.12). When the last 1% was included, the change in coefficient of determination was very subtle for the fast and medium groups, but the R^2 value dropped to 0.96 for the slow group.

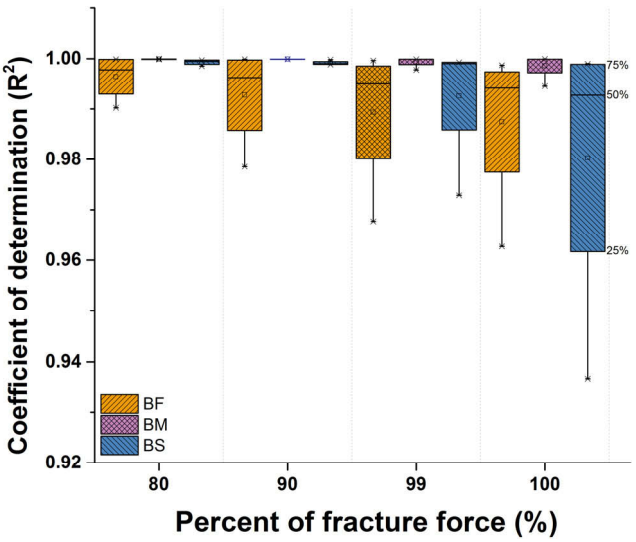

Figure 5.12: The linearity of the force-displacement curves are compared in this box-and-whisker diagram by calculating the coefficient of determination (R^2) for 0-80%, 0-90%, 0-99% and 0-100% of each curve. The plot shows that the force-displacement curves are highly linear up to the point of fracture.

The macro-scale fracture patterns of all the three groups are classified based on their initial crack initiation on the side of the bone under tension. Figure 5.13 below shows video frames from high-speed video recording showing how the crack propagates in transverse and oblique fracture patterns.

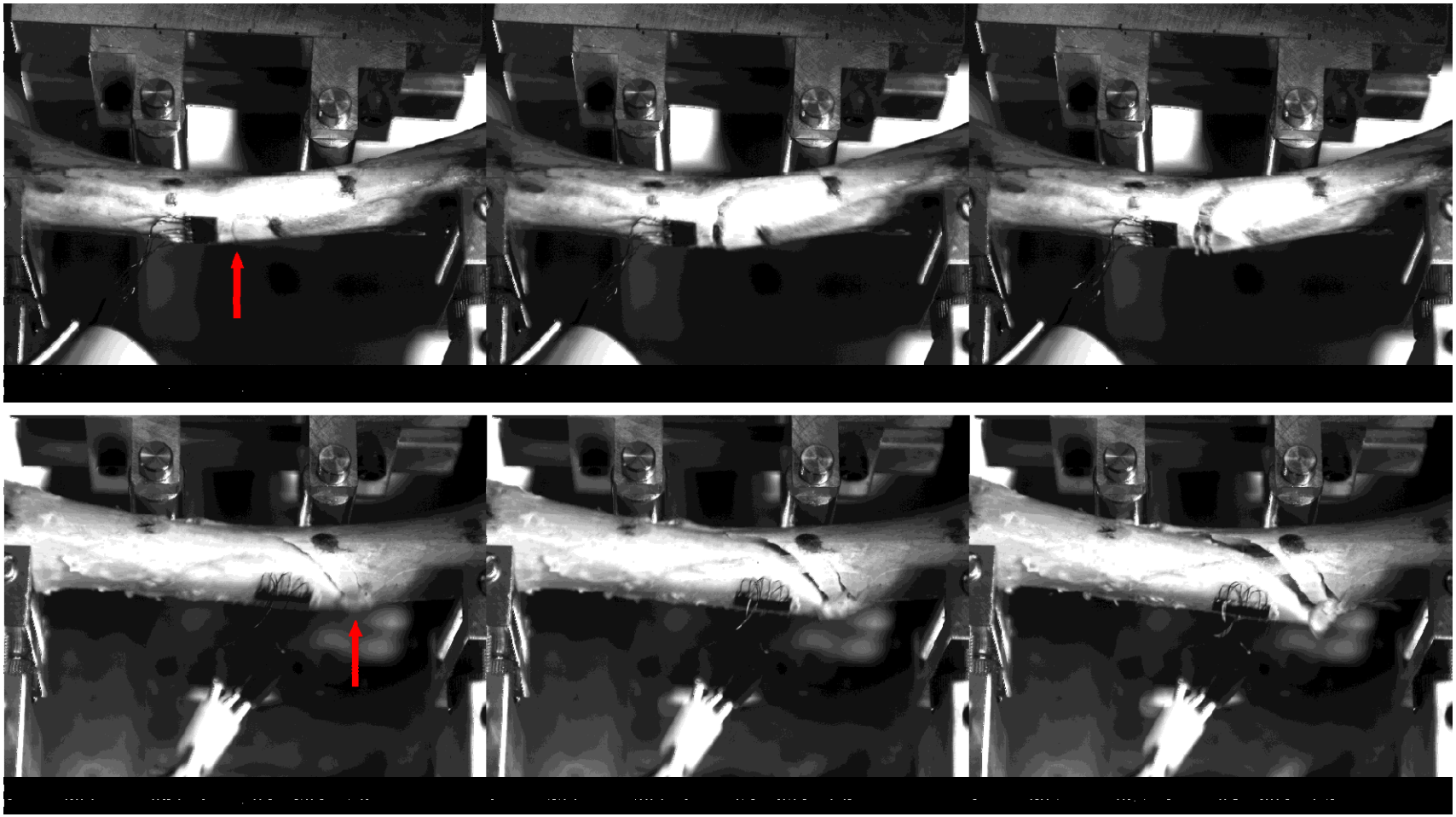

Figure 5.13: (Top) The fracture progression of a transverse fracture that took place over 0.286s in three video frames for a tibia tested at the low strain rate (BS1). (Bottom) The fracture progression of an oblique fracture is shown here over a total of 0.429ms tested at the medium strain rate (BM4). The red arrow points to the location of the crack initiation. The acquisition frame rate in both cases was 7000 fps.

In the slow group, all the bones broke within the region of constant bending moment, resulting in a transverse fracture pattern (Figure 5.13 - top). However, incomplete greenstick fractures were obtained for two cases and it was not possible to reassemble them without damaging the bone further. In both the medium and fast groups, there are two bones in each group that failed within the region of constant bending moment and two whose fractures initiated at the region between the internal and external supports, where shear stress is present highest. The resulting fracture pattern is thus oblique and in all four cases, the crack initiated on the proximal side of the bone (Figure 5.14). In one case where the initial fracture was transverse, an oblique fracture was later developed resulting in a butterfly wedge fracture (Figure 5.14). This case was accompanied by more plastic deformation than other bones.

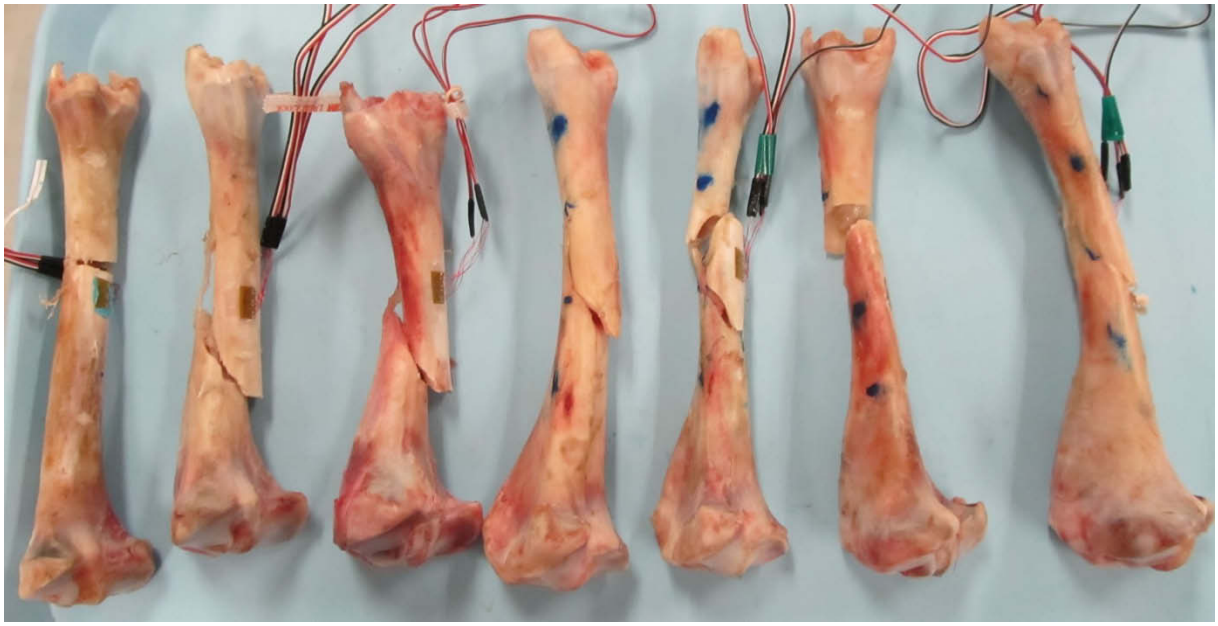

Figure 5.14: Fractured bones from the fast (first three) and the medium groups. The middle two dots in each bone marked the region of constant bending moment in four-point bending. All oblique fractures occurred proximally. A transverse fracture that later progressed into a butterfly fracture can be seen in the third bone from the right.

The results from the medium and fast groups were regrouped based on their fracture patterns and are summarised in Table 5.1. The bending stiffness of tibiae that have oblique fracture pattern is 24.9% higher than tibiae with transverse fracture patterns, which may be an effect of strain rate (Mann-Whitney U test, p = 0.014) but the peak and fracture force are not significantly different.

Table 5.1: Summary of the results of the four-point bending tests, grouped according to the fracture pattern and testing strain rate. Significant difference was found between the bending stiffness of ovine tibiae that fracture transversely and obliquely. BF= fast group, BM = medium group and BS slow group.

Specimen	Fracture Pattern	Location	Peak Force (kN)	Fracture Force (kN)	Bending Stiffness (kN/mm)
BF2	Oblique	Proximal	5.86	5.81	2.33
BF3	Oblique	Proximal	4.14	4.14	1.85
BM1	Oblique	Proximal	3.05	2.90	2.65
BM4	Oblique	Proximal	4.45	4.45	2.18
Mean	--	--	4.38	4.33	2.25
(SD)			(1.16)	(1.20)	(0.33)
BF1	Transverse	Middle	4.44	4.44	1.62
BF4	Transverse - multiple	Middle	4.78	4.74	1.95
BM2	Transverse- butterfly	Middle	5.34	5.29	1.85
BM3	Transverse	Middle	4.07	4.07	1.80
Mean	--	--	4.66	4.64	1.80
(SD)			(0.54)	(0.51)	(0.14)
BS1	Transverse	Middle	4.63	4.63	1.24
BS2	Transverse	Middle	4.54	4.54	1.57
BS3	Transverse	Middle	4.10	3.96	1.27
BS4	Transverse	Middle	3.64	3.64	1.36
Mean	--	--	4.23	4.19	1.36
(SD)			(0.45)	(0.47)	(0.15)

5.4.2 Torsional loading tests

Strain rates of 0.006-0.02s^{-1} and 0.07-0.2s^{-1} were achieved for the slow and fast group where fractures took place in approximately 2s and 0.2s, respectively (Figure 5.15). In all cases, the values from the strain gauges showed a good correlation to the torque values.

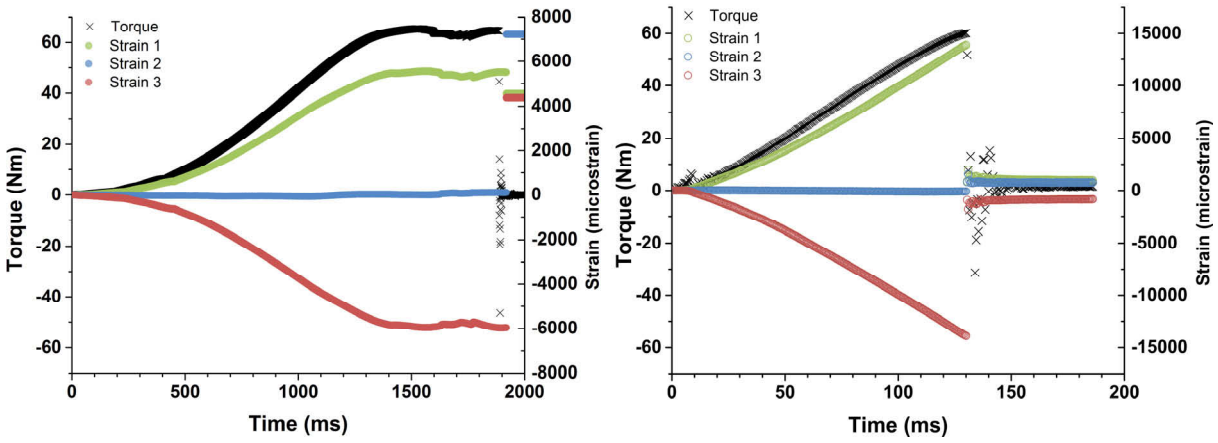

Figure 5.15: Example torque-time for bone specimens from the slow and fast groups respectively. All fractures took place in less than 0.1ms and were characterised by a sudden drop in force.

With the exception of one case from the slow group, bone fracture is characterised by a sudden drop in Instron-measured torque value (Figure 5.16). In that one specimen, the torque value fluctuated within 5Nm of the peak torque and experienced further crack propagation without any increase in torque prior to failure. Other cases from the slow group underwent plastic deformation, but to a smaller degree than this exceptional case. In contrast, the graphs show that tibiae from the fast group had little plastic deformation before fracture occurred. The coefficients of determination calculated for increasing portions of the torque-angle curves shows that the curves are highly linear up to 99% of the fracture force, with a minimum R^2 value of 0.98 for both groups (Figure 5.17). When the last 1% was included, the coefficient of determination remained relatively unchanged for the fast group, but dropped to 0.95 for the slow group.

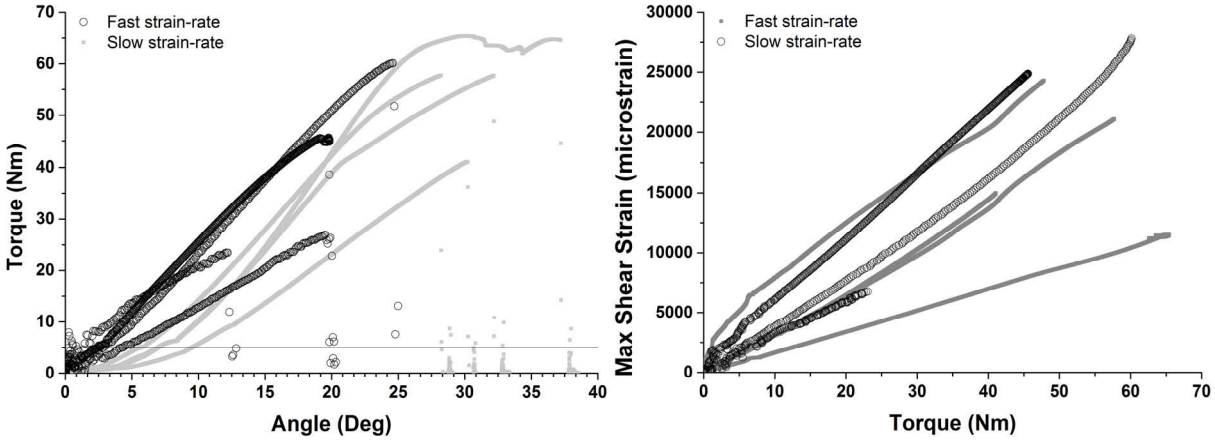

Figure 5.16: (Left) Torque-angle curves for all the tibiae. The part of the curve below the horizontal line was not included in the linear regression analysis. (Right) Strain-torque curves for all the specimens. The curves showed good linearity at all strain rates, and the maximum shear strain was calculated from the readings of the strain rosette.

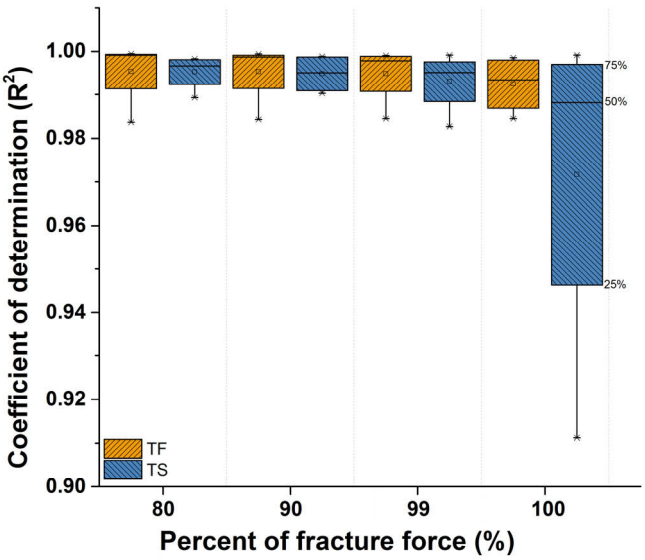

Figure 5.17: The linearity of the torque-angle curves are compared in this box-and-whisker diagram by calculating the coefficient of determination (R^2) for 0-80%, 0-90%, 0-99% and 0-100% of each curve. The plot shows that non-linearity only occurs in the last 1% of the fracture force.

Similar to the case in four-point bending, a toe-region is present in all the torque-angle curves (Figure 5.16). The corresponding strain-torque curves show good linearity which indicates the minimal contribution of eccentric loading. Therefore, the toe-region is the result of the gradual acceleration of the actuator before the target angular velocity is reached.

The torsional stiffness and work to fracture of the tibiae from the two groups are summarised in Figure 5.18 below. The mean torsional stiffness of the tibiae from the fast and slow groups

is 2.10 ± 0.66Nm/degree and 2.54± 0.65 Nm/degree, respectively. The corresponding work to fracture is 416.3 ± 251.0 J and 860.0 ± 347.0 J . Both the torsional stiffness and work to fracture of the two groups are not significantly different (p=0.470 and p=0.0606 respectively).

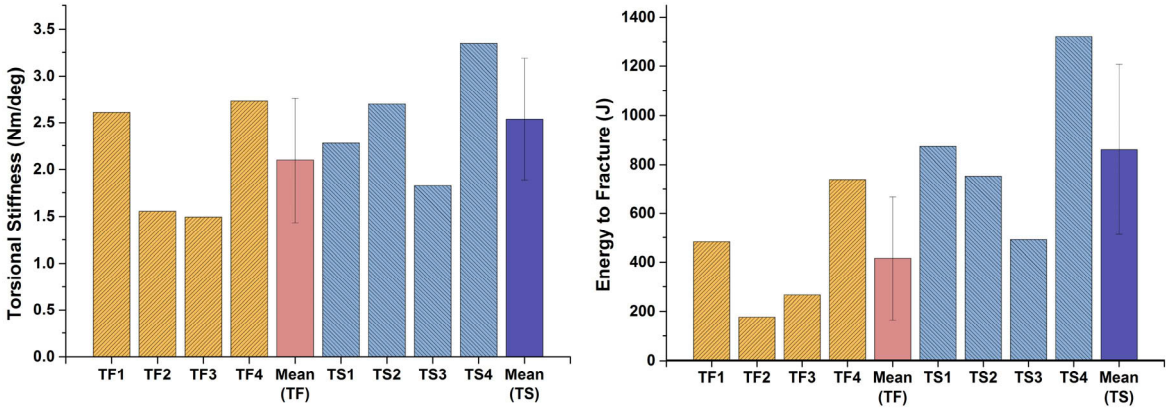

Figure 5.18: (Left) Torsional stiffness and (right) energy absorbed to fracture for all ovine tibiae. TF = bone from the fast group and TS = bone from the slow group

The peak torque and the fracture torque coincide in only 2 cases, one from each group. The peak torque falls within a range 23.5-65.4 Nm whereas the fracture torque (the last recorded value prior to a sudden drop in torque) lies between 23.4-64.6 Nm. Spiral fractures were produced in all cases and the bones remained intact even after fracture. Video frames from high-speed video recordings are presented in Figure 5.19 and document two different types of spiral fractures that were produced.

Figure 5.19: (Top) The fracture progression of a 'clean' spiral that took place over 0.572ms in three video frames (frame rate of 7000 fps) for a tibia tested at the low strain rate (TS4). (Bottom) The fracture progression of spiral fractures with several fracture paths (TF4) acquired at 10 000 fps.

In two cases, multiple tiny fragments were also present together with the spiral fractures. The recorded fracture torque is greater than 60Nm in both cases. Two bones from the slow group have a fracture torque of about 55Nm. A 'clean' spiral fracture can be seen in one case but a longitudinal fracture is also present in the remaining case (Figure 5.20). Only spiral fractures are seen in the remaining bones, as summarised in Table 5.2.

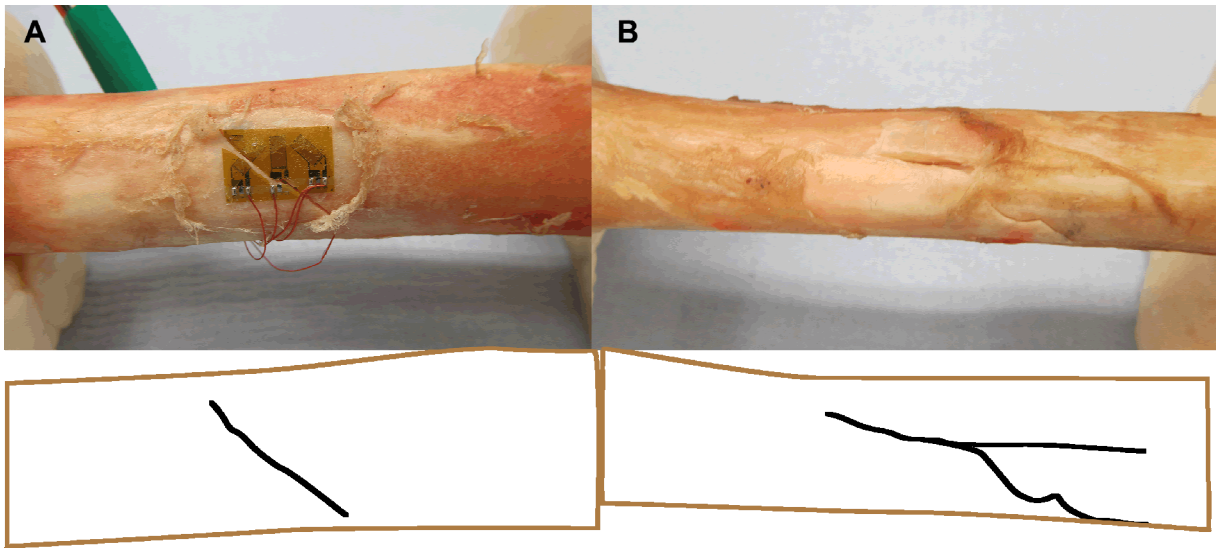

Figure 5.20: Posterior views of two different types of spiral fractures with the line tracings below the photos. (A) A 'clean' spiral fracture that broke through the strain gauge, produced at the higher strain rate (TF2). (B) Secondary longitudinal fracture was produced in this case after the initiation of the spiral fracture at the lower strain rate (TS2).

Table 5.2: Summary of the results of the torsional loading tests shows a spread of fracture torque but similar torsional stiffness. Spiral fractures were seen in all cases but secondary fractures were present in some specimens. TF= fast group, TS= slow group.

Specimen	Fracture Pattern	Location	Peak Torque (Nm)	Fracture Torque (Nm)	Torsional Stiffness (Nm/deg)
TF1	Spiral	Proximal	45.64	44.86	2.61
TF2	Spiral	Proximal	23.49	23.44	1.56
TF3	Spiral	Proximal	26.92	26.37	1.49
TF4	Spiral - multiple	Proximal	60.14	60.14	2.73
Mean	--	--	39.05	38.70	2.10
(SD)			(17.10)	(17.15)	(0.66)
TS1	Spiral	Middle	57.71	57.71	2.28
TS2	Spiral - longitudinal	Middle	57.76	57.69	2.70
TS3	Spiral	Middle	41.06	41.04	1.82
TS4	Spiral - multiple	Middle	65.42	64.60	3.35
Mean	--	--	55.48	55.26	2.54
(SD)			(10.28)	(10.02)	(0.65)

5.5 Discussion

This study developed and utilized a custom-designed experimental setup to conduct four-point bending and torsional loading tests on immature ovine tibiae using a subject-specific alignment system. No previous study has conducted four-point bending of immature bone to failure before and this work represents the first attempt to do so. Transverse fracture patterns were consistently produced at strain rates of 0.003-0.004s^{-1} while only half of the specimens exhibited transverse fractures at higher strain rates of 0.08-0.4s^{-1}. High-speed video recordings of the experiment documented the entire fracture process from crack initiation to failure and showed that all crack initiation took place in less than 0.1ms. Transverse fractures initiated in the region of constant bending moment whereas oblique fractures were found to initiate proximally, in between the internal and external rollers at the region of increasing shear stress. Linear

regression conducted on increasing portions of the force-displacement curve revealed that immature ovine tibiae behave linearly up to 99% of the fracture force. The bending stiffness of whole immature tibiae in the medium and fast group (strain rates of 0.08-0.4s^{-1}) was also characterised and classified based on the fracture patterns. It was found that bones that had oblique fracture patterns had significantly higher bending stiffness than bones that failed transversely even though the fracture force were similar. Oblique fractures were generated with a recorded strain rate of 0.09 to 0.2 s^{-1} whereas transverse fractures occurred between strain rates of 0.1 to 0.4 s^{-1}.

5.5.1 Torsion loading tests

For torsional loading, spiral fractures were consistently generated across strain rates of 0.006-0.2s^{-1}. No prior work had managed to generate spiral fractures so consistently in immature bones. However, tibiae that had a higher fracture force displayed the presence of secondary fracture patterns of longitudinal and multiple fractures. Tibiae loaded at strain rates of higher than 0.07s^{-1} behaved linearly up to failure, but tibiae from the slower group experienced higher plastic deformation prior to failure. This shows that the production of spiral fractures is invariant of strain rate, but secondary fractures may be a function of the fracture force.

The aims of this study were to test the hypothesis that reproducible and natural fracture patterns in pure bending and torsion at different strain rates can be produced by using a subject-specific alignment system based on its principal directions. The consistent production of spiral fractures across strain rates, and the generation of transverse fracture pattern in four-point bending at slow strain rate show that this hypothesis is true.

The creation of a reproducible fracture pattern has been the focus of many osteotomy studies (Wullschleger, 2010). However, all of these studies involved the creation of a partial osteotomy before an external torque or force is applied to initiate the fracture. The sheep is a popular laboratory animal for such studies and reproducible spiral and oblique fracture models in sheep tibiae have been published previously (Kregor et al., 1995; Tepic et al., 1997). However, the presence of a notch would affect the fracture pattern generated to a certain extent, and it is not representative of the case history of most injuries.

Pierce et al. (2000) have attempted to produce spiral fracture in immature porcine femora in-vitro without notching their specimens, but they obtained mainly fractures at the epiphyseal plates instead. They reported a fracture torque of 1.4-3.6Nm. Torsional tests to failure have been conducted on mature human tibiae, where a maximum torque of about 50Nm has been reported when tested at a rate of 1°/s (Varghese et al., 2011). In mature Merino Wethers sheep of 7-8 years old, femurs loaded in angular control at a constant velocity of 10°/min were found to have a maximum torque of 62.7-63.1Nm and a torsional stiffness of 0.51-0.65Nm/° (Wullschleger, 2010). The torque values of 55.26Nm from the slow group of this study are just slightly lower than the ultimate torque obtained for mature ovine femurs whereas the obtained mean torsional stiffness of 2.54Nm/° is much higher, even though all the above-mentioned setups did not have a mechanism to eliminate the transmission of unintended forces. However, the torsional stiffness found in this study agrees well with the values of 2.6Nm/deg in human tibiae loaded at 0.2°/s with a similar setup to that in this study (Cristofolini & Viceconti, 2000). In general, it is difficult to make biomechanical comparison with data collected on mature bones due to differences in microstructure. However, this study suggests that the structural behaviour of immature ovine tibiae loaded at a constant velocity of 19.6°/s is similar to that of mature human tibiae loaded at 0.2-1°/s. The much lower torsional stiffness of mature ovine femur when loaded at 10°/min suggests that ovine bones may have a strain rate dependency in torsion, even though the results from this study was insignificant. However, the consistent generation of spiral fractures shows that ovine tibiae fail primarily in its principal direction in torsion, regardless of strain rate.

5.5.2 Four-point bending tests

It is difficult to compare the results obtained in four-point bending to existing literature data as there is no four-point bending work of ovine bones to failure published in the open literature. Testing of ovine bones has only been conducted to failure in three-point bending but as mentioned earlier in Section 5.1.4, the loading mechanism in three-point bending is very different due to the presence of high shear stress throughout the span of the bone. This explains the much higher fracture force and bending stiffness obtained in this study compared to the three-point bending results of mature ovine tibiae where the fracture force and bending stiffness are 1.547 ±0.244 kN and 0.386 ± 0.066 kN/mm respectively (Rajaai et al., 2010). The values

obtained in this study are however very similar to the data presented by Ebacher et al. (2007) who fractured whole adult human tibiae at a speed of 6mm/min (0.3×10^{-3} s^{-1}) in four-point bending, and reported a maximum load of 4.25 kN and a strain of 1.2%. Similar to the case of torsional stiffness, the bending stiffness of lamb tibiae is very close to the result reported for adult human tibiae at 2 kN/mm even though the latter were loaded at a much lower speed of 0.05mm/s, suggesting the viscoelastic effect may cause immature bones that are loaded at high strain rates to behave like mature bone at low strain rate.

The force-displacement curves obtained in this study are highly linear up to 99% of the fracture load, which is characteristic of how adult human bones behave at physiological load (Juszczyk et al., 2011). The three point bending work by Currey and Butler (1975), conducted on regularly shaped specimens from the bone of a 2-year old, showed a load-deformation curve with a significant amount of plastic deformation. Nevertheless, because the response of bone is not strain-rate independent, the choice of a speed of 5mm/s here, which is ten times faster than the loading rate used by Currey and Butler (1975), may mean that the bones behave more as a brittle than a ductile material, as the results here show.

Transverse fracture patterns have been observed in both three-point and four-point bending tests at quasi-static strain rates (Ebacher et al., 2007; Pierce et al., 2000). However, a plethora of fracture patterns have been reported in dynamic three-point bending tests where the testing speed was greater than 1.5m/s (Forman et al., 2012; Kress et al., 1995). The work in this study bridged the gap by covering para-physiological strain rates (Juszczyk et al., 2011) at 0.08-0.4s^{-1} on top of quasi-static strain rate at 0.003-0.004s^{-1}. The consistent generation of a transverse fractures agrees well with the three-point bending results of immature pig femurs (Pierce et al., 2000). However, the four-point bending work of adult human tibiae (Ebacher et al., 2007) reported cases of oblique and comminuted butterfly fractures as well. These authors classified their transverse fractures as 'butterfly' fractures due to the presence of an oblique fracture path on the compressive side of the bone. Some of the transverse fractures obtained in this study would fall into this description, but a different fracture classification based on its fracture initiation was chosen because clinically, a 'butterfly' is a characterised by the presence of at least two oblique fracture lines (Green & Swiontkowski, 2009). Furthermore, the strain rates at

which their study was carried out was much lower than physiological bone fracture strain rates and therefore it is unlikely that their described fracture pattern would be seen commonly.

Nevertheless, it is interesting to note that oblique and fragmented wedge fractures were also produced in their studies, suggesting that their alignment method may have introduced shear components in their tests. Moreover, fragmented and comminuted fractures are view clinically as the result of a large impact on the bone and the results from Kress et al. (1995) support this clinical reasoning. The tibiae tested at para-physiological strain rates of 0.08-0.4s^{-1} exhibited only 3 out of the 9 fracture patterns detailed in Kress et al. (1995). Indeed, transverse fractures only occurred in 4 out of 50 specimens when impacted at a speed of 7.5m/s and 3 out of 11 specimens when tested at 1.2m/s. It is worthwhile to point out that only 3 fractures patterns of oblique, tension wedge and transverse fractures were observed in the latter experiment. Augmented with the results from this study, there is a clear shift from fracture pattern generated from transverse to oblique and tension wedge to more comminuted fractures as the impact velocity and strain rate increases.

5.5.3 Limitations

The tests conducted covered only a limited range of strain rates that were chosen based on loading speed as reported in case histories. Since whole bone testing of immature bones to failure at different strain rates has not been conducted before, this study could be improved if a larger range of strain rates were chosen. However, this was not done due to experimental limitations of the testing apparatus. The computer that commands the Instron controller is a Pentium 4 CPU 3.0Ghz with 504MB of RAM, running on Windows XP SP2. Due to the large amount of data acquired, and the computer being unable to cope, a GPIB error would result preventing the readout of the remaining data that have been acquired. Conducting the test at higher strain rate would also require much better synchronization method through the use of a real-time external timing source; this could be implemented in future studies.

Secondly, although the specimens used in this study are highly similar as they are of the same age and breed, the sample size used is relatively small. However, reproducible fracture patterns have been obtained in the tests and therefore it may only be necessary to increase the sample size only when testing is done at very high strain rates.

The strain readings were acquired through the use of strain rosettes in this set of experiments which reports the behaviour of the bone at a localised point. The use of digital imaging correlation (DIC) would yield much richer information by providing a strain map of the entire bone. This would also eliminate the possibility that the presence of the strain gauges may affect the location of the crack initiation.

5.6 Summary

Four point bending tests have been conducted on 5-months old lamb tibiae to failure at strain rates of 0.1-0.4s^{-1} and 0.08-0.1s^{-1} and 0.003-0.004s^{-1}, using a subject-specific alignment system developed in Chapter 4, to investigate their structural behaviour and to ascertain if a reproducible fracture pattern can be generated. Torsional testing was also conducted with the same aim but at two speeds that resulted in strain rates of 0.006-0.02s^{-1} and 0.07-0.2s^{-1}, respectively.

The results obtained showed that there is a significant increase in bending stiffness when going from the slower group to the two faster groups. However, the torsional stiffness was found to be strain invariant. The bones behaved linearly up to 99% of the fracture load or torque. Little plastic deformation was seen in both bending and torsion at strain rates of 0.07-0.4s^{-1}, as the R^2 value conducted on the linear regression of the slope of the force-displacement curve did not drop below 0.98. The bending stiffness was also found to be significantly higher for bones that exhibited an oblique fracture, compared to those with a transverse fracture line.

Four fracture morphologies have been produced in this study. Transverse fracture patterns only were produced at quasi-static strain rate loading in four-point bending. At para-physiological strain rates, the results are more mixed with half of them being oblique fracture and the other half transverse fractures. One of the bones with a transverse fracture pattern developed an oblique fracture line that caused the final fracture pattern to be a tension wedge (butterfly fracture). Finally, spiral fractures were generated consistently across all the torsion loading strain rates tested.

Therefore, the results from this study show that there is a differentiation of fracture patterns at different strain rates in four-point bending. This is crucial as it demonstrates the importance of

the link between the case history given of a child who has sustained an injury and the fracture pattern that is revealed in radiological images. The presence of oblique and comminuted fractures rules out all trivial case histories but may be accepted when transverse fractures are present.

The retrospective generation of bone fractures through a computational model is vital as an objective tool to identify false case histories. The model therefore needs to be able to generate different types of fracture patterns at different loading rate, especially in four-point bending. Therefore, based on the results obtained in this chapter, the focus of the next chapter is on the in-vitro replication of fractures in four-point bending and torsion.

6 THE IN-SILICO REPLICATION OF IN-VITRO BONE FRACTURES IN FOUR-POINT BENDING AND TORSION

6.1 Introduction

The simulation of the events leading up to the final catastrophic failure of bone is founded on the aims of understanding, predicting and preventing bone fractures. Finite Element (FE) analysis is a useful and practical technique for solving both simple and complex loading conditions in mechanical structures, thus making it the modelling technique of choice in bone fracture research (Keyak & Rossi, 2000; Ota et al., 1999). Furthermore, in situations where access to specimens may be limited or difficult, FE simulation becomes even more pertinent as it has an ability to simulate a range of loading conditions to determine the cause of clinically observed fracture patterns.

Most existing work in the literature has focussed on obtaining a strain or stress distribution pattern at maximum load to ascertain fracture risk (Cristofolini et al., 2007; Keyak & Rossi, 2000; Schileo et al., 2007; Spruijt et al., 2006). However, as noted by Ota and co-workers

(1999), the strain or stress map is not a representation of the final fracture path that will be generated, as this method sheds no information on crack initiation and arrest. Moreover, a method that truly predicts bone fracture should first be able to reproduce the fracture morphology that was obtained during experimental testing. This is thus a vital step in the development of an objective tool to identify false case histories in the detection of non-accidental injuries (Chapter 2).

6.1.1 Methods of simulating fracture patterns

Crack propagation in bone has been investigated primarily in the mature human femurs (Bessho et al., 2009; Hambli et al., 2011; Ota et al., 1999), which may be further categorized into the different types of loading conditions they attempt to simulate, namely single-leg stance phase loading, gait loading and loading during a fall. However, in all these cases, element deletion is used as a method to visualise the fracture profile, where the elements that have failed a predefined criteria are removed from the model.

An alternative approach comes from the field of fracture mechanics, which uses fracture toughness, flaw size, and cohesive zone in its determination of the fracture initiation and propagation. However, this type of fracture mechanics is only applicable in a planar material and it assumes that a single dominant crack with a predefined crack path will be developed. The geometrical structure of bone is fairly complex and furthermore the use of fracture mechanics would not be able to capture the multiple fracture patterns that occur in some instances, as seen in Chapter 5. Therefore, fracture mechanics as described above will not be considered further in this chapter.

6.1.2 Failure criteria

The effect of the choice of the failure criteria on the resulting fracture pattern has been the source of much research in the past (Edwards & Troy, 2012; Keyak & Rossi, 2000; Schileo et al., 2008), but none of these works simulated the propagation of the fracture path. The failure theories that were compared include von Mises, Coloumb-Mohr, Hoffman, maximum principal stress, maximum principal strain and shear strain. The von-Mises is an approach based on the deviatoric component of the stress tensor causing failure, assumes that the material in

question is able to absorb a significant amount of plastic energy, and has the same failure strength in both tension and compression. However, bone is able to experience more compression before failure than in tension and thus Coloumb-Mohr and Hoffman stress-based criteria were developed to overcome the limitations of the von-Mises theories.

6.1.2.1 Stress-based failure criteria

In terms of stress-based failure criteria, only maximum principal stress and the Drucker-Prager yield criterion have been used previously in the simulation of crack propagation. Principal stress criteria have been implemented by Ota et al. (1999) and Sakai et al. (2010) in modelling the fracture path generated in the stance phase loading of the femur and spiral humeral fracture in throwing respectively. In the former case, the stance phase loading achieved a correlation ($r = 0.81$) between their predicted and measured strain and the predicted fracture sites matched well with the CT images of the bones that were scanned after they had been tested in a similar experimental test. However, the results were only reported for one case. The spiral fracture patterns generated in the FE simulation of Sakai and co-workers (2010) correlated well with existing literature data on the location of spiral fractures. However, their study lacked an experimental validation, making it difficult to compare and ascertain the accuracy of their model.

The Drucker-Prager failure criterion is an approximation to the Mohr-Coloumb law, which accounts for degrees of asymmetry in compressive and tensile strength. This failure criterion also accounts for the presence of hydrostatic stress, by requiring a larger external load to be applied before the Drucker-Prager equivalent stress reaches its yield. This was thought to be a possible method to overcome the problem of using von-Mises and maximum principal stress criterion, implemented by Ota et al. (1999) and Keyak and Rossi (2000) respectively, which underestimated the value of experimentally-measured failure load (Bessho et al., 2007).

The results obtained by Bessho and colleagues (2007) in stance-phase loading obtained an R correlation of 0.979, and a confidence interval of 0.920-0.995 between predicted and measured fracture load. Although their regression curve was not significantly different from zero, a standard error in fracture load of 228N was reported, which suggests that their model is not predictive. The accuracy of the Drucker-Prager failure criterion in capturing the failure load in

stance-phase type of loading was verified by Derikx and co-workers (2011) who obtained a mean correlation of 0.925 between the experimentally-derived and FE-calculated load values. The stress distribution calculated in the Drucker-Prager FE model matched the experimental results more accurately than the von-Mises model. The authors did not go further to model the crack propagation in the two FE models.

Although stress-based criteria have performed relatively well in capturing the failure load and failure pattern, the experimental work of Nalla et al. (2003) showed that the failure of bone is strain-controlled. In their work, double notch four-point bending tests were conducted with the two notch located within the two inner spans. Their results showed that when one notch breaks, the failure process of the other notch is halted at the point immediately prior to fracture. Furthermore, their results indicated that fracture in bone initiated at the roof of the notch, instead of being ahead of the notch; the latter would be characteristic of a stress-controlled failure and thus a strain controlled failure mode is proposed.

6.1.2.2 Strain-based failure criteria

It is in light of this evidence that strain-based failure criteria seems like a more appropriate choice in modelling the failure of bone as these are able to capture the physical behaviour of the fracture process better. Moreover, children's bones have been observed to be able to undergo significantly more plastic deformation than mature bones (Currey and Butler (1975)); this is discussed in more detail in Chapter 3. Therefore, it would be advisable to implement a strain-based failure criterion in immature bone, since it would be able to capture the plastic behaviour of the bone better than a stress-based criteria.

The ability of a maximum principal strain criterion to predict failure risk and fracture site, compared against two criteria - the von Mises and maximum principal stress - was the subject of a study conducted by Schileo et al. (2008). FE models were built up from the CT-scans of three cadaveric human femurs before they were tested to failure in stance-phase loading as a validation for their simulation results. The von-Mises and principal stress failure criteria used were based on the two equations proposed by Keyak et al. (1994), which is a function of the ash density of the element. The use of these two criteria separately resulted in a larger area of bone failure at the experimental load, which is an order of magnitude higher than the results obtained

when the maximum principal strain criterion is implemented. Furthermore, the failure risk that was plotted showed the at-risk locations to be more similar to the experimental results. Therefore, their result confirmed that the use of the von-Mises failure criterion proposed by Keyak et al. (1994) tends to underestimate the failure risk. Moreover, the use of the principal strain criterion is able to capture the location of the fracture more accurately than the two stress-based criteria. However, as the propagation of the fracture was not conducted, its ability to model the failure path is unknown.

The use of different strain-based failure criteria have also been implemented through continuum damage mechanics to model crack initiation and propagation (Hambli et al., 2011; Hambli et al., 2013). In general, a quasi-brittle damage law is first implemented to measure the extent of the damage experienced by each element. This damage value is then used to modify the stiffness matrix of the element in question, as proposed by Lemaitre (1985). In the study by Hambli et al. (2011), a non-linear damage law that is a function of the failure strain of the element was used. In turn, the failure strain was calculated based on the bone mineral content of the element, in a similar fashion to the calculation of the maximum principal stress in the study by Schileo et al. (2008). In the 2D modelling of stance-phase loading, the fracture paths that were generated matched well against two fracture patterns as those that were observed in radiographs. Their work was later extended to 3D where they reproduced the experimental work of another group in sideway falls. In both studies, the predicted load-displacement curve exhibited plastic deformation prior to failure, which was not present in Keyak and Falkinstein (2003)'s model. However, the lack of validation against experimental data in their studies prevents further conclusions to be drawn on the accuracy of the model.

In all the studies, the failure criteria have only been tested against a specific loading condition, primarily in single-leg stance phase, or in sideway falls. One study simulated the generation of spiral fractures in torsion, but their work lacked an experimental validation. In addition, no previous work has been undertaken to model the fracture profile in four-point bending (Gray et al., 2008). Moreover, a useful predictive model should be able to capture the failure path in multiple loading conditions, and thus in this chapter, the fracture patterns that are generated in four-point bending and torsion will be compared against the experimental results that were presented in Chapter 5.

The load-displacement and torque-angle curves that were obtained when the bones were loaded in four-point bending and torsional loading, showed that the bones behaved linearly up to the point of failure at para-physiological strain rates (see Section 5.4). The shape of the curves displayed negligible plastic deformation prior to fracture and failure was mainly characterised by a sudden drop in load. This is similar to the results presented in Schileo et al. (2008), who used a principal strain criterion, and their experimental validation was conducted at a similar speed to the rate used in four-point bending and torsion, albeit their modelling was conducted for stance-phase loading and the actual fracture propagation was not modelled. This suggests that the use of the continuum damage mechanics might introduce too much plastic deformation into the FE model, which would not reflect the physiological behaviour of the bone at failure in four-point bending and torsion. Moreover, no work has tested their model at more than one strain rate but the results from Chapter 5 showed that bones that have been loaded at a lower strain rate undergo slightly more plastic deformation prior to fracture. Therefore, the use of a maximum principal strain criterion is expected to be able to capture the viscoelastic response of bone better than stress-based failure criteria. The performance of the 5 failure criteria reviewed are thus summarised in Table 6.1.

Table 6.1: The performance of 5 failure criteria that have been used to model bone failure and propagation. σ_1, σ_2, and σ_3 are principal stresses for an element in increasing order of magnitude. σ_y are σ_c are the tensile and compressive stresses respectively. σ_{yt} are σ_{ct} are the failure stress in yield and compression respectively. In the above statements, σ may substituted for ε to give the strain correspondent. ε_{eq} is the equivalent strain measure, ε_f is the failure strain, and D is the damage

Failure Criteria	Equations	Loading Conditions	Prediction/ Validity
von Mises	$([(\sigma_1-\sigma_2)^2 + (\sigma_2-\sigma_3)^2 + \ldots (\sigma_3-\sigma_1)^2] /6)^{0.5}/k>1$	Stance-phase loading	Failure risk and failure location
Maximum principal stress	$(\sigma_t/\sigma_{yt})>1$ or $(\sigma_c/\sigma_{yc})>1$	Stance-phase loading, torsion	Failure risk, failure location Fracture pattern and crack propagation (not validated)
Drucker-Prager	$\alpha I_1+\sqrt{J_2}-k=0$ $I_1 = \sigma_x- \sigma_y- \sigma_z$ J_2 is the second deviatoric stress invariant α is the degree of asymmetry in tensile and compressive strength	Stance-phase loading	Failure location, fracture pattern and crack propagation (validated)
Maximum principal strain	$(\varepsilon_t/\varepsilon_{yt})>1$ or $(\varepsilon_c/\varepsilon_{yc})>1$	Stance-phase loading	Failure risk and failure location (performed better than maximum principal strain and von Mises)
Continuum damage mechanics	$D = 0; \varepsilon_{eq}\leq\varepsilon_0$ $D=(\varepsilon_{eq}/\varepsilon_f)^n; \varepsilon_0\leq\varepsilon_{eq}\leq\varepsilon_f$ $D=1; \varepsilon_{eq}\geq\varepsilon_f$	Stance-phase loading	Fracture pattern and crack propagation (not validated)

6.1.3 Aims & Objectives

The aims and objectives of this chapter are to:

i. develop FE models of the ovine tibiae from Chapter 4 using the data from the μCT scans,

ii. model in FE the physical loading conditions of the bone in four-point bending and torsion,

iii. semi-automate the generation of the full FE models to make it easily extensible to the analysis of other long bones,

iv. verify the accuracy of the model by comparing the failure strain, peak load and the load-displacement or torque-angle graphs,

v. verify if the use of maximum principal strain is able to capture the fracture locations that were observed in four-point bending and torsion, and

vi. ascertain if the model is able to replicate the predicted crack path against the results obtained in experimental testing at different strain rates.

6.2 Model Generation

Before finite element (FE) analysis may be carried out, three different aspects of the models need to be built first. The first is the discretization of the spatial model into elements and nodes, so that a problem that is accompanied by a complex geometry may be broken down into elements with a known shape. The nodes then refer to special points that are at, along or in the elements, and are used to define the shape of the element. Secondly, the equations governing the system need to be established in the FE software. In this step, the boundary conditions and the external forces are identified and applied to the structural model. Thirdly, material properties need to be assigned for the model. The material properties of a material describe the behaviour of the object when it is subjected to external forces. The material property may be derived from material characterisation, or through imaging techniques. In commercially available FE software, the above-stated three steps do not need to occur in any sequential order; the FE software will generate the governing equations that need to be solved for each element based on user input. In this thesis, Marc 2013.1 (MSC Software Corporation, Santa Ana, USA) was used as the FE solver. The graphic user interface that ships with Marc, named Mentat, was used in the visualization and building up of the FE model.

6.2.1 Geometry Generation

As described in Chapter 4, a subject-specific alignment system of each bone that is most optimised for bending and torsion can be established, and used to orientate the specimen in experiments as conducted in Chapter 5. To accurately capture the positions of the rollers, other load applications and strain gauge locations, the surface meshes generated using the alignment

algorithm in Chapter 4, and the locations of points marked out in Rhinoceros, were exported separately in STL (STereoLithography) and IGES (Initial Graphics Exchange Specification) formats respectively to be imported into a software package to generate FE meshes.

Users are typically presented with a choice of quad or tri surface elements for surface meshing, which would subsequently allow for either hexahedral (Hex) or tetrahedral (Tet) volumetric mesh to be created. Hex meshes are usually favoured in explicit FE solvers, where the equations are solved directly using the Forward Euler method (Harewood & McHugh, 2007). Implicit FE solves the problem iteratively or directly using the Newton-Raphson method to ensure that the desired convergence level has been reached. A second advantage of hex mesh that arises from its solving method is that less computational time is required in solving the equation. However, its biggest drawback is the lack of algorithm to conduct meshing automatically. The geometry of bone is highly complex, and in the case of the ovine tibia, huge changes in the curvature of the bone can be seen in the distal end of the bone. Therefore, the successful creation of a hex mesh requires the subdivision of the bone into smaller sections and meshing them manually before combining them together. Such a method would be too time-consuming and cost-prohibitive to be implemented large scale in a clinical setting. Therefore, the automatic TetMesh in Patran 2013.0 (MSC Software Corporation, Santa Ana, USA) was chosen as it allows good quality meshes to be built while conforming to the geometrical structure of ovine bones. Moreover, it offers flexibility in the automatic generation of volumetric mesh through the use of user-subroutines, and the ability to control the locations of selected nodes of interest.

A custom-written Patran Command Language (PCL) script was used to generate FE meshes with Tet elements semi-automatically from the outputs after the optimised alignment has been found. The procedures in the script include the following:

1. set mesh size and type,
2. import IGES points of landmarks and create nodes at these points,
3. import outer cortical mesh,
4. create a new cortical mesh by forcing the use of hard nodes that have been created in step 2,
5. import trabecular mesh and remesh using the mesh size,

6. conduct volumetric mesh using the two surface meshes,
7. group the hard nodes and create node sets, namely the proximal external roller, the distal external rollers, and the two internal rollers, and
8. export the mesh and the points (Figure 6.1).

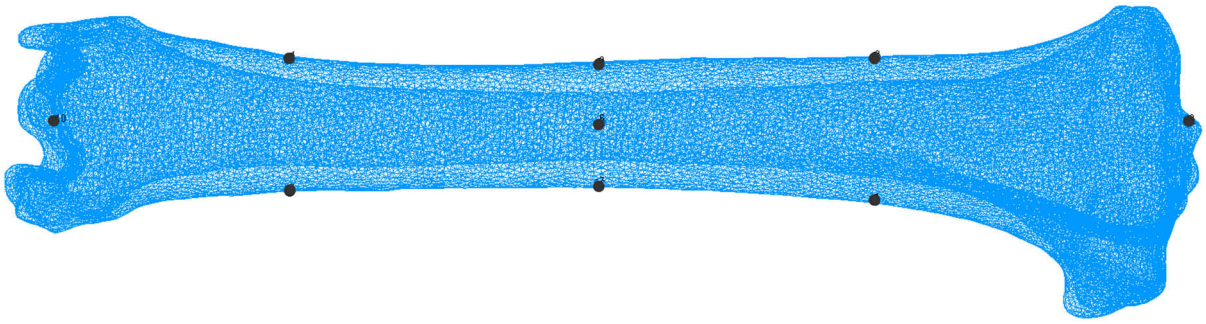

Figure 6.1: An example of an output mesh that is exported from Patran, a pre-processing software used for setting up the model for finite element analysis. The bones were meshed using Tet 4 elements using the black points as hard nodes which controlled where some nodes would be placed. The black points were landmarks that were calculated from the alignment method in Chapter 4. These elements and nodes were then grouped and exported in one file.

6.2.1.1 Convergence Testing

For an object that has a complex structure, the use of smaller-sized elements would lead to a higher quality mesh that represents the shape of the object better. Through the minimization of artefacts that may result in stress concentration, more accurate solutions should result, but this is done at the expense of higher computation cost. Moreover, the marginal increase in accuracy of results decreases with every mesh refinement and a point will be reached when a mesh is sufficiently fine enough to represent the geometry of the structure. This process of evaluating the appropriate mesh size to use is called convergence testing and it is usually done independent of the material allocation of the elements.

The smallest ovine tibia was selected to be used in the convergence study as it has sharpest curvature in its geometry. Nine finite element models of this ovine tibia in its optimised alignment were generated with different sizes, ranging from 0.8 to 4.2mm. The models were assigned transversely isotropic material properties of 7188MPa and 10782MPs in the transverse and longitudinal directions respectively, which were obtained from the material properties of sheep reported in the literature (Nafei et al., 2000; Simon et al., 2003; Spatz et al., 1996). The

shear modulus was set at 550 and 367 MPa in the transverse and longitudinal directions respectively. The poisson's ratio was set at 0.36 (Simon et al., 2003) and a three-point bending load was applied using displacement control at a rate of 0.2mm/s for 20s. All the models were meshed using linear Tet4 elements using the PCL scripts described above, because global remeshing (Section 6.2.1.2) is currently not supported for higher order quadratic elements. The details of the FE mesh generated for the convergence studies are found in Figure 6.1 below:

Table 6.2: Details of the models that were used in the convergence study

Element size (mm)	No. of elements	No. of nodes
4.2	8626	2716
2.9	23276	6529
2.0	30990	8408
1.8	40719	10696
1.6	51330	13320
1.5	88254	21864
1.3	106226	25843
1.1	132044	31467
0.8	231975	52668

The maximum principal stress was found to have converged at an element size of 1.5, as seen from the results in Figure 6.2. However, because the aim of this work is to simulate the fracture patterns observed in experiments, the use of smaller-sized elements would allow the fracture path to be captured more realistically. However, when an element size of 0.8 was selected in the initial mesh, Python would throw an out-of-memory error that prevents the materials mapping file to be created. Therefore, an element size of 1.0 was used in the initial meshing to retain the geometry of the bone as accurately as possible, before global remeshing takes place. When the mesher is unable to create meshes at this element size, the mesh size was then increased to 1.1 mm.

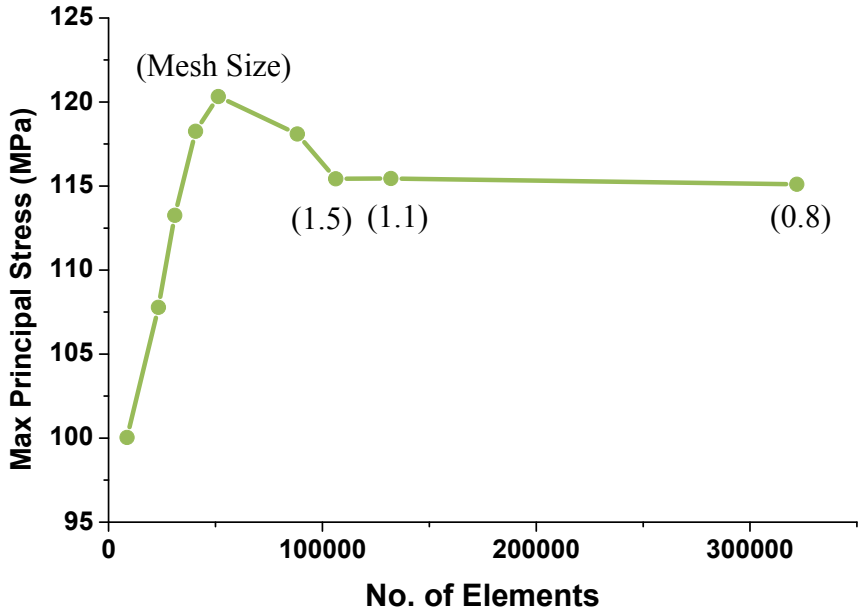

Figure 6.2: Mesh convergence studies conducted on the smallest bone in bending showed that the solution converged when the element size was decreased to 1.5.

6.2.1.2 Global Remeshing

To overcome the problem that Python is unable to create a material mapping file when there are too many elements, even though a finer mesh offers a better simulation of the fracture path that is produced, global remeshing was carried out immediately at the first increment to increase the density of the mesh at the area of interest. Moreover, in the case of four-point bending, the sections of the bone outside the external supports do not contribute significantly to the stress and strain experienced between the two inner rollers (Ebacher et al., 2007). In the case of the torsional loading, the proximal and distal ends of the bones are embedded in dental cement, and it is the middle of the bone where the greatest stress and strain would be experienced. Therefore, to reduce the element size count and to allow for the materials file to be generated, coarsening of the element size to 1.5 mm was carried out for the non-critical region as seen in Figure 6.3, which contrasts the internal mesh distribution along the bone. The element size of 1.5 mm was selected based on the result of the convergence testing conducted in the previous section. The hard nodes, which are locations where the boundary conditions are applied, were retained during the global remeshing process, ensuring that they do not change during the analysis.

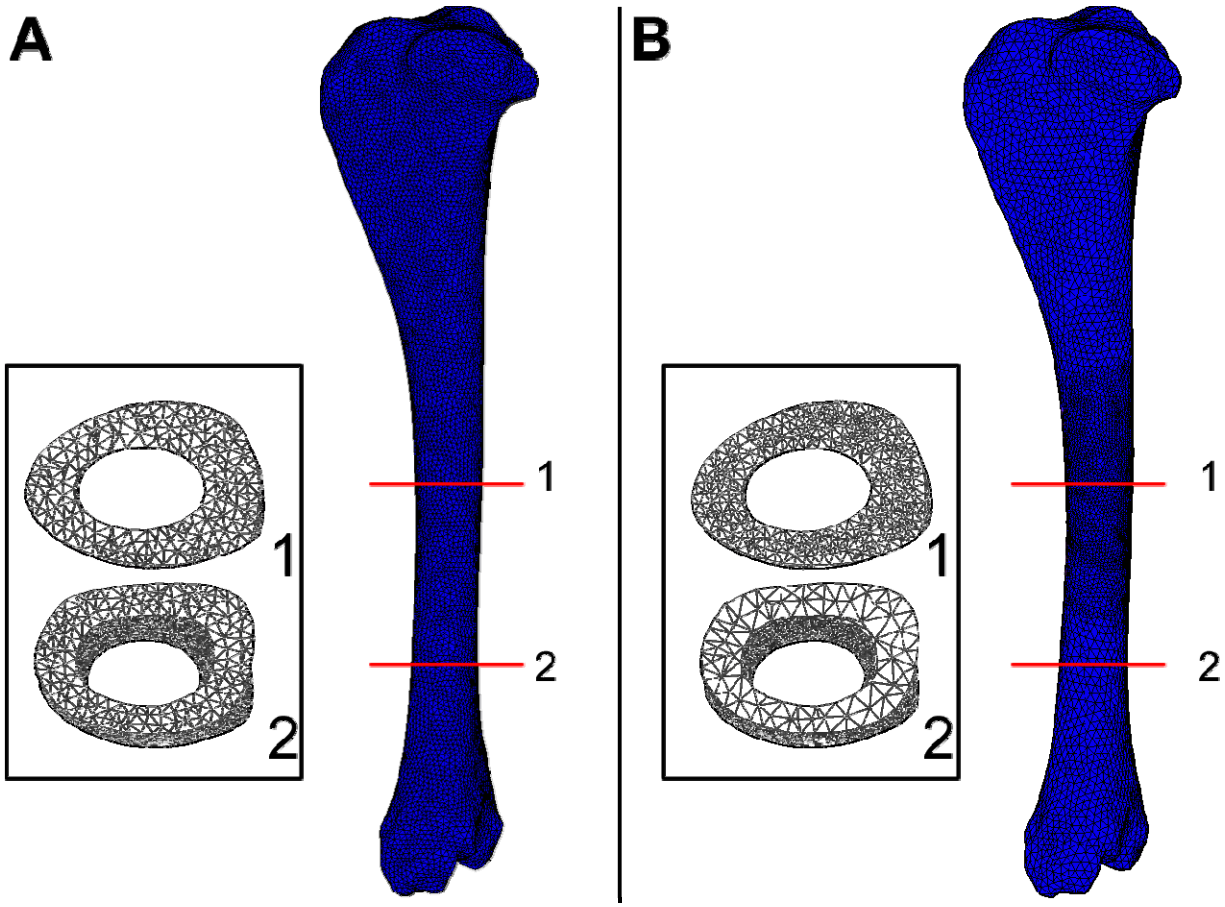

Figure 6.3: (A) Before global remeshing, the model has a fairly uniform mesh size throughout. The insert (1) and (2) shows the mesh density at the middle and distal diaphysis respectively. (B) Global remeshing increases the density of the mesh around the area of interest (1) and coarsens the remaining mesh (2).

6.2.1.3 **Boundary conditions**

6.2.1.3.1 ***Four-point bending***

A custom-written Python script was developed to automate, generate, and standardise the creation of FE models. In Mentat, the Patran output file that contains the FE mesh, and two geometries in IGES format (that represent the rollers and has the same dimensions as the supports used in four-point bending) were imported. The Python code picks out the node sets that were created in Patran (Figure 6.1) and assigns them with the relevant boundary conditions as seen in Figure 6.4. As the application of boundary conditions to just one node at each of the external rollers was insufficient to prevent the rotation of the bone, two adjacent nodes were added as well. Two different sets of analysis were carried out, to simulate the results obtained from the slow and medium strain rate of 0.08-0.1s^{-1} and 0.1-0.4s^{-1} respectively. One bone was also impacted at the high strain rate, where the speed of the actuator is twice that in the medium

group. However, the results showed insignificant difference of less than 1N with the medium strain rate, which could be the result of the lack of dynamic data above 10Hz in literature. Moreover, the fracture patterns that resulted from the medium and fast groups were very similar, as seen in Chapter 5. Therefore, FE simulations were only conducted to reproduce loading at the slow and medium strain rates.

Two nodes were selected as reference nodes for the calculation of strain. The first node is located on the posterior surface of the bone, and along the same z-plane as the centroid. In solid mechanics, this point corresponds to the point where the maximum strain is the greatest. However, due to the fact that failure occurs usually around this node, a second reference node, also on the posterior part of the bone, but along the same xz-plane as the proximal internal roller was also selected.

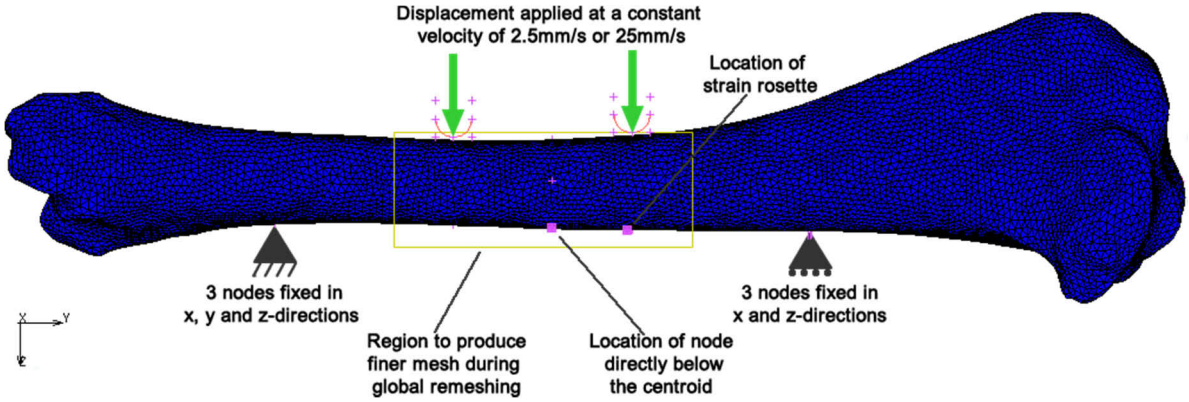

Figure 6.4: The boundary and loading conditions used to simulate four-point bending in the FE model. The pink dots represent the reference nodes used to retrieve information on strain. The yellow box marks the region that will have a higher density mesh after global remeshing.

6.2.1.3.2 ***Torsional loading***

The torsional loading conditions were simulated through the application of displacement in opposite directions at two nodes at the proximal end, to achieve a rotation of 19.6°/s or 196°/s for the slow and fast group respectively (Figure 6.5). A local coordinate system that is updated for each deformation was set up so that an angular displacement is applied to the node. To simulate the use of the XY-table and the rocker mechanism (Chapter 5), one node at the distal-medial end was constrained in the x- and z-directions while a node on the same x-plane but on the lateral side was fixed in all directions. However, as these were not sufficient to prevent rigid

body motion, the grey nodes at the distal end of the tibia were also fully constrained in all directions. One node on the posterior side of the bone, along the same xz-plane as the centroid was used as the reference node in the calculation of strain. The area of the bone enclosed in grey box showed the approximate regions of the bone that were embedded in dental cement (PMMA), and thus did not undergo mesh refinement.

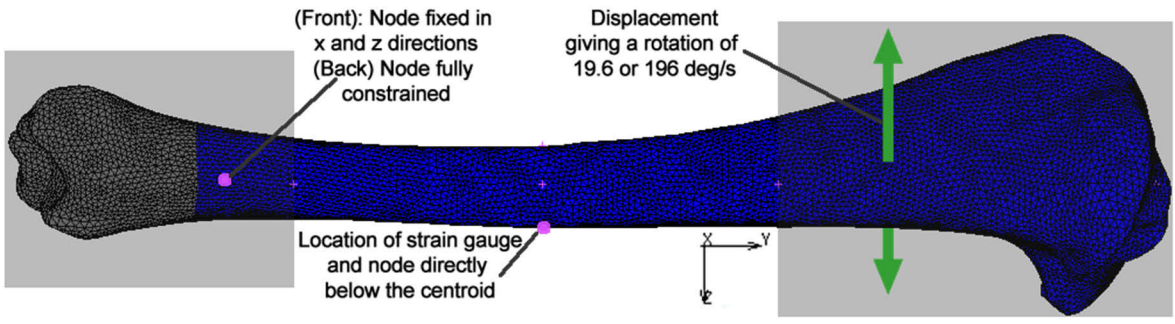

Figure 6.5: The boundary and loading conditions used to simulate torsional loading in the FE models. The grey boxes marked the areas that were embedded in dental cement in experimental testing. The part of the mesh that are selected grey were fully constrained in x, y and z directions.

6.2.1.4 **Modal Analysis**

Quasi-static problems are usually modelled in finite element analysis using the static load case. On the other hand, simulations involving automotive accidents are carried out in the dynamic load case. However, para-physiological strain rates, which were used during experimental testing, do not fall neatly into either of the two categories. Moreover, since lamb bones are being used as surrogates in this thesis, the contribution of mass inertia and damping in lamb bones is also unknown. According to Jazar (2008), the equation to be solved in dynamic analysis is:

$$F = Ma + Cv + kx$$

Where F is the forcing event, m is the mass, a is the second time derivative of the displacement in each point of the specimen, v is the first time derivative of the displacement in each point in the body, c is the viscous damping coefficient, k is the spring constant or stiffness and x is the displacement of the body.

When loading of an object takes place over a sufficiently long period, the response will be static as the contribution of the other two terms are negligible:

$$F = kx$$

The method for determining the choice of load case is to conduct a modal analysis of the bone to evaluate the natural frequencies of the bone under the loading and boundary conditions in service. By converting the time periods of the loading that occurred during experimental testing into frequencies, these can be compared against the natural frequencies of the bone. When the time period of loading is lower than the first natural frequency that is likely to be excited by the loading, then a static analysis can be carried out without losing any accuracy.

Therefore, dynamic harmonic analysis in four-point bending was carried out using the same boundary conditions as described in Section 6.2.1.3.1. The density of each element was assigned a constant value of 1.6 g/cm^3, which is averaged from the density of each element calculated from the greyscale values of the μCT images as described in 6.2.2.1. Shell elements were also created along the walls of the inner mesh to mimic the presence of bone marrow. They were assigned a density of 1 g/cm^3 and a very low elastic modulus as their contribution to the structural strength of a bone is negligible as it behaves like water. A harmonic point load with a magnitude of 5000N, corresponding to the median fracture force observed in four-point bending experiments as described in Chapter 5, was applied to the model through the two internal rollers. The force was permitted to oscillate between 0 to 2000 Hz and the FE solver picked out the first 20 eigenvalues.

The natural frequency of the smallest ovine tibia specimen occurred at 1052.63 Hz, while the first eigenvalue was found at 105.263 Hz. The mode shapes at these two frequencies were also checked and found to be in the same direction to the applied loading case (Figure 6.6). Figure 6.7 plots the eigenvalues against the x-displacement for the node that is expected to experience the maximum bending stress. As can be seen from the diagram, the additional displacement that results when a frequency of 105.263 Hz is applied is 0.0167 mm or 0.529%. However, this figure jumps to 17.4 mm or 570% at the natural frequency. Since the shortest time taken for fracture to occur is 0.008s during the four-point bending experiments, the frequency of the applied loading is thus 31.25 Hz, which implies that the contribution of the amplification as a

result of the inertial effects is less than 0.5%. Therefore, a static analysis would suffice in the modelling of para-physiological strain rates of 0.008-0.02 s^{-1}.

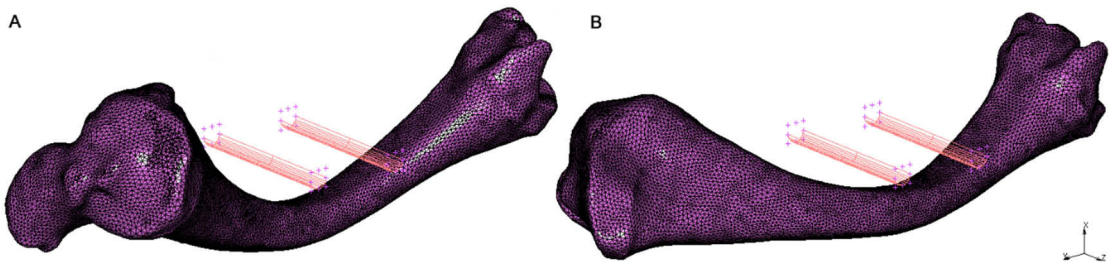

Figure 6.6: The two mode shapes that were obtained during modal analysis. (A) This mode shape corresponds to the response of the bone in four-point bending. (B) This mode shape shows lateral bending, which is a possible frequency response but is not relevant in this study.

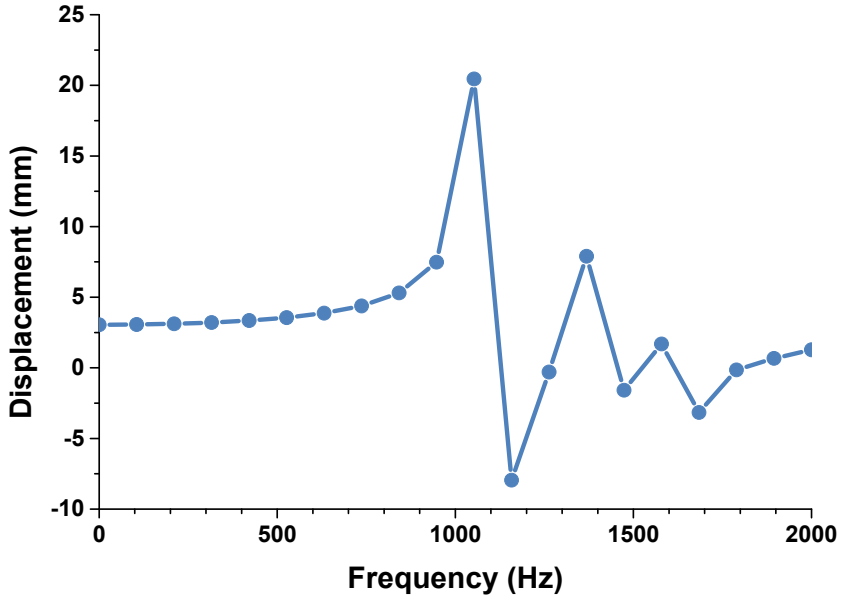

Figure 6.7: The displacement of the bone as a function of the frequency of the applied load in four-point bending. The resonance frequency occurs at about 1000 Hz, and the corresponding mode shape can be seen in Figure 6.6A. Below 500Hz, the contribution of the amplification as a result of the inertial effects is negligible.

6.2.1.5 Failure criteria

A maximum principal strain criterion was implemented as the crack initiation in most of the experimental tests occurred in the principal direction (see Figure 5.13 for an example). Moreover, good results have been reported in the use of principal strain criterion in the prediction of fracture location and risk (Bessho et al., 2007; Schileo et al., 2008) (see Section

6.1.2) . The maximum principal strain was set at 0.01 in tension, as it marks the upper bound of the maximum principal strain that was recorded in Chapter 5.

The simulation of the fracture path is achieved via the element deletion technique, in which the element that has failed is removed. Failure is defined to have occurred when either of the principal strain exceeds the stated threshold. However, without the use of further constraints, a large number of elements would fail in one increment, and the result would be a big hole in the bone. Therefore, two methods were employed to solve this problem.

Firstly, a connectivity matrix was built up after remeshing has occurred. This matrix maps out the neighbours of each element. Therefore, after the first element has been removed, subsequent removal of elements can only occur if they are adjacent to the element that has failed in the previous step. The initial time step is thus kept low to prevent any element from failing, so that the connectivity matrix may be built up successfully.

Secondly, the time step of each increment is controlled by the number of elements that has failed. To keep the fracture propagation as realistic as possible, the number of elements that fails in each time step cannot be large. Hence, a record is kept of the number of failed elements, which is compared against a threshold value. This value is the maximum number of neighbours in the FE model. Thereafter, this ratio is then used to determine the time increment for the next step. The time increment will keep decreasing until the excessive failure of crack is arrested.

6.2.2 Materials Assignment

The accurate replication of the boundary conditions used in four-point bending and torsion is only one key step in the simulation of fractures obtained in four-point bending and torsion. The assignment of inhomogeneous material properties is also important in the building of the FE model, for it affects the mechanical behaviour of the object. In the FE modelling of human bones, a fairly common method involves scanning the bone together with a phantom to calibrate the CT dataset (Bessho et al., 2007; Schileo et al., 2008). While different phantoms are commercially available, phantoms used in clinical CT scanners typically contain hydroxyapatite (HA) rods of different densities that have a corresponding greyscale value for a particular CT scanner. Significant work has been conducted to develop a density-elasticity relationship for

humans (Taddei et al., 2007), but no such mathematical formulations exist for ovine bones. Furthermore, the spine phantom that was available was opaque in the μCT scanner, and thus an aluminium phantom was used instead. An aluminium phantom has a further advantage of producing low artefacts in a CT scanner (Taddei et al., 2006). Therefore, this section explains the derivation of bone tissue density from μCT scans and the mapping of the elastic modulus to the FE ovine model.

The algorithm that was used to achieve the goal of material properties mapping is presented in Figure 6.8 and may be summarised into the following steps:

1. calculating the tissue density and elastic modulus based on the greyscale values of the μCT images,
2. obtaining the transformation matrix of the mesh in its optimal alignment and the original surface mesh,
3. reading the location of the centroid of each element from the FE file,
4. finding all the voxels that surrounds the element, and
5. applying an average value of all the nearest voxel to the element.

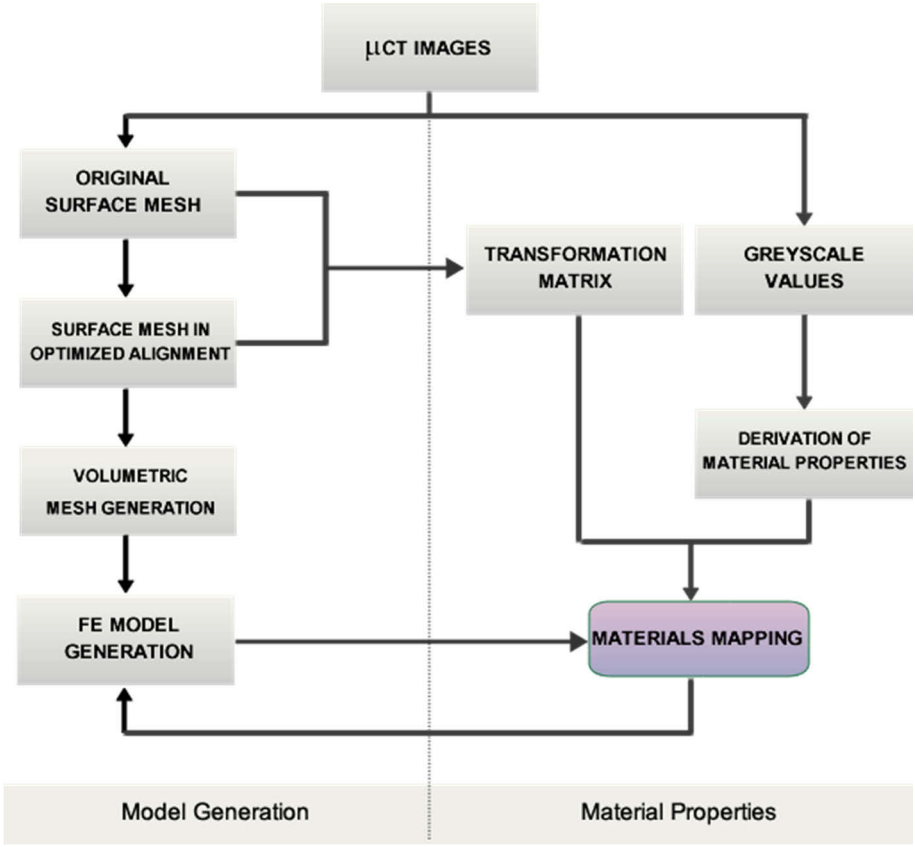

Figure 6.8: This algorithm shows the steps taken to generate the materials mapping file that will be used by the FE model. Information on the elements and their location are provided by the preliminary FE model while the location and values of each greyscale pixel is obtained from the µCT images. The transformation matrix registers the location of the pixels to the elements in the FE model.

The registration of meshes in Step 2 of this procedure is the same as that used in Section 5.2.3. Therefore, to extend the existing code, all the rest of the codes were also developed in Python and ran using the command line interface. Furthermore, as subroutines in the FE package are written in Fortran, these codes could be called automatically from Fortran when the required materials mapping file has not been generated.

6.2.2.1 Material Properties from µCT scans

6.2.2.1.1 Elastic modulus formation

Linear regression conducted on the force-displacement and torque-angle curves obtained during four-point bending and torsional loading tests up to a strain rate of $0.4s^{-1}$ in Chapter 5 revealed that immature ovine tibiae behave linearly up to the point of failure. Some non-linearity was observed in the last 1% of the fracture force, but it behaves primarily as a linearly-

elastic material. Although a transverse isotropic elastic formulation would capture the structural behaviour of bone better, such information is only available for trabecular bone in lambs, which is presented in detail in Nafei et al. (2000). Therefore, an isotropic linear elastic formulation was used to form the stiffness matrix for each element in the following equation, where E, σ, ε and ν represents the elastic modulus, stress component, strain component, and Poisson's ratio respectively.

$$\begin{bmatrix}\sigma_{xx}\\ \sigma_{yy}\\ \sigma_{zz}\\ \sigma_{yz}\\ \sigma_{zx}\\ \sigma_{xy}\end{bmatrix} = \frac{E}{(1+v)(1-2v)}\begin{bmatrix}1-v & v & v & 0 & 0 & 0\\ v & 1-v & v & 0 & 0 & 0\\ v & v & 1-v & 0 & 0 & 0\\ 0 & 0 & 0 & 1-2v & 0 & 0\\ 0 & 0 & 0 & 0 & 1-2v & 0\\ 0 & 0 & 0 & 0 & 0 & 1-2v\end{bmatrix}\begin{bmatrix}\varepsilon_{xx}\\ \varepsilon_{yy}\\ \varepsilon_{zz}\\ \varepsilon_{yz}\\ \varepsilon_{zx}\\ \varepsilon_{xy}\end{bmatrix}$$

6.2.2.1.1.1 Determination of bone tissue density

In terms of its chemical components, bone is composed of organic, inorganic, water and ash fraction. The calcium content of bone is thought to contribute primarily to the strength of bone and as early as 1990, a relationship between the calcium content and Young's modulus has been proposed (Currey, 1990). However, before the elastic modulus for each element may be found, a relationship that converts the grey scale values of the μCT scans to its tissue density first needs to be used. Although a few relationships for the derivation of bone tissue density have been developed, the method developed by Wagner et al. (2011) recognizes and differentiates the contribution of all the bone constituents, which is important due to the slight differences between the bone composition of ovine and human bones (see Chapter 2). According to those authors, the tissue mineral density of bone may be expressed as:

$$\rho_t = \left(1 - \frac{\rho_w}{\rho_{HA}}\right)\rho_{HA} + R_o(\rho_o - \rho_w) + \rho_w$$

The subscripts *HA*, *w*, *o*, *a* and *t* in the above equations stand for water, organic component, ash and tissue respectively. R_o, which stands for the volume fraction of the organic component of the bone, is a constant. ρ_{HA} is the mineral density of bone that can be calculated directly from a μCT scan:

$$\rho_{HA} = \frac{\mu_b \mu_{Al(pub)}}{\mu_{Al}\mu_{mHA}}$$

where μ_b and μ_{Al} are the measured linear attenuation coefficient (grey level) of bone and aluminium respectively, $\mu_{Al(pub)}$ the linear coefficient of attenuation of aluminium and μ_{mHA} the mass attenuation coefficient of hydroxyapatite (HA). The latter two values were obtained from National Institute of Standards and Technology (NIST)'s database (NIST, Gaithersburg, MD, USA).

As described previously in Chapter 4, the μCT images were loaded into Mimics x64 15.0 (Materialse NV, Leuven, Belgium) to segment the geometry of the bones. In addition, grey values are available from the DICOM images and they are representations of the linear attenuation coefficients of all the materials present during the scan.

To extract the linear attenuation coefficient of the aluminium phantom, profile lines were drawn in Mimics, passing through the aluminium phantom. The values were then read off the graph generated as seen in Figure 6.9 below.

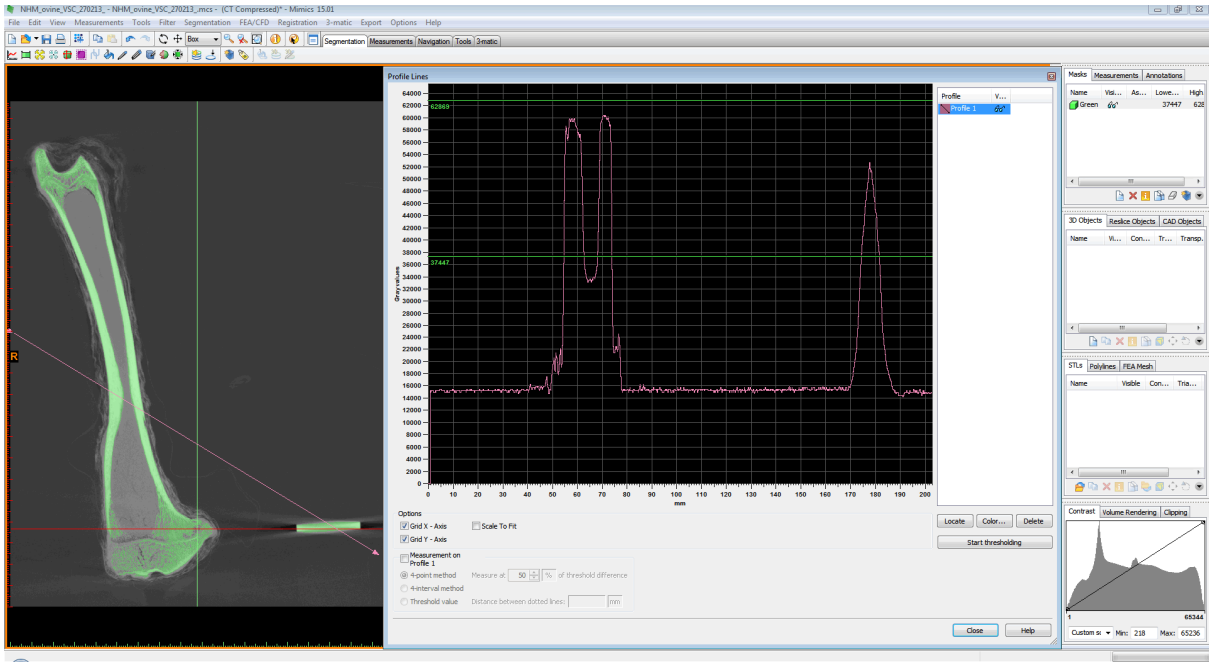

Figure 6.9: A print screen from Mimics 15.0 that shows the profile line function that was used to obtain the greyscale value of the cortical bone and the aluminium phantom. A line is drawn through the bone and the aluminium phantom (in green) and a graph displaying the intensity values is generated.

As a preliminary check, the profile line was also allowed to pass through the mid-diaphysis to obtain the grey values of the cortical bone, which gave a range of values from 47916 to 62591. By using a value of 0.122 cm^2/g for μ_{mHA}, 0.33 cm^{-1} for $\mu_{Al(pub)}$, the mean bone mineral density of

the immature ovine tibia is 1.72g/cm^3. This value is just 25% higher than the bone mineral density for cortical bone reported by Willems et al (2012) for immature lambs between 18-26 weeks old, which shows that the values obtained using this method is reasonable.

The voxel-by-voxel grey values were then exported to enable calculation of the elastic modulus of the cortical bone later.

6.2.2.1.1.2 Determination of elastic modulus

The elastic modulus was calculated based on the composition of bone constituents as developed by Wagner et al. (2011):

$$\log_{10}(E_t) = -8.58 + 4.05 \cdot \log_{10}\left(\frac{400 \cdot \rho_{HA}}{\rho_{HA} + \rho_o \cdot R_o}\right)$$

The bone mineral content of immature sheep bone (111-148 kg/m^3) in Willems et al. (2013) was found to be similar to the value in children's bone obtained by Mueller et al. (1966) (125-200 kg/m^3). Thus, the upper bound of R_o for children below 5 years old, 0.35, was used. Moreover, the data presented by Mueller et al showed that the ash, organic and volume constituent of bone do not change much with age, suggesting that structural change plays a major component in the contribution of bone strength as it matures. The value of 0.35 falls within the volume fraction of the organic component of 33-38% reported for steer and dog (Gong et al., 1964; Robinson, 1975). Since these animals have a bone architecture that is more similar to sheep bones than human bones, the value of R_o used can be considered to be reasonable. Finally, the density of water, ash and organic component were assumed to be 1.0, 3.0 and 1.4 g/cm^3 as suggested by the authors.

6.2.2.2 Material properties mapping

Although voxel-by-voxel material properties may be calculated from the μCT images, the FE model is lower in resolution by at least an order of magnitude. Therefore, the mapping of the material properties of the closest voxel to the centroid of the element may result in highly disparate material assignments across the FE mesh. Therefore, the nearest neighbours (voxels) to the centroid of each element were found and their mean material properties were used instead. To handle the large number of voxels, elements and nodes (approximately 2 million

voxels, 200 000 elements and 50 000 nodes), k-dimensional (or k-d) tree data structure was used to build up a quick search tree based on the spatial location of the voxels. This computer-science algorithm is freely available in the public domain in many languages. Thereafter, the sub-function of nearest neighbour search, which is part of k-d tree, was used to find the points on the tree that are closest to the centroid of the elements. However, due to the fact that the orientation of the surface mesh has changed during the calculation of the optimized alignment, the point correspondence between the two meshes needs to be input into this algorithm.

After mapping has been conducted, it may be read into the FE to build up the stiffness matrix as discussed in Section 6.2.2.1.1. A visual representation of the distribution of the elastic modulus along the tibia can be seen in Figure 6.10.

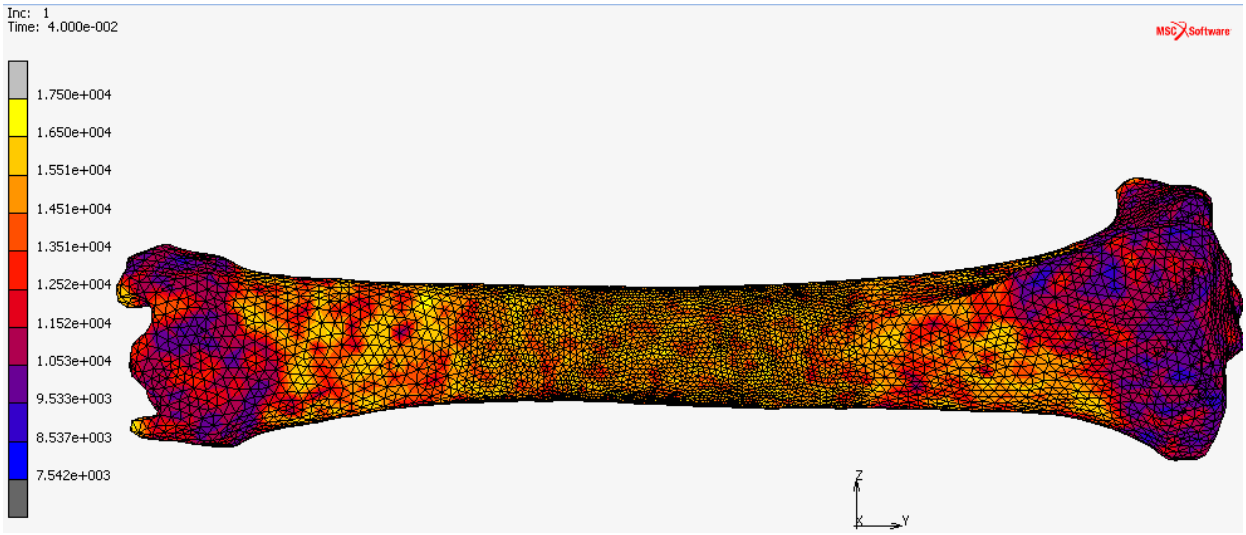

Figure 6.10: The elastic modulus (in MPa) assigned to each element is visualized here using a user-subroutine. The midshaft of the bone has a higher elastic modulus than the two ends of the bone.

6.2.2.3 Viscoelasticity

Human cortical bones have been found to exhibit strain-rate dependency both in pre-yield and post-yield (Hansen et al., 2008; Ouyang et al., 2003). While such data is not available for paediatric bones, the results obtained in Chapter 5 showed that the bending stiffness of immature ovine tibiae increased when the strain rate was increased from 0.003-0.004s^{-1} to 0.08-0.4s^{-1}. The myriad of fracture patterns that are seen clinically also suggests a viscoelastic response of the bone when impacted.

For a viscoelastic material, its viscoelastic modulus may be expressed using a Prony series as:

$$G_R(t) = G_o(1 - \sum_{i=1}^{N} g_i \left[1 - e^{-\frac{t}{\tau_i}}\right])$$

Laplace transform of this equation would eventually lead to:

$$G'(\omega) = G_o \left[1 - \sum_{i=1}^{N} g_i\right] + G_o \sum_{i=1}^{N} \frac{g_i {\tau_i}^2 \omega^2}{1 + {\tau_i}^2 \omega^2}$$

$$G''(\omega) = G_o \sum_{i=1}^{N} \frac{g_i \tau_i \omega}{1 + {\tau_i}^2 \omega^2}$$

Where *G'(ω)*and *G"(ω)* represent the storage modulus and loss modulus in the frequency domain respectively. Physically, the storage modulus is a measure of the object's capability to store elastic energy and is thus equivalent to the elastic modulus in the time domain. The loss modulus measures the dissipation of energy by the viscous components of the material. Dynamic data conducted over a frequency range of 1-10Hz are available for sheep in bending (Yeni et al., 2007). Therefore, a custom-written Python code was used to find the terms of the Prony series by using the Simplex algorithm available in Python to minimise the errors of the residuals. The Simplex algorithm requires the user to provide initial inputs of require values before the best solution can be found. A two-term Prony series was found to provide the lowest error of 0.184, yielding the following values as seen in Table 6.3, which were used in the FE model.

Table 6.3: Details of the Prony series used to define viscoelasticity in the FE models.

Elastic modulus (g) (Nmm^{-2})	Time constant (τ) (s^{-1})
0.10042077	0.036624089
0.18106535	0.67047326

For four-point bending, one bone was also initially impacted at the high strain rate, where the speed of the actuator is twice that in the medium group. However, the results showed insignificant difference of less than 1N. Moreover, the fracture patterns that resulted from the

medium and fast groups were very similar, as seen in Chapter 5. Therefore, FE simulations were only conducted to reproduce loading at the slow and medium strain rates for bending.

Materials and Methods

Ten ovine tibiae (5 left, 5 right) from 5 months old British Texel lambs that have undergone μCT scanning were used in this study. The left bones were all used to build up the FE models in four-point testing whereas the right bones were used to simulate the conditions of torsional loading. The bones were all orientated in their optimised alignment (Chapter 4) prior to conducting FE analysis. Further details on the image acquisition can be found in Chapter 4. Out of these ten bones, 3 tibiae each in bending and torsion were also tested experimentally and their results are compared with the FE simulations.

6.2.2.4 Model Results

All the quantitative results presented in this Chapter were obtained by running a custom-written code to extract the relevant data. All the nodes of interest have already been placed in relevant groups in Patran, so this script enables these nodes to be picked out easily. Moreover, the nodes are renumbered during the global remeshing process so this script automatically establishes the new node number to use in subsequent increments of the file. The maximum principal strain is calculated from the values of the 6 strain components that are available in the output file to solve the following equation for ε_p, the principal strain.

$$\begin{vmatrix} \varepsilon_x - \varepsilon_p & \gamma_{xy} & \gamma_{xz} \\ \gamma_{yx} & \varepsilon_y - \varepsilon_p & \gamma_{yz} \\ \gamma_{zx} & \gamma_{zy} & \varepsilon_z - \varepsilon_p \end{vmatrix} = 0$$

This equation may be expanded into:

$$\varepsilon^3{}_p - I_1\varepsilon^2{}_p + I_2\varepsilon_p - I_3 = 0$$

where

$I_1 = \varepsilon_{11} + \varepsilon_{22} + \varepsilon_{33}$

$I_2 = \varepsilon_{11}\varepsilon_{22} + \varepsilon_{22}\,\varepsilon_{33} + \varepsilon_{33}\,\varepsilon_{11} - \varepsilon^2{}_{12} - \varepsilon^2{}_{13} - \varepsilon^2{}_{23}$

$I_3 = \varepsilon_{11}\varepsilon_{22}\,\varepsilon_{33} - \varepsilon_{11}\varepsilon^2{}_{23} - \varepsilon_{22}\,\varepsilon^2{}_{13} - \varepsilon_{33}\varepsilon^2{}_{12} + 2\,\varepsilon_{12}\varepsilon_{13}\varepsilon_{23}$

6.2.2.5 Statistical Analysis

Non-linear analysis using Netwon-Raphson method was conducted by the FE solver but all the graphs obtained were highly linear. Therefore, linear regression was carried out for the strain-force and force-displacement curves of each bone. The peak values and slopes from the results of the two testing speed were compared using Wilcoxon signed rank test to check if any significant difference existed. All statistical tests were conducted using OriginPro 9.0 (OriginLab Corp., Northampton, MA).

6.3 Results and Comparison with Physical Experiments

6.3.1 Four-point bending

The testing speed of 2.5mm/s and 25mm/s produced a strain rate of 0.008-0.015s^{-1} and 0.08-0.15s^{-1} respectively at the region of maximum strain, which falls within the strain rates obtained in experimental testing (Chapter 5). The force-displacement curves of the experimental and FE simulation results of 3 bones are compared in Figure 6.11. The FE simulations produced a premature failure of the bones as seen in the lower failure force and displacement when compared to the experimental result. In the two cases where a higher strain rate of 0.08-0.4 s^{-1} was experienced, FE-calculated failure force and displacement lie almost on the experimentally derived curves. However, these values do not correspond as well for the bone that was tested at the lower strain rate.

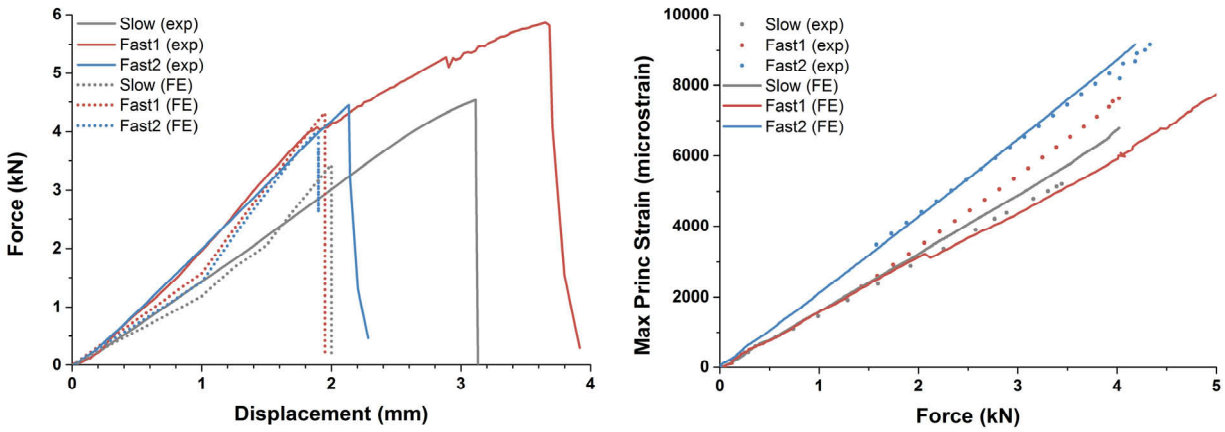

Figure 6.11: (Left) The predicted force-displacement curves obtained in the FE models, in comparison to the experimental results. (Right): The corresponding maximum principal strain-force curves. 'Slow' corresponds to BS3, 'Fast1' to BM4 and 'Fast2' to BM2.

The FE models predicted a linear response of maximum principal strain against force, similar to the results recorded from the strain gauges (Figure 6.11). However, the gradient of the strain-force curve is lower in the FE-calculation for the *Slow* case but higher in the *Fast1* case. Among the three specimens, the gradients of the FE-calculated and experimentally-derived curves are closest to each other for the *Fast2* specimen and they differ by 6.2% (2040 ± 18 and 2166 ± 2 microstrain/kN respectively). The experimentally-derived strains were plotted against the FE-calculated strains (Figure 6.12), and the obtained regression line has an intercept of -59.1, a slope of 1.03 and a coefficient of determination (R^2) of 0.99. When data in the non-linear region were also included in the regression analysis, the R^2 dropped to 0.97.

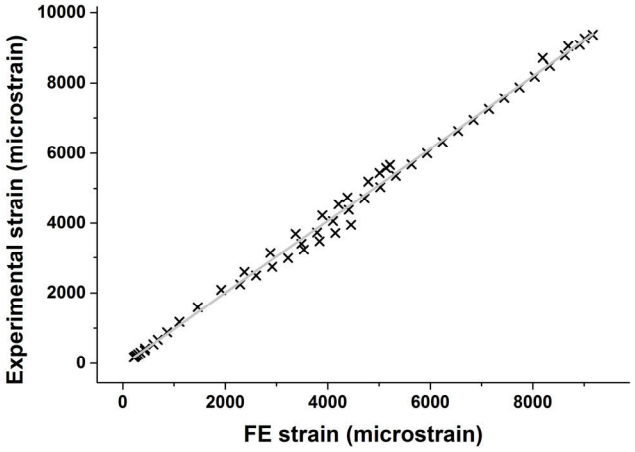

Figure 6.12: Experimentally-derived maximum principal strain of the three specimens within their linear region, plotted against the FE-calculated maximum principal strain. The regression line is shown in grey.

Moreover, the qualitative comparison of the final fracture profile in Figure 6.13 shows that the location and pattern of transverse and oblique fracture from the FE-calculated models matched well with the experimental results, showing that the model is capable of predicting the experimental results fairly well in four-point bending.

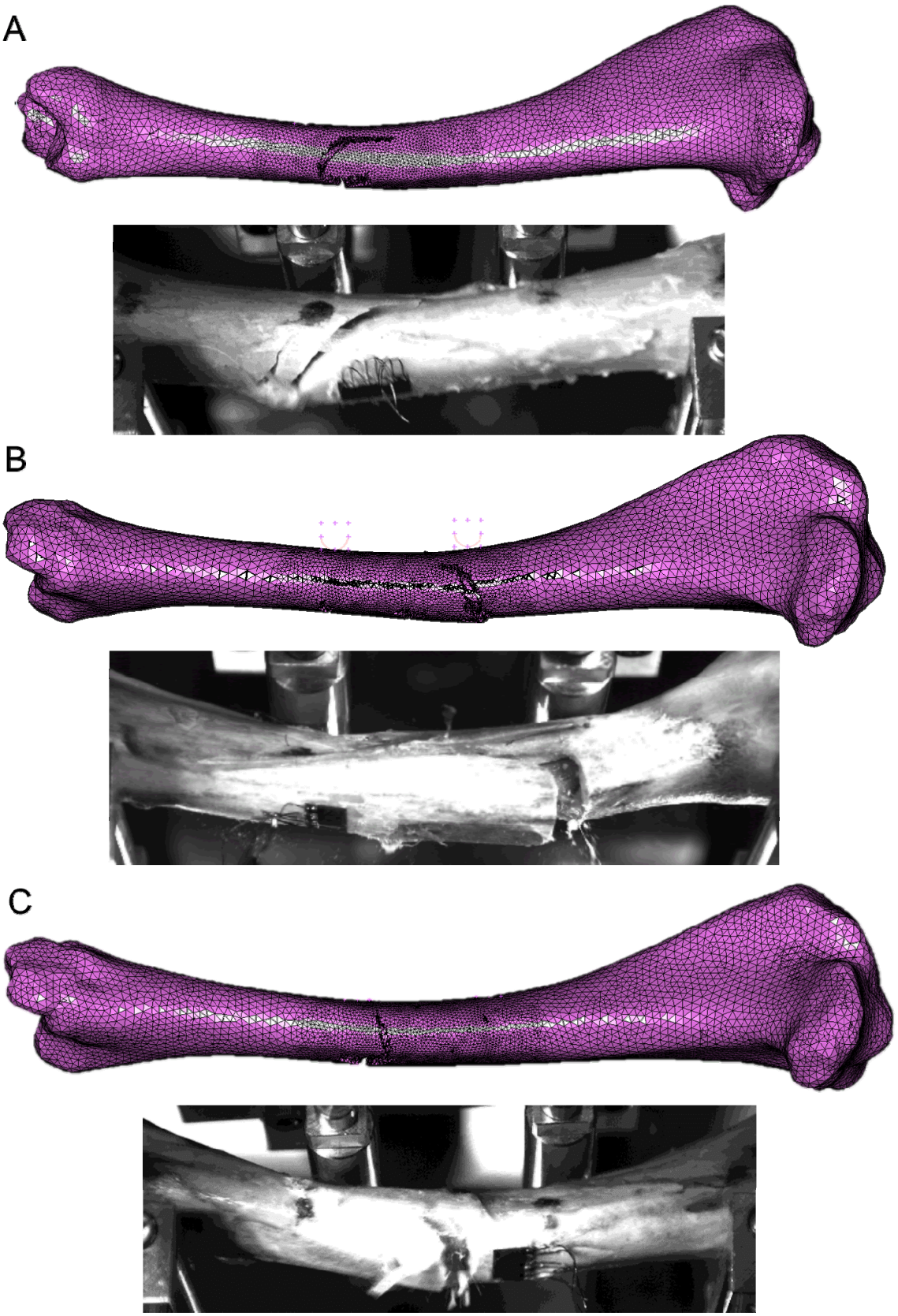

Figure 6.13: The results of the FE simulations are compared with the experimental results obtained in Chapter 5. Oblique fractures were produced at the testing speed of 25mm/s. The distal oblique fracture in (A) corresponds to BM4 while the proximal oblique fracture in (B) corresponds to BM2 . Transverse fracture was generated when the speed was decreased 10 times and it corresponds to BS3 (C).

Upon simulating five ovine tibiae at two different strain rates, only transverse fracture pattern were generated when the bones were impacted at a rate of 2.5mm/s in four-point bending, whereas both transverse and oblique fractures were produced when the testing rate was increased 10 times; these findings are similar to the results obtained in experimental testing. The FE models generated two different types of transverse (Figure 6.14) and oblique (Figure 6.15) fracture patterns. However, the transverse fractures are consistently located towards the middle of the bone whereas the oblique fractures originated near one of the internal rollers.

Figure 6.14 and Figure 6.15 show that regardless of the loading rate, the crack appears through the failure of a few elements initially. Most of them initiate transversely, but in one case which was loaded at 25mm/s, the fractures initiated obliquely (Figure 6.15B). This was also the only case where the initiation of fracture occurred at more than one location, and the final fracture morphology is oblique with signs of comminution. Augmented with the fracture being located at the proximal midshaft, this reflected the oblique fractures that were generated at higher strain rate in experimental testing (Chapter 5).

The other oblique fracture that can be seen in Figure 6.15 occurs near the distal internal rollers and the fracture initiated more proximally before it propagates distally on the posterior aspect of the bone. As it nears the distal internal rollers, the crack then makes a change in direction and proceeded towards the proximal roller, resulting in an oblique fracture.

The two transverse fracture patterns shown may be classified as an incomplete greenstick and a complete transverse fracture. The cracks both initiated transversely, but for the incomplete case, the fracture spread along the long axis of the bone far more than the complete case.

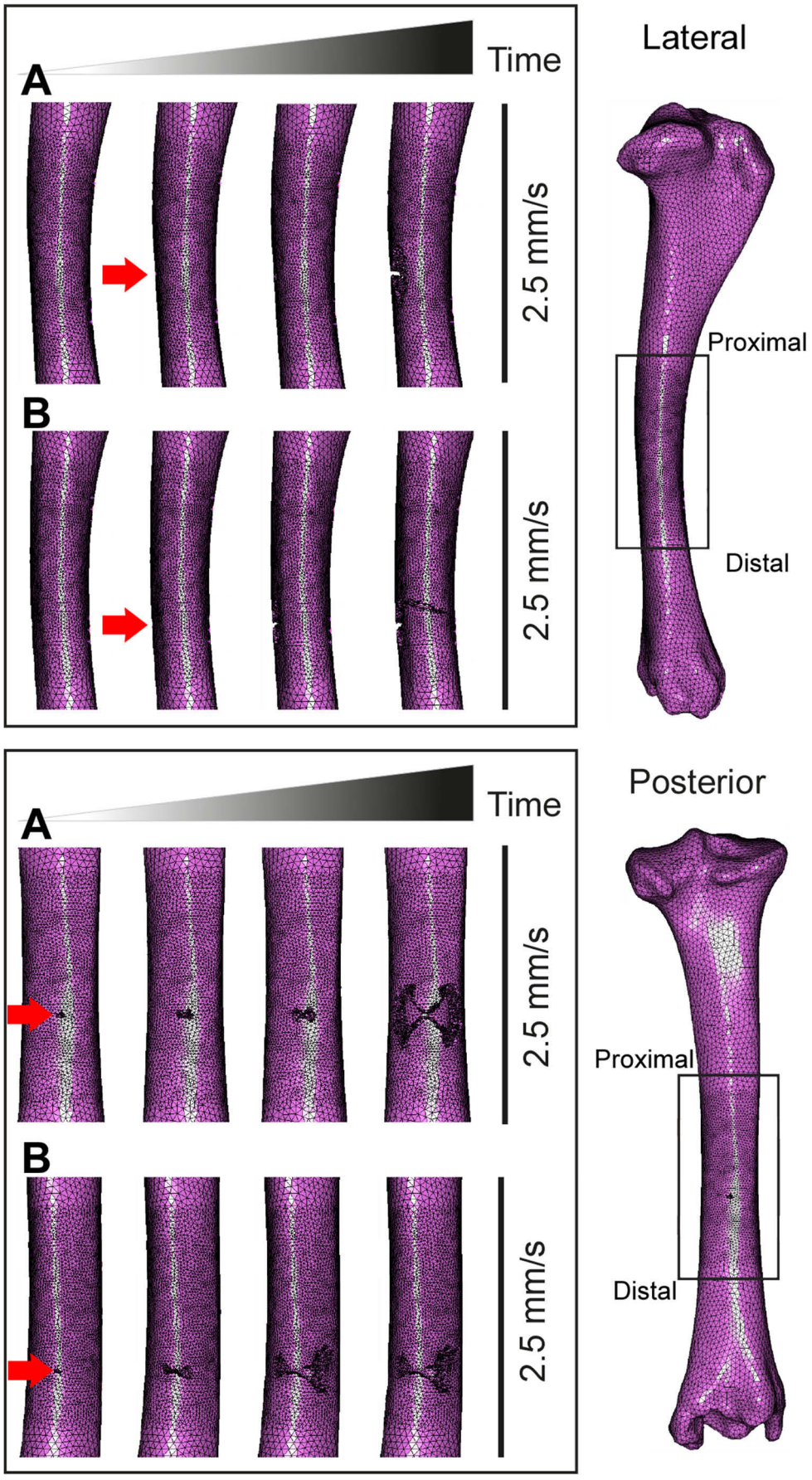

Figure 6.14: The top and bottom inserts show the progression of the fracture in the lateral and posterior views respectively of Bone 5 and Bone 3 when loaded at the lower rate of 2.5mm/s in four-point bending.

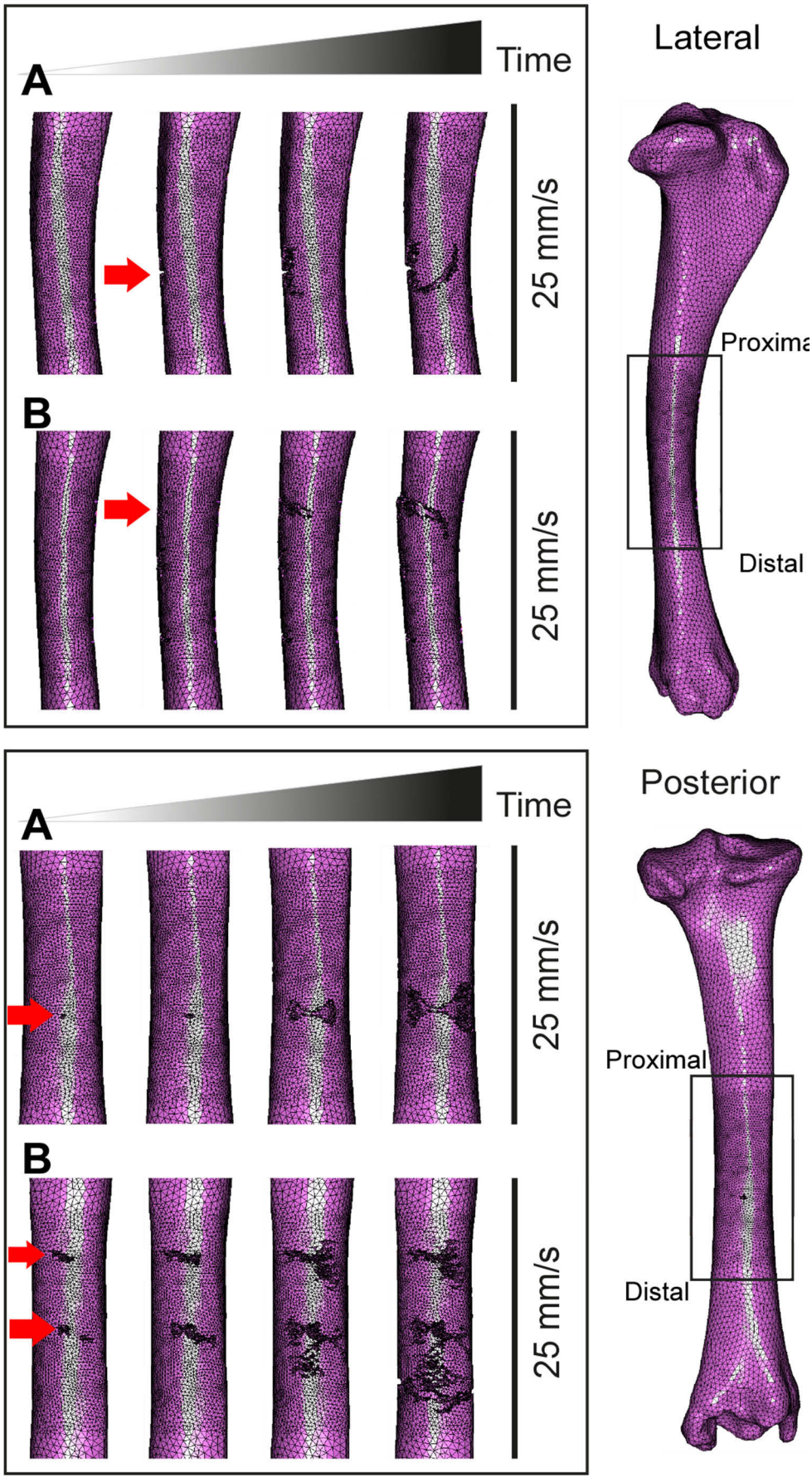

Figure 6.15: The top and bottom inserts show the progression of two different oblique fractures in the lateral and posterior views respectively of Bone 5 and Bone 2 when loaded at 25mm/s in four-point bending.

The maximum principal strains show a linear response for the two reference nodes (Figure 6.16) at both testing speeds. The graphs in black plot the response of the node where the maximum principal strain is the greatest. The graphs in grey are the responses of the nodes that correspond to the locations of the strain rosettes in the physical experiments (Chapter 5), thereafter also known as strain gauge node. Figure 6.16B shows that the peak maximum principal strain is recorded at a higher force for the strain gauge node than the node that experiences the maximum strain. On the other hand, the graph on the left shows no indication of a time delay.

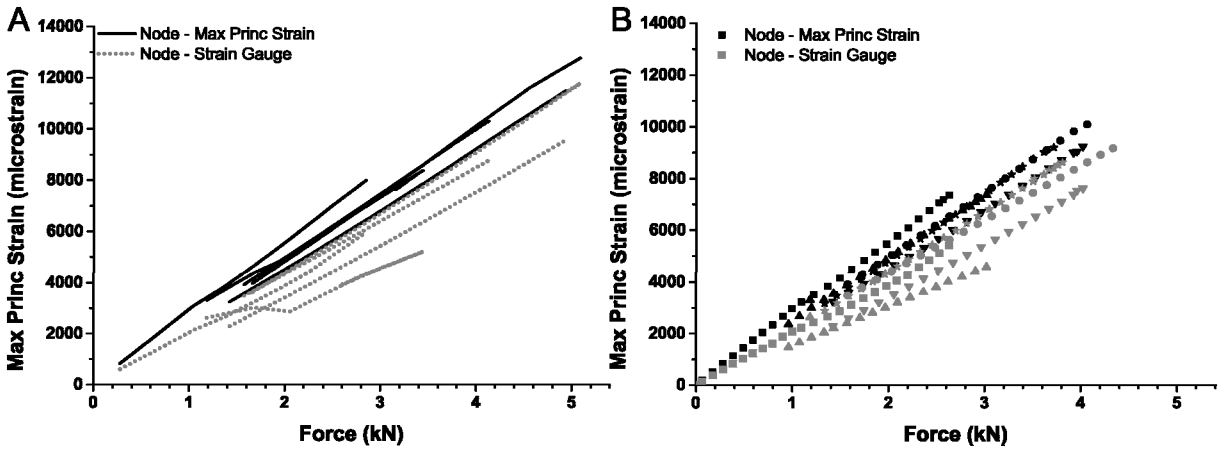

Figure 6.16: The readings of the maximum principal strain at two nodes at low strain rate for all 5 specimens (A) and high strain rate (B). The maximum principal strain occurs at the same force magnitude for both nodes at low strain rate (A) but the highest value of maximum principal strain for the strain gauge node occurred later at the higher strain rate.

The FE simulations produced a maximum principal strain of 0.0102 ± 0.00203 and 0.00865 ± 0.00123 at the slower and faster testing speed respectively (Figure 6.17). This 18% increase in maximum principal strain when the bone is simulated at a lower strain rate is significantly different (Wilcoxon signed rank test, p = 0.0295). However, the gradient of the strain-force graphs at the two testing speeds are very similar at 0.00250 ± 0.00019 kN^{-1} and 0.00249 ± 0.00017 kN^{-1}, which are not significantly different (p = 0.787).

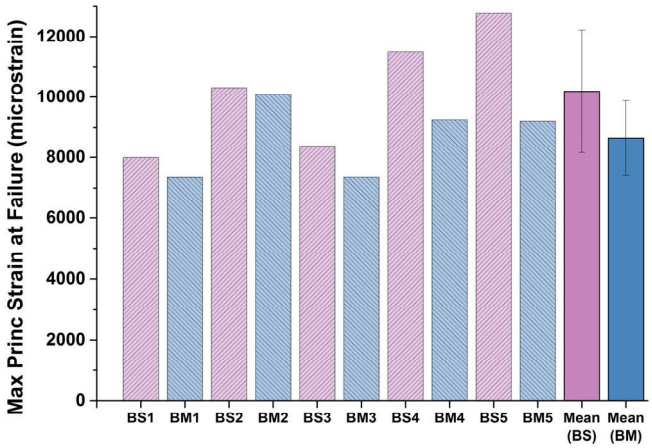

Figure 6.17: The changes in maximum principal strain as a result of increasing the loading speed for each bone are seen here. There is a significant decrease in peak maximum principal strain when the strain rate is increased. BM and BS stand for testing conducted at the medium and slow strain rates respectively.

The force-displacement graph exhibits a linear response even though non-linear analysis was carried out in the FE solver (Figure 6.18). The results show that bones failed suddenly, characterised by a sudden decrease in force. Prior to failure, the time step between each increment was bigger compared to immediately after the first crack had occurred. The time step between each increment along the vertical portion of the graphs was smaller to give a more realistic picture of the progress of fracture propagation.

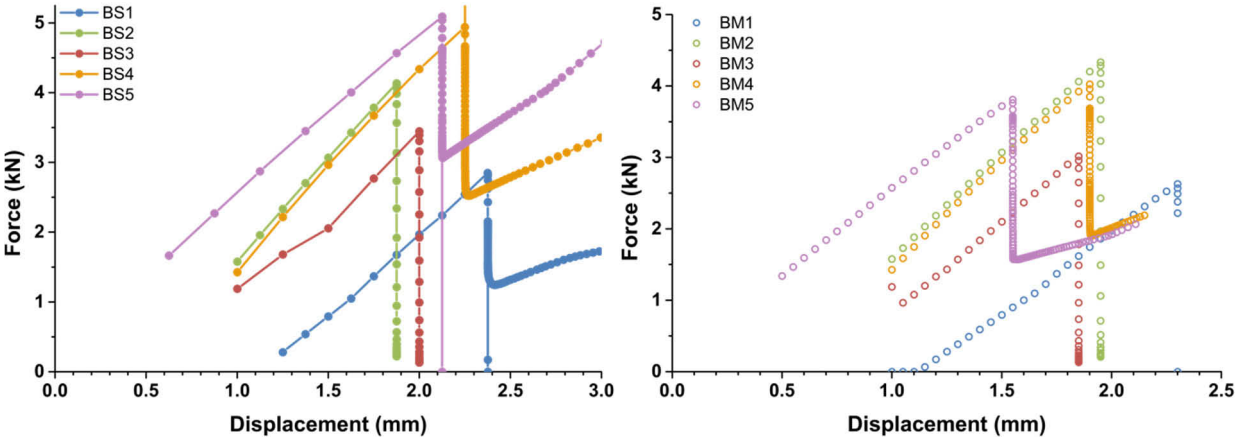

Figure 6.18: Force-displacement curves for 5 tibiae at low strain rate (left) and high strain rate (right). The graphs showed that the bones behaved linearly up to the point of failure.

Linear regression conducted on the portion of the graphs up to the point of failure had a minimum R^2 of 0.983 for the bones that were impacted at a velocity of 25mm/s. This value rises only slightly to 0.986 when the speed was reduced 10 times.

The bending stiffness of the five bones do not show a significant difference whether four-point bending test is conducted at a speed of 2.5mm/s or 25mm/s (Wilcoxon signed rank test, p = 0.281) (Figure 6.19). Moreover, when tested at slower strain rate, the bones absorbed 2.83 ± 0.5 J prior failure, compared to 2.20 ± 0.6 J of energy absorbed to failure at the higher strain rate. This difference was also not found to be significantly different (p = 0.0625).

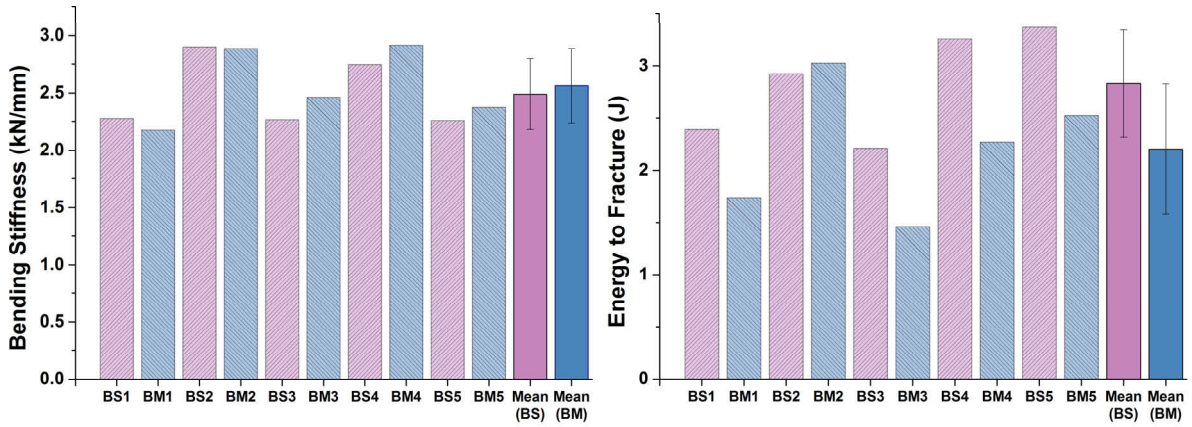

Figure 6.19 (Left) Bending stiffness for 5 left ovine tibiae. The effect of increasing the testing rate in four-point bending led to a varied response in the bending stiffness of the bone. (Right) The energy absorbed to failure also shows a mixed response when the impact speed was increased. BM and BS stand for testing conducted at the medium and slow strain rates respectively.

6.3.2 Torsional loading tests

The FE simulations for torsional loading recorded a linear response to the point of failure, where there is a sudden decrease in the torque value. Similar to the case of four-point bending, more solution points were calculated at the onset of fracture, in order to achieve a more realistic picture of the fracture propagation process. The torque-angle curves of the experimental and simulation results are highly similar from the fast groups (Figure 6.20). In the slow case, the experimental result exhibits three sections including a toe region but the FE-calculated curve is linear throughout and is only similar to the first part of the experimental results.

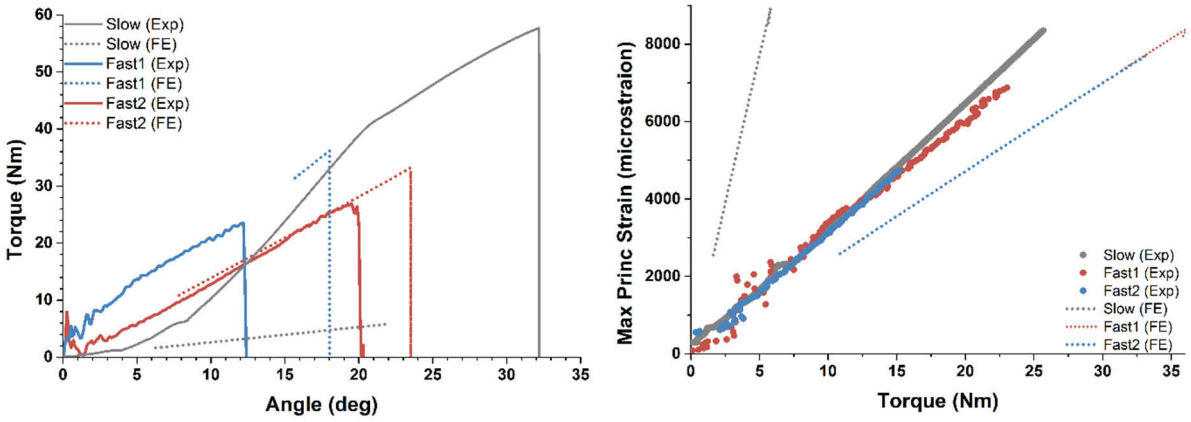

Figure 6.20: The FE-calculated torque-angle graphs are contrasted against the experimentally-derived values. 'Slow, 'Fast1' and 'Fast2" corresponds to TS2, TF1 and TF3 respectively.

The maximum principal strain from both the FE calculations and experimentally -derived strain gauges were highly linear (R^2 > 0.97). However, similar to the torque-angle result, the FE simulations were not able to predict the maximum principal strain of the slow case accurately (Figure 6.20). Therefore, the plot of maximum principal strain of the FE simulations against that obtained from the strain gauges only included the 2 fast cases (Figure 6.21). The line of linear regression has an intercept and slope of -71.4 microstrain and 1.30 respectively. The coefficient of determination of the regression analysis has a R^2 value of 0.99.

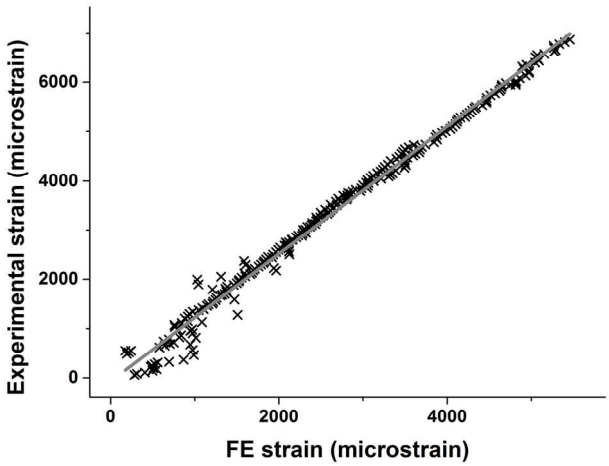

Figure 6.21: Experimentally-derived maximum principal strain of the two specimens tested at high strain rate in torsion, plotted against the FE-calculated values. The regression line is shown in grey.

The final fracture profiles of the experimental and FE results are contrasted in Figure 6.22. The results showed good correspondence even though the exact locations of the fractures are not

very precise. The spiral and longitudinal patterns matched the experimental results that were obtained in Chapter 5.

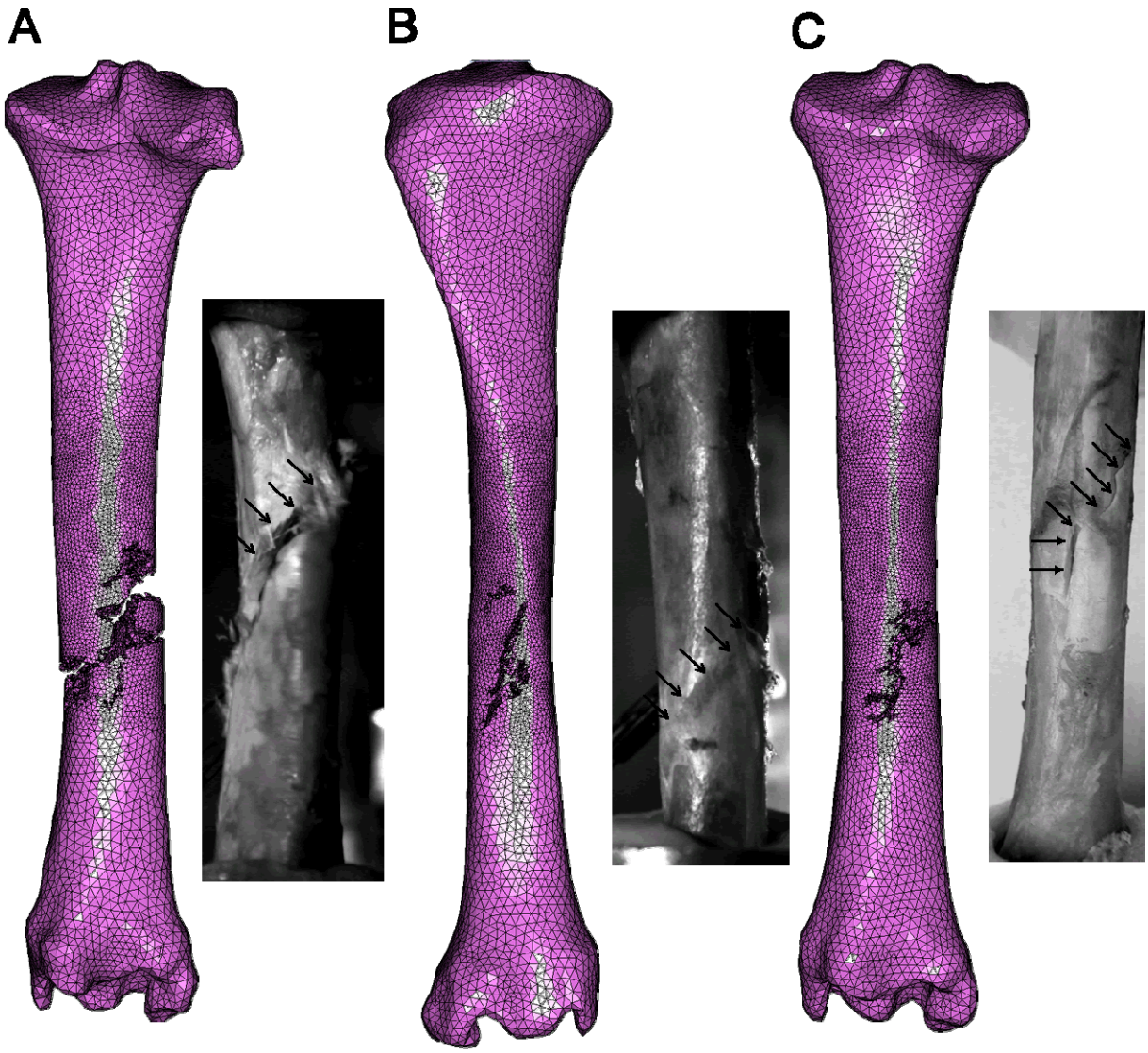

Figure 6.22: The final fracture pattern predicted from FE simulations are compared against experimental results. Arrows have been added to show the fracture paths. At high strain rate, two kinds of spiral fractures were predicted - a more comminuted spiral fracture (A) and an incomplete one where the bone is still intact (B). A spiral fracture with secondary longitudinal fracture was produced at low strain rate (C). Model A, B and C corresponds to TF1, TF3 and TS2.

For the 5 tibiae that were simulated in torsion at 2 different strain rates, a torsional stiffness of 21.9 ± 12.9 Nm/deg and 21.5 ± 13.5 Nm/deg is found in ovine tibiae when torsional loading was applied at a rate of 19.6°/s compared to 196°/s (Figure 6.23). This decrease in torsional stiffness when the bones are loaded at a higher speed is not statistically significant (p = 0.295).

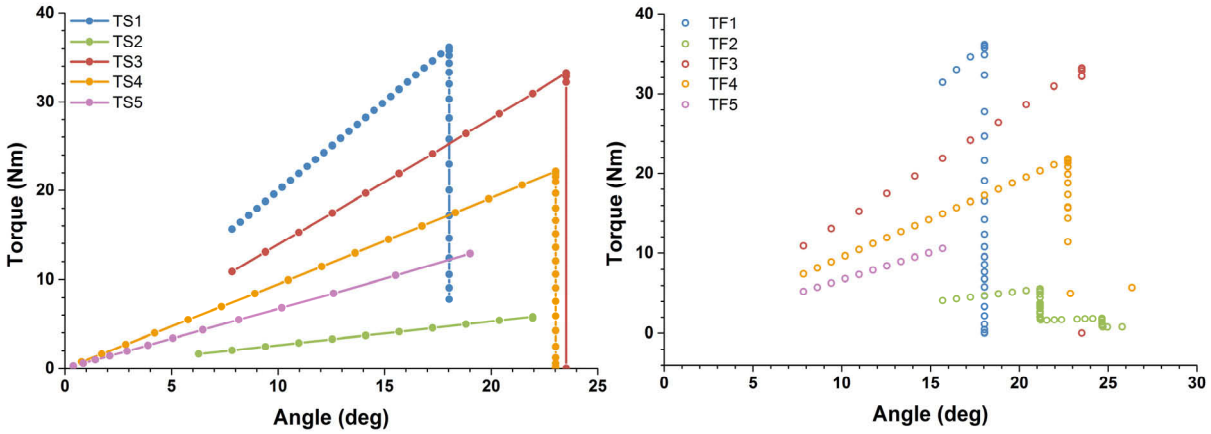

Figure 6.23: The FE-calculated torque-angle curves for 5 right ovine tibiae at a loading rate of 19.6°/s (left) and 196°/s. The curves showed a linear response to the point of failure, with the bones failing at about the same torque and angle at both strain rates.

A comparison between the torsional stiffness of the 5 bones when subjected to an angular displacement of 19.6°/s and 196°/s is presented in Figure 6.24. The torsional stiffness of the bones when tested at the lower speed has a mean value of 1.067 ± 0.677 Nm/deg. This value is significantly lower than the value of 1.074 ± 0.680 Nm/deg that is calculated at the higher strain rate (Wilcoxon signed rank test, p = 0.0295). The energy absorbed to failure for all 5 bones at the two strain rates can be seen in Figure 6.24. Although the value of 7.03 ± 1.11 J is slightly higher when a slower angular displacement is applied compared to 6.52 ± 1.09 J when angular velocity is increased 10 times, the decrease in value is not statistically significant (p = 0.0502), although this approaches significance.

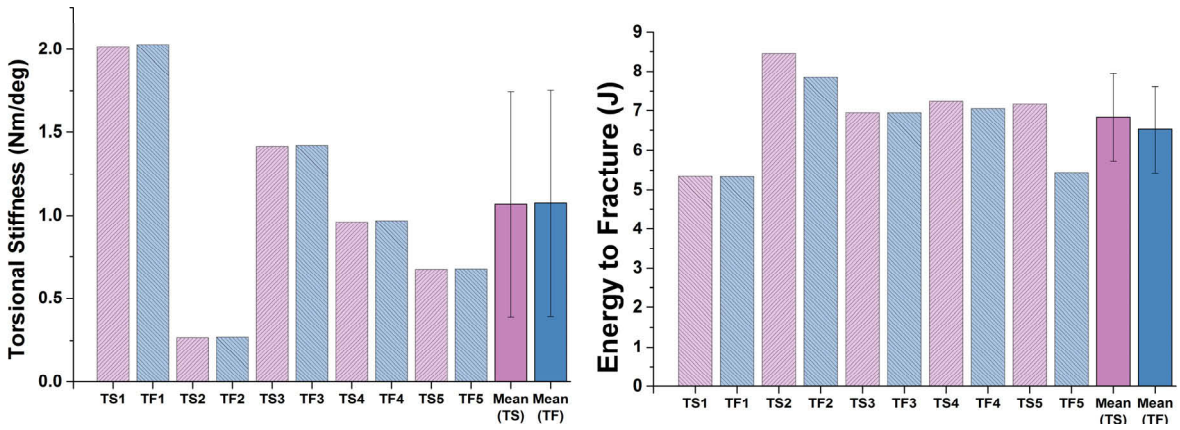

Figure 6.24: (Left) Torsional stiffness for 5 left ovine tibiae. The effect of increasing the testing rate in four-point bending led to a small increase in torsional stiffness that is statistically significant. (Right) The energy absorbed to failure shows a mixed response when the impact speed was increased.

Torsional loading simulations at the angular displacement of 19.6°/s and 196°/s produced a strain rate of 0.006-0.010 s^{-1} and 0.06-0.10 s^{-1}, which falls within the range of 0.006-0.02 s^{-1} and 0.07-0.2 s^{-1} that were achieved for the slow and fast groups in experimental testing. The FE simulations calculated a higher maximum principal strain at failure for simulations carried out at the slower speed than simulations carried out at the higher speed (0.00882 ± 0.00078 compared to 0.00840 ± 0.00078) but this difference was not found to be significant (Wilcoxon signed rank test, p = 0.0528). Figure 6.25 plots this maximum principal strain at the same reference position on the posterior aspect of the bone, which shows that the maximum principal strain remains virtually unchanged at some strain rate although the value dropped at higher strain rate for some bones. The gradients of the maximum principal strain against torque of ovine tibiae are almost independent of the testing rate (Figure 6.25). Wilcoxon signed ranked test confirms this with a p value of 0.0528.

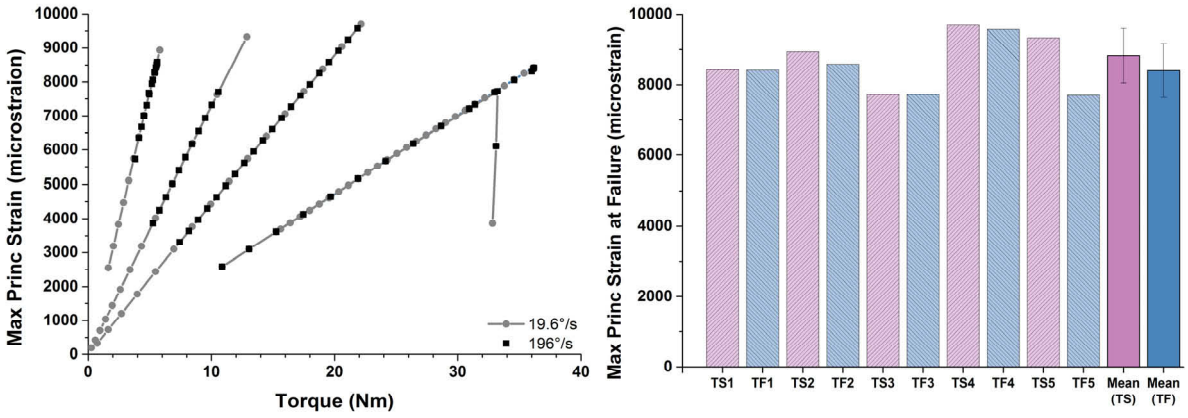

Figure 6.25: (Left) The maximum principal strain obtained at two different strain rates are overlaid in this diagram and it shows that the strain-force gradients are very similar. (Right) The maximum principal strain at failure decreased in some cases at higher strain rate whereas it remained almost unchanged for the rest.

Spiral fractures were produced in all cases but one (TS5). In three cases (TS2, TS3 and TF3) longitudinal fractures were additionally also present. In TS5, longitudinal fracture is present in the absence of spiral fracture. In all these 5 cases, the longitudinal fracture occurs on the posterior side of the bone. There is differentiation of fracture pattern that is produced at different strain rates in only 2 bones (Bone 2 and 5); in the remaining 3 bones, the same kind of fracture pattern is produced. The presence of a combined spiral and longitudinal fracture pattern seems to be accompanied by a higher maximum principal strain at failure. When the

maximum principal strains are very similar, then the same kind of fracture pattern is produced at both low and high strain rates. The crack propagation of two distinct fracture morphologies that resulted when a different loading rate was applied can be seen in Figure 6.26. Although all other boundary conditions have been kept the same, the increase in strain rate from 0.01 to $0.1s^{-1}$ caused a change in the location of the crack initiation that eventually resulted in longitudinal and spiral fractures to be produced in TS5 and TF5 respectively. Although this figure contrasts two distinct fracture patterns that were generated when this bone was tested at two different strain rates (Bone 5), only spiral fractures were produced in some other cases. Bone failure occurred first on the posterior side of the bone but the exact location is more distal and lateral in the longitudinal than the spiral case. The crack from the spiral fracture later then extends to the anterior side of the bone for the fast case but the anterior aspect of the bone remains undamaged for the slow case.

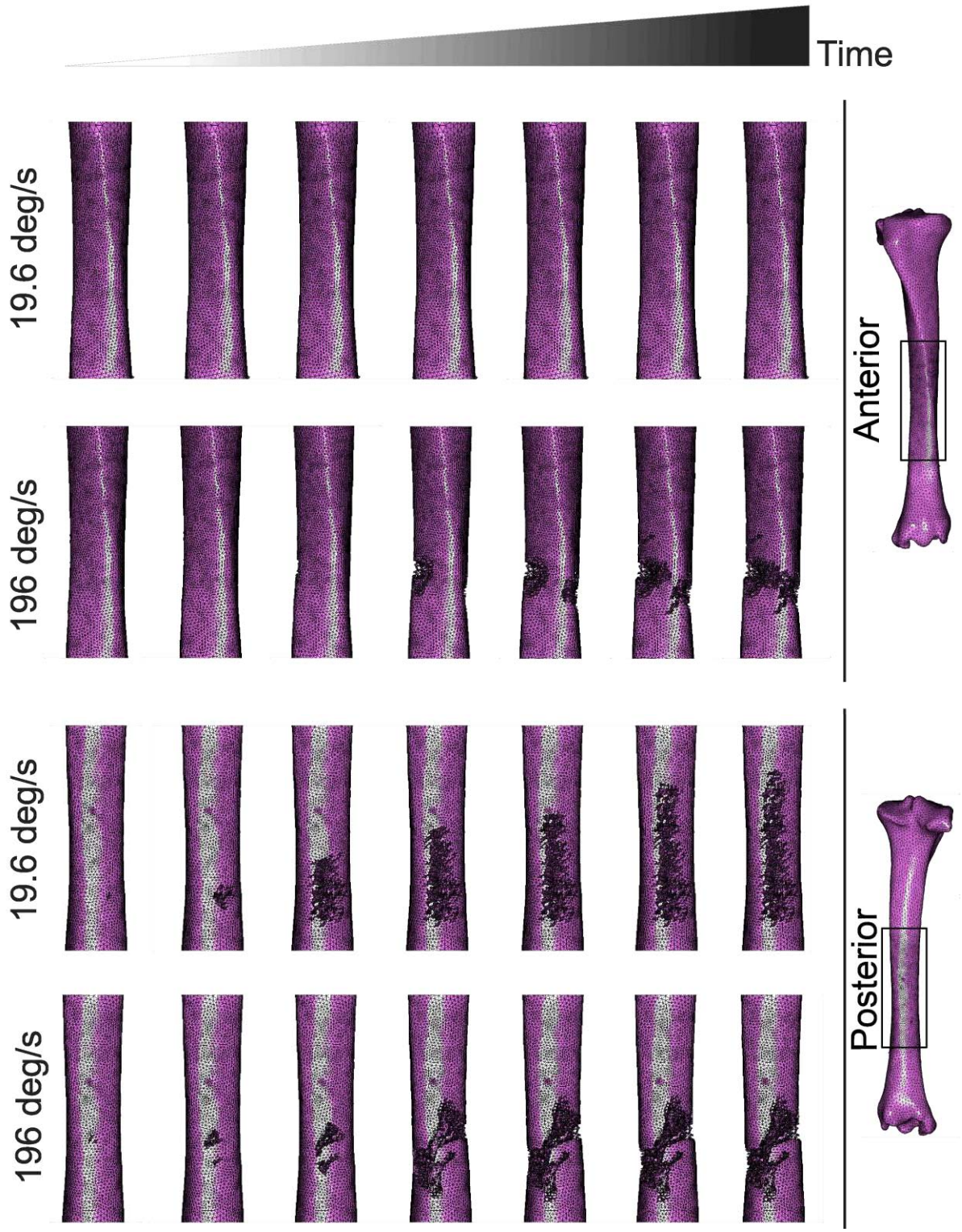

Figure 6.26: The predicted fracture propagation of two distinct patterns from the same bone is seen in this diagram in the posterior and anterior views. A longitudinal fracture was produced when Bone 5 was subjected to a torsional loading of 19.6°/s (TS5). However, a spiral fracture resulted when the testing speed was increased 10 times (TF5).

6.4 Discussion

This study covered the semi-automated development and validation of FE models for immature bone to replicate bone fractures observed in four-point bending and torsion, by the simulation of the process of the crack propagation. Although one study has conducted computer simulation of spiral fractures previously, their model has not been validated against experimental results (Sakai et al., 2010). Moreover, their study was conducted on adult bones and not immature bones. Other studies that replicated the fractures produced in experimental testing exist, but validation was only conducted for one set of loading conditions (Bessho et al., 2007; Hambli et al., 2011; Ota et al., 1999). However, through the use of maximum principal strain as the failure criteria and with damage constrained to the neighbouring elements of the crack in both four-point bending and torsion, fracture patterns that corresponded to experimental results have been produced in the FE simulations. Therefore, this study represents the first attempt to validate fracture models under multiple loading conditions.

In torsional loading, spiral fractures were produced in FE simulations at strain rates of 0.006-0.010 s^{-1} and 0.06-0.10 s^{-1}. Secondary longitudinal fractures were also produced in some bones at both strain rates, and there was one case at low strain rate where longitudinal fracture occurred in the absence of a spiral fracture. In four-point bending, transverse fractures were produced at strain rates of 0.008-0.015s^{-1} and 0.08-0.15s^{-1}, but oblique and comminuted fractures were only observed when bones were loaded at the higher strain rate of 0.08-0.15s^{-1}. These fracture patterns corresponded almost exactly to the experimental results.

6.4.1 Torsional loading

The comparison between the experimental and FE maximum principal strain showed a high degree of correlation for the 2 fast cases (R^2 = 0.99), indicating that the choice of the principal strain as a failure criteria is appropriate. Wilcoxon signed ranked test conducted on the mechanical behaviour of the 5 bones at the two loading rates revealed that there was a significant increase in torsional stiffness in the computational model from 1.067 ± 0.677 Nm/deg to 1.074 ± 0.680 Nm/deg when the strain rate was increased from 0.006-0.010 s^{-1} to 0.06-0.10 s^{-1} (p = 0.0295). The torsional stiffness of ovine tibiae at the two strain rates were also very similar in experimental testing, although the results were not significant. Similar to the case of maximum

principal strain, the torsional stiffness of the bone in the FE model when loaded at the higher strain rate corresponded better to the experimental results than when loaded at the lower strain rate. The slope of 1.29 that deviates significantly from zero, and an intercept of -71.4 in the regression curve of the maximum principal strain, together with the huge difference in the FE-calculated and experimentally-derived torsional stiffness, suggests that it is insufficient to model bone as an isotropic material as the effect of anisotropy might have dominated through axial loading, or that shear relaxation needs to be implemented in the constitutive equation for the material assignments. Other possible reasons include Tet4 elements are not suited for use in FE simulations in torsion or that the boundary conditions have not been captured fully, Furthermore, the FE-calculated curve behaved linearly up to the point of failure, whereas the experimentally-derived curve at lower speed has three sections, including a toe region. In addition, bone failure occurred much earlier in FE simulations than in experiments. Therefore, the disparity could either be due to the model being over-constrained for the case of lower loading rate, or to the lack of an optimization of material properties.

Simulation of the whole bone in torsional testing has been conducted previously and all involved the selection of two nodes where point loads are applied so that a torque may be generated, with the surface fully constrained on the other end of the bone (Gray et al., 2008; Sakai et al., 2010; Spruijt et al., 2006). The models in this study differed from the above-mentioned studies as angular displacements were applied in order to replicate the conditions of the bones being under angular control in the Instron testing machine. In contrast, the tibiae were tested under torque control in the study conducted by Gray et al. (2008), and a series of points and load combinations had to be applied in their FE simulation to find the torque that matched the value that was applied during their experiments.

Although experimental validation of FE models has also been conducted in torsional loading under angular control by Spruijt et al. (2006) and Varghese and co-workers (2011), their FE models also utilized the application of two point loads. This cannot be considered to be a replication of the experimental boundary conditions as a force magnitude in simulations while an angle was applied in experimental testing. However, the methodology employed in this study reproduces the application of an angular displacement through the use of a local coordinate system that is updated with time. This method is also simpler as it eliminates the need to find

the combination of the points and loads that match the torsional load that is applied during experiments.

The spiral fractures obtained in this study agree with the study of Sakai et al. (2010), who simulated the generation of spiral fracture in the humerus caused by the motion of throwing. Despite using the same FE solver, the method employed in their fracture simulation was very different. Firstly, the authors applied forces to two nodes to generate a torque, and these forces were increased gradually until the elements failed. Von Mises stress was set as the failure criterion and the elements that reached the threshold were deleted from the model. This process was then repeated until a complete fracture line was obtained. Therefore, it is probable that different magnitude of torque was used for each increment, but these data are not available to compare against existing load-time or torque-time curves in the literature. Indeed, fracture mechanics would predict a lower force to drive the crack propagation than to initiate it. The aims of the authors were simply to reproduce fracture of the humerus, but their method of fracture simulation would not be suitable to build a validated fracture model.

6.4.2 Four-point bending

In contrast to the plethora of FE models that have been built to simulate torsional loading, only Gray and colleagues (2008) have developed a FE model of a whole bone in four-point loading. Validated FE models of whole bones in three-point bending have also been developed (Varghese et al., 2011), but no fracture model is available in bending, unlike the one available case for torsion (Sakai et al., 2010).

The curves obtained in experimental testing and FE simulations were highly linear at all the strain rates tested, and a very high degree of correlation between the FE strain and experimental strain was obtained in four-point bending (R^2= 0.99) and a slope of 1.03. This compares favourably with the results from Gray et al. (2008) even though the latter conducted their studies at a much lower strain rate. Similar to the case of torsional loading, the FE-calculated bending stiffness corresponded better to the curves obtained in experimental testing at the higher strain rate of 0.08-0.15s^{-1}, even though the differences in bending stiffness for the two groups were not statistically significant. Moreover, the intercept value of the regression analysis was more than 50 microstrains from zero, suggesting that the disparity could be caused by the

lack of model fitting, or the lack of anisotropy in the material properties. There was however, a significant decrease in maximum principal strain when the strain rate was increased from 0.008-0.015s^{-1} to 0.08-0.15s^{-1} (p = 0.0295) in four-point bending, which shows that viscoelasticity has been successfully implemented in the models.

The loading conditions applied in this study differ slightly from the work of Gray et al. (2008) due to the differences in the type of load that was applied in experimental testing. In their work, four-point bending was conducted via the application of a load, whereas in this study, displacement-control was used instead. However, the simulation of the load through the internal rollers was achieved via the application of a displacement. The magnitude was chosen so that the reaction force matched the load that was applied in the experiments. In contrast to the use of three nodes at each external rollers for the application of boundary conditions in this study, more nodes were used in their models. Furthermore, a clamp was used to prevent the tibiae from rotating and that was simulated in their models as well. Therefore, the models developed in this chapter are less constrained and are more susceptible to differences in simulations and experiments, yet they are more likely to simulate the boundary conditions in cases on non-accidental injury. However, the consistent oblique and transverse fracture patterns that were produced as seen in Figure 6.13 shows that the chosen boundary conditions were sufficient to replicate the fracture patterns that were obtained in in-vitro loading.

6.4.3 Model Generation

This study also developed a pipeline that generated semi-automated FE models in four-point bending and torsion in their principal directions. The material properties were obtained from μCT images and the relationship that mapped the attenuation coefficient (or greyscale value) to the density and elastic modulus of each element was obtained from literature. Specifically, the elements were assigned inhomogeneous isotropic material properties. Although the modelling of the fracture propagation of bone would be more accurate if inversely isotropic material properties were used (Keyak et al., 1994), such material properties were only available for ovine trabecular but not cortical bone (Nafei et al., 2000). Moreover, anisotropy is present mostly at the ends of the bones, mainly near the tibial plateau and malleolus, and around the

region of the epiphyseal plates. However, since loading was conducted within the diaphysis of the bone, the assumption of isotropy is sufficient in this study.

The structural behaviour of bones in FE simulations have been found to correlate better to experimental results when a direct density mapping method is used in place of a bi-phasic material (Taddei et al., 2006). Moreover, since bone marrow which fills the core of the bone contributes minimally to the strength of bone, the bone may be considered to be effectively hollow and the use of a solid core would not accurately capture the geometrical structure of bone. Therefore the computer models were built with a hollow core as the focus of this study was to simulate fracture in the diaphysis. Most existing fracture model for human bone focuses on the proximal femur, which is modelled as a solid structure (Bessho et al., 2007; Hambli et al., 2013). It is not clear if the models in Gray et al. (2008) were modelled as a hollow cylinder in the midshaft, although earlier works from one of the authors have done so (Taddei et al., 2006). No information on this aspect of modelling is available in other works (Sakai et al., 2010; Varghese et al., 2011). Therefore, this may be the first time that fracture propagation is simulated by modelling the diaphysis as a hollow shaft.

There are very few studies in the literature that have implemented a fracture model and validated them against experimental results. Ota and co-workers (1999) were one of the first to build a three-dimensional model to investigate fracture propagation and compared the simulations against experimental results. Through the use of a maximum principal stress criterion, the two sets of results matched, but only one bone was tested in their work. Bessho et al. (2007) used a Drucker-Prager failure criteria to predict the failure strength and location of five bones in stance-phase loading, and while good accuracy for their models were reported, results of the fracture sites was only presented for one case. Fracture propagation in stance-phase loading was also conducted by Hambli and colleagues (2011), and through the use of a strain-based continuum damage mechanics approach instead. Two simulated fracture patterns were compared qualitatively against fracture sites in radiographs but the model used was in two-dimension. This is limited as a two-dimensional model is scarcely able to capture the complex loading conditions experienced in reality, making it difficult for their model to be extended to other loading conditions. A three-dimensional model was presented in their later work but a traditional validation was not carried out as the authors built the three-dimensional model from

a bone that was not tested experimentally (Hambli et al., 2013). Nevertheless, in all the cases stated above, the failure criterion used was only tested against one set of loading conditions. In contrast, the models developed in this work were tested in two different loading conditions of bending and torsion and it was found that the use of a maximum principal strain criterion was effective in modelling the entire process of fracture propagation, in spite of the fact that no model fitting was employed throughout this study.

6.4.4 Limitations

The FE models predicted the fracture pattern at two different strain rates fairly well but they underestimated the absolute values of force, displacement, torque and angle in both four-point bending and torsional loading simulations (Figure 6.11; Figure 6.20). This is the result of the use of a constant failure strain values for all elements, a lack of calibration data available for sheep bones, and the elastic modulus were mapped from existing equations using suggested values for some parameters. However, there is no clinical need for obtaining the density-elasticity relationship of ovine bones in great accuracy and the main aim of this chapter is to replicate the fracture patterns obtained in the in-vitro testing of lamb bones. Nevertheless, the models could be made more accurate if further calibration work between μCT data, elastic modulus, and failure strain were carried out.

Secondly, FE simulations predicted a higher bending stiffness and torsional stiffness of the bones than experimental results revealed. This problem is accentuated at low strain rate than high strain. This suggests that either the viscoelasticity parameters need to be fine-tuned or that the FE model is over-constrained. The viscoelastic parameters were obtained from literature and they may be different for each breed of sheep. In terms of boundary conditions, the number of nodes with boundary conditions assigned is fewer in this study, compared to the models employed in other studies (see Gray et al. (2008) as an example). Furthermore, reducing the number of nodes with boundary conditions caused convergence issues that caused the simulations to be terminated prematurely, and the initial selection of nodes to assign boundary conditions was done automatically. The FE models also did not model the presence of the periosteum, but they have been reported to exhibit high level of viscoelasticity (Uchiyama et al., 1998). Furthermore, the periosteum is often seen to hold the bone in place, preventing a

complete fracture from occurring (Figure 6.13), and it would be vital to model the periosteum in future work.

Finally, a truly predictive fracture model should be able to model the morphology in other loading conditions, including combined loading. Only 3 models each in four-point bending and torsion have been validated and the fracture locations are currently limited to the diaphysis. The modelling of the proximal and distal ends of the bones have also been reported to be very challenging due to the presence of only a thin cortical layer (Gray et al., 2008). Fractures of the growth plates have also not been investigated and thus this model is currently limited to predicting fractures in four-point bending and torsion.

6.5 Summary

A semi-automated method has been developed to build FE models from μCT scans of immature ovine tibiae to simulate the conditions of four-point bending and torsion, using a subject-specific alignment system developed in Chapter 4, to investigate if the models were able to replicate the fracture patterns obtained in experimental testing as discussed in Chapter 5. The models were tested at strain rates of 0.006-0.015s^{-1} and 0.06-0.15s^{-1} and different fracture patterns were obtained. In four-point bending, transverse and oblique fractures were obtained, and while the transverse fractures were located in the middle of the diaphysis, the oblique fractures were produced nearer the rollers. In torsion, spiral fractures were produced at both strain rates, but longitudinal fractures sometimes accompanied spiral fractures as well. In one case, longitudinal fracture occurred in the absence of spiral fractures.

No model fitting was employed throughout the study and the material properties used in this study were mapped from the μCT images using relationships available in literature. In spite of this, the use of a maximum principal strain failure criteria successfully captured the fracture patterns that were observed in experimental testing in both bending and torsion. Since an automated meshing technique was used, and no matching of material properties in the FE model was employed, this methodology is general enough to be applied to the fracture analysis of other long bones.

The in-vitro replication of fractures in four-point bending and torsion is a crucial step in the development of an objective tool to differentiate injuries caused by different loading rates. The successful generation of different morphologies show that is possible to verify the case history given of a child with a suspicious injury by conducting simulations and comparing the results with the fracture patterns that is revealed in radiological images. This model thus has potential to be developed further so that it may one day be suitable for use in a clinical setting in the detection of non-accidental injuries (NAI).

7 Conclusions and Future Work

7.1 Conclusions

The overall aim of this thesis was to develop a tool that could objectively evaluate injuries and differentiate between the causation of various types of bone fractures. The application of this tool, in injury assessment within the paediatric population, can serve as an identifier for child abuse cases. This work draws together techniques from different fields in engineering and medicine, including system design, in-vitro biomechanical testing, finite element modelling, dynamic mechanical analysis, and epidemiology.

A detailed literature conducted on the incidence rate and the epidemiology of long bone fractures revealed that long bone fractures make up 31-76% of all non-accidental injury (NAI) cases (Caffey, 1946; King et al., 1988; Loder et al., 2006; Worlock et al., 1986). The presentation of a single diaphyseal fracture poses a great diagnostic challenge for physicians, as these do not point specifically to abuse (Carty, 1993), yet they are one of the most common orthopaedic occurrences in infants and young children (Caffey, 1946). The current method used for the detection of NAI does not permit the clear differentiation between fractures sustained from child abuse and those caused by mere injuries through radiological features. Therefore, an

objective tool that validates the case history provided by the care-giver against images of the fracture bone was proposed.

The first approach was to conduct research on the mechanisms that result in each fracture morphology. However, it is difficult to obtain paediatric *ex-vivo* specimens in the United Kingdom and thus a suitable animal surrogate had to be selected. Detailed literature review showed that sheep were suitable animal models, as the focus of this study was on the structural failure of bones and ovine bones have the most similar osteology to humans when compared to other animals. 5-month old ovine femurs and tibiae were thus collected since they are comparable to the bones of a 5-year old child (Nafei et al., 2000), a vulnerable group as they are unable to coherently describe what has happened (Leventhal, 1999).

A key step in the elucidation of the failure mechanisms in common fracture morphologies is the consistent generation of bone fractures in a state of pure loading, such as pure bending and torsion. Micro CT images of 11 ovine tibiae were used to reconstruct their surface models, which could be used in the analysis. A novel methodology was developed to align bones to their principal axes through their surface models, since under the assumption of beam theory, solid mechanics describes these orientations as states where no shear stress would be present. Therefore, in this alignment, the fracture initiation that resulted solely from normal stresses or shear stresses can be studied when the bone is loading in four-point bending or torsion, respectively.

The effect of using this proposed methodology was compared against the implementation of an anatomical coordinate system. The results from the second moment of area across the bone showed that the cross-section of the specimen is more regular when the new methodology is used. Although the anatomical reference frame is normally specified in the literature in the alignment of the bone prior to any biomechanical testing, the results here showed that the use of the novel alignment method presented in the thesis is superior for the use in four-point bending and torsion, as the presence of eccentric loading is minimised.

Four-point bending tests were conducted for the first time on immature bone, to characterise their structural behaviour at three different strain rates of 0.1-0.4s^{-1} and 0.08-0.1s^{-1} and 0.003-0.004s^{-1}, using the subject-specific alignment system described above. Custom-designed rigs

were manufactured for the purpose of this experiment and a low-cost platform was built to synchronise the data acquisition from the strain gauges and the Instron testing machine. The experiments also successfully reproduced only transverse fractures at low strain rates, and a mixture of oblique and transverse fracture patterns at higher strain rates. Similarly, torsional testing was conducted with the same aim but at two loading rates that resulted in strain rates of 0.006-0.02s^{-1} and 0.07-0.2s^{-1}. Spiral fractures were reproduced at all strain rates, although higher degree of comminution was seen in fractures at higher strain rates. This demonstrates, for the first time, the possibility of distinguishing the loading rate of the injury based on the fracture pattern that is produced. In particular, the presence of oblique and comminuted fractures suggests that any trivial trauma given as explanation for the cause of injury is suspicious of abuse as these fractures were generated only at higher strain rates.

Finite element models were generated from the outputs of the surface models, in their subject-specific alignment system, to replicate the bone fractures that were obtained in in-vitro testing at different strain rates. The material properties were mapped from μCT images using density-elasticity relationships and the effect of viscoelasticity was implemented by calculating the Prony series from the results of dynamic mechanical tests found in literature. Detailed literature review showed that the use of a maximum principal strain as a failure criterion enabled the prediction of the fracture location and of the load, and was thus implemented using the strain rosette readings obtained in the experimental testing. The FE models successfully generated fracture morphologies matching those obtained in experimental testing at different strain rates, despite the fact that no model fitting was carried out. Previously no FE model had successfully captured the fracture propagation process at more than one strain rate, and at more than one loading condition, and this work illustrates that an objective computational model can indeed be implemented using the case history provided by care-givers, to validate it using the fracture patterns that are revealed in radiological images.

In summary, the novel features of this thesis include the following:

vii. the first study to develop an algorithm to align bones to their principal directions, by using the surface models of bones obtained from μCT images,

viii. the comparison of the effect of the cross-sectional geometry of bones between the use of the proposed subject-specific alignment system and an anatomical coordinate system,

ix. the successful reproduction of fracture patterns in immature bone consistently at different strain rates, in four-point bending and torsion, and the characterisation of their structural behaviour prior to fracture, and

x. the development of an FE model that replicates the fracture patterns produced in experimental testing at two loading conditions and at two strain rates each.

7.2 Limitations

One of the biggest limitations of this work is that an animal model had to be used to study immature bone fracture in place of human paediatric bones due to the difficulty of obtaining specimens. Therefore, the results obtained in this thesis are not directly translatable to human bones and inferences on how paediatric bone breaks may only be made based on the assumption that microscopic bone structure is adequately similar. However, as seen in the results in Chapter 5, the bending stiffness and torsional stiffness of the tested lamb tibiae loaded at a strain rate of 0.003-0.2s^{-1} were very close to that of the adult human tibiae loaded at a constant velocity that is 100 times slower. This suggests that immature ovine bone might be much stronger than human paediatric bone due to the presence of plexiform bone or that the month-to-year correlation for sheep-to-human (Nafei et al., 2000) may not be applicable for the structural testing of bones. The breed of sheep used in the testing might also have an impact on the results and it has been shown previously in Chapter 5 that the torsional stiffness and bending stiffness of British Texel lambs that were used in this study are larger than the values obtained for Merino Wethers.

This study is also limited in experimental testing due to the small number of bones that were tested, only at three different strain rates in four-point bending (two strain rates in torsion), and only in ovine tibiae. The strain rates were chosen so that they fall within the 0.2s timescale of physiological and para-physiological loading (Bergmann et al., 2004), and estimated from the loading rates of common case histories, due to unavailability of a detailed case history and taped recording. The bones were also tested in two idealised conditions of pure bending and torsion

but the actual force application is likely to cause eccentric loading resulting in complex loading scenarios. The full failure mechanisms have also not been fully elucidated as testing in other loading conditions such as axial loading in tension and compression need to be conducted.

The mechanical setup built for the purpose of this thesis is also not suitable for testing at higher strain rate, without further significant modifications. The computer that was used to drive the Instron controller is a Pentium 4 computer and it causes the Instron testing machine to stop for a period of time whenever it cannot process information in time, or if it has too much data to handle. The high-speed camera that was used to capture the fracture process was thus not recorded on the same computer. The current platform relies on the internal clock of the LABView nano-second engine of the computer as a common time base and a feedback signal of the Instron controller as a trigger. While this method is adequate for the testing rates used in this thesis, a more accurate external timing source would be required for testing at a high strain rate to synchronize the acquisition of all data, including that of the high-speed camera.

For FE modelling, the relationships that were used to obtain the elastic density and viscoelastic properties were obtained from literature. No model fitting was conducted and thus all modifiable parameters in the equations were obtained directly from literature, but using the attenuation coefficient from μCT images as a starting point. Therefore, as the results in Chapter 6 show, the FE models calculated a much smaller failure strength than experimental results in both bending and torsion. As such, the current models cannot be used to predict failure strength and strain as it has not accurately captured the structural behaviour of the bones. However, the stiffness calculations were highly accurate.

The maximum principal strain was implemented as the failure criteria but the failure strain used is not a function of the elastic density of the element at present, which could have given a better prediction of the failure strength and strain. The might explain why the model is not able to predict the actual failure site very accurately, even though the fracture patterns are similar and located in the same region of the bone as that in experimental testing. Moreover, the choice of failure criterion has also not been tested against other possible methods, and the fracture pattern that was generated does not have a high resolution, making the identification of the fracture morphology rather difficult at times.

The FE model is currently set up to conduct static analysis. As discussed in Chapter 6, any loading that occurs in less than 0.001s would need to be carried out via dynamic analysis. The density of the bone and the bone marrow would need to be factored in, but it was not done so in this thesis. The presence of the trabecular bone has also not been modelled, since the focus of this thesis is on fractures in the diaphysis. Therefore, attention has not been paid to capturing the geometry of the tibial plateau and of the malleolus as precisely as of the diaphysis. The response of the current model at those locations is not likely to be accurate: as has been stated elsewhere, the presence of the thin cortical shell there makes it a challenge in the modelling process. Finally, it has been shown that the periosteum holds the bone together in place even after the occurrence of bone fracture in some cases (Ogden, 2000) but the lack of data on its material properties means that they have not been modelled in this study.

7.3 Future Work

For experimental testing, the experimental setup would need to be improved to allow for better synchronization across all strain rates without the system crashing. The computer that is used to drive the Instron controller needs to be updated, which has the further advantage of allowing for more strain readings to be acquired, and for the recordings from the high-speed camera to be synchronized directly with the force and strain reading. An external timing source would also need to be purchased to act as the common clock to start the Instron testing machine and the strain gauge amplifier and to synchronize the acquisition of data. The LabVIEW program would thus need to be modified to include the sample clock.

The current setup utilized strain gauges to obtain strain measurements. However, these devices require a planar surface for the measurement data to be valid, and they acquire data only at a localised point. A richer understanding of the response of bone prior to fracture can be obtained using digital imaging correlation (DIC). By spray-painting the bone before the experiment is conducted, a surface strain map can be obtained, which when used with the high-speed camera can reveal the region of the highest strain. This is particularly needed in experiments involving combined loading to understand the failure process, which may be more complex. Moreover, it would serve as a validation for whether the FE models have captured the boundary conditions

or not. Thus the use of DIC may also help to identify the presence of strain concentration that may have arisen due to misalignment, causing premature failing of bones.

Thereafter, axial testing in both tension and compression can be carried out to obtain the structural response of immature bone, using the new mechanical setup described above. Focus should also be placed on the material characterisation of ovine cortical bone, so that the FE model will show greater fidelity. The first step is to machine cortical bone samples in three orthogonal directions to be used in four-point bending, torsion, tensile, compression, and dynamic mechanical tests, before subjecting them to a CT or μCT scan. The coefficient attenuation obtained would then be used to obtain the parameters that are needed for the relationships between the greyscale values density and elastic modulus in six directions, so that bone may be modelled using transversely isotropic material properties in the FE models. The results of modal analysis could then be used to define the Prony series, and also to validate the material mapping equations used. Finally the machined-specimens would be tested to failure with the use of DIC to obtain the elastic and shear modulus in the static state. The strain at failure would also be used to improve the failure criteria so that is a function of the density.

To obtain more accurately the para-physiological strain rates at which direct experimental testing on bones should be conducted, testing of lamb legs needs to be conducted based on common case histories. For three-point bending tests, a small cut would be made on the side of the bone opposite the impactor so that strain gauges can be attached directly to the bone. The strain rate generated would then be used to calculate the loading speed required in direct bone testing. Whole leg testing would also give information on the damping coefficient of the muscles, based on its volume, which can then be used to scale the loads that should be applied to the FE models based on the size of the legs.

To extend the FE models to predict bone fracture in the meta- and epiphysis, work needs to be done to capture the response at the tibial plateau and the malleolus accurately, as a forensic tool that is truly applicable in a clinical setting would need to be able to reproduce fracture patterns in all parts of the bones. Shell elements would thus be added to the inner surface of the bone at these areas to model the presence of the trabecular bone, using material properties obtained

from experimental testing. This new model would then be validated for its structural response in four-point bending, torsion and axial loading across a range of strain rates.

To improve the ability of the FE models to capture the fracture propagation, the performance of the maximum principal strain failure criterion first needs to be compared against maximum principal stress, Drucker-Prager and continuum damage mechanics criteria in all the loading conditions across strain rates. At this stage, it may be necessary to develop a new failure criterion for immature bone if the results proved unsatisfactory. The standard Newton-Raphson method technique that is used in FE modelling does not allow for a reduction in load to be applied to the element that has yielded, and hence they are deleted soon after failure has occurred. There are two methods that may be used to distinguish between elements that have yielded but not failed completely. The first is through the use of user-subroutines to modify the load that is applied to the element based on a user-defined criteria, such as its damage level. The second approach is to implement advanced Crisfield incremental loading in the model. This method is available in some FE packages and is currently used in buckling analyses. The difference with the first approach is that the reduction in load applied to the elements is affected through a change in geometry of the elements, which has the further advantage of capturing the physical response of the bone more accurately in compression and buckling.

The proposed framework also needs to be improved to make the implementation of an objective tool to detect NAI a reality. Figure 7.1 reproduces the proposed framework from Chapter 2 but shows the steps that have been addressed in this thesis. The use of an imaging modality has been used to obtain material properties and build up an FE model, and the FE-calculated fracture pattern was validated against experimental results. However, a confidence indicator that quantitatively compares the fracture patterns generated by the FE models to the radiographs has yet to be developed. Moreover, a system that translates the case histories given by care-givers into a set of loading conditions that can be applied in the FE models need to be developed. A taped recording could be fed into the system to transcribe the story given and to find the appropriate set of boundary conditions from a database. The system might also have machine-learning algorithm implemented to improve its performance. The database of case histories and the associated forces generated would need to be built up from case-based biomechanical investigations involving anthropomorphic test devices. In particular, falls from a

height is a commonly given case history and rigorous research would need to be conducted to ascertain how the effect of height affects the fracture pattern that is generated. In addition, the current regulations in the UK do not generally permit CT scans to be conducted on children out of medical concerns. MRI scans are also not carried out unless there are special concerns. Therefore, statistical shape models of paediatric bones at different age would need to be developed based on the inputs of radiographic images to generate the appropriate three-dimensional models to be used in FE analysis.

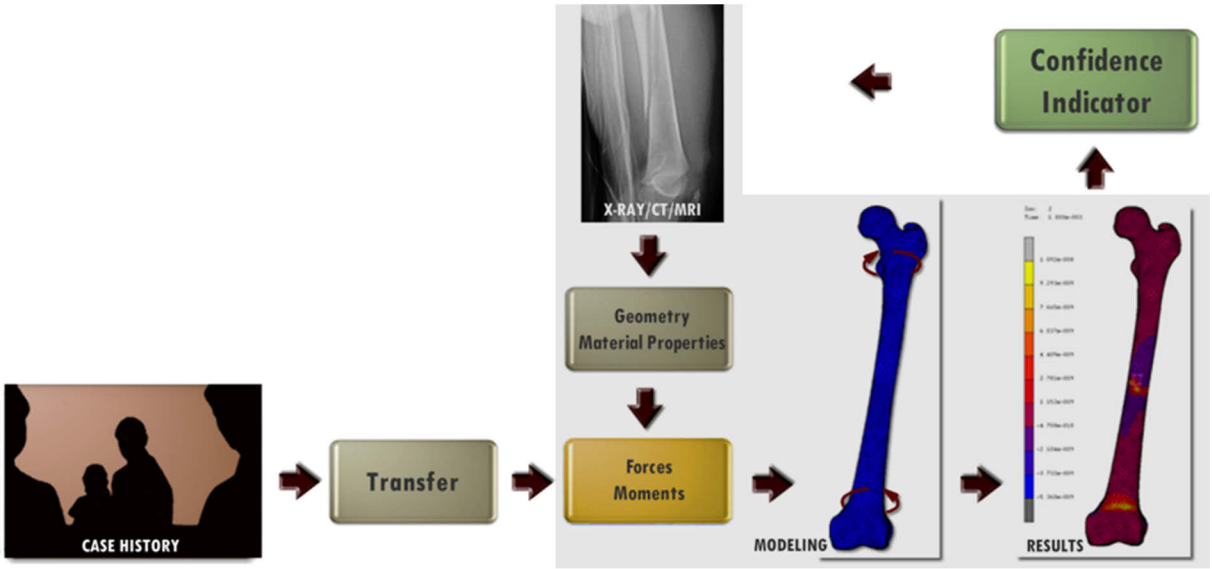

Figure 7.1: The aspects of the proposed framework from Chapter 2 that has been studied in this work. The regions in grey show the focus of this thesis while the regions that have not been highlighted need to be developed in further work.

Finally, FE modelling represents only one method that may be used in forensic analysis, but it has several advantages over manual biodynamic calculations, multi-body modelling, and case-based investigations using anthropometric test devices. These methods are currently used to determine the force, velocity, and acceleration of the body segment and the risk of injuries (Pierce & Bertocci, 2008), but they are unable to model the process of fracture propagation. Therefore, these methods are unable to produce a result that allows for a direction comparison with the fractures in radiographic images. However, the work of this thesis has widespread impact as it is not restricted to paediatric specimens but may also be extended to wider forensic use in the adult population, especially in the reconstruction of the incident scene.

8 References

Adams, B., & Crabtree, P. (2011). Comparative osteology: a laboratory and field guide of common North American animals: Academic Press.

Akbarnia, B., Torg, J. S., Kirkpatrick, J., & Sussman, S. (1974). Manifestations of the Battered-Child Syndrome. *Journal of bone and joint surgery. American volume (Am), 56-A*(6), 1159-1166.

Allen, M. J., Houlton, J. E., Adams, S. B., & Rushton, N. (1998). The surgical anatomy of the stifle joint in sheep. *Veterinary Surgery, 27*(6), 596-605.

Arun, K. S., Huang, T. S., & Blostein, S. D. (1987). Least-squares fitting of two 3-D point sets. *Pattern Analysis and Machine Intelligence, IEEE Transactions on*(5), 698-700.

Athanasiou, K., Zhu, C.-F., Lanctot, D., Agrawal, C., & Wang, X. (2000). Fundamentals of biomechanics in tissue engineering of bone. *Tissue engineering, 6*(4), 361-381.

Augat, P., Reeb, H., & Claes, L. (1996). Prediction of fracture load at different skeletal sites by geometric properties of the cortical shell. *Journal of Bone and Mineral Research, 11*(9), 1356-1363.

Baumer, T. G., Powell, B. J., Fenton, T. W., & Haut, R. C. (2009). Age Dependent Mechanical Properties of the Infant Porcine Parietal Bone and a Correlation to the Human. *Journal of Biomechanical Engineering, 131*(11), 111006.

Bergmann, G., Graichen, F., & Rohlmann, A. (2004). Hip joint contact forces during stumbling. *Langenbeck's Archives of Surgery, 389*(1), 53-59.

Bertollo, N., Bell, D. J., Yu, Y., & Walsh, W. R. (2011). Effects of patellar position and defect healing on in vitro stifle joint kinematics following removal of the central one-third of the patellar tendon in an ovine model. *Journal of Orthopaedic Research, 29*(4), 572-581.

Bessho, M., Ohnishi, I., Matsumoto, T., Ohashi, S., Matsuyama, J., Tobita, K., Kaneko, M., & Nakamura, K. (2009). Prediction of proximal femur strength using a CT-based nonlinear finite element method: Differences in predicted fracture load and site with changing load and boundary conditions. *Bone, 45*(2), 226-231.

Bessho, M., Ohnishi, I., Matsuyama, J., Matsumoto, T., Imai, K., & Nakamura, K. (2007). Prediction of strength and strain of the proximal femur by a CT-based finite element method. *Journal of Biomechanics, 40*(8), 1745-1753.

Caffey, J. (1946). Multiple fractures in the long bones of infants suffering from chronic subdural hematoma. *American Journal of Roentgenology, Radium Therapy, and Nuclear Medicine, 56*(2), 163-173.

Carty, H. M. (1993). Fractures caused by child abuse. *Journal of bone and joint surgery. British volume, 75*(6), 849-857.

Carty, H. M., & Pierce, A. (2002). Non-accidental injury: a retrospective analysis of a large cohort. *European radiology, 12*(12), 2919-2925.

Coffey, C., Haley, K., Hayes, J., & Groner, J. I. (2005). The risk of child abuse in infants and toddlers with lower extremity injuries. *Journal of pediatric surgery, 40*(1), 120-123.

Conti, G., Cristofolini, L., Juszczyk, M., Leardini, A., & Viceconti, M. (2008). Comparison of three standard anatomical reference frames for the tibia–fibula complex. *Journal of Biomechanics, 41*(16), 3384-3389.

Cordey, J., & Gautier, E. (1999). Strain gauges used in the mechanical testing of bones Part II:"In vitro" and "in vivo" technique. *Injury, 30*, SA14-SA20.

Cramer, K. E., & Green, N. E. (2009). Child Abuse. In N. E. Green & M. F. Swiontkowski (Eds.), *Skeletal trauma in children* (4th ed. ed., Vol. 3, pp. 587-605). Philadelphia, Pa. ; London: Saunders.

Cristofolini, L. (1997). A critical analysis of stress shielding evaluation of hip prostheses. *Critical Reviews™ in Biomedical Engineering, 25*(4-5).

Cristofolini, L., Conti, G., Juszczyk, M., Cremonini, S., Sint Jan, S. V., & Viceconti, M. (2010). Structural behaviour and strain distribution of the long bones of the human lower limbs. *Journal of Biomechanics, 43*(5), 826-835.

Cristofolini, L., Juszczyk, M. M., Martelli, S., Taddei, F., & Viceconti, M. (2007). In vitro replication of spontaneous fractures of the proximal human femur. *Journal of Biomechanics, 40*(13), 2837-2845.

Cristofolini, L., & Viceconti, M. (2000). Mechanical validation of whole bone composite tibia models. *Journal of Biomechanics, 33*, 279-288.

Cristofolini, L., Viceconti, M., Cappello, A., & Toni, A. (1996). Mechanical validation of whole bone composite femur models. *Journal of Biomechanics, 29*(4), 525-535.

Currey, J. (1990). Physical characteristics affecting the tensile failure properties of compact bone. *Journal of Biomechanics, 23*(8), 837-844.

Currey, J., & Butler, G. (1975). The mechanical properties of bone tissue in children. *The Journal of Bone & Joint Surgery, 57*(6), 810-814.

Derikx, L. C., Vis, R., Meinders, T., Verdonschot, N., & Tanck, E. (2011). Implementation of asymmetric yielding in case-specific finite element models improves the prediction of femoral fractures. *Computer Methods in Biomechanics and Biomedical Engineering, 14*(02), 183-193.

Ebacher, V., Tang, C., McKay, H., Oxland, T. R., Guy, P., & Wang, R. (2007). Strain redistribution and cracking behavior of human bone during bending. *Bone, 40*(5), 1265-1275.

Edwards, W. B., & Troy, K. L. (2012). Finite element prediction of surface strain and fracture strength at the distal radius. *Medical Engineering & Physics, 34*(3), 290-298.

Finlay, J., Hurtig, M., Hardie, W., Liggins, A., & Batte, S. (1995). Geometrical properties of the ovine tibia: a suitable animal model to study the pin-bone interface in fracture fixation? *Proceedings of the Institution of Mechanical Engineers, Part H: Journal of Engineering in Medicine, 209*(1), 37-50.

Forman, J. L., de Dios, E., Symeonidis, I., Duart, J., Kerrigan, J. R., Salzar, R. S., Balasubramanian, S., Segui-Gomez, M., & Kent, R. W. (2012). *Fracture tolerance related to skeletal development and aging throughout life: 3-point bending of human femurs.* Paper presented at the IRCOBI Conference Proceedings, Dublin, Ireland.

Gaudiosi, J. A., US Department of Health and Human Services, & Administration on Children, Y. a. F. (2006). Child Maltreatment 2004. Washington, DC: U.S. Government Printing Office.

Goel, V., Drinker, H., Panjabi, M., & Strongwater, A. (1982). Selection of an animal model for implant fixation studies: anatomical aspects. *The Yale journal of biology and medicine, 55*(2), 113.

Gong, J., Arnold, J., & Cohn, S. (1964). Composition of trabecular and cortical bone. *The Anatomical Record, 149*(3), 325-331.

Gray, H. A., Taddei, F., Zavatsky, A. B., Cristofolini, L., & Gill, H. S. (2008). Experimental validation of a finite element model of a human cadaveric tibia. *J Biomech Eng, 130*(3), 031016.

Green, N. E., & Swiontkowski, M. F. (2009). *Skeletal trauma in children* (4th ed. ed.). Philadelphia, Pa. ; London: Saunders.

Hambli, R., Bettamer, A., & Allaoui, S. (2011). Finite element prediction of proximal femur fracture pattern based on orthotropic behaviour law coupled to quasi-brittle damage. *Medical Engineering & Physics*.

Hambli, R., Lespessailles, E., & Benhamou, C.-L. (2013). Integrated remodeling-to-fracture finite element model of human proximal femur behavior. *Journal of the mechanical behavior of biomedical materials, 17*, 89-106.

Haney, S. B., Boos, S. C., Kutz, T. J., & Starling, S. P. (2009). Transverse fracture of the distal femoral metadiaphysis: a plausible accidental mechanism. *Pediatric Emergency Care, 25*(12), 841-844.

Hansen, U., Zioupos, P., Simpson, R., Currey, J. D., & Hynd, D. (2008). The effect of strain rate on the mechanical properties of human cortical bone. *Journal of Biomechanical Engineering, 130*(1), 011011.

Hardy, S., & Pipelzadeh, M. (1991). Static analysis of short beams. *The Journal of Strain Analysis for Engineering Design, 26*(1), 15-29.

Harewood, F., & McHugh, P. (2007). Comparison of the implicit and explicit finite element methods using crystal plasticity. *Computational Materials Science, 39*(2), 481-494.

Heiner, A. D. (2008). Structural properties of fourth-generation composite femurs and tibias. *Journal of Biomechanics, 41*(15), 3282-3284.

Heiner, A. D., & Brown, T. D. (2001). Structural properties of a new design of composite replicate femurs and tibias. *Journal of Biomechanics, 34*(6), 773-781.

Hibbeler, R. C., & Fan, S. (2004). *Statics and mechanics of materials*: Prentice Hall Singapore.

Hirsch, C., & Evans, F. G. (1965). Studies on some physical properties of infant compact bone. *Acta orthopaedica, 35*(1-4), 300-313.

Hoskote, A. U., Martin, K., Hormbrey, P., & Burns, E. C. (2003). Fractures in infants: one in four is non-accidental. *Child Abuse Review, 12*(6), 384-391.

Jayakumar, P., Barry, M., & Ramachandran, M. (2010). Orthopaedic aspects of paediatric non-accidental injury. *Journal of Bone and Joint Surgery (Br), 92-B*(2), 189-195.

Jazar, R. N. (2008). Vehicle dynamics: theory and application: Springer.

Johnson, G. W., & Jennings, R. (2006). *LabVIEW graphical programming* (4th ed.). New York: McGraw-Hill.

Jones, E. T. (2009). Skeletal growth and development as related to trauma. In N. E. Green & M. F. Swiontkowski (Eds.), *Skeletal trauma in children* (4th ed. ed., Vol. 3, pp. 1-16). Philadelphia, Pa. ; London: Saunders.

Juszczyk, M. M., Cristofolini, L., & Viceconti, M. (2011). The human proximal femur behaves linearly elastic up to failure under physiological loading conditions. *Journal of Biomechanics, 44*(12), 2259-2266.

Kemp, A. M., Dunstan, F., Harrison, S., Morris, S., Mann, M., Rolfe, K., Datta, S., Thomas, D. P., Sibert, J. R., & Maguire, S. (2008). Patterns of skeletal fractures in child abuse: systematic review. *BMJ, 337*, a1518.

Keyak, J. H., & Falkinstein, Y. (2003). Comparison of in situ and in vitro CT scan-based finite element model predictions of proximal femoral fracture load. *Medical Engineering & Physics, 25*(9), 781-787.

Keyak, J. H., Lee, I., & Skinner, H. (1994). Correlations between orthogonal mechanical properties and density of trabecular bone: use of different densitometric measures. *Journal of biomedical materials research, 28*(11), 1329-1336.

Keyak, J. H., & Rossi, S. A. (2000). Prediction of femoral fracture load using finite element models: an examination of stress- and strain- based failure theories. *Journal of Biomechanics, 33*, 209-214.

Keyak, J. H., Rossi, S. A., Jones, K. A., Les, C. M., & Skinner, H. B. (2001). Prediction of fracture location in the proximal femur using finite element models. *Medical Engineering & Physics, 23*(9), 657-664.

Kilborn, S. H., Trudel, G., & Uhthoff, H. (2002). Review of growth plate closure compared with age at sexual maturity and lifespan in laboratory animals. *Journal of the American Association for Laboratory Animal Science, 41*(5), 21-26.

King, J., Diefendorf, D., Apthorp, J., Negrete, V. F., & Carlson, M. (1988). Analysis of 429 Fractures in 189 Battered Children. *Journal of Pediatric Orthopaedics, 8*(5), 585-589.

Kowal-Vern, A., Paxton, T. P., Ros, S. P., Lietz, H., Fitzgerald, M., & Gamelli, R. L. (1992). Fractures in the Under 3-Year-Old Age Cohort. *Clinical Pediatrics, 31*, 653-659.

Kraft, J. K. (2011). (iv) Imaging of non-accidental injury. *Orthopaedics and Trauma, 25*(2), 109-118.

Kregor, P. J., Senft, D., Parvin, D., Campbell, C., Toomey, S., Parker, C., Gillespy, T., & Swiontkowski, M. F. (1995). Cortical bone perfusion in plated fracutured sheep tibiae. *Journal of Orthopaedic Research, 13*(5), 715-724.

Kress, T. A., Porta, D. J., Snider, J. N., Fuller, P. M., Psihogios, J. P., Heck, W. L., Frick, S. J., & Wasserman, J. F. (1995). *Fracture patterns of human cadaver long bones.* Paper presented at the International Research of Crash Biomechanics and Impact (IRCOBI), Brunnen, Switzerland.

Laming, H. (2003). The Victoria Climbie Inquiry: report of an inquiry by Lord Laming.

Lanyon, L., Magee, P., & Baggott, D. (1979). The relationship of functional stress and strain to the processes of bone remodelling. An experimental study on the sheep radius. *Journal of Biomechanics, 12*(8), 593-600.

Lemaitre, J. (1985). A continuous damage mechanics model for ductile fracture. *Journal of Engineering Materials and Technology, 107*(1), 83-89.

Leventhal, J. M. (1999). The challenges of Recognizing Child Abuse: Seeing Is Believing. *Journal of American Medical Association, 281*(7), 657-659.

Levine, R. (2002). Injury to the extremities. In A. Nahum & J. Melvin (Eds.), *Accidental Injury Biomechanics and Prevention* (pp. 491-522). New York: Springer-Verlag.

Liebschner, M. A. K. (2004). Biomechanical considerations of animal models used in tissue engineering of bone. *Biomaterials, 25*(9), 1697-1714.

Loder, R. T., & Bookout, C. (1991). Fractured Patterns in Battered Children. *Journal of Orthopaedic Trauma, 5*(4), 428-433.

Loder, R. T., O'Donnell, P. W., & Feinberg, J. R. (2006). Epidemiology and Mechanisms of Femur Fractures in Children. *Journal of Pediatric Orthopaedics, 26*(5), 561-566.

Martini, L., Fini, M., Giavaresi, G., & Giardino, R. (2001). Sheep model in orthopedic research: a literature review. *Comparative medicine, 51*(4), 292-299.

Mashru, R. P., Herman, M. J., & Pizzutillo, P. D. (2005). Tibial shaft fractures in children and adolescents. *Journal of the American Academy of Orthopaedic Surgeons, 13*(5), 345-352.

Merten, D. F., Radkowski, M. A., & Leonidas, J. C. (1983). The Abused-Child - a Radiological Reappraisal. *Radiology, 146*(2), 377-381.

Moreno, J., & Forriol, F. (2002). Effects of preservation on the mechanical strength and chemical composition of cortical bone: an experimental study in sheep femora. *Biomaterials, 23*(12), 2615-2619.

Mueller, K. H., Trias, A., & Ray, R. D. (1966). Bone density and compostiton. Age-related and pathological changes in water and mineral content. *Journal of bone and joint surgery. American volume, 48*(1), 140-148.

Nafei, A., Danielsen, C., Linde, F., & Hvid, I. (2000). Properties of growing trabecular ovine bone Part I: mechanical and physical properties. *Journal of Bone & Joint Surgery, British Volume, 82*(6), 910-920.

Nalla, R. K., Kinney, J. H., & Ritchie, R. O. (2003). Mechanistic fracture criteria for the failure of human cortical bone. *Nature Materials, 2*(3), 164-168.

Offiah, A., van Rijn, R. R., Perez-Rossello, J. M., & Kleinman, P. K. (2009). Skeletal imaging of child abuse (non-accidental injury). *Pediatric radiology, 39*(5), 461-470.

Ogden, J. A. (2000). *Skeletal injury in the child* (3rd ed. ed.). New York ; London: Springer.

Öhman, C., Baleani, M., Pani, C., Taddei, F., Alberghini, M., Viceconti, M., & Manfrini, M. (2011). Compressive behaviour of child and adult cortical bone. *Bone, 49*(4), 769-776.

Osterhoff, G., Löffler, S., Steinke, H., Feja, C., Josten, C., & Hepp, P. (2011). Comparative anatomical measurements of osseous structures in the ovine and human knee. *The Knee, 18*(2), 98-103.

Ota, T., Yamamoto, I., & Morita, R. (1999). Fracture simulation of the femoral bone using the finite-element method: how a fracture initiates and proceeds. *Journal of bone and mineral metabolism, 17*(2), 108-112.

Ouyang, J., Zhu, Q., Zhao, W., Xu, Y., Chen, W., & Zhong, S. (2003). Biomechanical character of extremity long bones in children. *Chinese Journal of Clinical Anatomy, 21*(6), 620-623.

Pearce, A., Richards, R., Milz, S., Schneider, E., & Pearce, S. (2007). Animal models for implant biomaterial research in bone: a review. *Eur Cell Mater, 13*(1), 1-10.

Perz, R., Toczyski, J., & Subit, D. (2014). Variation in the human ribs geometrical properties and mechanical response based on X-ray computed tomography images resolution. *Journal of the mechanical behavior of biomedical materials*.

Pierce, M. C., & Bertocci, G. E. (2008). Injury biomechanics and child abuse. *Annual Review of Biomedical Engineering, 10*, 85-106.

Pierce, M. C., Bertocci, G. E., Vogeley, E., & Moreland, M. S. (2004). Evaluating long bone fractures in children: a biomechanical approach with illustrative cases. *Child abuse & neglect, 28*(5), 505-524.

Pierce, M. C., Valdevit, A., Anderson, L., Inoue, N., & Hauser, D. L. (2000). Biomechanical Evaluation of Dual-Energy X-Ray Absorptiometry for Predicting Fracture Loads of the Infant Femur for Injury Investigation: An In Vitro Porcine Model. *Journal of Orthopaedic Trauma, 14*(8), 571-576.

Radesky, J. S., & Sugar, N. F. (2009). Femur fracture in an infant. *BMJ, 338*, b1583.

Rajaai, S., Saffar, K. P., & JamilPour, N. (2010). *Mechanical Properties of Long Bone Shaft in Bending.* Paper presented at the XII Mediterranean Conference on Medical and Biological Engineering and Computing 2010.

Reichert, J. C., Saifzadeh, S., Wullschleger, M. E., Epari, D. R., Schütz, M. A., Duda, G. N., Schell, H., van Griensven, M., Redl, H., & Hutmacher, D. W. (2009). The challenge of establishing preclinical models for segmental bone defect research. *Biomaterials, 30*(12), 2149-2163.

Rex, C., & Kay, P. R. (2000). Features of Femoral Fractures in Nonaccidental Injury. *Journal of Pediatric Orthopaedics, 20*(3), 411-413.

Robinson, R. A. (1975). Physicochemical structure of bone. *Clinical orthopaedics and related research, 112*, 263-315.

Ruff, C. B., & Hayes, W. C. (1983). Cross-sectional geometry of Pecos Pueblo femora and tibiae—A biomechanical investigation: I. Method and general patterns of variation. *American Journal of Physical Anthropology, 60*(3), 359-381.

Sakai, K., Kiriyama, Y., Kimura, H., Nakamichi, N., Nakamura, T., Ikegami, H., Matsumoto, H., Toyama, Y., & Nagura, T. (2010). Computer simulation of humeral shaft fracture in throwing. *Journal of Shoulder and Elbow Surgery, 19*(1), 86-90.

Schileo, E., Taddei, F., Cristofolini, L., & Viceconti, M. (2008). Subject-specific finite element models implementing a maximum principal strain criterion are able to estimate failure risk and fracture location on human femurs tested< i> in vitro</i>. *Journal of Biomechanics, 41*(2), 356-367.

Schileo, E., Taddei, F., Malandrino, A., Cristofolini, L., & Viceconti, M. (2007). Subject-specific finite element models can accurately predict strain levels in long bones. *Journal of Biomechanics, 40*(13), 2982-2989.

Schwend, R. M., Werth, C., & Johnston, A. (2000). Femur shaft fractures in toddlers and young children: Rarely from child abuse. *Journal of Pediatric Orthopaedics, 20*(4), 475-481.

Shannak, A. O. (1988). Tibial fractures in children: follow-up study. *Journal of Pediatric Orthopaedics, 8*(3), 306-310.

Simon, U., Augat, P., Ignatius, A., & Claes, L. (2003). Influence of the stiffness of bone defect implants on the mechanical conditions at the interface—a finite element analysis with contact. *Journal of Biomechanics, 36*(8), 1079-1086.

Singleton, R. (2010). The chief adviser on the safety of children, First annual report to the parliament - 2010.

Skellern, C., Wood, D., Murphy, A., & Crawford, M. (2000). Non-accidental fractures in infants: Risk of further abuse. *Journal of Paediatrics and Child Health, 36*(6), 590-592.

Spatz, H.-C., O'Leary, E., & Vincent, J. F. (1996). Young's moduli and shear moduli in cortical bone. *Proceedings of the Royal Society of London. Series B: Biological Sciences, 263*(1368), 287-294.

Spruijt, S., Van Der Linden, J. C., Sander Dijkstra, P., Wiggers, T., Oudkerk, M., Snijders, C. J., Van Keulen, F., Verhaar, J. A., Weinans, H., & Swierstra, B. A. (2006). Prediction of torsional failure in 22 cadaver femora with and without simulated subtrochanteric metastatic defects: a CT scan-based finite element analysis. *Acta orthopaedica, 77*(3), 474-481.

Stotts, A. K. (2007). Orthopaedic aspects of child abuse. *Current Opinion in Orthopaedics, 18*(6), 550-554 510.1097/BCO.1090b1013e3282ef1096ecc.

Strait, R. T., Siegel, R. M., & Shapiro, R. A. (1995). Humeral Fractures without Obvious Etiologies in Children Less-Than 3 Years of Age - When Is It Abuse. *Pediatrics, 96*(4), 667-671.

Taddei, F., Cristofolini, L., Martelli, S., Gill, H. S., & Viceconti, M. (2006). Subject-specific finite element models of long bones: An in vitro evaluation of the overall accuracy. *Journal of Biomechanics, 39*(13), 2457-2467.

Taddei, F., Schileo, E., Helgason, B., Cristofolini, L., & Viceconti, M. (2007). The material mapping strategy influences the accuracy of CT-based finite element models of bones: An evaluation against experimental measurements. *Medical Engineering & Physics, 29*(9), 973-979.

Tapper, J. E., Ronsky, J. L., Powers, M. J., Sutherland, C., Majima, T., Frank, C. B., & Shrive, N. G. (2004). In vivo measurement of the dynamic 3-D kinematics of the ovine stifle joint. *Journal of Biomechanical Engineering, 126*(2), 301-305.

Taylor, D., O'Reilly, P., Vallet, L., & Lee, T. C. (2003). The fatigue strength of compact bone in torsion. *Journal of Biomechanics, 36*(8), 1103-1109.

Taylor, W. R., Ehrig, R. M., Heller, M. O., Schell, H., Seebeck, P., & Duda, G. N. (2006). Tibio-femoral joint contact forces in sheep. *Journal of Biomechanics, 39*(5), 791-798.

Tenenbein, M., Reed, M. H., & Black, G. B. (1990). The toddler's fracture revisited. *The American Journal of Emergency Medicine, 8*(3), 208-211.

Tepic, S., Remiger, A. R., Morikawa, K., Predieri, M., & Perren, S. M. (1997). Strength recovery in fractured sheep tibia treated with a plate or an internal fixator: an experimental study with a two-year follow-up. *Journal of Orthopaedic Trauma, 11*(1), 14-23.

The Royal College of Radiologists and Royal College of Paediatrics and Child Health. (2008). Standard for skeletal surveys in suspected non-accidental injury (NAI) in children. Retrieved 30 August 2014, from https://www.rcr.ac.uk/docs/radiology/pdf/RCPCH_RCR_final.pdf

Thomas, S. A., Rosenfield, N. S., Leventhal, J. M., & Markowitz, R. I. (1991). Long-Bone Fractures in Young Children: Distinguishing Accidental Injuries From Child Abuse. *Pediatrics, 88*, 471-476.

Travis, J., & Kring, J. (2007). LabVIEW for Everyone: Graphical Programming Made Easy and Fun: Prentice Hall.

Turner, C. H., & Burr, D. B. (1993). Basic Biomechanical Measurements of Bone - a Tutorial. *Bone, 14*(4), 595-608.

Uchiyama, E., Yamakoshi, K., & Sasaki, T. (1998). Measurement of mechanical characteristics of tibial periosteum and evaluation of local differences. *Journal of Biomechanical Engineering-Transactions of the Asme, 120*(1), 85-91.

Varghese, B., Short, D., Penmetsa, R., Goswami, T., & Hangartner, T. (2011). Computed-tomography-based finite-element models of long bones can accurately capture strain response to bending and torsion. *Journal of Biomechanics, 44*(7), 1374-1379.

Vinz, H. (1970). Studies on the density, water and mineral contents of compact human bone tissue depending on age. *Gegenbaurs morphologisches Jahrbuch, 115*(3), 273.

Wagner, D. W., Lindsey, D. P., & Beaupre, G. S. (2011). Deriving tissue density and elastic modulus from microCT bone scans. *Bone, 49*(5), 931-938.

Willems, H., Leiber, F., Kohler, M., Kreuzer, M., & Liesegang, A. (2013). Altitude, pasture type, and sheep breed affect bone metabolism and serum 25-hydroxyvitamin D in grazing lambs. *Journal of Applied Physiology, 114*(10), 1441-1450.

Worlock, P., Stower, M., & Barbor, P. (1986). Patterns of fractures in accidental and non-accidental injury in children: a comparative study. *British medical journal (Clinical research ed.), 293*(6539), 100-102.

Wullschleger, M. (2010). Effect of surgical approach on bone vascularisation, fracture and soft tissue healing: comparison of less invasive to open approach. (PhD), Queensland University of Technology, Brisbane.

Yang, J.-P., & Letts, R. M. (1997). Isolated Fractures of the Tibia with Intact Fibula in Children: A Review of 95 Patients. *Journal of Pediatric Orthopaedics, 17*(3), 347-351.

Yeni, Y. N., Shaffer, R. R., Baker, K. C., Dong, X. N., Grimm, M. J., Les, C. M., & Fyhrie, D. P. (2007). The effect of yield damage on the viscoelastic properties of cortical bone tissue as measured by dynamic mechanical analysis. *Journal of biomedical materials research Part A, 82*(3), 530-537.

Zioupos, P., & Currey, J. (1998). Changes in the stiffness, strength, and toughness of human cortical bone with age. *Bone, 22*(1), 57-66.

APPENDIX

List of conference proceedings

Cheong, V. S., Masouros, S. D., Bull, A. M. J. (2013). Fracture Simulation of Femoral Bone using Finite Element Method. Presented at the International Research Council on the Biomechanics of Injury in September 2013 (Gothenburg, Sweden).

Cheong, V. S., Bull, A. M. J. (2014). Long bone alignment for mechanical testing: Optimization from geometrical properties. Poster presented at the World Congress of Biomechanics in July 2014 (Boston, USA).

Cheong, V. S., Bull, A. M. J. (2014). Development of a methodology to optimize the alignment of long bones for biomechanical testing and finite element analysis. Presented at the Computer Methods in Biomechanics and Biomedical Engineering in October 2014 (Amsterdam, Netherlands).

```
1    Option Explicit
2    'Script written by CHEONG Vee San
3    'Script version 8 September 2013 - requires manual input of dblStart1,
      dblStart2, dblEnd1, dblEnd2 (run monkeywash2_precursor first) for
      visualization of segments and landmarks
4    'Script version 16 September 2013 11:01:30 AM
5    'Script version 24 September 2013 2:09:54 PM - mesh is now watertight
      and can compute meshvolumemoments correctly
6    Public ptTip
7    Public dblLandmarkCoord
8
9    Call Main()
10   Sub Main()
11
12     Dim arrObjects, strMesh
13     arrObjects = Rhino.GetObjects("Select mesh to calculate", 32)
14     If IsNull(arrObjects) Then Exit Sub
15
16     Rhino.EnableRedraw(False)
17
18     If Not Rhino.IsLayer("Layer 04") Then
19          Rhino.AddLayer "Layer 04", RGB(125, 38, 205)
20     End If
21
22     If Not Rhino.IsLayer("Layer 02") Then
23          Rhino.AddLayer "Layer 02", RGB(0, 127, 0)
24     End If
25     Rhino.CurrentLayer("Layer 02")
26
27     ' 1. join the 2 meshes (Rhino 5 only)
28     If UBound(arrObjects) > 0 Then
29          strMesh = Rhino.JoinMeshes(arrObjects, False)
30     Else
31          strMesh = arrObjects(0)
32     End If
33
34     Dim strMesh1, strMesh2
35     strMesh1 = Sectioning(strMesh, array(0, 0.6))
36
37     If UBound(arrObjects) > 0 Then
38          strMesh = Rhino.JoinMeshes(arrObjects, False)
39     Else
40          strMesh = arrObjects(0)
41     End If
42
43     strMesh2 = Sectioning(strMesh, array(0.6, 1.0))
44
45     strMesh1 = Rhino.MeshBooleanUnion(array(strMesh1, strMesh2))
46     strMesh = strMesh1(0)
47     Rhino.ObjectLayer strMesh, "Default"
48
49     'Rhino.EnableRedraw(True)
50
51     Dim arrMeshandAxis
52
53     arrMeshandAxis = AlignObject(strMesh, arrObjects)
54     strMesh = arrMeshandAxis(0)
55     If Not Rhino.IsLayer("Original") Then
56          Rhino.AddLayer "Original", RGB(105, 105, 105)
57     End If
58     Rhino.ObjectLayer strMesh, "Original"
59     Rhino.LayerVisible "Original", False
60
61
```

```
62      ' Stores a copy of the original mesh
63      'Dim strOldMesh: strOldMesh = Rhino.CopyObject(strMesh)
64
65      Dim arrDeleteLandmarks: arrDeleteLandmarks =
Rhino.ObjectsbyLayer("Landmarks")
66      If Not IsNull(arrDeleteLandmarks) Then
67           Rhino.DeleteObjects(arrDeleteLandmarks)
68      End If
69
70      ''''''''''''''''''''''
71      Dim dblPercent
72      Dim i,j
73      Dim icount: icount = 0
74
75      'Need to specify the size manually
76      Dim dblStart1: dblStart1 = 0.23
77      Dim dblEnd1: dblEnd1 = 0.23
78      Dim dblStart2: dblStart2 = 0.735
79      Dim dblEnd2: dblEnd2 = 0.735
80
81
82      'Sets the number of column (or first cut/more distal cuts)
83      ReDim dblWriteR2((dblEnd1-dblStart1)/0.05)
84      ReDim dblWriteI((dblEnd1-dblStart1)/0.05)
85      'Sets the number of rows (or second cut/more proximal cuts)
86      ReDim dblTemp((dblEnd2-dblStart2)/0.05)
87      ReDim dblITemp((dblEnd2-dblStart2)/0.05)
88      For i=dblStart1 To (dblEnd1 + 0.01) Step 0.05
89
90           Dim jcount: jcount = 0
91           For j=dblStart2 To (dblEnd2 + 0.01) Step 0.05
92
93                Rhino.Print i & "," & j
94
95                ' For speed, turn of screen redrawing
96                'Call Rhino.EnableRedraw(False)
97
98                If Not (i = 0 And j = 1) Then
99                     strMesh = Rhino.JoinMeshes(arrObjects, False)
100                    dblPercent = array(i, j)
101                    ' First function
102                    strMesh = Sectioning(strMesh, dblPercent)
103               End If
104
105               ' Second function
106
107               arrMeshandAxis = AlignObject(strMesh, arrObjects)
108               strMesh = arrMeshandAxis(0)
109               Dim strAxis
110               strAxis = arrMeshandAxis(1)
111               'strAxis = AxisPlot(strMesh, arrObjects)
112
113               'Monkey function 3 modified
114               'Monkey Function 3 - calculate the depth/length ratio
115               Dim dblSectionDimensions
116               dblSectionDimensions = Rhino.BoundingBox(strMesh)
117               Dim dblDepth(2)          'x,y,z
118               dblDepth(0) = Rhino.Distance(dblSectionDimensions(0),
dblSectionDimensions(1))
119               dblDepth(1) = Rhino.Distance(dblSectionDimensions(0),
dblSectionDimensions(3))
120               dblDepth(2) = Rhino.Distance(dblSectionDimensions(0),
dblSectionDimensions(4))
121
```

```
122                 ' Third function
123                 Dim arrTwoAxisPts
124                 arrTwoAxisPts = CalculateCentroid(strMesh, strAxis)
125                 'Array of CalculateCentroid = array(arrCentroidV,
arrNeutralPtV, arrSliceV)
126
127                 Dim dblIxxyyzz
128                 dblIxxyyzz = CalculateDeviation(arrTwoAxisPts(1),
arrTwoAxisPts(2), strMesh)
129
130                 'dblTemp(jcount) = array(i, j, dblR2YLine)
131                 dblITemp(jcount) = array(i, j, dblIxxyyzz)
132                 jcount = jcount + 1
133
134                 'So not to take up too much memory...
135                 'Rhino.DeleteObject(strMesh)
136                 Rhino.PurgeLayer("v_Slice")
137
138                 ' Don't forget to turn redrawing back on
139                 'Call Rhino.EnableRedraw(True)
140           Next
141           'dblWriteR2(icount) = dblTemp
142           dblWriteI(icount) = dblITemp
143           icount = icount + 1
144
145     Next
146     ''''''''''''''''''''''
147
148     'Call Rhino.EnableRedraw(False)
149
150     ReDim dblMeshVol(UBound(arrObjects))
151     Dim intObj, strCort
152     For intObj = 0 To UBound(arrObjects)
153          dblMeshVol(intObj) = Rhino.MeshVolume(arrObjects(intObj))
154     Next
155
156     If (dblMeshVol(0)(1) > dblMeshVol(1)(1)) Then
157          strCort = arrObjects(0)
158     Else
159          strCort = arrObjects(1)
160     End If
161
162     Call RollerPos(strAxis, strCort)
163     'strMesh = Rhino.JoinMeshes(arrObjects, False)
164     Call ProminentPoints(strCort)
165
166
167     ' Write to output file
168     'Call ExportPointsToExcel(dblWriteR2, dblStart1, dblEnd1, dblStart2,
dblEnd2)
169     Call ExportIToExcel(dblWriteI, dblStart1, dblEnd1, dblStart2,
dblEnd2, dblDepth)
170     ' Can be either a sub or function since no return value is required
171
172     Rhino.DeleteLayer("Layer 02" + "Layer 04")
173     Rhino.CurrentLayer "Landmarks"
174     Rhino.LayerVisible "v_Sections", False
175
176     Call Rhino.EnableRedraw(True)
177
178
179  End Sub
180
181  Function Sectioning (ByVal strMesh, dblPercent)
```

```
182
183     ' 2. calculates the max length of bone
184     Dim arrBounding : arrBounding = 0
185     arrBounding = Rhino.BoundingBox(strMesh)
186     Dim dblLengthV : dblLengthV = Rhino.Distance(arrBounding(0),
arrBounding(3))
187
188
189     ' 3. Creates the cutting line and plane
190     Dim arrStartPt: arrStartPt = arrBounding(0)
191     arrStartPt(2) = 0
192     Dim arrEndPt: arrEndPt = arrBounding(1)
193     arrEndPt(2) = 0
194
195     ' 4. Defines the amount to cut and call the special cutter function.
196     'dblPercent = (value from distal end, value from proximal end)
197
198     Dim position: position = array(1, 2)
199     Dim i
200
201     For i=0 To 1
202          If (dblPercent(i) > 0 And dblPercent(i) < 1 ) Then
203               strMesh = Cutter(dblPercent(i), position(i), arrStartPt,
arrEndPt, strMesh, dblLengthV)
204          End If
205     Next
206     'strMesh = Cutter(dblPercent, position, arrStartPt, arrEndPt,
strMesh, dblLengthV)
207
208     ' 5. Assigns to New Mesh (not essential) and close the mesh
209
210     Dim strCmd3
211     strCmd3 = "MatchMeshEdge _selid " & strMesh & " _enter _enter"
212     Rhino.Command strCmd3
213
214     ' 6. Checks if it's really closed as the previous step will fail
sometimes
215     If Not Rhino.IsMeshClosed(strMesh) Then
216          strCmd3 = "_FillMeshHoles _selid " & strMesh
217          Rhino.Command strCmd3
218     End If
219
220     strCmd3 = "_UnifyMeshNormals _selid " & strMesh & " _enter"
221     Rhino.Command strCmd3
222
223     'Dim arrToDelete: arrToDelete = Rhino.ObjectsByType(4 + 8)
224     'For i = 0 To UBound(arrToDelete)
225     '    If (Rhino.ObjectLayer(arrToDelete(i)) = "Layer 02") Then
226     '          Rhino.DeleteObject(arrToDelete(i))
227     '    End If
228     'Next
229     'Alternative way to delete objects by layer
230
231     '7. Declutter.Delete all curves, planes And open meshes.Or move them
To another layer
232     Dim arrToDelete: arrToDelete = Rhino.ObjectsbyLayer("Layer 02")
233     If Not IsNull(arrToDelete) Then
234          Rhino.DeleteObjects(arrToDelete)
235     End If
236
237     arrToDelete = Rhino.ObjectsByType(32)
238     For i = 0 To UBound(arrToDelete)
239          If Not (arrToDelete(i) = strmesh) Then
240               If Not Rhino.IsMeshClosed(arrToDelete(i)) Then
```

```
241                     Rhino.DeleteObject(arrToDelete(i))
242                End If
243           End If
244      Next
245
246      Sectioning = strMesh
247
248  End Function
249
250  Function ProminentPoints(ByRef arrObjects)
251
252      Dim strCort: strCort = Rhino.CopyObject(arrObjects)
253      ' 2. calculates the max length of bone
254      Dim arrBounding : arrBounding = 0
255      arrBounding = Rhino.BoundingBox(strCort)
256      Dim dblLengthV : dblLengthV = Rhino.Distance(arrBounding(0),
arrBounding(3))
257
258
259      ' 3. Creates the cutting line and plane
260      Dim arrStartPt: arrStartPt = arrBounding(0)
261      arrStartPt(2) = 0
262      Dim arrEndPt: arrEndPt = arrBounding(1)
263      arrEndPt(2) = 0
264
265      ' 4. Defines the amount to cut and call the special cutter function.
266      'dblPercent = (value from distal end, value from proximal end)
267
268      Dim dblPercent
269      dblPercent = array(0.02, 0.995)
270      Dim position: position = array(1, 2)
271      Dim i
272
273      For i=0 To 1
274           If (dblPercent(i) > 0 And dblPercent(i) < 1 ) Then
275                strCort = Cutter(dblPercent(i), position(i), arrStartPt,
arrEndPt, strCort, dblLengthV)
276           End If
277      Next
278      'strMesh = Cutter(dblPercent, position, arrStartPt, arrEndPt,
strMesh, dblLengthV)
279
280
281      '7. Declutter.Delete all curves, planes And open meshes.Or move them
To another layer
282      Dim arrToDelete
283
284      arrToDelete = Rhino.ObjectsByType(32)
285      For i = 0 To UBound(arrToDelete)
286           If Not Rhino.ObjectLayer(arrToDelete(i)) = "Layer 04"  Then
287
288                If Not Rhino.IsMeshClosed(arrToDelete(i)) Then
289                     Rhino.DeleteObject(arrToDelete(i))
290                End If
291
292           End If
293      Next
294
295      Rhino.DeleteObject(strCort)
296      arrToDelete = Rhino.ObjectsByLayer("Layer 02")
297      Rhino.DeleteObjects(arrToDelete)
298
299      Dim strMeshEnds, strMeshVertices(), VertCount, j
300      VertCount = 0
```

```
301     strMeshEnds = Rhino.ObjectsbyLayer("Layer 04")
302     Dim strEndsSplit(1)
303
304     If Not Rhino.IsLayer("Features") Then
305          Rhino.AddLayer "Features", RGB(125, 38, 205)
306     End If
307
308     Rhino.CurrentLayer("Features")
309
310     For i = 0 To 1
311          strEndsSplit(i) = Rhino.SplitDisjointMesh(strMeshEnds(i))
312
313          If Not IsNull(strEndsSplit(i)) Then
314                For j=0 To UBound(strEndsSplit(i)) Step 1
315                     Dim arrVertices
316                     arrVertices = Null
317                     arrVertices =
Rhino.MeshVertices(strEndsSplit(i)(j))
318                     If IsNull(arrVertices) Then
319                          arrVertices =
Rhino.MeshVertices(strEndsSplit(i)(j))
320                     End If
321
322                     Dim v, pointMin, pointMax
323
324                     If IsArray(arrVertices) Then
325
326                          If (i = 1) Then
327
328                               For Each v In arrVertices
329                                    If Not isArray(pointMin) Then
330                                         pointMin = v
331                                    ElseIf v(1) < pointMin(1) Then
332                                         pointMin = v
333                                    End If
334                               Next
335
336                               Rhino.AddPoint(pointMin)
337                               'Call Rhino.AddtextDot("YMin",
pointMin)
338                               pointMin = Null
339                          Else
340                               For Each v In arrVertices
341                                    If Not isArray(pointMax) Then
342                                         pointMax = v
343                                    ElseIf v(1) > pointMax(1) Then
344                                         pointMax = v
345                                    End If
346                               Next
347
348                               Rhino.AddPoint(pointMax)
349                               pointMax = Null
350                          End If
351
352                     End If
353
354                Next
355          End If
356
357     Next
358
359     arrToDelete = Rhino.ObjectsByLayer("Layer 04")
360     Rhino.DeleteObjects(arrToDelete)
361
```

```
362     arrToDelete = Rhino.ObjectsByType(4)
363     For i = 0 To UBound(arrToDelete)
364          If Not Rhino.ObjectLayer(arrToDelete(i)) = "Neutral Axes" Then
365               Rhino.ObjectLayer arrToDelete(i), "Layer 04"
366          End If
367     Next
368
369     'Sectioning = strMesh
370
371   End Function
372
373   Function RollerPos (ByRef strAxis, ByRef strCort)
374
375     Rhino.CurrentLayer "Landmarks"
376
377     '7 Finds the roller positions
378     Dim strSegment: strSegment = Rhino.ObjectsByLayer("v_Segments")
379     Dim strBox: strBox = Rhino.BoundingBox(strSegment(0))
380     Dim arrCentroid: arrCentroid =
Rhino.MeshVolumeCentroid(strSegment(0))
381     Dim arrRollerPt: arrRollerPt = arrCentroid
382     arrRollerPt(1) = strBox(0)(1)
383     Dim strRollerAxes(1)
384     strRollerAxes(0) = Rhino.CopyObject(strAxis(1), arrCentroid,
arrRollerPt)
385     arrRollerPt(1) = strBox(3)(1)
386     strRollerAxes(1) = Rhino.CopyObject(strAxis(1), arrCentroid,
arrRollerPt)
387     'For 4 point bending, 3 segments are needed, so
(strBox(0)(1)+strBox(3)(1))/3+strBox(0)(1). And change to Dim
strRollerAxes(3)
388     arrRollerPt(1) = (strBox(3)(1) - strBox(0)(1)) / 3 + strBox(0)(1)
389     arrRollerPt(1) = strBox(3)(1) - (strBox(3)(1) - strBox(0)(1)) / 3
390
391
392     Rhino.ObjectLayer strRollerAxes, "Layer 04"
393
394
395
396     Dim intLine, arrCMX, arrEv
397     For intLine = 0 To 1
398          arrCMX = Rhino.CurveMeshIntersection(strRollerAxes(intLine),
strCort, True)
399
400          If IsArray(arrCMX) Then
401
402               For Each arrEv In arrCMX
403                    'Rhino.Print Rhino.Pt2Str(arrEv(0)) & ", Face index
= " & CStr(arrEv(1))
404                    Rhino.AddPoint arrEv(0)
405                    'dblLandmarkCoord(LCount) = arrEv(0)
406                    'LCount = LCount + 1
407               Next
408
409          End If
410     Next
411   End Function
412
413   Function Cutter(dblPercent, Position, arrStartPt, arrEndPt, strMesh,
dblLengthV)
414     'Longer computational time by calling this function twice. But
solves the problem of null values in arrays
415
```

```
416     ' 4.1 Reference positions of cutting line and planes based on the
original objects selected
417     Dim strCutCrvV: strCutCrvV = Rhino.addCurve(array(arrStartPt,
arrEndPt))
418     Dim strCutPlaneV: strCutPlaneV = Rhino.AddCutPlane(strMesh,
arrStartPt, arrEndPt)
419
420     ' 4.2 Moves cutting line and plane to point of interest
421     Dim arrMoveV: arrMoveV = array(0, dblPercent * dblLengthV, 0)
422     Dim strCutter : strCutter = Rhino.MoveObject(strCutCrvV, arrMoveV)
423     strCutPlaneV = Rhino.MoveObject(strCutPlaneV, arrMoveV)
424
425     ' 4.3 Projects the cutting line to create surfaces for both objects.
426     Dim arrSectionV: arrSectionV = Rhino.ProjectCurveToMesh(strCutter,
strMesh, Array(0, 0, -1))
427     If IsNull(arrSectionV) Then
428          arrSectionV = Rhino.ProjectCurveToMesh(strCutter, strMesh,
Array(0, 0, -1))
429     End If
430     Dim arrSrf: arrSrf = Rhino.AddPlanarSrf(arrSectionV)
431     Dim strCmd
432     strCmd = "-_Mesh _selid " & arrSrf(0) & " _enter PolygonDensity 1
_enter"
433     Rhino.Command strCmd
434
435     Dim arrCap
436     arrCap = Rhino.LastCreatedObjects
437
438     ' 4.4 Use the cutting plane to section the mesh
439     Dim strCmd2
440     strCmd2 = "_MeshSplit _selid " & strMesh & " _enter" & " _selid " &
strCutPlaneV & " _enter"
441     Rhino.Command strCmd2
442
443     Dim arrMeshSplit
444     arrMeshSplit = Rhino.LastCreatedObjects
445
446
447
448     Dim strMeshToDiscard
449
450     ' 4.5. Cap the new meshes and fill any gaps *arrMeshSplit(0) is the
mesh on the more +ve y direction
451     'Check if it's to cut at the distal (1) or proximal (2) end
452     If (position = 1) Then
453          strMesh = Rhino.JoinMeshes(array(arrMeshSplit(0), arrCap(0)),
False)
454          If (UBound(arrMeshSplit) = 1) Then
455               strMeshToDiscard = arrMeshSplit(1)
456          End If
457
458     Else
459          strMesh = Rhino.JoinMeshes(array(arrMeshSplit(1), arrCap(0)),
False)
460          strMeshToDiscard = arrMeshSplit(0)
461     End If
462
463     If Not IsEmpty(strMeshToDiscard) Then
464          Rhino.ObjectLayer strMeshToDiscard, "Layer 04"
465     End If
466     Rhino.AddLayer "v_Segments", RGB(255, 0, 0)
467     Rhino.ObjectLayer arrSrf, "Layer 02"
468     Rhino.ObjectLayer strCutPlaneV, "Layer 02"
469     Rhino.ObjectLayer strMesh, "v_Segments"
```

```
470
471     Cutter = strMesh
472   End Function
473
474   Function AlignObject (strMesh, arrObjects)
475     '2. plot the centroid
476     Dim arrCentroid : arrCentroid = Rhino.MeshVolumeCentroid(strMesh)
477     Rhino.AddPoint arrCentroid
478
479     '3. retrieve principal directions
480     Dim arrMeshMoment
481     arrMeshMoment = Rhino.MeshVolumeMoments(strMesh)
482
483     'Sort through so that I1>12>I3
484     Dim arrPrincipalAxes
485     arrPrincipalAxes = sorter(arrMeshMoment)
486
487     Dim arrCombinedMesh
488
489     arrCombinedMesh = array(strMesh, arrObjects(0), arrObjects(1))
490
491     Dim strAxis(2)
492
493     'Use an IF function because loop while arrRotate(1)<1 crashes at
times
494     Dim dblerror: dblerror = 0
495     'If (dblerror < 1) Then
496     'Rotate both the neutral axis and the object
497     Dim rotateaxis
498     Dim dblerrorcount, dblmaxcount
499     dblerrorcount = 0
500     Do While (dblerror < 1)
501          rotateaxis = "Y"
502          Dim arrRotateResults
503          arrRotateResults = RotateObject(arrPrincipalAxes(0),
arrCombinedMesh, arrCentroid, rotateaxis)
504          strMesh = arrRotateResults(0)(0)
505
506          'Recalculate the VolumeMoment
507          arrMeshMoment = Rhino.MeshVolumeMoments(strMesh)
508          arrPrincipalAxes = sorter(arrMeshMoment)
509
510          'Calculate the new neutral axis
511          strAxis(0) = AddVector(arrPrincipalAxes(0), arrCentroid, 250)
512          '''End loop
513          dblerror = arrRotateResults(1)
514          If (dblerror > 0.999999999999999) Then
515               dblerrorcount = dblerrorcount + 1
516               dblerror = 1
517          End If
518          dblmaxcount = dblmaxcount + 1
519          If dblerrorcount = 1 Then Exit Do
520
521          'If (dblmaxcount = 100) Then
522          '     If (dblerrorcount < 0.99) Then
523          '          dblmaxcount = 0
524          '     End If
525          'End If
526
527          If dblmaxcount = 250 Then Exit Do
528     Loop
529
530
531     dblerror = 0
```

```
532
533     'Do
534     If (dblerror < 1) Then
535
536          rotateaxis = "Z"
537          arrRotateResults = RotateObject(arrPrincipalAxes(1),
arrCombinedMesh, arrCentroid, rotateaxis)
538          strMesh = arrRotateResults(0)(0)
539
540          'Recalculate the VolumeMoment
541          arrMeshMoment = Rhino.MeshVolumeMoments(strMesh)
542          arrPrincipalAxes = sorter(arrMeshMoment)
543
544          'Calculate the new neutral axis
545          strAxis(1) = AddVector(arrPrincipalAxes(1), arrCentroid, 50)
546          dblerror = arrRotateResults(1)
547          'If (loopcounter > 5) Then Exit Do
548          'Loop While arrRotateResults(1) < 1
549
550
551     End If
552
553     Dim arrToDelete: arrToDelete = Rhino.ObjectsByType(4 + 8192)
554     Rhino.DeleteObjects arrToDelete
555
556
557     '4. draws the principal axes
558     Rhino.AddLayer "Neutral Axes", RGB(255, 255, 255)
559     Rhino.CurrentLayer "Neutral Axes"
560     strAxis(0) = AddVector(arrPrincipalAxes(0), arrCentroid, 250)
561     Dim strText : strText = Rhino.AddTextDot("I1", ptTip, 10.0)
562     strAxis(1) = AddVector(arrPrincipalAxes(1), arrCentroid, 50)
563     strText = Rhino.AddTextDot("I2", ptTip, 10.0)
564     strAxis(2) = AddVector(arrPrincipalAxes(2), arrCentroid, 50)
565     strText = Rhino.AddTextDot("I3", ptTip, 10.0)
566
567
568     '5. calculates the mesh volume to find the cortical mesh (more
complete version in MonkeyHear
569     ReDim dblMeshVol(UBound(arrObjects))
570     Dim intObj, strCort
571     For intObj = 0 To UBound(arrObjects)
572          dblMeshVol(intObj) = Rhino.MeshVolume(arrObjects(intObj))
573     Next
574
575     If (dblMeshVol(0)(1) > dblMeshVol(1)(1)) Then
576          strCort = arrObjects(0)
577     Else
578          strCort = arrObjects(1)
579     End If
580
581     '6. finds the landmarks
582     Dim intLine, arrCMX, arrEv, LCount
583     LCount = 0
584     ReDim dblLandmarkCoord(5)
585     Rhino.AddLayer "Landmarks", RGB(0, 127, 0)
586     Rhino.CurrentLayer "Landmarks"
587     For intLine = 0 To UBound(strAxis)
588          arrCMX = Rhino.CurveMeshIntersection(strAxis(intLine), strCort,
True)
589
590          If IsArray(arrCMX) Then
591
592               For Each arrEv In arrCMX
```

```
593                     'Rhino.Print Rhino.Pt2Str(arrEv(0)) & ", Face index
= " & CStr(arrEv(1))
594                     Rhino.AddPoint arrEv(0)
595                     dblLandmarkCoord(LCount) = arrEv(0)
596                     LCount = LCount + 1
597                 Next
598
599             End If
600         Next
601
602
603         AlignObject = array(strMesh, strAxis)
604     End Function
605
606     Function RotateObject(vecDir, arrCombinedMesh, arrCentroid,
rotateaxis)
607         Dim arrVector1, arrVector2, arrVector, dotAngle, arrVecScaled,
ptTip, line, dblerror
608
609         'First draw the original neutral axis
610         arrVecScaled = Rhino.VectorScale(vecDir, 250)
611         ptTip = Rhino.PointAdd(arrCentroid, arrVecScaled)
612         line = Rhino.AddLine(arrCentroid, ptTip)
613         Rhino.ObjectLayer line, "Default"
614
615         'Then calculate the rotation stuff
616
617         Select Case rotateaxis
618             Case "Y"
619                 arrVector1 = Array(0, 1, 0)
620             Case "Z"
621                 arrVector1 = Array(0, 0, 1)
622
623         End Select
624         dotAngle = Rhino.VectorDotProduct(vecDir, arrVector1)
625
626         If (dotAngle < 0) Then
627             dblerror = -dotAngle
628
629             dotAngle = -dotAngle
630             dotAngle = ACos(dotAngle) / PI * 180
631         Else
632
633             dblerror = dotAngle
634             dotAngle = -ACos(dotAngle) / PI * 180
635         End If
636
637         arrVector = Rhino.VectorCrossProduct(arrVector1, vecDir)
638         arrVector2 = Rhino.VectorRotate(vecDir, dotAngle, arrVector)
639
640         'Rotate the line to check if the angle is correct - no need. all
working now
641         Dim AddVectorChanged
642         AddVectorChanged = Rhino.RotateObject(line, arrCentroid, dotAngle,
arrVector, True)
643         Rhino.ObjectLayer AddVectorChanged, "Neutral Axes"
644
645         'Then rotate the object
646         Dim strMesh2
647         Select Case rotateaxis
648             Case "Y"
649                 strMesh2 = Rhino.RotateObjects(arrCombinedMesh,
arrCentroid, dotAngle, arrVector, False)
650             Case "Z"
```

```
       strMesh2 = Rhino.RotateObjects(arrCombinedMesh,
arrCentroid, -dotAngle, arrVector, False)
 End Select

 RotateObject = array(strMesh2, dblerror)


End Function

Function sorter(arrMeshMoment)
 Dim arrI1, arrI2, arrI3, i, j

 Dim arrPriMoment
 arrPriMoment = arrMeshMoment(14)

 'The real sorter
 If (arrPriMoment(1) > arrPriMoment(0)) Then
    If (arrPriMoment(1) > arrPriMoment(2)) Then
       If (arrPriMoment(2) > arrPriMoment(0)) Then
          arrI1 = arrMeshMoment(16)
          arrI2 = arrMeshMoment(17)
          arrI3 = arrMeshMoment(15)
       Else
          arrI1 = arrMeshMoment(16)
          arrI2 = arrMeshMoment(15)
          arrI3 = arrMeshMoment(17)
       End If

    Else
       arrI1 = arrMeshMoment(17)
       arrI2 = arrMeshMoment(16)
       arrI3 = arrMeshMoment(15)
    End If

 Else
    If (arrPriMoment(0) > arrPriMoment(2))Then
       If (arrPriMoment(1) > arrPriMoment(2)) Then
          arrI1 = arrMeshMoment(15)
          arrI2 = arrMeshMoment(16)
          arrI3 = arrMeshMoment(17)
       Else
          arrI1 = arrMeshMoment(15)
          arrI2 = arrMeshMoment(17)
          arrI3 = arrMeshMoment(16)
       End If

    Else
       arrI1 = arrMeshMoment(17)
       arrI2 = arrMeshMoment(15)
       arrI3 = arrMeshMoment(16)

    End If

 End If
 sorter = array(arrI1, arrI2, arrI3)
End Function

'''''''''''''''''''''''''''''''''''''''''''''''''''''''''''''''''
Function AxisPlot(ByRef strmesh, ByRef arrobjects)
 Rhino.AddLayer "Neutral Axes", RGB(255, 255, 255)
 Rhino.CurrentLayer "Neutral Axes"
 Const rhObjectMesh = 32
 'Dim arrObjects
 'Dim strMesh
```

```
    'arrObjects = Rhino.GetObjects("Select meshes to join",
rhObjectMesh)

    '1. some coding to join the 2 objects (Rhino 5 only)
    'strMesh = Rhino.GetObject("Select mesh to calculate", rhObjectMesh)
    'If IsNull(strMesh) Then
    '    If UBound(arrObjects) > 0 Then
    '          strMesh = Rhino.JoinMeshes(arrObjects, False)
    '    End If
    'End If

    '2. plot the centroid
    Dim arrCentroid : arrCentroid = Rhino.MeshVolumeCentroid(strMesh)
    Rhino.AddPoint arrCentroid

    '3. retrieve principal directions
    Dim arrMeshMoment : arrMeshMoment = Rhino.MeshVolumeMoments(strMesh)
    Dim arrVecdir(2)
    arrVecDir(0) = arrMeshMoment(15)
    arrVecDir(1) = arrMeshMoment(16)
    arrVecDir(2) = arrMeshMoment(17)

    '4. draws the principal axes
    Dim strAxis(2)
    strAxis(0) = AddVector(arrVecDir(0), arrCentroid, 50)
    strAxis(1) = AddVector(arrVecDir(1), arrCentroid, 50)
    strAxis(2) = AddVector(arrVecDir(2), arrCentroid, 250)

    'arrRefVec records the reference vector, ie the smallest principal
axis
    'I will be measured from this line
    Dim arrPrincipalMoment, arrRefVec
    arrPrincipalMoment = arrMeshMoment(14)
    '    If arrPrincipalMoment(0) < arrPrincipalMoment(1) Then
    '          Rhino.ObjectLayer strAxis(0), "Layer 01"
    '          arrRefVec = atn(arrVecDir(0)(2) / arrVecDir(0)(0))
    'arrRefVec = (1 - arrVecDir(0)(0)) * 90
    'Rhino.RotateObject strAxis(0), arrCentroid, arrRefVec, array(0, 0,
1), True
    '    Else
    '          Rhino.ObjectLayer strAxis(1), "Layer 01"
    '          arrRefVec = atn(arrVecDir(1)(2) / arrVecDir(1)(0))
    '    End If
    '5. calculates the mesh volume to find the cortical mesh (more
complete version in MonkeyHear
    ReDim dblMeshVol(UBound(arrObjects))
    Dim intObj, strCort
    For intObj = 0 To UBound(arrObjects)
         dblMeshVol(intObj) = Rhino.MeshVolume(arrObjects(intObj))
    Next

    If (dblMeshVol(0)(1) > dblMeshVol(1)(1)) Then
         strCort = arrObjects(0)
    Else
         strCort = arrObjects(1)
    End If

    '6. finds the landmarks
    Dim intLine, arrCMX, arrEv
    Rhino.AddLayer "Landmarks", RGB(0, 127, 0)
    Rhino.CurrentLayer "Landmarks"
    For intLine = 0 To UBound(strAxis)
         arrCMX = Rhino.CurveMeshIntersection(strAxis(intLine), strCort,
True)
```

```
773
774         If IsArray(arrCMX) Then
775
776               For Each arrEv In arrCMX
777                     '          Rhino.Print Rhino.Pt2Str(arrEv(0)) & ",
Face index = " & CStr(arrEv(1))
778                     Rhino.AddPoint arrEv(0)
779               Next
780
781         End If
782     Next
783
784     AxisPlot = strAxis
785     'Rhino.DeleteObject(strMesh)
786   End Function
787
788
789
790   Function AddVector(ByVal vecDir, ByVal ptBase, ByVal scale)
791     On Error Resume Next
792     AddVector = Null
793
794     If IsNull(ptBase) Or Not IsArray(ptBase) Then
795          ptBase = Array(0, 0, 0)
796     End If
797
798     Dim vecDirScaled : vecDirScaled = Rhino.VectorScale(vecDir, scale)
799     Dim vecRev: vecRev = Rhino.VectorReverse(vecDirScaled)
800     vecRev = Rhino.VectorScale(vecRev, 0.75)
801
802     Dim ptRev : ptRev = Rhino.PointAdd(ptBase, vecRev)
803     ptTip :    ptTip = Rhino.PointAdd(ptBase, vecDirScaled)
804
805     Dim intOption
806     intOption = 1
807
808     If Not (intOption = 1) Then
809
810          AddVector = Rhino.AddLine(ptBase, ptTip)
811          Dim AddVecRev: AddVecRev = Rhino.AddLine(ptBase, ptRev)
812     Else
813          AddVector = Rhino.AddLine(ptRev, ptTip)
814
815     End If
816
817     'Rhino.CurveArrows AddVector, 2
818
819     If IsNull(AddVector) Then
820          Exit Function
821     End If
822   End Function
823   '''''''''''''''''''''''''''''''''''''''''''''''''''''''''''''''''''''''''''
824   Function CalculateCentroid(strObjects, strAxis)
825
826     'If IsNull(strObjects) Then Exit Sub
827     Dim arrBounding : arrBounding = Rhino.BoundingBox(strObjects)
828     Dim dblDomainU : dblDomainU = Rhino.Distance(arrBounding(0),
arrBounding(1))
829     Dim dblDomainV : dblDomainV = Rhino.Distance(arrBounding(0),
arrBounding(3))
830     Dim dblDomainW : dblDomainW = Rhino.Distance(arrBounding(0),
arrBounding(4))
831     Dim intCutsU
832     'intCutsU = Rhino.GetInteger("How many sections in U direction?", 0)
```

```
833     Dim intCutsV: intCutsV = 20
834     'intCutsV = Rhino.GetInteger("How many sections in V direction?", 0)
835     Dim intCutsW
836     'intCutsW = Rhino.GetInteger("How many sections in W direction?", 0)
837
838     'Calculates the number of sections
839     If Not (intCutsU = 0) Then
840          Dim dblStepU : dblStepU = dblDomainU / (intCutsU)
841          Rhino.AddLayer "u_Sections", RGB(255, 0, 128)
842     End If
843     If Not (intCutsV = 0) Then
844          Dim dblStepV : dblStepV = dblDomainV / (intCutsV)
845          Rhino.AddLayer "v_Sections", RGB(0, 102, 204)
846
847     End If
848     If Not (intCutsW = 0) Then
849          Dim dblStepW : dblStepW = dblDomainW / intCutsW
850          Rhino.AddLayer "w_Sections", RGB(128, 0, 128)
851     End If
852
853     Dim i,j,k
854     Dim strCmd, arrObjects
855     '''''''''''''''''''''''''''''''''''''''''''''''''''''''''''''''''''''''''''
856     ' V_Section
857     If Not (intCutsV = 0) Then
858          Rhino.CurrentLayer "v_Sections"
859          Dim arrStartPt: arrStartPt = arrBounding(0)
860          arrStartPt(2) = 0
861          Dim arrEndPt: arrEndPt = arrBounding(1)
862          arrEndPt(2) = 0
863
864          Dim intVcount : intVcount = 0
865          ReDim arrCutLineV(intCutsV), arrCutPlaneV(intCutsV),
arrNeutralPtV(intCutsV)
866          Dim arrCSX, strNeutralPt
867          ' 1. Creation of cutting lines
868          Dim strLineV: strLineV = Rhino.AddCurve(array(arrStartPt,
arrEndPt))
869          Dim strCutPlaneV: strCutPlaneV = Rhino.AddCutPlane(strObjects,
arrStartPt, arrEndPt)
870          For i = 0 To (dblDomainV + 0.1) Step dblStepV
871               '                If Not (intVCount > intCutsV) Then
872               If (i = 0) Then
873                    arrCutLineV(intVCount) = Rhino.CopyObject(strLineV,
array(0, 1, 0))
874                    arrCutPlaneV(intVCount) =
Rhino.CopyObject(strCutPlaneV, array(0, 1, 0))
875
876               Else
877                    If (intVCount = intCutsV) Then
878                         arrCutLineV(intVCount) =
Rhino.CopyObject(strLineV, array(0, dblDomainV - 1, 0))
879                         arrCutPlaneV(intVCount) =
Rhino.CopyObject(strCutPlaneV, array(0, dblDomainV - 1, 0))
880                         If IsNull(arrCutLineV(intVCount)) Then
881                              arrCutLineV(intVCount) =
Rhino.CopyObject(strLineV, array(0, dblDomainV - 1, 0))
882                         End If
883
884                    Else
885
886                         Dim arrMoveV: arrMoveV = array(0, i, 0)
887                         arrCutLineV(intVCount) =
Rhino.CopyObject(strLineV, arrMoveV)
```

```
888                           arrCutPlaneV(intVCount) =
Rhino.CopyObject(strCutPlaneV, arrMoveV)
889
890                       End If
891                 End If
892                 arrCSX = Rhino.CurveSurfaceIntersection(strAxis(0),
arrCutPlaneV(intVCount))
893                 If IsNull(arrCSX) Then
894                       arrCSX = Rhino.CurveSurfaceIntersection(strAxis(0),
arrCutPlaneV(intVCount))
895                 End If
896
897                 arrNeutralPtV(intVCount) = arrCSX(0, 1)
898                 strNeutralPt = Rhino.AddPoint(arrCSX(0, 1))
899                 Rhino.ObjectLayer strNeutralPt, "Neutral Axes"
900                 intVCount = intVCount + 1
901                 '                 End If
902           Next
903           Rhino.ObjectLayer strLineV, "Layer 02"
904           Rhino.ObjectLayer strCutPlaneV, "Layer 02"
905           Rhino.ObjectLayer arrCutLineV, "Layer 02"
906           Rhino.ObjectLayer arrCutPlaneV, "Layer 02"
907
908           ' 2. Creates surfaces and calculates their centroid
909           ReDim arrSrf(UBound(arrCutLineV))
910           ReDim arrCentroidV(UBound(arrCutLineV))
911           ReDim arrSliceV(UBound(arrCutLineV))
912           For j =0 To UBound(arrCutLineV)
913                 Dim arrSectionV
914                 arrSectionV = Rhino.ProjectCurvetoMesh(arrCutLineV(j),
strObjects, Array(0, 0, -1))
915                 arrSrf(j) = Rhino.AddPlanarSrf(arrSectionV)
916
917                 If (UBound(arrSrf(j)) > 0) Then
918                       If Not IsNull(arrSrf(j)(1)) Then
919                             'strCmd = "_Group _selid " & arrSrf(j-1)(0) &
" _selid " & arrSrf(j-1)(1) & " _enter"
920                             strCmd = "_AreaCentroid "
921                             For k=0 To UBound(arrSrf(j))
922                                   strCmd = strCmd & " _selid " &
arrSrf(j)(k)
923                             Next
924                             strCmd = strCmd & " _enter"
925                             Rhino.Command strCmd
926                             arrObjects = Rhino.LastCreatedObjects
927                             arrCentroidV(j) =
Rhino.PointCoordinates(arrObjects(0))
928                             arrSliceV(j) = arrObjects(0)
929                       End If
930                 Else
931                       Dim arrMP: arrMP =
Rhino.SurfaceAreaCentroid(arrSrf(j)(0))
932                       arrCentroidV(j) = arrMP(0)
933                       Dim strMP: strMP = Rhino.AddPoint(arrCentroidV(j))
934                       arrSliceV(j) = arrSrf(j)(0)
935                 End If
936
937           Next
938
939           Dim arrToDelete : arrToDelete = Rhino.ObjectsByLayer("Layer
02")
940           'For i = 0 To UBound(arrToDelete)
941           '     Rhino.DeleteObject(arrToDelete(i))
942           'Next
```

```
        Rhino.DeleteObjects(arrToDelete)

        ' 3. Connects the centroid
        Dim strNeutralAxisV : strNeutralAxisV = Rhino.AddPolyline(arrCentroidV)

        CalculateCentroid = array(arrCentroidV, arrNeutralPtV, arrSliceV)

    End If

    ''''''''''''''''''''''''''''''''''''''''''''''''''''''''''''''''''''''

    ' U_Sections
    If Not (intCutsU = 0) Then
        Rhino.CurrentLayer "u_Sections"
        arrStartPt = arrBounding(0)
        arrStartPt(2) = 0
        arrEndPt = arrBounding(3)
        arrEndPt(2) = 0

        Dim intUcount : intUcount = 0
        ReDim arrCutLineU(intCutsU), arrCutPlaneU(intCutsU), arrNeutralPtU(intCutsU)

        ' 1. Creation of cutting lines
        Dim strLineU: strLineU = Rhino.AddCurve(array(arrStartPt, arrEndPt))
        Dim strCutPlaneU: strCutPlaneU = Rhino.AddCutPlane(strObjects, arrStartPt, arrEndPt)
        For i = 0 To dblDomainU Step dblStepU
            If (intUCount <= intCutsU) Then
                If (i = 0) Then
                    arrCutLineU(intUCount) = Rhino.CopyObject(strLineU, array(1, 0, 0))
                    arrCutPlaneU(intUCount) = Rhino.CopyObject(strCutPlaneU, array(1, 0, 0))
                Else
                    If (i = dblDomainU) Then
                        arrCutLineU(intUCount) = Rhino.CopyObject(strLineU, array(dblDomainU - 1, 0, 0))
                        arrCutPlaneU(intUCount) = Rhino.CopyObject(strCutPlaneU, array(dblDomainU - 1, 0, 0))
                    Else
                        Dim arrMoveU: arrMoveU = array(i, 0, 0)
                        arrCutLineU(intUCount) = Rhino.CopyObject(strLineU, arrMoveU)
                        arrCutPlaneU(intUCount) = Rhino.CopyObject(strCutPlaneU, arrMoveU)

                    End If
                End If
                arrCSX = Rhino.CurveSurfaceIntersection(strAxis(2), arrCutPlaneU(intUCount))
                arrNeutralPtU(intUCount) = arrCSX(0, 1)
                strNeutralPt = Rhino.AddPoint(arrCSX(0, 1))
                Rhino.ObjectLayer strNeutralPt, "Neutral Axes"
                intUCount = intUCount + 1
            End If
        Next

        ' 2. Creates surfaces and calculates their centroid
```

```
        ReDim arrSrf(UBound(arrCutLineU))
        ReDim arrCentroidU(UBound(arrCutLineU))
        For j =0 To UBound(arrCutLineU)
            Dim arrSectionU
            arrSectionU = Rhino.ProjectCurvetoMesh(arrCutLineU(j), strObjects, Array(0, 0, -1))
            arrSrf(j) = Rhino.AddPlanarSrf(arrSectionU)

            If (UBound(arrSrf(j)) > 0) Then
                If Not IsNull(arrSrf(j)(1)) Then
                    'strCmd = "_Group _selid " & arrSrf(j-1)(0) & " _selid " & arrSrf(j-1)(1) & " _enter"
                    strCmd = "_AreaCentroid "
                    For k=0 To UBound(arrSrf(j))
                        strCmd = strCmd & " _selid " & arrSrf(j)(k)
                    Next
                    strCmd = strCmd & " _enter"
                    Rhino.Command strCmd
                    arrObjects = Rhino.LastCreatedObjects
                    arrCentroidU(j) = Rhino.PointCoordinates(arrObjects(0))
                End If
            Else
                arrMP = Rhino.SurfaceAreaCentroid(arrSrf(j)(0))
                arrCentroidU(j) = arrMP(0)
                strMP = Rhino.AddPoint(arrCentroidU(j))
            End If
        Next
        arrToDelete = Rhino.ObjectsByType(4)
        For i = 0 To UBound(arrToDelete)
            If (Rhino.ObjectLayer(arrToDelete(i)) = "u_Sections") Then
                Rhino.DeleteObject(arrToDelete(i))
            End If
        Next

        Dim strNeutralAxisU : strNeutralAxisU = Rhino.AddPolyline(arrCentroidU)

    End If

    ''''''''''''''''''''''''''''''''''''''''''''''''''''''''''''''''''''''''
    'strCutPlaneW is incorrect...
    ' W_Sections
    If Not (intCutsW = 0) Then
        Rhino.CurrentLayer "w_Sections"
        arrStartPt = arrBounding(0)
        arrEndPt = arrBounding(1)

        Dim intWcount : intWcount = 0
        ReDim arrCutLineW(intCutsW), arrCutPlaneW(intCutsW), arrNeutralPtW(intCutsW)
        ' 1. Creation of cutting lines
        Dim strLineW: strLineW = Rhino.AddCurve(array(arrStartPt, arrEndPt))
        Dim strCutPlaneW: strCutPlaneW = Rhino.AddCutPlane(strObjects, arrStartPt, arrEndPt)
        For i = 0 To dblDomainW Step dblStepW
            If (intWCount <= intCutsW) Then
                If (i = 0) Then
```

```
1045                              arrCutLineW(intWCount) =
Rhino.CopyObject(strLineW, array(0, 0, 1))
1046                              arrCutPlaneW(intWCount) =
Rhino.CopyObject(strCutPlaneW, array(0, 0, 1))
1047                        Else
1048                              If (i = dblDomainW) Then
1049                                    arrCutLineW(intWCount) =
Rhino.CopyObject(strLineW, array(0, 0, dblDomainW - 1))
1050                                    arrCutPlaneW(intWCount) =
Rhino.CopyObject(strCutPlaneW, array(0, 0, dblDomainW - 1))
1051                              Else
1052                                    Dim arrMoveW: arrMoveW = array(0, 0, i)
1053                                    arrCutLineW(intWCount) =
Rhino.CopyObject(strLineW, arrMoveW)
1054                                    arrCutPlaneW(intWCount) =
Rhino.CopyObject(strCutPlaneW, arrMoveW)
1055                              End If
1056                        End If
1057                        arrCSX = Rhino.CurveSurfaceIntersection(strAxis(1),
arrCutPlaneW(intWCount))
1058                        arrNeutralPtW(intWCount) = arrCSX(0, 1)
1059                        strNeutralPt = Rhino.AddPoint(arrCSX(0, 1))
1060                        Rhino.ObjectLayer strNeutralPt, "Neutral Axes"
1061                        intWCount = intWCount + 1
1062                  End If
1063            Next
1064
1065            ' 2. Creates surfaces and calculates their centroid
1066            ReDim arrSrf(UBound(arrCutLineW))
1067            ReDim arrCentroidW(UBound(arrCutLineW))
1068            For j =0 To UBound(arrCutLineW)
1069                  Dim arrSectionW
1070                  arrSectionW = Rhino.ProjectCurvetoMesh(arrCutLineW(j),
strObjects, Array(0, 1, 0))
1071                  arrSrf(j) = Rhino.AddPlanarSrf(arrSectionW)
1072
1073                  If (UBound(arrSrf(j)) > 0) Then
1074                        If Not IsNull(arrSrf(j)(1)) Then
1075                              'strCmd = "_Group _selid " & arrSrf(j-1)(0) &
" _selid " & arrSrf(j-1)(1) & " _enter"
1076                              strCmd = "_AreaCentroid "
1077                              For k=0 To UBound(arrSrf(j))
1078                                    strCmd = strCmd & " _selid " &
arrSrf(j)(k)
1079                              Next
1080                              strCmd = strCmd & " _enter"
1081                              Rhino.Command strCmd
1082                              arrObjects = Rhino.LastCreatedObjects
1083                              arrCentroidW(j) =
Rhino.PointCoordinates(arrObjects(0))
1084                        End If
1085                  Else
1086                        arrMP = Rhino.SurfaceAreaCentroid(arrSrf(j)(0))
1087                        arrCentroidW(j) = arrMP(0)
1088                        strMP = Rhino.AddPoint(arrCentroidW(j))
1089                  End If
1090            Next
1091            arrToDelete = Rhino.ObjectsByType(4)
1092            For i = 0 To UBound(arrToDelete)
1093                  If (Rhino.ObjectLayer(arrToDelete(i)) = "w_Sections")
Then
1094                        Rhino.DeleteObject(arrToDelete(i))
1095                  End If
1096            Next
```

```
1097
1098        Dim strNeutralAxisW : strNeutralAxisW =
Rhino.AddPolyline(arrCentroidW)
1099
1100    End If
1101
1102 End Function
1103
1104
1105 Function CalculateDeviation (ByVal neutPts, ByVal srfSlice, ByVal
strMesh)
1106    Dim i, arrEnd, arrSrfMoment
1107    ReDim strNeutPts(UBound(neutPts)), strYSlice(UBound(neutPts))
1108    ReDim dblIyy(UBound(neutPts)), dblIxx(UBound(neutPts)),
dblIzz(UBound(neutPts))
1109    For i = 0 To UBound(neutPts)
1110         'strNeutPts(i) = Rhino.Pt2Str(neutPts(i))
1111         arrEnd = array(0, 0, 0)
1112         'Rhino.CopyObjects array(strNeutPts(i), srfSlice(i)),
neutPts(i), arrEnd
1113         strYSlice(i) = Rhino.CopyObject(srfSlice(i), neutPts(i),
arrEnd)
1114         arrSrfMoment = Rhino.SurfaceAreaMoments(strYSlice(i))
1115         If Not IsNull(arrSrfMoment) Then
1116               dblIxx(i) = arrSrfMoment(6)(0)
1117               dblIyy(i) = arrSrfMoment(6)(1)
1118               dblIzz(i) = arrSrfMoment(6)(2)
1119         Else
1120               dblIxx(i) = 0
1121               dblIyy(i) = 0
1122               dblIzz(i) = 0
1123         End If
1124
1125    Next
1126
1127    If Not Rhino.IsLayer("v_Slice") Then
1128         Rhino.AddLayer "v_Slice", RGB(0, 0, 255)
1129    End If
1130    Rhino.ObjectLayer strYSlice, "v_Slice"
1131
1132    arrSrfMoment = Rhino.MeshVolumeMoments(strMesh)
1133    If (arrSrfMoment(10)(0) > arrSrfMoment(10)(2)) Then
1134         CalculateDeviation = array(dblIyy, dblIxx, dblIzz, "Y", "X",
"Z")
1135    Else
1136         CalculateDeviation = array(dblIyy, dblIzz, dblIxx, "Y", "Z",
"X")
1137    End If
1138
1139 End Function
1140
1141
1142 Sub ExportIToExcel(dblWriteI, dblStart1, dblEnd1, dblStart2, dblEnd2,
dblDepth)
1143
1144    Dim objXL
1145    Set objXL = CreateObject("Excel.Application")
1146
1147    objXL.Visible = True
1148
1149    objXL.WorkBooks.Add
1150
1151    objXL.ActiveWorkbook.Sheets.Add.Name = "Length"
1152    Dim i
```

```
objXL.Cells(1, 1) = "Dimension of Segment"
objXL.Cells(2, 1) = "X (Max)"
objXL.Cells(2, 2) = "Y"
objXL.Cells(2, 3) = "Z (Max)"
objXL.Cells(2, 4) = "Span Y/Z"
objXL.Cells(2, 5) = "Span Y/X"
For i=0 To 2
    objXL.Cells(3, i + 1).Value = dblDepth(i)
Next

objXL.Cells(3, 4) = dblDepth(1) / dblDepth(2)
objXL.Cells(3, 5) = dblDepth(1) / dblDepth(0)

objXL.Cells(4, 1) = "Distance between Landmarks"
For i=3 To 1 Step -1
    Select Case i
        Case 3
            objXL.Cells(5, 1) = Rhino.Distance(dblLandmarkCoord(2 * i - 2), dblLandmarkCoord(2 * i - 1))
        Case 2
            objXL.Cells(5, 3) = Rhino.Distance(dblLandmarkCoord(2 * i - 2), dblLandmarkCoord(2 * i - 1))
        Case 1
            objXL.Cells(5, 2) = Rhino.Distance(dblLandmarkCoord(2 * i - 2), dblLandmarkCoord(2 * i - 1))
    End Select
Next

''''''''''''''''''''''''''''''''''''''''''''''''''''
'Value Dump

Dim chartnum
For chartnum = 1 To 3

    objXL.ActiveWorkbook.Sheets("Sheet" & chartnum).Activate

    'Input the values for the first row (first cut)
    Dim j,k, icount, jcount
    icount = 0

    Dim intIndex
    intIndex = 2

    ReDim s((UBound(dblWriteI)+1)*(UBound(dblWriteI(UBound(dblWriteI))+1))
    For i=0 To UBound(dblWriteI)
        For j=0 To UBound(dblWriteI(i))
            'Sets the first and second cut location
            objXL.Cells(intIndex + icount, 1).Value = dblWriteI(i)(j)(0)
            objXL.Cells(intIndex + icount, 2).Value = dblWriteI(i)(j)(1)

            'Labels the series/legend
            s(icount) = CStr(objXL.Cells(intIndex + icount, 1)) & " - " & CStr(objXL.Cells(intIndex + icount, 2))

            'Value dump
            For k=0 To UBound(dblWriteI(i)(j)(2)(0))
                objXL.Cells(intIndex + icount, 3 + k).Value = dblWriteI(i)(j)(2)(chartnum - 1)(k)
            Next
            icount = icount + 1
        Next
```

```
1209        Next
1210
1211        'Labels the Second Moment of Inertia
1212        objXL.Cells(1, 1).Value = dblWriteI(0)(0)(2)(chartnum + 2)
1213
1214        'Formatting of the first two columns. Just to make things look
pretty
1215        Dim strRange, r1, r2
1216        strRange = "A2 :" & "B" & icount + 1
1217        Dim iSeries, rSeries, rPattern
1218        Set rPattern = objXL.Range(strRange)
1219        objXL.Range(strRange).Select
1220        objXL.Selection.Font.Bold = True
1221        objXL.Selection.Interior.ColorIndex = 1
1222        objXL.Selection.Interior.Pattern = 1 'xlSolid
1223        objXL.Selection.Font.ColorIndex = 2
1224
1225        'Create a chart
1226        'objXL.Range("A1:C1").Select
1227        Dim valRange
1228        valRange = UBound(dblWriteI(0)(0)(2)(0))
1229        strRange = "C2 :" & Chr(67 + valRange) & icount + 1
1230        objXL.Range(strRange).Select
1231        'objXL.ActiveSheet.Cells.Select
1232        objXL.Charts.Add
1233        objXL.ActiveChart.ChartType = 65 'xlLineMarkers
1234
1235        ' Some formatting of the chart
1236        Dim objChart
1237        Set objChart = objXL.ActiveChart
1238        With objChart
1239              .HasTitle = True' Add some titles
1240              If (chartnum = 1) Then
1241                    .ChartTitle.Text = "Segmental variation of Iyy"
1242              ElseIf(chartnum = 2) Then
1243                    .ChartTitle.Text = "Segmental variation of Ixx"
1244              Else
1245                    .ChartTitle.Text = "Segmental variation of Izz"
1246
1247              End If
1248              .ChartTitle.Characters(25, 2).Font.Subscript = True
1249              '.HasTitle.ChartTitle.Text.Characters(2,
2).Font.Subscript = True
1250              .Axes.Item(1).HasTitle = True
1251              .Axes.Item(1).AxisTitle.Caption = "Location of Segment/
%"
1252              .Axes.Item(1).TickLabels.Orientation = 0
1253              .Axes.Item(2).HasTitle = True
1254              .Axes.Item(2).AxisTitle.Caption = "Second Moment of
Inertia/ mm4 "
1255              .Axes.Item(2).AxisTitle.Characters(29,
1).Font.Superscript = True
1256
1257              .SeriesCollection(1).Name = "Desired Name"
1258
1259
1260              For iSeries = 1 To .SeriesCollection.Count
1261                    .SeriesCollection(iSeries).Name = s(iSeries - 1)
1262              Next
1263              '.HasLegend = False
1264
1265              'Retained the following in case there needs to be a value
dump of location vs I in future
```

```
1266              'Set xrng = wbMain.Sheets(1).Range("A2:A" +
CStr(lastRow))
1267              '.SeriesCollection(1).XValues = Array(0, 10, 20, 30, 40,
50, 60, 70, 80, 90, 100)
1268              .SeriesCollection(1).XValues = Array(0, 5, 10, 15, 20,
25, 30, 35, 40, 45, 50, 55, 60, 65, 70, 75, 80, 85, 90, 95, 100)
1269          End With
1270    Next
1271
1272    objXL.UserControl = True
1273
1274 End Sub
1275
1276 Public Function PI()
1277    PI = 4 * Atn(1)
1278 End Function
1279
1280 Public Function ASin(val)
1281    If (val >= 0.999999999999999) Then
1282          ASin = 2 * Atn(1)
1283    Else
1284          ASin = 2 * Atn(val / (1 + Sqr(1 - (val * val))))
1285    End If
1286
1287 End Function
1288
1289 Public Function ACos(val)
1290    If (val > 0.999999999999999) Then
1291          ACos = 0
1292    Else
1293          ACos = PI / 2 - ASin(val)
1294    End If
1295
1296 End Function
```